SCIENCE & ENGINEERING RESEARCHES

Editor

Ali KILIÇER

Science & Engineering Researches

Editor

Ali KILIÇER

LIVRE DE LYON

Science & Engineering Researches

Editor

Ali KILIÇER

Science & Engineering Researches

LIVRE DE LYON

PREFACE

This book, titled Science & Engineering Researches, is an important resource that presents innovative, pioneering academic studies in the fields of Engineering, Architecture and Science. Rather than monotonous books focusing on specific subjects, studies that include intellectual planning in the field of Engineering and Architecture and analytical studies in the field of Science and evaluate these studies on a statistical scale are much more successful and shed light on subsequent studies. Considering these conditions, the studies in the book you have in your hand include engineering, architecture, science and statistical studies that contribute to these fields. When the studies are examined, it will be seen that the information in the book contains current, latest data. When all these data are evaluated, it is aimed that the information in the book will shed light on future academic studies.

While creating the book, the articles were meticulously evaluated and went through referee and editor processes. We would like to thank the authors who shared their valuable work with us in the creation of the book, and our referees who quickly evaluated all the submitted studies without wasting time and contributed with their valuable opinions.

<div align="right">

Asst. Prof. Dr. Ali KILIÇER
Editor

</div>

CONTENTS

ADAPTIVE MICROCONTROLLER TRAINING SET DESIGN

Emre ÖZDEMİRCİ[1] & Çağatay ERSİN[2]

[1](Lt.) Vocational School - Çankırı Karatekin University
E-mail: emre_ozdemirci@hotmail.com
ORCID: https: 0000-0003-2619-4010

[2](Lt. Dr.) Vocational School - Çankırı Karatekin University
E-mail: cagatayersin@karatekin.edu.tr
ORCID: 0000-0001-5018-9313

1. Introduction

Rapid developments in the field of electronics and communication technology in recent years have enabled the use of microcontrollers with high accuracy and speed in different areas (Özcan and Günay, 2009). Students of electronics and computer departments of universities, vocational schools and vocational high schools need to take introductory microcontroller/ microprocessor design courses (Bachnak, 2005, Çalik et al.,2011, Aydın, 2019). During their education, graduates must have the ability to perform at least basic applications such as digital input and output, analog digital converter, LED applications, 7-segment display, LCD, various sensor applications, PWM generation, keypad and motor driving (Chaya, 2002). Even if the relevant training studies start with a theoretical explanation, they cannot be considered complete without practical studies. These application studies are carried out using different experimental sets, both in educational institutions and in places where hobby activities are carried out.

is carried out. Students can reinforce the knowledge and skills they learn in theoretical courses with experimental work in the laboratory. The purpose of any experiment can be considered to help students remember their theoretical knowledge and ensure the permanence of the information. Experiments should

support the theoretical lesson as much as possible and be easy to understand (Süzen and Kayaalp, 2019). It should be low-cost and scalable, with a laboratory where students can conduct experiments and provide permanent learning. It should also provide students with hands-on interaction and realistic data. Extensive development time is usually required for the design of laboratory experiment sets (John and Kymissis, 2010).

It has been determined that the application sets sold commercially are for hobby purposes rather than education. It has been determined that the application experiment sets carried out for educational purposes have some deficiencies or are high cost. When the studies titled implementation of application sets are examined, the modular structure of application sets limits the application diversity (Özdemirci, 2020). One of the tools used for application training is the Arduino microcontroller development board, which is an Italian development board (Babaoğlu, et al., 2020). Arduino is widely used because its application is simple and open source. Starting as a microcontroller project, various educational applications can be carried out in STEAM (Science, Technology, Engineering, Art and Mathematics) education, IoT (Internet of Things) and IoT-related areas. As the use of Arduino development boards increases, research on the development of various educational tools based on Arduino has also increased (Heo, 2019). At the same time, Arduino is a microcontroller that interacts with its environment with the help of sensors, collects data, records it and turns it into action. It is preferred in many areas because it has open-source software and hardware, is cheap and easily obtainable, and its programming language is easy and understandable (Babaoğlu, et al., 2020). When the experimental sets in use are examined, they are designed based on one or a certain group of microcontrollers and a limited variety of applications. However, as microcontrollers change day by day, existing experimental sets become obsolete. These working systems, which require cost and storage during use, become technological waste with the replacement of microcontrollers. In this study, an Arduino-based adaptive training set was developed to be used in the microcontrollers course. There are 31 different sensors and input and output applications in the training set. Thanks to the adaptive training set, students will be able to perform applications that are widely used today.

2. Material and Metod

One of the most common departments among technical education branches is the Electronics and Automation department. As in many branches of education,

it requires practical training as well as theoretical training. The applied training process is carried out, especially with microcontroller training sets (Kesler, 2021). However, the sets used in training and R&D studies are designed for only one type or a specific group of microcontrollers or development boards. This situation requires redesigning the training sets for each new variety. Each set of experiments performed has almost the same variety of applications as the sets made before it. So, essentially the same sets are produced over and over again. When the existing training sets are examined structurally, they emerge as two basic groups. The first of these are fixed-structure sets mounted on a single circuit (PCB) board. Although it provides ease of use, it creates negative situations in terms of flexibility of use. For example, in cards where the number of applications is increased, selection operations between applications are made through commutators. However, this also creates the necessity of choosing between two applications. The second group includes breadboards and training modules that allow more flexible working systems compared to fixed training sets. However, the installation process of such a working apparatus causes a loss of time. Unfortunately, operating problems that may occur due to lack of contact at the connection points in the circuits installed on the breadboard cannot be determined in most cases. In addition, it requires a greater cost to implement training modules and applications compared to training sets.

2.1. Purpose of Microcontroller Training Set

When it comes to microcontroller training, it is necessary to have a theoretical knowledge of the circuit structures in which algorithm development and coding will be done (Çıltık, 2008). For this reason, it is aimed at students and/or individuals who will do hobby work to be involved in the subject both structurally and in terms of coding. As stated

Table 1: Problems İdentified in the Study, Solutions
Found and Their Contributions

Problem	Solution	Contribution
Microcontroller diversity	Separating microcontroller structures from the physical structure of the training set,	To ensure widespread education by removing the limitation in microcontroller education.
Variety of applications and functions	Variety of uses with 31 applications and combinations, and interchangeable connection usage using jumper cables.	To prevent the "rote" approach caused by fixed PINs used in coding resources.
Timelessness	Making the microcontroller structure independent from the training set.	Unlike training sets with structural stability, it can be easily adapted to microcontroller development boards that can be developed.

in the explanation of the problems, a semi-modular structure was preferred as a solution to the negative conditions that emerged. As a semi-modular structure, one part of the experimental set will have a circuit structure, while the other part will consist of training modules. The main problem that the training set is planned to solve will be to eliminate the microcontroller limitation. This problem has been solved with the semi-modular system used. Pinout connections of all kinds of microcontrollers can be made using jumper cables used in training modules. This will allow us to continue our work by simply changing the microcontroller instead of purchasing a new experiment set with each new microcontroller. In addition, the necessity of choosing between the cable connections intended to be used and the applications encountered in fixed test sets will also be eliminated. The problems identified in the study, the solutions found and their contributions are shown in Table 1.

The design of Microcontroller Training set was designed in the Proteus Design Suite interface to have a semi-fixed combination. Header ports are used to ensure that the circuit connections of the applications are fixed and that the microcontrollers are replaceable. For professional use, the single-piece PCB design is designed with 2 layers. To enable amateur use of the training set, a three-piece card was designed and manufactured using the ironing technique. The 3D image is shown in Figure 1 and the PCB card design of the training set is shown in Figure 2.
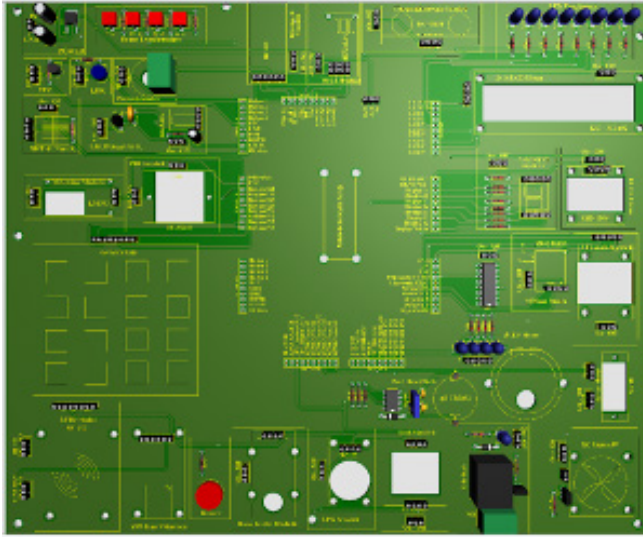
Figure 1. 3D image of the training set design
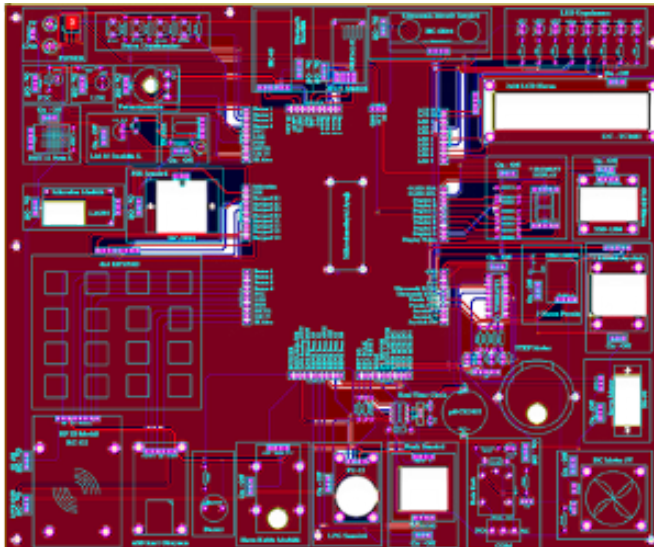
Figure 2. PCB card design of the training set

2.2. Design of Microcontroller Training Set

To raise students who enjoy algorithm development and microcontroller training courses and who can reflect basic circuit applications into their daily lives, it was decided, as a team, to develop a more comprehensive educational

material with more comprehensive applicability. It was deemed appropriate to use the semi-modular structure in the development of the relevant material. Thanks to the semi-modular structure, the "rote approach", which is an undesirable feedback that occurs when the connection ports of the applications are fixed, will be prevented. For the structural design of the training set, the applications that were explained within one academic year, were most commonly used among hobby studies, and were most suitable for use in the desktop training set were selected. The selection process was determined by interviews with faculty members who were actively involved in the relevant courses and by examining the resources used. The microcontroller is developed using basic input and output applications. The electronic circuit board design (PCB) of the training set was drawn using the Proteus 8 program. The open circuit diagram, PCB layout and 3D images of the circuit board are given in the figures. The manufacturing process of the PCB card of the circuit board is outsourced to a professional company because the circuit board has a two-layer structure. Due to the time given by the company for the production of the card, the prototype production of the training set could not be completed. The coding studies of the circuit structures and sample circuit studies of the applications selected to be used within the training set were carried out with modular studies. Additionally, as stated before, most of these applications have been used and tested in almost all existing experimental sets.
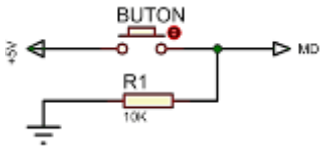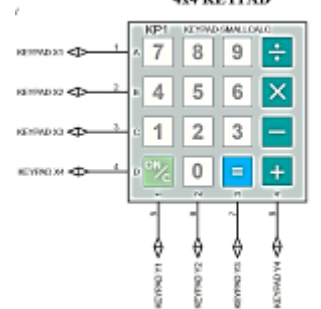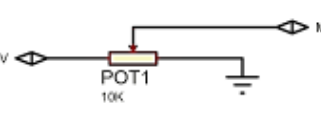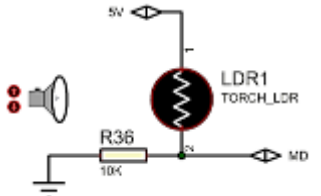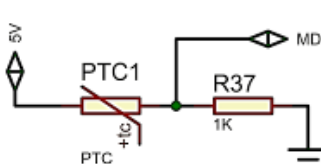
2.2.1. Applications and Modules Used
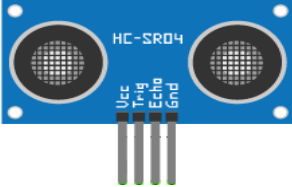
The selection process of the applications included in the training set was mentioned. In this section, application layers will be briefly mentioned. (Since there are thirty-one application floors, detailed explanations and examples cannot be given.)

2.2.1.1. Input Applications

The most basic analog and digital input applications used for microcontrollers have been compiled. With digital input applications, the signal applied to the inputs is read digitally as 0 or 1. Microcontrollers can make more precise measurements by sampling the signals applied to their inputs, depending on their conversion rate, with the Analog Digital Converters (ADC) they contain. Visuals and explanations of the login applications are shown in Table 2.

Table 2. Images and Explanations of Login Applications
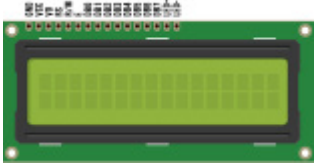
Application Name	Application connection type or visual	Description of the application card
Button Application		The buttons whose inputs are supplied with 5V DC voltage will send the digital position 1 to the microcontroller input as long as they are pressed. The pull-down resistor principle is used.
Keypad Application		It consists of a switch array with a matrix connection. It is named according to the number of rows and columns of its key sequence. It was deemed appropriate to use a 4x4 Keypad in this project. It works on the principle that the relevant row and column combination is short-circuited depending on the button pressed.
Potentiometer Application		Potentiometers are resistors whose setting can be changed by hand control. With its connection type in the circuit, POT is used alone as a voltage divider.
LDR Application		In addition to being a type of resistor, LDR is also a passive sensor and its resistance value varies depending on the light intensity. It produces an analog input signal by working as a voltage divider with the resistor connected in series in the training set.
PTC Application		PTCs are circuit elements whose resistance value changes positively with the ambient temperature. Together with the resistor connected in series, they form the voltage divider structure. Thus, it can be used as a temperature sensor.

Joystick Application		The joystick application consists of two originally positioned potentiometers and one button. It also has the same working principles.
IR Receiver Application		In this application layer, the values corresponding to the buttons on the remote control to be used with the IR receiver will be read and the control process will be provided depending on the application combinations.
LM 35 Application		LM35 is a sensor that changes the DC voltage level at its output depending on the temperature level of its environment. (10mV for 1oC)
DHT11 Application		The humidity of the environment is measured with DHT11. When the temperature is measured, the actual humidity value becomes clear.
Microphone App		The sound sensor card is a card that has a microphone on it and gives digital output according to the sound level in the environment. With the potentiometer on the card, instantaneous sound output can be obtained by eliminating ambient noise.
PIR Sensor Application		The name PIR comes from the initials of the words Passive Infra-Red. This means that this sensor works with infrared waves. Motion sensors are sensors that detect temperature and infrared wave changes in the environment. They have a fresnel lens in their structure. Thanks to this lens, the rays coming from objects in the environment allow the sensor to focus. When there is a wave change in the environment, the sensor performs detection.

Ultrasonic Distance Application		The signal applied from the Trig pin of the sensor emits an ultrasonic sound at a frequency of 40 kHz. When this sound wave hits any object and returns to the sensor, the Echo pin becomes active. By measuring the time between these two signals, the distance of the object from the sensor can be determined.
LPG Sensor Application		Its structure includes a wire sensitive to detect gas, a heating element and a load resistor. Methane gas passes over the wire in the sensor and causes the resistance of the wire to change. Analog output is obtained between 0V and 5V.
Air Quality Sensor Application		It detects gases such as carbon monoxide, alcohol and benzene in the air. Due to the measurement mechanism, the measurement results do not give separate measurement values for the gases. It produces analog value at the air quality level.
Color Sensor Application		TCS3200 provides the data it creates with the help of photodiodes and a current-frequency converter. The sensor produces a square wave at a frequency proportional to the intensity of the light falling on it, and color information can be obtained using this square wave.
3-Axis Compass Application		By using the HMC5883L sensor and voltage regulator on this module, it can be used easily in different systems and various applications. Measurements can be made in the range of ±1.3-8 Gauss using the I²C digital communication protocol at the sensor output.

2.2.1.2. Output Application

The most basic analog and digital output applications used for microcontrollers have been compiled. A numerical value of 0 or 1 is sent to applications using digital outputs. The microcontroller also has an analog output feature with its Pulse Width Modulation (PWM) function. Analog applications such as angular and speed control operations can also be performed with the PWM function. Visuals and descriptions of output applications are shown in Table 3.

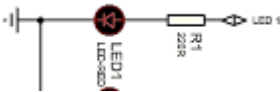**Table 3.** Images and Explanations of Output Applications

Application Name	Application connection type or visual	Description of the application card
LED Application		A resistor is connected in series to the LED in the circuit. This prevents high currents from passing through the LED and damaging the LED. When the microcontroller output reaches position 1, the LED turns on.
RGB LED Application		There are three different color LEDs in the structure of RGB LEDs. These are red, green and blue. RGB LEDs have a common anode or common cathode pin, as well as pins representing 3 colors. While fixed colors are obtained with digital outputs, intermediate color tones can also be obtained with analog outputs.
LCD Application		Consisting of 16 columns and 2 rows, it is used for character display. It has 16 pins. However, since using too many pins causes problems in practice, the I2C communication protocol is used.
OLED Application		OLED displays use organic compounds containing carbon and other components to create colors. Oled displays to be used with control cards use two different communication interfaces (I2C-SPI). Depending on the project to be used, these two different communication interfaces can be preferred.

7 Segment Display Application		Common anode 7 segment display is a type of LED display in which all LEDs + legs are used in common. In this case, the 3rd and 8th pins should be connected to the Arduino 5V pin. Data outputs are used by connecting to the relevant segment.
Buzzer Application		Piezo buzzers can produce different sounds depending on the intensity of the electrical signal. In this way, they can be used to play simple music.
RTC Application		DS1302 is a low-cost, highly sensitive RTC chip. This chip manages all timekeeping functions. It can easily interface with any microcontroller of your choice.
ROLE Application		Relay is a circuit element used to switch devices that draw high current using low currents. Briefly, the operating principles: When the coil of the relay is energized, the magnetized coil moves an armature, allowing the contacts to come into contact with each other, and transmission is achieved in the circuit.
Step Motor Application		They are stepper motors with high positioning precision. They are used in projects that require precision such as 3D printers and CNC. There are two types of stepper motors: bipolar and unipolar.
DC Motor Application		DC motors are machines that convert direct current energy into mechanical energy. It is based on the principle that when an electric current is applied to the windings inside the motor, they move under the influence of the magnetic force created in the opposite direction to the permanent magnets inside the motor. Speed control is done via analog output.

Servo Motor Application		They are DC motors that are not as sensitive as stepper motors but are not as free as brushless motors. It is very easy to drive directly with microcontroller cards such as Arduino. Although there are plenty of versions that rotate between 0-180 degrees on the market, there are also infinite rotation servo motors.

2.2.1.3. Input – Output Applications

There are also applications used in microcontroller applications that perform both input and output functions, beyond just input or output only. Input-Output applications that were decided to be used in the training set are given in Table 4.

Table 4. Images and explanations of Input-Output applications

Application Name	Application connection type or visual	Description of the application floor
Wi-Fi (NRF24L01) Application		The module is a low-power consumption module that allows you to communicate wirelessly at 2.4GHz frequency. The module supports the SPI interface and 1 module can be connected to up to 126 modules.
Bluetooth (HC-05) Application		Bluetooth is a technology that exists in almost all devices capable of wireless communication, from our mobile phones to our headphones. The most useful module for adding Bluetooth to microcontroller applications is the HC-05 model.
RFID (RC522) Application		It stands for Radio Frequency Identification, that is, identification with radio frequency. RFID technology is the technology used to recognize objects using radio waves. In our daily lives, we frequently encounter it on public transportation tickets and turnstiles at workplaces and schools.

USB Card Reader Application		There are two ways to connect with micro sd cards; SPI mode and SDIO mode. In applications, SPI mode is preferred, which is compatible with every SD card module and is simple and easy to use with any microcontroller.

2.3. Material Production Process and Creating the Training Set

The most highlighted feature of the microcontroller training set is the elimination of microcontroller limitations. This is not just about pin-out or PCB design. Physically, the layout of the microcontroller also requires free space. In order to provide this free space, a 2cm high stand was drawn using the Solidworks program and manufactured using a 3D printer to hold the microcontroller and/or microcontroller development board in a position independent of the training set. The microcontroller stand drawing is shown in Figure 3 and its usage is shown in Figure 4.
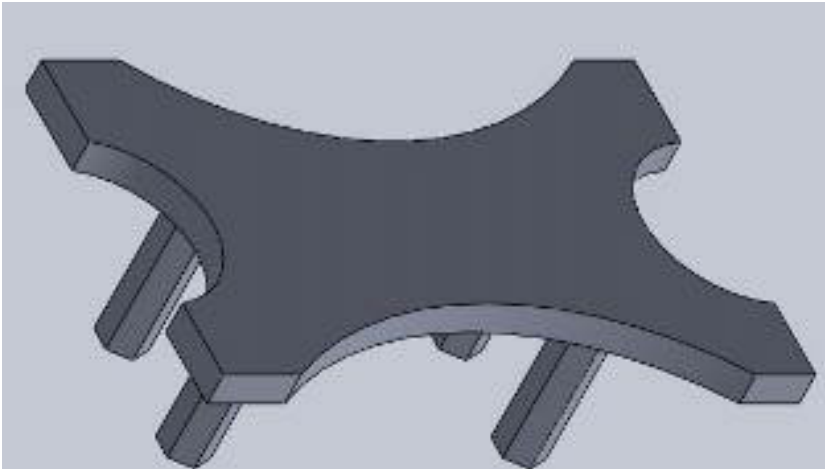
Figure 3. Microcontroller stand drawing
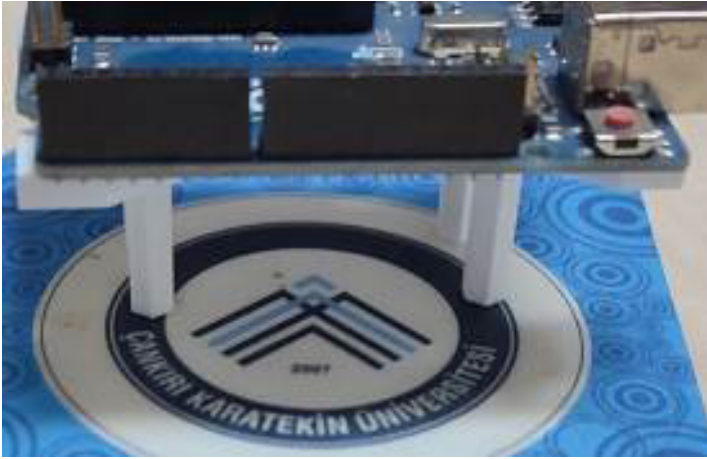
Figure 4. Microcontroller stand usage

The specified input and output modules are added to the system and circuit board for which the stand drawing is created. The image of the created training material is shown in Figure 5.
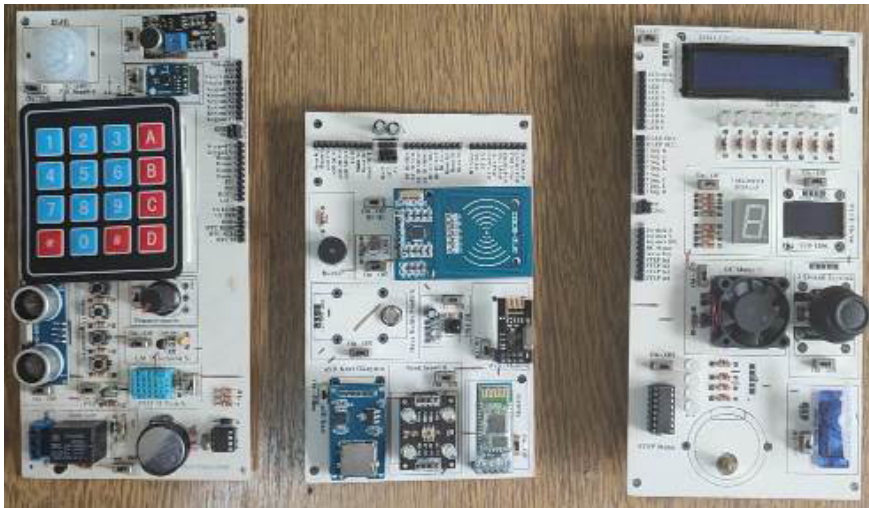
Figure 5. Microcontroller training set

3. Results

Educational experiment sets are materials used to better understand the theoretical course and achieve permanent learning. In this study, a training set that can be used with the Arduino microcontroller development board, which is

widely used today and allows students to learn input and output applications, was designed and implemented. The application modules to be used in the study are placed on the drawn circuit board. With the application experiment set, students will be able to code input and output applications with Arduino IDE software and will have the opportunity to make many applications. The design of the adaptive microcontroller training set will appeal to students who receive microcontroller and coding training in vocational high schools providing technical and vocational education, associate and undergraduate education institutions, and all users with special interest levels. In addition, Microcontroller coding training will have a much richer variety of applications than the existing experiment sets. With its variable structure and timelessness, it will move users away from a rote approach.

References

Özcan M., Günay H., "Mikrodenetleyici Geliştirme Seti Tasarım ve Uygulamaları", Selçuk Üniversitesi, Journal of Technical-Online, ISSN 1302/6178, (2009), 8(3), 307.

Bachnak R., "Teaching microcontrollers with hands-on hardware experiments", Journal of Computing Sciences in Colleges archive (2005), 20(4), 207 – 213.

Çelik, Ö. G. H., Aksaraylı, M., & Akkan, T. Mekatronik Programı Öğrencilerinin Başlangıç Bilgi Seviyelerinin Belirlenmesi İçin Bir Yöntem.

Aydın, S. (2019). Elektronik Ve Otomasyon Bölümü Müfredatının Değişimi ve II. Öğretim Elektronik Haberleşme Programı Öğrencilerinin Başarı Durumları. Milli Eğitim Dergisi, 48(223), 129-146.

Chaya H., "An embedded systems course using the PIC microcontroller", Proc. of the 2002 ASEE Annual Conference, (2002, June), 7.

Süzen, A. A., and Kayaalp, K. (2019). Free Fall Test System Controlled By Computer With Arduino. Mühendislik Bilimleri Ve Tasarım Dergisi, 7(4), 878-884.

John, S., & Kymissis, I. (2010). Lab kits using the Arduino prototyping platform. In IEEE Frontiers in Education Conference (FIE), pp. T3C-1.

Özdemirci, E. (2020). Realızation of Arduino Uno Application Set for Microcontroller Course. Electronic Letters On Science and Engineering, 16(1), 9-16.

Babaoğlu, M. G., Durmaz, K. K., & Öztekin, M. E. (2020). Arduino İle Yer Çekim İvmesinin Hesaplanması. Fen Bilimleri Öğretimi Dergisi, 8(1), 92-100.

Heo, G. (2019). Implementation of an Arduino Compatible Modular Kit for Educational Purpose. Journal of the Korea Institute of Information and Communication Engineering, 23(5), 547-554.

Kesler, P. (2021). Arduino-arm uyumlu esnek yapılı mikrodenetleyici eğitim seti (Master's thesis, Pamukkale Üniversitesi Fen Bilimleri Enstitüsü).

Çıltık, A. (2008). Sayısal tasarım kavramları ve algoritmik düşüncenin mimari tasarıma etkileri.

ARTIFICIAL NEURAL NETWORKS AND THEIR USE

Mehmet Selim KIZGIN[1] & Sevcan AYTAÇ[2]

[1]Fırat University, Deparment of Biotechnology, Elazığ
E-mail: mselimkizgin@gmail.com
ORCID: 0009-0004-8261-0028

[2]Fırat University, Deparment of Electronics and Automation, Elazığ
E-mail: saytac@firat.edu.tr
ORCID: 0000-0001-6689-2337

1. Introduction

1.1. Artificial Neural Networks

1.1.1. What is Artificial Neural Network?

Artificial Neural Networks (ANN) are computer software developed to automatically realize the abilities of the human brain, such as deriving new information through learning, creating and discovering new information, from data samples in the relevant field (Öztemel, E., 2012; Yılmaz, A., 2017; Alpaydın, E., 2011).

Our goal in engineering is not only to understand the brain but also to build useful machines. The reason we are interested in artificial neural networks is that we believe they will be useful in making us better computers. The brain is far superior to current engineering products in terms of some of its capabilities, such as image and speech recognition and learning, and these capabilities will be economically important applications when realized on computers. If we can understand how the brain performs these functions, we can create algorithms for these tasks and perform them artificially. The brain is one possible hardware implementation for learning or pattern recognition. If we can reverse engineer the representation and algorithm used from this implementation, and then derive

the computational theory from there, we can create our own representation and algorithm, and then our own hardware implementation, appropriate to the resources and constraints we have. We expect this new implementation we have created to be cheaper, faster, and more accurate. Just as the flying machines built until the discovery of the science of aerial motion resembled birds, it is natural that the experiments that imitated the brain until the discovery of the computational theory of intelligence consisted of processor networks like the brain. In other words, it can be said that we are currently at the level of representation and algorithm when understanding the brain. One day, we may understand that the effect of nerve cells and the connections between them on intelligence is a hardware detail, like the effect of feathers on flying. If we compare the brain to a processor network, what we need to do is distribute the problem to the processor network and determine local parameters. This is where learning comes into play. If such computers could learn from examples, we wouldn't have to program them and determine local parameters. So, artificial neural networks are a way to use parallel computers that we can produce with our current engineering knowledge, and they do not require programming thanks to learning (Öztemel, E.,2012; Yılmaz, A., 2017; Alpaydın, E., 2011).

1.1.2. History of ANN

In the early 1940s, neurophysicist McCulloh and mathematician Pittsilk developed the basic parametric nonlinear process model that provides the logical operation of a single neuron. In 1958, Rosenblatt developed a multilayer perceptron and an algorithm that could adjust the parameters of the model he developed. On the same date, Widrow and Hoff developed ADALINE (Adaptive Linear Model) and MADALINE (Multiple ADALINE) multi-adaptive linear neuron artificial neural network models and first used ANN to solve digital signal processing, weather forecasting and adaptive control problems. In 1969, Misky and Papert, in their book "Perceptron", showed that the single-layer perceptron network could not solve very simple operations (for example: the XOR problem) and claimed that there were insurmountable obstacles in the calculations. Based on this, Minsky and Papert emphasized that ANNs are not an interesting subject and almost brought the studies on ANNs to a halt (Keskenler, M.F.,Keskenler, E.F.,2017).

In the 1980s, as a result of the rapid development of computer technology and the increase in individual computers, studies on ANN were returned and a very rapid development was achieved in this field (Keskenler, M.F.,Keskenler,

E.F.,2017). The modern ANN era began with the study "Neural Networks and Physical systems" by Hopfield in 1982. (Keskenler, M.F.,Keskenler, E.F.,2017).

Nowadays, since the ANN theory is well known and has reached the completion stage, applied studies on ANN have gained great intensity in parallel with the developments in computer systems (Keskenler, M.F.,Keskenler, E.F.,2017).

1.1.3. General Features of Artificial Neural Networks

The characteristic features of artificial neural networks vary depending on the applied network model. While explaining the relevant models, the features of each model will be explained in detail. Here are the general characteristics valid for all models. These can be listed as follows:

The working style of the programs is not similar to known programming methods. It has a completely different information processing method than the information processing methods in which traditional programming and artificial intelligence methods are applied.

Storing information: In artificial neural networks, information is measured by the values of the connections of the network and stored in the connections. The data is not embedded in a database or within the program as in other programs. Information is hidden in links (weight) on the network and is difficult to reveal and interpret.

They learn using artificial neural networks examples. In order for artificial neural networks to learn events, examples related to that event must be determined. They gain the ability to make generalizations about the relevant event by using examples. If the example cannot be found or does not exist, it is not possible to train the artificial neural network. Examples are events that have happened. For example, a doctor asks his patient some questions and makes a diagnosis based on the answers he receives and prescribes medication. The diagnosis made through the questions asked and the answers given is considered an example. If the conversations a doctor has with his patients over a certain period of time and the diagnoses he makes are noted down and taken as an example, the artificial neural network can make similar diagnoses for similar diseases. It is very important that the samples obtained can fully show the event. If the event cannot be shown in all its aspects and relevant examples are not presented, successful results cannot be achieved. This is not because the network is problematic, but because the event is not displayed well to the

network. Therefore, creating and collecting samples is of special importance in artificial neural network science.

In order for artificial neural networks to be operated safely, they must first be trained and their performance tested. Training artificial neural networks means that existing examples are shown to the network one by one and the network determines the relationships between the events in the example by operating its own mechanisms. To train each network, the available samples are divided into two separate sets. The first is used to train the network (training set) and the other is used to test the performance of the network (test set). Each network is first trained with the training set. The training job is considered completed when the network starts giving correct answers to all examples. Then, the samples in the test set that the network has never seen are shown to the network and the answers given by the network are examined. If the network responds to samples it has never seen with acceptable accuracy, then the performance of the network is considered good and the network is put into use and used online if necessary. If the performance of the network is insufficient, then a solution is found such as retraining or training with new examples. This process continues until the network performance reaches an acceptable level.

They can produce information about unseen samples.

They can be used in detection-oriented events. Networks are mostly used to process information for perception. It can be seen from the applications that they are successful in this regard. Expert systems are used in knowledge-based solutions. In some cases, combining artificial neural networks and expert systems leads to creating more successful systems.

They can make pattern association and classification. In general, the purpose of most networks is to associate the patterns given as examples with themselves or others. Another purpose is to classify. The aim is to cluster the given examples and separate them into certain classes to decide which class a subsequent example will fall into.

They can perform pattern completion. In some cases, the network is given a pattern that contains missing information. The network is asked to find this missing information. For example, the network may be asked for a responsibility such as determining who owns a torn picture and providing the full picture. It is known that artificial neural networks produce very effective solutions in such events.

They have the ability to self-organize and learn. It is possible for artificial neural networks to adapt to new situations shown through examples and to constantly learn new events.

They can work with incomplete information. Once artificial neural networks are trained, they can work with incomplete information and produce results despite incomplete information in new samples. They continue to work with incomplete information. However, traditional systems do not work when information is missing. It is useful to draw attention to a point here. The fact that artificial neural networks operate with incomplete information does not mean that their performance will decrease. The decrease in performance depends on the importance of the missing information. The network itself learns which information is important during training. Users have no idea about this. When the performance of the network is poor, it is decided that the missing information is important. If the performance of the network does not decrease, it becomes clear that the missing information is not important.

They have fault tolerance. The ability of artificial neural networks to work with incomplete information makes them tolerant to errors. If some cells of the network fail and become inoperable, the network continues to operate. Depending on the importance of the responsibilities of the damaged cells of the network, the performance of the network may decrease. The network itself decides which cells' responsibilities are important during training. The user does not know this. This is why the network's information cannot be interpreted.

They can process ambiguous, incomplete information. Artificial neural networks have the ability to process ambiguous information. After learning the events, networks can make decisions under uncertainty by establishing relationships regarding the events they have learned.

They show gradual deterioration. The fact that artificial neural networks are tolerant to errors causes their degradation to be gradual (relative). A network breaks down slowly and gracefully over time. This is due to missing information or damage to the cells. Networks do not fail immediately when a problem arises.

They can only work with numerical information. Artificial neural networks work only with numerical information. Information represented with symbolic expressions must be converted into numerical representation. How this is done will be explained later. Expressing symbolic information with numerical values makes it difficult to interpret the information and explain the decisions (produced solutions).

In addition to the features mentioned above, each model developed may have its own unique features. If the features described here are carefully examined, it can be seen that artificial neural networks actually make very advantageous contributions to computer science. It can be seen that many problems that

cannot be solved with traditional computer software technology can be solved with artificial neural networks. For example, it would not be wrong to say that artificial neural networks are the most powerful problem-solving technique that can process incomplete, abnormal and ambiguous information. Even if there are techniques such as fuzzy propositional logic to process uncertain information, it is very difficult to find techniques that can work with incomplete information (Keskenler, M.F.,Keskenler, E.F.,2017).

1.1.4. Structure of Artificial Neural Network

As mentioned before, artificial nerve cells come together to form the artificial neural network. Nerve cells coming together does not happen randomly. In general, cells come together in 3 layers and in parallel within each layer to form the network (Özkaynak, E., 2012; Yılmaz, A., 2017; Alpaydın, E., 2011).

1.1.5. Advantages of ANNs

Although ANNs show different characteristics depending on the network model applied, they have a few basic common features (Canan, S., 2006).

1. ANNs consist of many cells, and these cells work simultaneously and perform complex functions. In other words, complex functions are produced by the simultaneous work of many cells. Even if any of these cells loses its function during the process, the system can continue to operate safely (Canan, S., 2006).

2. It obtains the general properties of the problem from the numerical information used during training and thus produces meaningful answers for inputs not used during training (Canan, S., 2006).

3. Certain types of non-linear subunits distributed on the structure make it possible to solve non-linear problems (Canan, S., 2006).

4. They can make logical decisions in the face of similar events (Canan, S., 2006).

5. Information processing methods are different from traditional programming. For this reason, many negativities brought by traditional programming can be eliminated (Canan, S., 2006).

6. It is spread throughout the network and stored in network connections measured by values. Loss of function of some cells does not cause loss of meaningful information (Canan, S., 2006).

7. They have distributed memory. In ANNs, information is kept distributed throughout the network. The connection and weight degrees of the cells show

the information of the network. For this reason, a single link has no meaning on its own (Canan, S., 2006).

8. They learn by using examples. In order for the ANN to learn, examples must be determined, these examples must be shown to the network and the network must be trained according to the desired outputs (Canan, S., 2006).

9. They can produce information about previously unseen samples. ANNs derive generalizations from the examples given to them during their training and can produce information about new examples with these generalizations (Canan, S., 2006).

10. They can be used in detection-oriented events. The areas where ANNs are most successful are application areas for perception. Their success in these areas has been proven.

11. ANNs can associate the patterns given to them as examples with themselves or others. In addition, by clustering the samples given to them, they can be used to decide which cluster the next data will be included in (Canan, S., 2006).

12. They can complete patterns. When patterns containing missing information are given to the network, they are successful in completing the missing information (Canan, S., 2006).

13. They have the ability to self-learn and organize. ANNs can learn online and train themselves (Canan, S., 2006).

14. They can work with incomplete information. Unlike traditional systems, once ANNs are trained, they can produce output even if the data contains incomplete information. This situation does not cause a loss of performance, the loss of performance depends on the importance of the missing information. Here, the importance of the information is learned during training (Canan, S., 2006).

15. They have error tolerance. The fact that ANNs can work with incomplete information and work even if some of their cells are damaged makes them tolerant to errors (Canan, S., 2006).

16. They show graceful degradation. A network undergoes slow, relative degradation over time. Networks do not break down immediately when a problem occurs (Canan, S., 2006).

1.1.6. Disadvantages of ANNs

ANNs have many advantages but also some disadvantages. Certain disadvantages (Canan, S., 2006).

1. It is hardware dependent. The most important problem of ANNs is that they are hardware dependent. The ability to perform parallel processing, which is one of the most important features and reasons for the existence of ANNs, shows performance with parallel processors (Canan, S., 2006).

2. There is no specific rule in determining the appropriate network structure. In ANNs, there is no rule developed to determine the appropriate network structure for the problem. The appropriate network structure is determined by experience and trial and error (Canan, S., 2006).

3. There is no specific rule in determining the parameter values of the network. There are no specific rules in determining parameters such as learning coefficient, number of cells, and number of layers in ANNs. Although there is no specific standard for determining these values, there may be a different approach for each problem (Canan, S., 2006).

4. The behavior of the network cannot be explained. This problem is the most important problem of ANNs. When ANN produces a solution to a problem, it does not give a clue as to why and how. This situation is a factor that reduces trust in the network (Canan, S., 2006).

2. Conclusion

Many studies have been conducted to date using machine learning techniques on cancer. (Korkmaz, S. A., & Esmeray, F., 2020 ; Korkmaz, S. A., & Binol, H., 2018; Korkmaz, S. A., Akçiçek, A., Bínol, H., & Korkmaz, M. F., 2017; Korkmaz, S. A., Bínol, H., Akçiçek, A., & Korkmaz, M. F., 2017; Korkmaz, S. A. ,2021; Korkmaz, S. A., & Esmeray, F. ,2018).

2.1. Uses of Artificial Neural Networks

• Artificial neural networks can be considered as one of the most up-to-date and perfect pattern recognizers and classifiers developed today; What makes these networks so up-to-date is their ability to work with incomplete information and process abnormal data, as mentioned above. They can produce very advantageous results, especially in jobs that require processing a large amount of data (such as radar data). Nowadays, many problems are actually turned into shape recognition problems and then solved. Therefore, there are many areas where artificial neural networks can be used. It has been shown that they are successful with thousands of examples seen in industrial and social life. However, it may not be logical to solve every problem with an artificial neural network. If there is a solution method that is sufficiently effective and efficient

to solve any problem, there is no point in using an artificial neural network. The lack of examples about the relevant event is also an important reason why these networks cannot be used. In order for a problem to be solved with an artificial neural network, one of the following conditions must be met (Canan, S., 2006).

- It should be possible to produce practical solutions to problems only with artificial neural networks (Canan, S., 2006).
- Although there are other solutions, it is necessary to ensure that artificial neural networks can produce easier and more effective solutions (Canan, S., 2006).
- When successful applications are examined, it can be seen that artificial neural networks are widely used in cases where there is non-linear, multi-dimensional, noisy, complex, imprecise, incomplete, flawed, high-error-prone sensor data and there is no mathematical model or algorithm to solve the problem. Networks developed for this purpose generally fulfill the following functions (Canan, S., 2006).
- It is possible to talk about many applications used in daily life, from financial issues to engineering and medical science. Some of these can be listed as follows (Canan, S., 2006).

- Data mining
- Optical character recognition and check reading
- Evaluating applications seeking loans from banks
- Predicting the product's performance in the market
- Detecting credit card fraud
- Optimum route determination for intelligent vehicles and robots
- Speech and fingerprint recognition in security systems
- Controlling robot movement mechanisms
- Predicting the lifespan and breakage of mechanical parts
- Quality control
- Filtering invalid echoes in communication channels
- Controlling and switching traffic density in communication channels
- Radar and sonar signals classification
- Production planning and scheduling
- Classifying blood cell reactions and blood analysis
- Detection of cancer and treatment of heart attacks
- Brain modeling studies
- Speech and facial recognition
- Word recognition, language translation

It is possible to reproduce them. The above is for the sole purpose of illustrating the areas in which they will generally be used; Otherwise, it is possible to see examples in almost every field (Canan, S., 2006).

References

Öztemel, E.,2012. Yapay Sinir Ağları (3.Baskı). İstanbul: Papatya Yayıncılık.

Yılmaz, A., 2017.Yapay Zeka(5.Baskı). Ankara: Kodlab Yayıncılık.

Alpaydın, E., 2011. Yapay Öğrenme(4.Baskı). İstanbul: Boğaziçi Üniversitesi Yayınevi.

Canan, S., 2006. Yapay Sinir Ağları ile GPS Destekli Navigasyon Sistemi. Doktora Tezi, Selçuk Üniversitesi, Fen Bilimleri Enstitüsü, Konya.

Keskenler, M.F.,Keskenler, E.F.,2017. Geçmişten Günümüze Yapay Sinir Ağları ve Tarihçesi. Takvim-i Vekayi dergisi ,5(2),8-18.

Korkmaz, S. A., & Esmeray, F., 2020. ANALYSIS OF LUNG CANCER WITH MACHINE LEARNING TECHNIQUES. *Theory and Research in Science and Mathematics II*, 201.

Korkmaz, S. A. (2017). Detecting cells using image segmentation of the cervical cancer images taken from scanning electron microscope. *The Online Journal of Science and Technology-October*, 7(4).

Korkmaz, S. A., & Binol, H., 2018. Classification of molecular structure images by using ANN, RF, LBP, HOG, and size reduction methods for early stomach cancer detection. Journal of Molecular Structure, 1156, 255-263.

Korkmaz, S. A., Akçiçek, A., Bínol, H., & Korkmaz, M. F. ,2017 September). Recognition of the stomach cancer images with probabilistic HOG feature vector histograms by using HOG features. In *2017 IEEE 15th International Symposium on Intelligent Systems and Informatics (SISY)* (pp. 000339-000342). IEEE.

Korkmaz, S. A., Bínol, H., Akçiçek, A., & Korkmaz, M. F., 2017). A expert system for stomach cancer images with artificial neural network by using HOG features and linear discriminant analysis: HOG_LDA_ANN. In 2017 IEEE 15th International Symposium on Intelligent Systems and Informatics (SISY) (pp. 000327-000332). IEEE.

Korkmaz, S. A., 2021. Classification of histopathological gastric images using a new method. Neural Computing and Applications, 33, 12007-12022.

Korkmaz, S. A., & Esmeray, F., 2018. A new application based on GPLVM, LMNN, and NCA for early detection of the stomach cancer. Applied Artificial Intelligence, 32(6), 541-557.

SHORT-TERM POWER LOAD FORECASTING USING DEEP LEARNING METHODS: A BENCHMARKING APPROACH

Ogan DEMİRHAN[1] & Mustafa Yasin ERTEN[2] & Hüseyin AYDİLEK[3]

*[1](Researcher), Department of Electrical and Electronics Engineering
Faculty of Engineering, Kırıkkale University, 71300, Kırıkkale, Turkey,
E-mail: ogandemirhan@hotmail.com,
ORCID: 0009-0008-0759-0126*

*[2](Asst. Prof.), Department of Electrical and Electronics Engineering
Faculty of Engineering, Kırıkkale University, 71300, Kırıkkale, Turkey,
E-mail: mustafaerten@kku.edu.tr,
ORCID: 0000-0002-5140-1213*

*[3](Asst. Prof.), Department of Electrical and Electronics Engineering
Faculty of Engineering, Kırıkkale University, 71300, Kırıkkale, Turkey,
E-mail: huseyinaydilek@kku.edu.tr,
ORCID: 0000-0003-3051-4259*

1. Introduction

In traditional power systems, the focus has generally been on the estimation of production resources. However, with the proliferation of Intelligent Electronic Devices (IEDs) and the advent of smart grid technology, the necessity for consumer-side load forecasting has emerged (Tascikaraoglu & Sanandaji, 2016). While long-term load forecasting is pursued to overcome challenges in power system infrastructure planning, mid-term and short-term load forecasting optimize system operations (Kong et al., 2017).

Accurate residential community load forecasting not only aims to increase the power source capacity of the residential community and enhance the

reliability of the electric power system, but also, through innovative approaches of public utilities, seeks to reduce households' energy consumption and bills (Zheng et al., 2018; Zheng et al., 2018).

Regarding methodologies for short-term load forecasting, the literature has frequently addressed the topic. However, most of these studies focus on production or commercial consumption (Semero et al., 2020; Chitalia et al., 2020). Customer-based forecasts, on the other hand, occupy a limited space in the literature and general forecasting methodologies do not focus on such users. Initially, traditional statistical methods were employed (Kim et al., 2019; Nguyen et al., 2021). However, these studies have not yielded satisfactory results, especially in short-term load forecasting. The primary deficiency of studies using traditional statistical methods, especially those correlating weather conditions with energy forecasting, is the non-linear nature of the data. Therefore, studies employing machine learning methods, thanks to their non-linear structure, have been able to capture connections between non-linear data, producing more successful results compared to traditional statistical methods (Shapi et al., 2021; Shin et al., 2022; Li et al., 2022). Furthermore, deep learning-based approaches, which have emerged in recent years, are increasingly preferred due to their sequential network structure enabling the capture of deeper connections (Sekhar & Dahiya, 2023; Chen et al., 2023; Motwakel et al., 2023).

In this study, the aim is to contribute to the resolution of issues related to short-term residential load forecasting. For this purpose, Recurrent Neural Network (RNN)-based deep learning methods, which have been successfully implemented in time series load forecasting models, are preferred. Methods such as Simple RNN, Long Short-Term Memory (LSTM), and Gated Recurrent Unit (GRU) have been employed for short-term residential load prediction. The Simple RNN, in comparison to the traditional RNN, comprises fewer layers. Owing to its simplified structure, it requires less computational effort and utilizes lower memory. On the other hand, LSTM and GRU possess more advanced structures, offering superior handling of long-term dependencies. Their advantages over the Simple RNN include a reduced vanishing gradient problem, thereby enhancing learning efficacy. Among these, LSTM exhibits an even more advanced structure than GRU. The performance of an RNN model is contingent upon the structure of the dataset. Consequently, this study separately examines the performance of the dataset in these three models.

The remainder of the study is organized as follows. Section 2 encompasses a literature review targeting studies using the same dataset and those focusing

on deep learning-based load forecasting. Section 3 describes the dataset used and the methodologies employed. Section 4 introduces Simple RNN, LSTM, and GRU models for short-term residential load forecasting and shares the results obtained. Section 5 contains the comparison and discussion of the results achieved.

2. Literature Review

In this study, the literature review is divided into two main sections. Firstly, research utilizing the ElectricityLoadDiagrams20112014 dataset (Trindade, A.,2015) has been examined. Subsequently, deep learning studies conducted in residential buildings, specifically those employing Simple RNN, LSTM, and GRU, as used in this study, have been considered.

Initially, studies using the same dataset have been systematically searched and reviewed in the indexes up to the end of 2023. Based on the information gathered so far, 11 studies have been identified, and details pertaining to these studies are provided below.

(Cao et al., 2023) developed an enhanced XGBoost model, termed WR-XGBoost, aimed at short-term district power load prediction. This model integrates a causal sliding window mechanism, differential processing of power data, and employs a random grid search for optimizing hyperparameters. The WR-XGBoost model demonstrates superior predictive capabilities and generalization compared to five other models, as evidenced by its performance across four datasets using seven statistical indicators. This model shows promise for application in power grid systems and intelligent power distribution. (Emami & Graf, 2023) introduced BuildingsBench, a comprehensive dataset and evaluation platform for short-term load forecasting (STLF) in both residential and commercial buildings. This dataset comprises over 900,000 simulated buildings representative of the U.S. building stock and more than 1,900 real residential and commercial buildings from diverse datasets. Their benchmark analysis using BuildingsBench reveals that while pretrained models trained on simulated data perform well with real commercial buildings, they exhibit lower efficacy in residential settings. They also identify limitations within the framework and propose future enhancements, including the integration of weather and metadata information into the datasets. (Chen, Q. and Zhang, 2023) developed a new U-shaped Transformer model that combines the strengths of MLP networks and transformer-based networks for time series analysis. This model includes skip layer connections and patch-based operations to preserve

high-frequency context and extract features at different scales. The efficiency and adaptability of the model is increased through a pre-training and fine-tuning approach using a larger dataset. The U-shaped Transformer model has been shown to achieve superior performance on various datasets with minimal computational requirements. It is emphasized that the developed approach has become a suitable solution for various time series analysis tasks. (Centofanti et al. 2023) established a robust method called RObust Cross-Directional Estimation of SSA (RODESSA) to analyze complex temporal data using Multivariate Singular Spectrum Analysis (MSSA). Since MSSA is a non-parametric approach, it enables simultaneous analysis of multiple time series by taking advantage of the dependencies between variables. The article also creates an advanced time series plot for outlier detection. A real data example of temperature analysis on passenger railway vehicles is presented to demonstrate the benefits of RODESSA. (Dooley et al., 2023) introduced ForecastPFN, a new approach to time series forecasting trained on synthetic data. The model provides a synthetic data distribution that reflects common real-world time series patterns and a solution to zero-shot predictions with a versatile transformer architecture. After extensive experiments, it was emphasized that ForecastPFN is more successful than existing methods in low-resource environments and offers faster calculation times. A new framework for long-term forecasting called Multi-Resolution Time Series Transformer (MTST) is introduced in the paper. MTST combines multi-resolution analysis and relative positional coding as a solution to the limitations of previous time series transformers. The developed model consists of a multi-branch architecture that models temporal patterns simultaneously at various resolutions. The results obtained showed that MTST outperformed the state-of-the-art models in terms of mean squared error and mean absolute error, confirming the effectiveness of the proposed design choices, with experimental results on multiple datasets (Zhang et al., 2023). This article introduces a new attention mechanism called correlated attention for multivariate time series analysis in Transformer models. This mechanism is designed to capture feature-based dependencies and cross-correlations between different variables in time series data. The correlated attention can be easily integrated into existing transformer models and increases performance in issues such as anomaly detection and classification. Experimental studies carried out the correlated attention mechanism has demonstrated its effectiveness in strengthening basic Transformer patterns (Nguyen et al., 2023). In this study, a Gaussian Mixture Model Based Detection (GMMD) scheme was developed to

detect data integrity attacks in the smart grid. The developed framework works by clustering historical data and learning the minimum and maximum values of each cluster, thus refining the normal data range. The performance of the GMMD scheme was evaluated using the ElectricityLoadDiagrams20112014 dataset and achieved a higher detection rate and a lower error rate compared to existing schemes based on the Min-Max model (Yang et al., 2016). (Amri et al., 2016) used Principal Component Analysis (PCA) and K-Means algorithm to cluster electricity usage patterns. The study used the ElectricityLoadDiagrams20112014 dataset, which is a dataset of electricity consumption of 370 customers over a year and performed clustering to identify similarities in consumption patterns. The results show that it may be useful for electricity providers in planning production based on consumption patterns. (Brunn et al., 2023) analyzed the feasibility of continuous ks-anonymization for smart meter data in the ElectricityLoadDiagrams20112014 dataset. The study compared the performance of CASTLE's continuous ks-anonymization with a global process focusing on metrics such as information loss and sensitive attribution features. The findings show that privacy is achieved with relatively low loss of utility and that continuous ks-anonymization is feasible. In the paper, a new algorithm known as Coefficient Tree Regression (CTR) is developed to analyze longitudinal data. The algorithm identifies groups of predictions with similar coefficients and reveals temporal patterns in high-dimensional data. The algorithm creates a tree structure by recursively splitting. The results obtained show that CTR outperforms other methods in terms of prediction accuracy and provides a more interpretable model (Sürer et al., 2023).

After summarizing the studies using the same data set, studies using the same method in residential buildings, that is, Simple RNN, LSTM and GRU methods, were examined. In this context, a summary of the literature is presented below. Since there are not many studies on Simple RNN in the literature, the only study found is described.

The paper describes a new system using RNN model for short-term load forecasting based on Multiple Time Series (MTS). The concept of the system is that time series datasets must consist of both continuous and discrete sequences. The model uses four different time series datasets to provide comprehensive information aimed at accurate load forecasting. In the study, it was shown that the proposed MTS-RNN model is superior to other methods in short-term load forecasting according to mean absolute percentage error (MAPE), mean absolute error (MAE) and mean square logarithmic error

(MSLE) metrics (Zhang et al., 2018). Since LSTM is frequently used in time series forecasting, it has also been discussed in short-term load forecasting studies. In the paper, a comparative analysis is carried out between the LSTM model and traditional forecasting techniques such as exponential smoothing and autoregressive integrated moving average (ARIMA) models for short-term residential load forecasting. The superior performance of the LSTM model in predicting residential load demand highlights its importance for precise load forecasting in smart grids. (Muneer et al., 2022). The article addresses the challenge of short-term load forecasting for individual residential households using LSTM. Within the scope of the study, data obtained from the Smart Grid Smart City project in Australia was used. Data analysis was conducted to reveal the diversity and variability of energy consumption at the individual household level. The study highlighted that the LSTM approach outperforms other methods in terms of accuracy of individual residential load estimation. (Kong et al., 2017). The article focuses on short-term residential load forecasting and examines the impact of weather characteristics on power load forecasting for individual energy users with an LSTM-based model. The study showed that using weather data improves the accuracy of load forecasting for most users but negatively affects customers who are not weather-sensitive (Wang et al., 2021). Finally, studies conducted with the GRU method, another method used within the scope of the study, are included. The article aims to optimize operational strategies for smart grids. For this purpose, a two-stage framework for short-term electricity power forecasting is presented. The first stage deals with data preprocessing steps, while the second stage uses a deep residual Convolutional Neural Network (CNN) combined with stacked LSTM layers to model sequential electrical patterns. It was emphasized that the proposed model reached the lowest error rates in terms of MAE, Mean Square Error (MSE) and Root Mean Square Error (RMSE) and was more successful than traditional forecasting models. (Khan et al., 2022). An improved sequence-to-sequence recurrent unit network (S2S-IGRU) is used in the paper. A new method for multi-horizon short-term electric load forecasting (STLF) with adaptive temporal dependence is proposed. The approach includes pre-training and fine-tuning steps to improve prediction accuracy. The effectiveness of the method has been evaluated on two electrical charge datasets and has been shown to exhibit improved accuracy and adaptability (Li et al., 2022). In this article, hybrid models, namely GRU and random forest (RF), are developed for short-term electric power load forecasting. In

the study, GRU-HAM-Model1 and GRU-DAM-Model1 models designed to predict the electrical load in different time intervals are introduced. The research also aimed to implement RF in reducing input sizes to create more efficient, lightweight GRU models. The effectiveness of the proposed models was compared with existing models to reveal their potential applicability in energy trading (Veeramsetty et al., 2022).

3. Material & Method

3.1 Material

Within the scope of the study, data obtained from Electricity LoadDiagrams20112014 and weather data provided by Solcast were utilized for training and testing purposes. The ElectricityLoadDiagrams20112014 dataset encompasses 15-minute interval energy consumption data in kW for 370 Portuguese customers between the years 2011 and 2014, sourced from the UCI Machine Learning Repository. Solcast, on the other hand, is a company with approximately 20 years of historical data in international solar forecasting and modeling. Their 15-minute weather data was utilized for this analysis. The downloaded data pertains to Portugal, where each row represents a timestamp, and columns contain distinct values. All variables are time-stamped in the ISO 8601 format and are in 15-minute intervals.

3.2 Methods

3.2.1 Simple RNN

The Simple RNN is fundamentally similar to the traditional RNN. Although they are fundamentally similar, the Simple RNN is a more straightforward variant of the RNN and comes with limitations. Simple RNNs are primarily used for connecting inputs to each other and for feedback. They have limited ability to learn long-term dependencies, leading to the vanishing gradient problem. Hence, advanced RNNs such as LSTMs and GRUs are preferred. In this structure, hidden states are updated, and outputs are obtained with the assistance of the tanh function. Figure 1 illustrates the cell structure of a Simple RNN. The mathematical expression used to find the hidden state in a Simple RNN is represented as Equation 1. The primary objective is to update the hidden state using current inputs and information from the previous hidden state (Tealab, 2018).
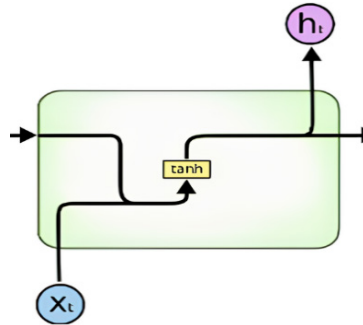
Figure 1. Simple RNN Cell Structure

$$h_t = tanh(W_{ih}x_t + W_{hh}h_{t-1} + b_h)$$

(1)

- h_t : Current hidden state
- x_t : Input at the current timestamp
- W_{ih} : Input-to-hidden weight matrix
- W_{hh} : Hidden-to-hidden weight matrix
- h_{t-1} : Hidden state from the previous timestamp
- b : Bias term for the hidden state

3.2.2. LSTM

Long Short-Term Memory (LSTM) networks are referred to as a specialized type of RNN capable of learning long-term dependencies. They were developed by Sepp Hochreiter and Jürgen Schmidhuber in 1997 to address the vanishing gradient problem observed in RNNs. LSTMs find applications in various fields such as handwriting recognition, speech recognition, machine translation, speech activity detection, robot control, video games, healthcare applications, time series-based data classification, processing, and prediction (Hochreiter, 1991; Hochreiter & Schmidhuber, 1997).

In the structure of an LSTM (Long Short-Term Memory) network, there exist the cell state, input gate, forget gate, and output gate. The cell state retains past information in the model across optional time intervals and facilitates the transmission of this information to other cells. Additionally, the result from the forget gate is multiplied by the result from the previous layer. Afterwards, it is combined with the value from the input gate. Figure-2 illustrates the LSTM cell structure.

The forget gate is a layer that determines which information from the previous layer and current input should be forgotten or retained. This gate applies a sigmoid function to assign values between 0 and 1 to this information. Values close to zero indicate the information to be forgotten, while values close to one signify the information to be retained. The mathematical expression for the forget gate is provided in Equation 2.
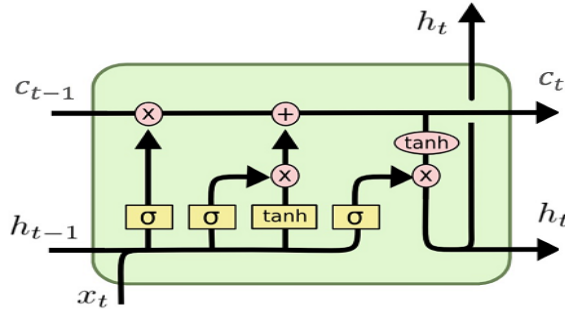
Figure 2. LSTM Cell Structure

$$f_t = \sigma\big(W_f[H_{t-1}, x_t] + b_f\big) \tag{2}$$

- f_t : The forget gate
- x_t : The input at the current timestamp
- b_f : The forget gate bias term
- H_{t-1} : The hidden state from the previous timestamp
- W_f : The weight matrix associated with the hidden state

The mathematical expressions representing which information within the forget gate will be discarded or retained are depicted in Equations 3 and 4.

$$C_{t-1} * f_t = 0 \qquad\qquad \text{eğer } f_t = 0 \tag{3}$$

$$C_{t-1} * f_t = C_{t-1} \qquad\qquad \text{eğer } f_t = 1 \tag{4}$$

The input gate shares a similar structure to the forget gate and, together with the sigmoid function, determines which information will be retained. Additionally, to regulate the network, values are scaled down to a range between -1 and 1 using the hyperbolic tangent function. The resulting two outcomes are multiplied to obtain new information. The mathematical expression for the input gate is provided in Equation 5.

$$i_t = \sigma(W_i[H_{t-1}, x_t] + b_i) \tag{5}$$

- i_t : The input gate
- x_t : The input at the current timestamp
- b_t : The bias term of the input gate
- H_{t-1} : The hidden state from the previous timestamp
- W_i : The weight matrix associated with the hidden state

The mathematical expression for the reduction of information in the input gate through the hyperbolic tangent function is given in Equation 6.

$$N_t = tanh(W_c[H_{t-1}, x_t] + b_c) \tag{6}$$

- N_t : The reduced form of information through the hyperbolic tangent function

The mathematical expression for the newly obtained information in the input gate is provided in Equation 7.

$$C_t = f_t * C_{t-1} + i_t * N_t \tag{7}$$

- C_{t-1} : The cell state at the current timestamp

Output gate is utilized to determine which information from the current state will be included in the output. Considering past and current states, it assigns a value between 0 and 1 to this information, determining the output. These values undergo another sigmoid function. Within the output gate, the value from the Cell State is combined with the product of the two values after passing through the hyperbolic tangent function, informing the next layer as the 'Previous Value'. The mathematical expression for the output gate is provided in Equation 8.

$$o_t = \sigma(W_o[H_{t-1}, x_t] + b_o) \tag{8}$$

- x_t : The input at the current timestamp
- b_o : The bias term of the function
- H_{t-1} : The hidden state from the previous timestamp
- W_o : Weight matrix associated with the hidden state

Finally, the mathematical expression used to compute the hidden state, i.e., the cell output, is provided in Equation 9 (Hochreiter & Schmidhuber, 1996; Felix et al., 2000).

$$H_t = o_t * \tanh(C_t) \tag{9}$$

3.2.3. GRU

Gated Recurrent Units (GRU) are a type of recurrent neural network (RNN) that emerged as an innovative solution to the vanishing gradient problem observed in traditional RNNs. Introduced by Kyunghyun Cho and colleagues in 2014, GRU incorporates gate mechanisms for selective information update and reset. These mechanisms enable GRU to retain significant information while forgetting irrelevant data. It finds applications across various domains, including natural language processing, time series analysis, among others. GRU bears similarities to LSTM; however, it requires less memory usage and offers faster processing advantages (Hochreiter, 1998; Cho et al., 2014).

GRU architecture encompasses an update gate and a reset gate. In some sources, the update gate is referred to as the input gate, while the reset gate is labeled as the forget gate. These gates significantly contribute to high efficiency in the model. While the update gate identifies long-term dependencies, the reset gate characterizes short-term relationships. Figure-3 illustrates the cell structure of the GRU (Chung, 2014).

Figure 3. GRU Cell Structure

The decision regarding how much the state should be updated is determined within the update gate, utilizing the current input and the previous hidden state. At this stage, a sigmoid function is employed. The mathematical expression for the update gate is provided in Equation 10.

$$z_t = \sigma(W_z[h_{t-1}, \ x_t] + b_z) \tag{10}$$

- z_t : The update gate
- W_z : The weight matrix of the update gate
- h_{t-1} : The hidden state from the previous timestamp
- b_z : The bias term for the update gate
- x_t : The input at the current timestamp

In the reset gate, the determination of how much of the past information will be discarded is established. Calculations in this gate are performed similarly to the update gate, employing a sigmoid function. The mathematical expression for the reset gate is provided in Equation 11.

$$r_t = \sigma(W_r[h_{t-1}, \ x_t] + b_r)$$ (11)

- r_t : The reset gate
- W_r : The weight matrix of the reset gate
- h_{t-1} : The hidden state from the previous timestamp
- b_r : The bias term for the reset gate
- x_t : The input at the current timestamp

Harnessing calculations within the reset gate, the previous hidden state is computed using the hyperbolic tangent function. The reset gate's value determines the influence of the previous hidden state. Consequently, new representations are formed by considering both the input and the past hidden state. The mathematical expression for the previous hidden state is provided in Equation 12.

$$h'_t = tanh(W[r_t * h_{t-1}, \ x_t] + b)$$ (12)

- r_t : The reset gate
- h'_t : After the reset gate, the hidden state in the current condition
- W : The weight matrix utilized in the computation
- h_{t-1} : The hidden state of the previous timestamp
- b : Bias term
- x_t : Input at the current timestamp

The final hidden state constitutes a blend of new and old memories governed by the update gate. Subsequently, this final hidden state is defined using linear interpolation. This interpolation encompasses the previous hidden state and a potential hidden state, with the update gate influencing the extent of this condition. The mathematical expression utilized for the final hidden state is provided in Equation 13.

$$h_t = (1 - z_t) * h_{t-1} + z_t * h'_t$$ (13)

4. Model Development and Experimental Results

The datasets span the period between 2011 and 2014 and are in CSV file format. Initial examination of the datasets revealed the use of commas to denote numerical values within the dataset containing records for 370 customers. Due to column separation by commas in the CSV files, a transformation was conducted to convert comma-separated numbers into a 'dot' ('.') format to prevent erroneous interpretations between values during processing. Subsequently, the total consumption values of users were computed, and these values were separately averaged and organized into two distinct columns. Considering that energy consumption by customers may vary based on weather conditions, the subsequent step aimed to merge these two derived columns with weather dataset information to predict energy consumption influenced by prevailing weather conditions.

During the consolidation phase, ensuring temporal alignment between datasets necessitated an inspection of date formats in both datasets, revealing disparities. To facilitate accurate matching, the date formats were rectified and standardized. The original format, prior to correction, adhered to the YYYY-MM-DDTHH:MM:SSZ structure; post-correction, this format transitioned into YYYY-MM-DD HH:MM:SS. Hence, a new format emerged by separating the date and time information delimited by the 'T' and 'Z' characters with a space. Subsequently, a check was performed for 'NaN' (empty) and duplicate values within the date columns of the datasets. Any identified empty or repeated date entries were removed. Following this, consolidation involved merging identical dates within the datasets, scrutinizing them, and forming a unified date column. Upon completing this process, the datasets were merged.

Table 1. The Hyperparameter Values for the Models

Hyperparameter	LSTM	GRU	Simple RNN
Layer Size	4	6	4
Model Nodes	1 LSTM Layer	1 GRU Layer	1 Simple RNN
Epoch	5	7	5
Batch Size	32	32	32
Optimizer	Adam	Adam	Adam
Learning Rate	1e-5	1e-6	1e-6
Dense	3	5	3
# of Neurons in Layers	128, 64, 32, 1	256, 126, 64, 64, 32, 1	256, 128, 32, 1
Loss Function	MSE	MSE	MSE

Three prediction models were developed using LSTM, GRU, and Simple RNN for forecasting electricity consumption. The hyperparameter values for the created models are provided in the table above.

Following preparation for analysis, the consolidated dataset was divided into 80% training and 20% test data portions. Models were then executed, and the resulting metric outcomes are presented below.

Table 2. Daily Prediction

	Simple RNN	LSTM	GRU
MAE	43,103	37,925	36,185
RMSE	55,850	50,365	47,778
MAPE	0,289	0,277	0,263

Table 3. Weekly Prediction

	Simple RNN	LSTM	GRU
MAE	56,088	40,476	40,413
RMSE	70,847	52,027	50,878
MAPE	0,342	0,299	0,283

Table 4. Monthly Prediction

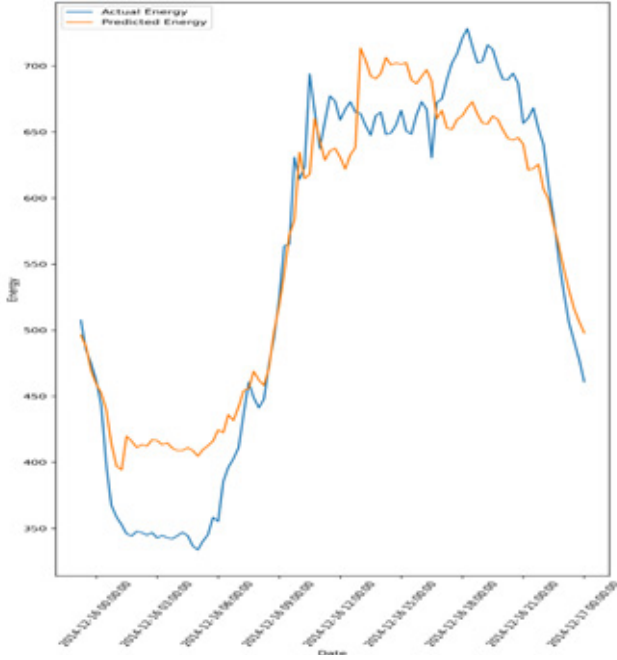|	Simple RNN	LSTM	GRU
MAE	45,396	42,613	43,537
RMSE	56,488	53,336	53,862
MAPE	0,295	0,303	0,290

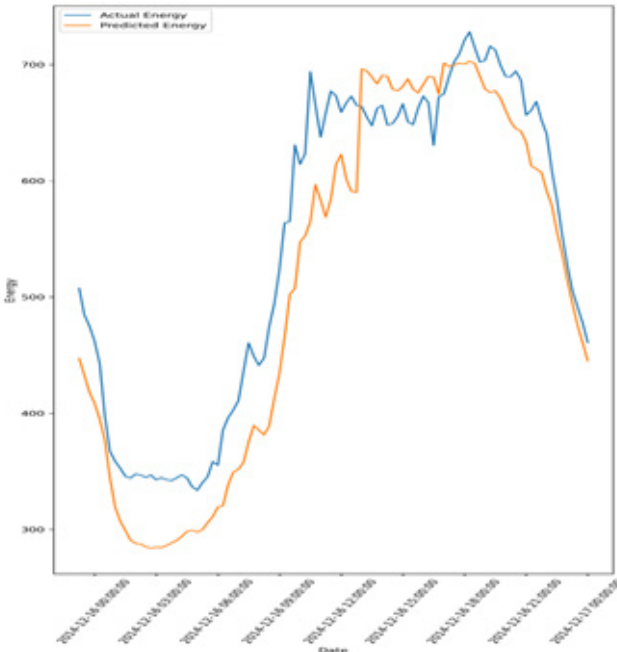**Figıre 4.** Simple RNN Prediction Graph (Daily)

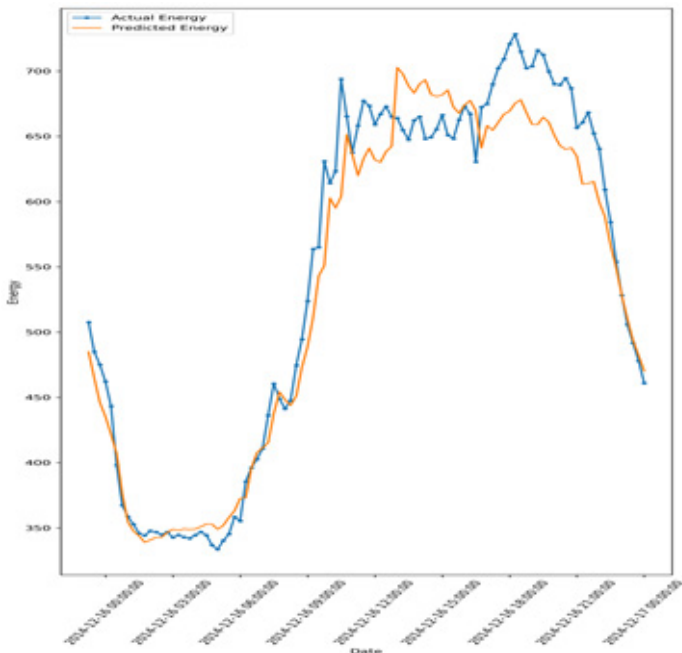**Figıre 5.** LSTM Prediction Graph (Daily)

Fıgıre 6. GRU Prediction Graph (Daily)
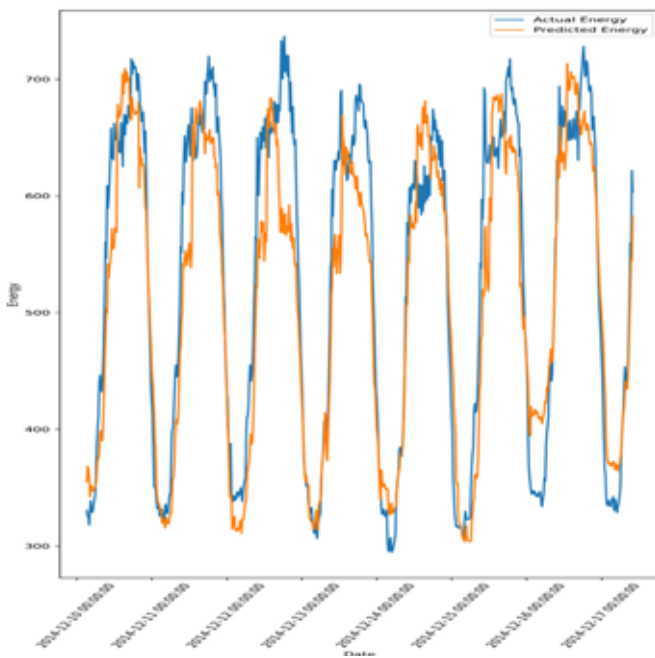
Fıgıre 7. Simple RNN Prediction Graph (Weekly)
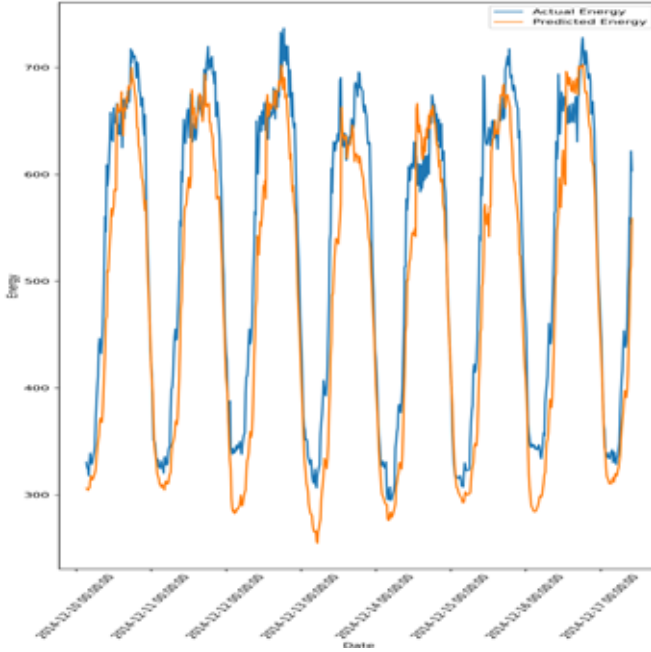
Figıre 8. LSTM Prediction Graph (Weekly)
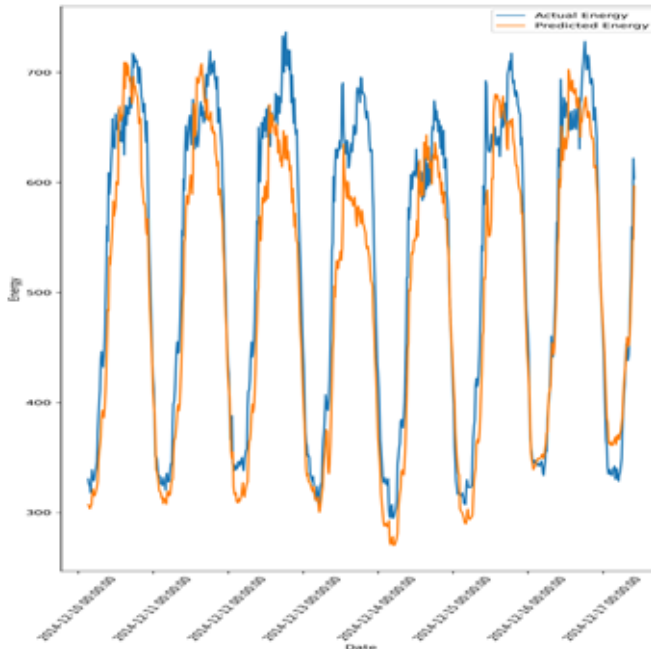
Figıre 9. GRU Prediction Graph (Weekly)
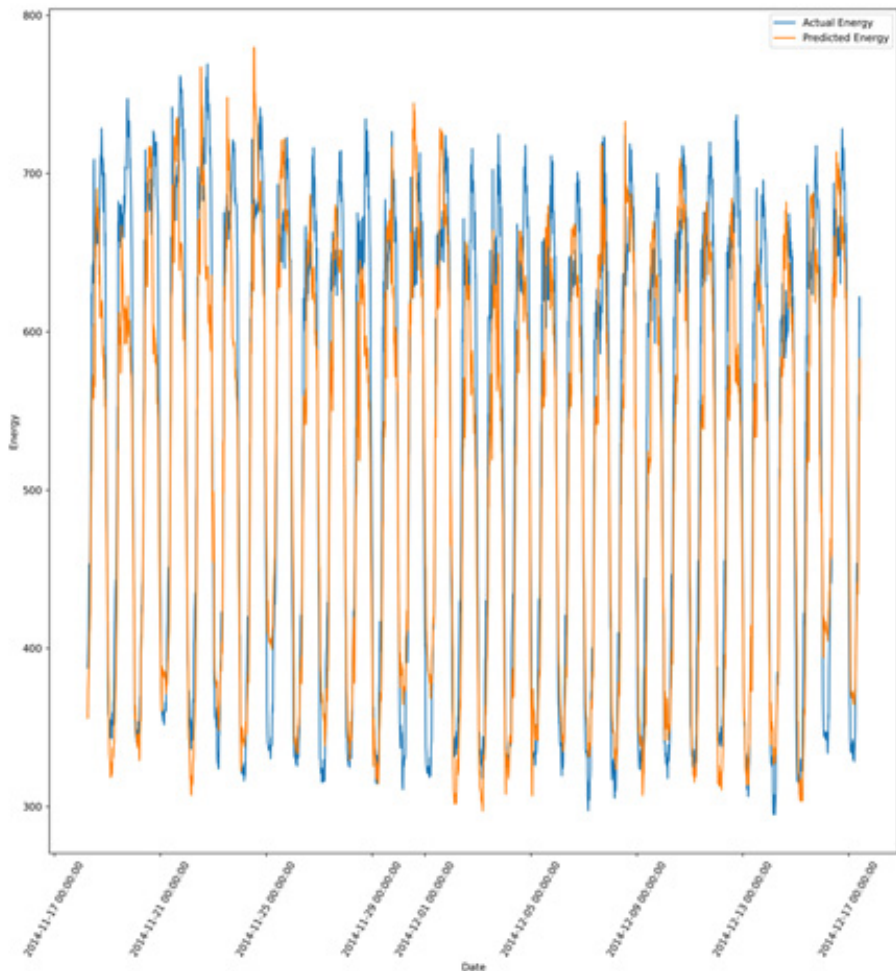
Figıre 10. Simple RNN Prediction Graph (Monthly)
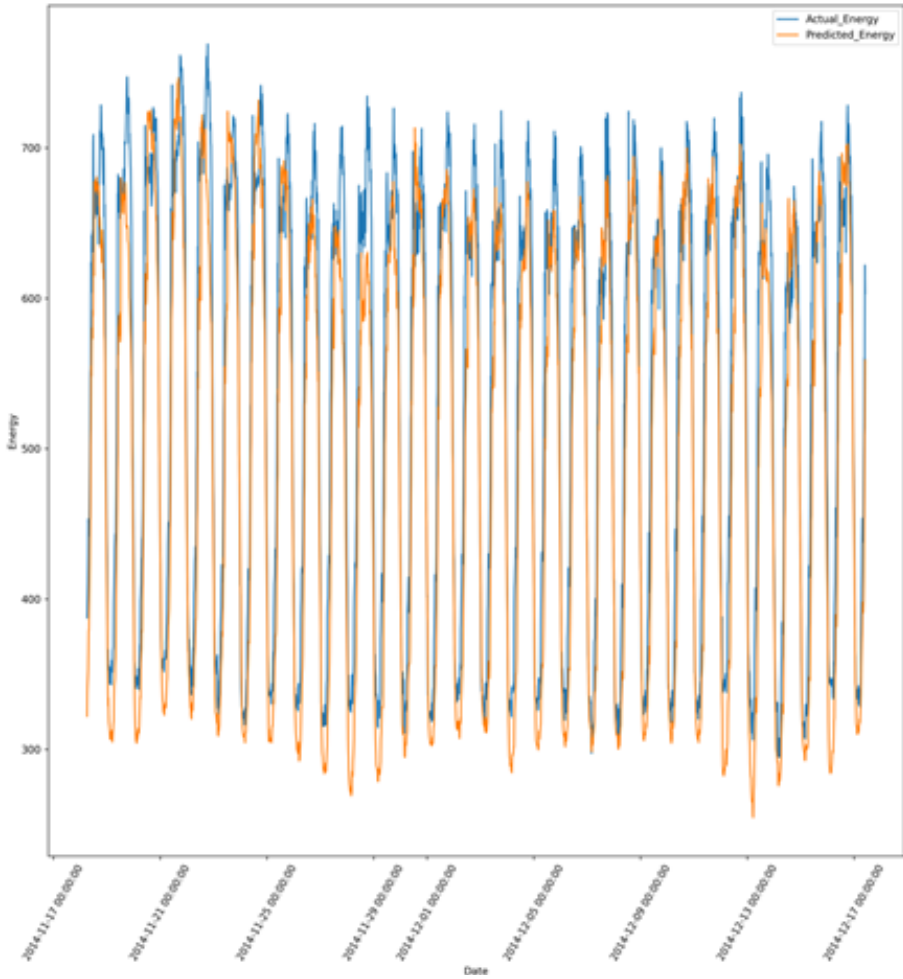
Figıre 11. LSTM Prediction Graph (Monthly)
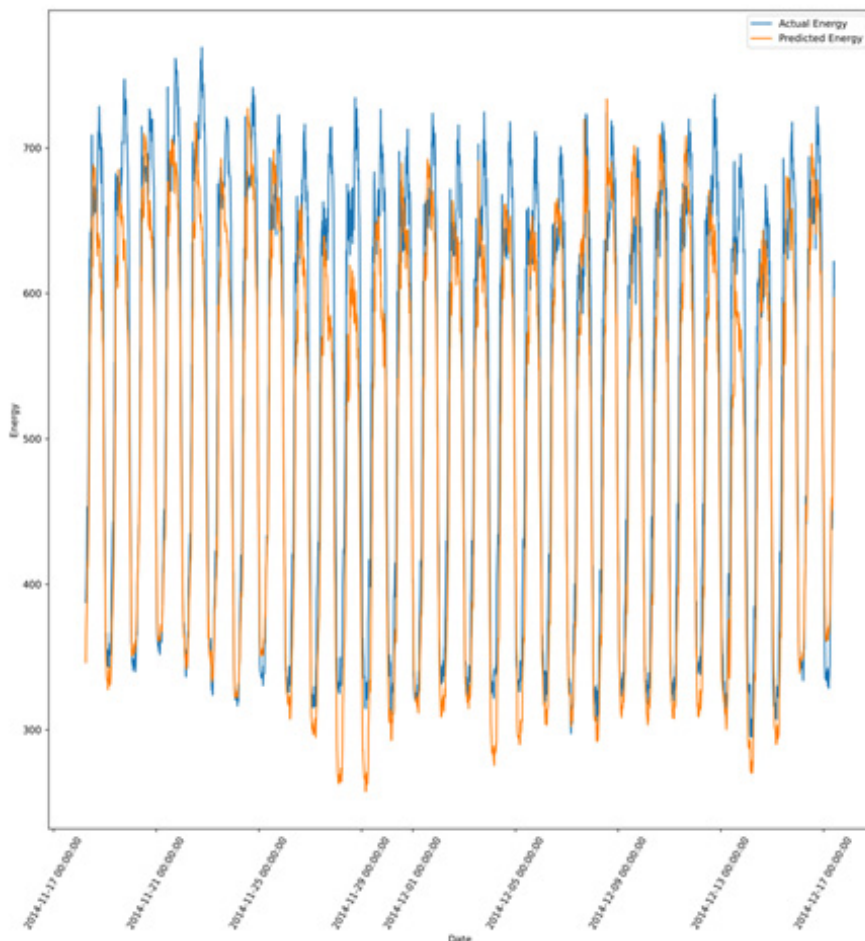
Figıre 12. GRU Prediction Graph (Monthly)

5. Conclusion

The prediction of electricity consumption holds significant importance across multiple facets such as grid planning, investment strategies, and the design of educational initiatives aimed at consumer awareness. Effectively forecasting energy consumption aligns with the prudent utilization of finite energy resources, addressing environmental and societal concerns at their forefront. However, the multifaceted nature of individual consumer behaviors introduces a complex dimension to the challenge of predicting consumption patterns. In addition to the diverse array of consumer characteristics that do not conform to a linear framework, the volatility of weather data, continually influenced by global warming, further complicates this issue.

Within the scope of this study, three different artificial intelligence models—namely, RNN, LSTM and GRU have been analyzed for daily, weekly, and monthly time intervals in relation to users' average consumption patterns. Overall, the findings obtained from the Simple RNN, LSTM, and GRU models can be considered successful. Upon examining the metric outcomes and prediction graphs, it has been demonstrated that the GRU model performs better in weekly forecasts, while the LSTM model yields more accurate results in daily and monthly predictions. The Simple RNN model, possessing a simpler architecture compared to LSTM and GRU models, has been expectedly found to lag slightly in performance, which is considered an anticipated outcome.

References

Amri, Y., Fadhilah, A. L., Setiani, N., & Rani, S. (2016). Analysis clustering of electricity usage profile using k-means algorithm. In IOP Conference Series: Materials Science and Engineering (Vol. 105, No. 1, p. 012020). IOP Publishing.

Brunn, C., Nuñez von Voigt, S., & Tschorsch, F. (2023). Analyzing Continuous ks-Anonymization for Smart Meter Data.

Cao, W., Liu, Y., Mei, H., Shang, H., & Yu, Y. (2023). Short-term district power load self-prediction based on improved XGBoost model. Engineering Applications of Artificial Intelligence, 126, 106826.

Centofanti, F., Hubert, M., Palumbo, B., & Rousseeuw, P. J. (2023). Multivariate Singular Spectrum Analysis by Robust Diagonalwise Low-Rank Approximation. arXiv preprint arXiv:2310.01182.

Chen, Q., & Zhang, Y. (2023). U-shaped Transformer: Retain High Frequency Context in Time Series Analysis. arXiv preprint arXiv:2307.09019.

Chen, X., Chen, W., Dinavahi, V., Liu, Y., & Feng, J. (2023). Short-Term Load Forecasting and Associated Weather Variables Prediction Using ResNet-LSTM Based Deep Learning. IEEE Access, 11, 5393-5405.

Chitalia, G., Pipattanasomporn, M., Garg, V., & Rahman, S. (2020). Robust short-term electrical load forecasting framework for commercial buildings using deep recurrent neural networks. Applied Energy, 278, 115410.

Cho, K., Van Merriënboer, B., Gulcehre, C., Bahdanau, D., Bougares, F., Schwenk, H., & Bengio, Y. (2014). Learning phrase representations using RNN encoder-decoder for statistical machine translation. arXiv preprint arXiv:1406.1078.

Chung, J., Gulcehre, C., Cho, K., & Bengio, Y. (2014). Empirical evaluation of gated recurrent neural networks on sequence modeling. arXiv preprint arXiv:1412.3555.

Dooley, S., Khurana, G. S., Mohapatra, C., Naidu, S., & White, C. (2023). ForecastPFN: Synthetically-Trained Zero-Shot Forecasting. arXiv preprint arXiv:2311.01933.

Emami, P., Sahu, A., & Graf, P. (2023). BuildingsBench: A Large-Scale Dataset of 900K Buildings and Benchmark for Short-Term Load Forecasting. arXiv e-prints, arXiv-2307.

Gers, F. A., Schmidhuber, J., & Cummins, F. (2000). Learning to forget: Continual prediction with LSTM. Neural computation, 12(10), 2451-2471.

Hochreiter, S., & Schmidhuber, J. (1996). LSTM can solve hard long time lag problems. Advances in neural information processing systems, 9.

Hochreiter, S., & Schmidhuber, J. (1997). Long short-term memory. Neural computation, 9(8), 1735-1780.

Hochreiter, S., (1998). The vanishing gradient problem during learning recurrent neural nets and problem solutions. Int. J. Uncertainty, Fuzziness Knowledge-Based Syst. 6, 107–116.

Khan, Z. A., Ullah, A., Haq, I. U., Hamdy, M., Mauro, G. M., Muhammad, K., ... & Baik, S. W. (2022). Efficient short-term electricity load forecasting for effective energy management. Sustainable Energy Technologies and Assessments, 53, 102337.

Kim, Y., Son, H. G., & Kim, S. (2019). Short term electricity load forecasting for institutional buildings. Energy Reports, 5, 1270-1280.

Kong, W., Dong, Z. Y., Jia, Y., Hill, D. J., Xu, Y., & Zhang, Y. (2017). Short-term residential load forecasting based on LSTM recurrent neural network. IEEE transactions on smart grid, 10(1), 841-851.

Li, D., Sun, G., Miao, S., Gu, Y., Zhang, Y., & He, S. (2022). A short-term electric load forecast method based on improved sequence-to-sequence GRU with adaptive temporal dependence. International Journal of Electrical Power & Energy Systems, 137, 107627.

Li, F., & Jin, G. (2022). Research on power energy load forecasting method based on KNN. International Journal of Ambient Energy, 43(1), 946-951.

Motwakel, A., Alabdulkreem, E., Gaddah, A., Marzouk, R., Salem, N. M., Zamani, A. S., ... & Eldesouki, M. I. (2023). Wild Horse Optimization with Deep Learning-Driven Short-Term Load Forecasting Scheme for Smart Grids. Sustainability, 15(2), 1524.

Muneer, A., Ali, R. F., Almaghthawi, A., Taib, S. M., Alghamdi, A., & Ghaleb, E. A. A. (2022). Short term residential load forecasting using long short-term memory recurrent neural network. International Journal of Electrical & Computer Engineering (2088-8708), 12(5).

Nguyen, Q. M., Nguyen, L. M., & Das, S. (2023). Correlated Attention in Transformers for Multivariate Time Series. arXiv preprint arXiv:2311.11959.

Nguyen, Q. D., Nguyen, N. A., Tran, N. T., Solanki, V. K., Crespo, R. G., & Nguyen, T. N. A. (2021). Online SARIMA applied for short-term electricity load forecasting.

Sekhar, C., & Dahiya, R. (2023). Robust framework based on hybrid deep learning approach for short term load forecasting of building electricity demand. Energy, 268, 126660.

Sepp, H. (1991). Untersuchungen zu dynamischen neuronalen netzen. Diploma, Technische Universitat Munchen, 91(1), 1991.

Shapi, M. K. M., Ramli, N. A., & Awalin, L. J. (2021). Energy consumption prediction by using machine learning for smart building: Case study in Malaysia. Developments in the Built Environment, 5, 100037.

Shin, S. Y., & Woo, H. G. (2022). Energy Consumption Forecasting in Korea Using Machine Learning Algorithms. Energies, 15(13), 4880

Semero, Y. K., Zhang, J., & Zheng, D. (2020). EMD–PSO–ANFIS-based hybrid approach for short-term load forecasting in microgrids. IET Generation, Transmission & Distribution, 14(3), 470-475.

Sürer, Ö., Apley, D. W., & Malthouse, E. C. (2023). Discovering interpretable structure in longitudinal predictors via coefficient trees. Advances in Data Analysis and Classification, 1-41.

Tascikaraoglu, A., & Sanandaji, B. M. (2016). Short-term residential electric load forecasting: A compressive spatio-temporal approach. Energy and Buildings, 111, 380-392.

Tealab, A. (2018). Time series forecasting using artificial neural networks methodologies: A systematic review. Future Computing and Informatics Journal, 3(2), 334-340.

Trindade, A. (2015). ElectricityLoadDiagrams20112014. UCI Machine Learning Repository. https://doi.org/10.24432/C58C86.

Veeramsetty, V., Reddy, K. R., Santhosh, M., Mohnot, A., & Singal, G. (2022). Short-term electric power load forecasting using random forest and gated recurrent unit. Electrical Engineering, 104(1), 307-329.

Wang, Y., Zhang, N., & Chen, X. (2021). A short-term residential load forecasting model based on LSTM recurrent neural network considering weather features. Energies, 14(10), 2737.

Yang, X., Zhang, X., Lin, J., Yu, W., & Zhao, P. (2016, August). A Gaussian-mixture model based detection scheme against data integrity attacks in the smart

grid. In 2016 25th International Conference on Computer Communication and Networks (ICCCN) (pp. 1-9). IEEE.

Zhang, Y., Ma, L., Pal, S., Zhang, Y., & Coates, M. (2023). Multi-resolution Time-Series Transformer for Long-term Forecasting. arXiv preprint arXiv:2311.04147.

Zhang, X. M., Grolinger, K., Capretz, M. A., & Seewald, L. (2018, December). Forecasting residential energy consumption: Single household perspective. In 2018 17th IEEE International Conference on Machine Learning and Applications (ICMLA) (pp. 110-117). IEEE.

Zheng, J., Chen, X., Yu, K., Gan, L., Wang, Y., & Wang, K. (2018, November). Short-term power load forecasting of residential community based on GRU neural network. In 2018 International conference on power system technology (POWERCON) (pp. 4862-4868). IEEE.

CHAPTER IV

ADDITIVE MANUFACTURING OF METALLIC MATERIALS APPLICATION AND DESIGN

Hacer Cemre DANACI[1] & Serkan ISLAK[2]

[1](Student), Department of Mechanical Engineering, Faculty of Engineering
and Architecture, Kastamonu University, Kastamonu, Türkiye
E-mail: 3737hacercemre@gmail.com
ORCID: 0000-0003-3381-9656

[2](Prof. Dr.), Department of Mechanical Engineering, Faculty of Engineering
and Architecture, Kastamonu University, Kastamonu, Türkiye
E-mail: serkan@kastamonu.edu.tr
ORCID: 0000-0001-9140-6476

1. Introduction

The first foundation of Additive Manufacturing Technology (AMT) in engineering was laid in 1987 with the construction of a 3D polymer printer. AMT covers the process of converting a 3D design into a tangible part. Since its inception, AMT, which is part of Industry 4.0, has facilitated the production of parts with complex geometries. AMT, which is still developing, contributes to mass and rapid production. In particular, it allows the components of parts with complex geometry to be produced in series and come out as a single piece. Another advantage of AMT is that it can start production at any time without the need for any equipment/mold, so the demand for this manufacturing technology is increasing considerably. The quality of the parts produced or to be produced is directly proportional to the determination of the appropriate production methods and the selection of the quality of the material to be used. AMT saves material compared to other traditional manufacturing methods. AMT avoids material waste by combining the material in layers, which has a positive

financial impact. In the traditional manufacturing method, the production of the desired part is achieved by reducing and shaping. Additive manufacturing is more efficient and economical compared to this method (Yalçın and Ergene, 2017; Özsolak, 2019).
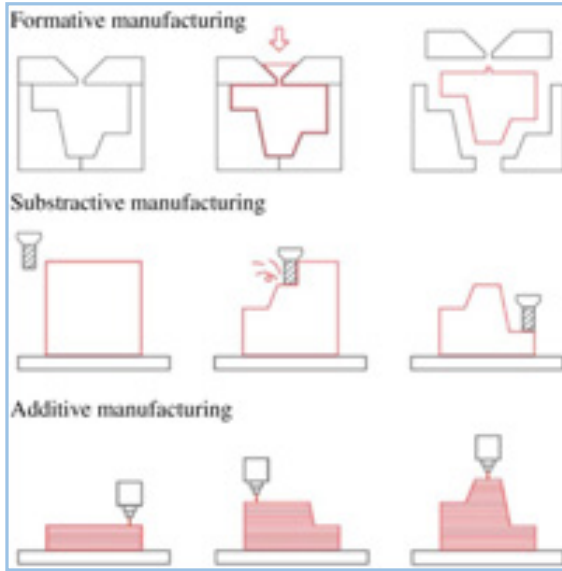
Figure 1. Additive manufacturing and traditional manufacturing methods (Ayan and Kahraman, 2018; Lang et al., 2019)

2. Additive Manufacturing Technology

Additive Manufacturing, which has revolutionized with the positive developments it has shown since 1980, was used for part prototyping in its early years. When it first appeared on the market, it was known as 3D Printer/ Printer. Over time, its name has turned into Additive Manufacturing. Today, thanks to various drawing programs, we can digitize the designs we have in mind. Additive Manufacturing Technology involves the process of turning digital designs into concrete parts. One of the most important criteria when transferring the designs in our minds to the drawing program is that the design is manufacturable. Today, the manufacturing of designs with complex geometry and difficult to produce has been facilitated by Additive Manufacturing. Additive Manufacturing Technology has almost eliminated the question 'can the design be made tangible? This technology, which is used in countless countries and organizations around the world, has become the favorite of Industry 4.0 (URL-

1). The American Materials Association defines Additive Manufacturing as the process of joining material in layers to produce parts from 3D designs, unlike traditional manufacturing methods. As shown in Figure 2, America, which is among the developed countries with Additive Manufacturing machines, ranks first with a ratio of 1/3. Turkey is still a developing country in terms of Additive Manufacturing Technology. With the percentage of Additive Manufacturing machines in Turkey, it has an important place in Europe (URL-1).
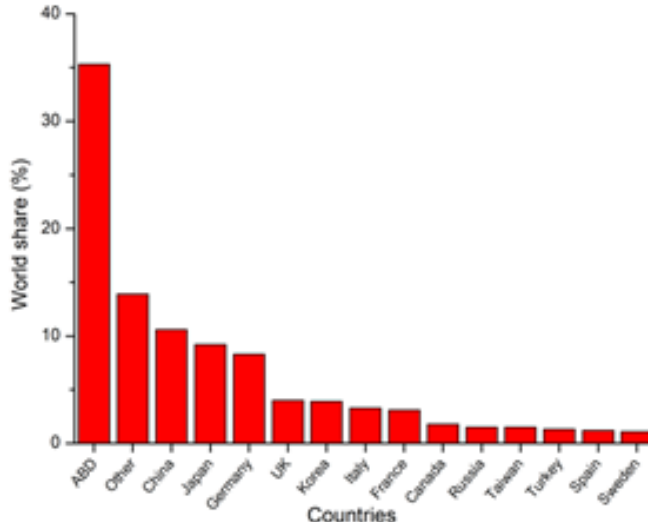
Figure 2. Percentage Distribution of Additive Manufacturing by Countries (URL-1)

The obvious difference of Additive Manufacturing Technology from other manufacturing methods is that it gives people unlimited design rights. When we look at the production stage in additive manufacturing, after drawing the design of the part in 3D in the CAD program, the necessary PC software needs to be made in order to produce the part. The purpose of the software is to determine the tool paths needed for production (Çelik and Özkan, 2017). Our 3D model is converted to Stereolithography (STL) format. Then the part is decomposed into triangular slices using the appropriate software. Then, after the manufacturing conditions are determined, it is given to additive manufacturing. And the part starts to be formed layer by layer (Özer, 2020). The final process is applied according to the material of the finished product and the method used; for example, after the processes such as cleaning and baking are completed, the production of the part is finished (Bozkurt et al., 2021).

Figure 3. Additive manufacturing process (Bozkurt et al., 2021)

2.1. Classification of Additive Manufacturing

It is almost impossible to gather additive manufacturing technologies under a single roof because it depends on the material and method used. Since different materials such as liquid, powder and solid are used in additive manufacturing, there are different classifications. ASTM (American Society for Testing and Materials) is the organization that brings all of these different groups together. This organization has divided Additive Manufacturing Technology into 7 different classes according to its standards under ASTM F42. In this section, Additive Manufacturing Technologies will be covered under the headings classified in the ASTM F42 standard (Yalçın and Ergene, 2017).
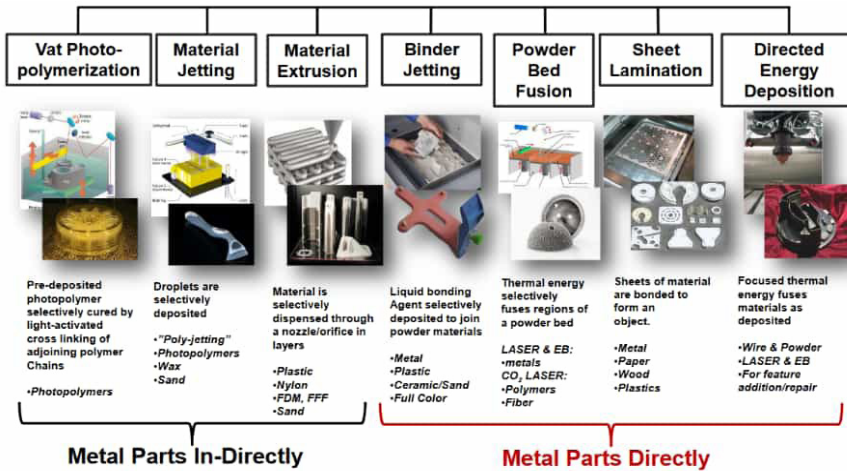
Figure 4. Classification of additive manufacturing (URL-2)

2.1.1. Photo polymerization

Photo Polymerization process is used to form solid layers. Photo Polymerization method is used in polymer and composite materials. Photo Polymerization processes, in which the use of polymer materials is at the forefront, is the solidification process of the liquid resin in the tank with the help

of radioactive rays, usually ultraviolet rays, and its formation as a layer (İlhan, 2020). The strength of the product produced with the resin used in the Photo Polymerization method will not be high. For this reason, the places of use also change. For example, it is not correct to use it in places that require strength (Bardakçı, 2019).

2.1.1.1. Sterelithography (SLA)

The resin solidified with the help of ultraviolet (UV) rays can produce 3D parts with the help of the Stereolithography process. The cross-sectional image of the layer that will emerge with the help of the rays coming out of the laser will be reflected in the mirror and will scan the upper surface of the resin and solidify the upper layer of the resin (İlhan, 2020). After the required height is provided for the second layer, the hardening step of the incoming layer is performed. The laser beam can perform the hardening process from above or below. In short, it will apply solidification to the limited area with the help of ultraviolet rays. At the end of this process, the product is removed from the manufacturing table and surface improvement applications are made if necessary (Bardakçı, 2019).
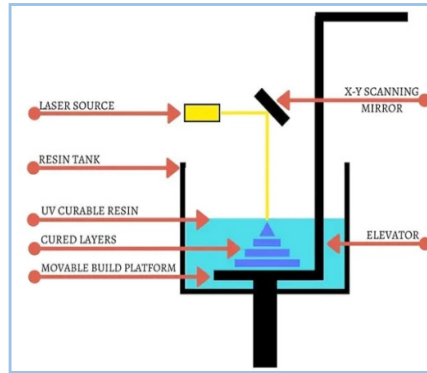
Figure 5. Stereolithography Processes (URL-3)

The SLA process has a higher preference rate because it progresses faster than other methods and is financially more affordable. This method, which can process many materials, can produce complex nanocomposites, but the raw materials and equipment required are of high financial value (Özer, 2020).

2.1.1.2. Digital Light Processing (DLP)

Almost identical to stereolithography, this method is faster. The biggest difference between the two methods is that the ultraviolet rays of digital, with

the help of a projector, solidify the entire 2D section of the 3D part. In the stereolithography method, the geometry of the part is more distinct or sharper due to the more step-by-step solidification. The DLP method is applied faster, but the geometry of the part is not very sharp due to the application of a process to the whole. In DLP, with the help of the projector, it usually performs the hardening process from bottom to top (İlhan, 2020).
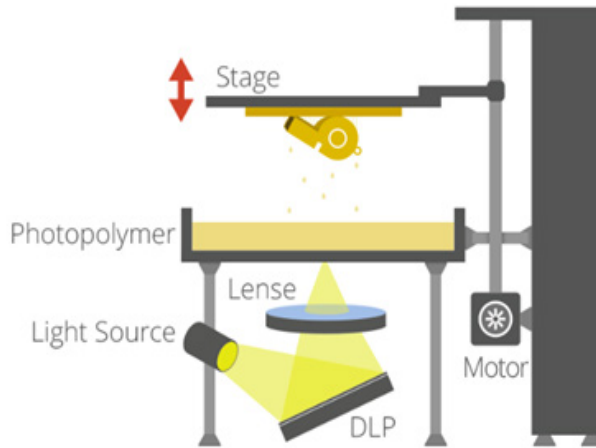
Figure 6. Digital Light Processing (URL-4)

2.1.2. Material Extrusion

One of the most important methods of Additive Manufacturing is material extrusion. In this method, where mostly polymer-based materials are used, the material is compressed with supports. For example; a pulley is used. The material is melted and a thin thin layer is formed (İlhan, 2020).

2.1.2.1. Fused Deposition Modeling

The melt stacking method is suitable for polymers and composites. To produce the 3-dimensional part, thermoplastic filaments are the feedstock. Generally, ABS and PLA core filaments are supported. The average diameter of the filaments, which also help us determine the color of the produced part, varies between 1.75 or 2.85 mm. In this method, the filaments are first wound on spools and then sent towards the nozzle with the help of the spools. The heater is located just before the nozzle, melting the filaments and sending them onto the platform to solidify. It takes a lot of time to create the part in Melt Deposition.

However, the properties of the part produced at the end of the process will be suitable for the place to be used (İlhan, 2020). The melt deposition method is the most widely used/sold additive manufacturing method for plastic materials today, as it is pro-environmental, suitable for mass production and the material can be recycled without waste (Özer, 2020).
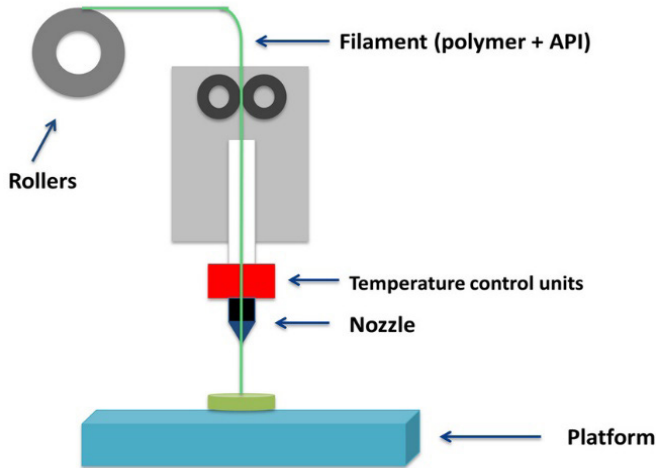
Figure 7. Melt Deposition Modeling (Konta et al., 2017).

2.1.3. Material Spraying

This method is an adaptation of the material spraying process in 2D printers to the production of 3D parts. It is an ideal method for using metal, polymer and wax materials. However, wax and polymer materials are more preferred than metals for this method. The reason for this is that they are produced in droplets and they are sticky and viscosity will be important for us. We also have the possibility to change the material we use during the process. We can use different materials and spray them at the same time. The material is sprayed onto the auxiliary platform by choosing one of the Drop On Demand or Drop On Demand approaches. Ultraviolet rays are also present in the part that sprays the material, so that the sprayed droplets are hardened and layer by layer parts are formed. Since UV rays, which provide the attitude of the layers to each other, can provide good solubility, there is no need for an additional operation. However, parts produced in this method may not be preferred in places where good strength is required, this is due to the material selected (İlhan, 2020).
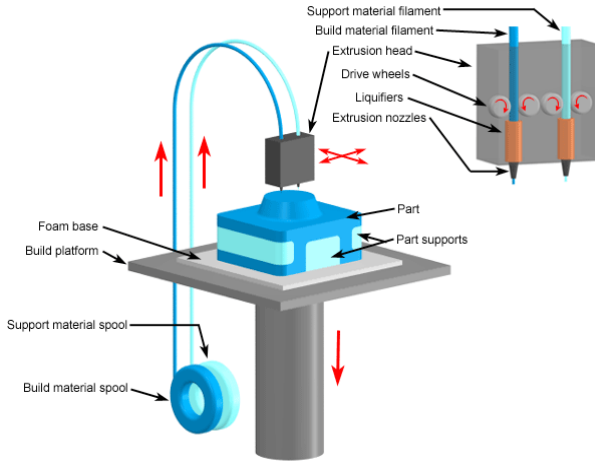
Figure 8. Material spraying method (URL-5)

2.1.3.1. Polyjet Printer (or multijet - MJ)

In Polyjet technology, there is a spray head with many nozzles. The nozzles here perform the spraying process in the form of 40-50-micron sized photopolymer liquid droplets (İlhan, 2020). The nozzles are accelerated with computer-aided software and moved in the injection block (Özsoy and Duman, 2017). Spray heads with ultraviolet light perform the spraying process according to the cross-sectional geometry of the product to be produced. After spraying the material, the cooling process takes place with the help of UV rays. In each layer, the table is directed downwards respectively, resulting in a layered product. When the production is completed in this way, the process is completed by removing the auxiliary elements on the part removed from the table (Özsoy and Duman, 2017).
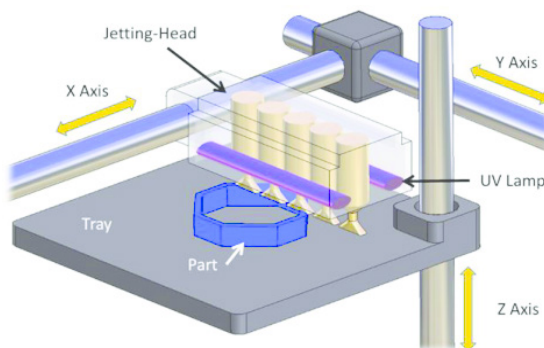
Figure 9. Polyjet Printer Method (Gay et al., 2015)

2.1.4. Powder Bed Melting

This method constitutes one of the main topics of additive manufacturing. The main idea in the powder bed melting method is to melt the material with the help of laser or electron beams and fuse them together. In this method, we need a vacuum environment that helps powder materials to combine better with each other and increases their durability (İlhan, 2020). This method, in which metallic materials are mainly used, contributes greatly to the production of metallic parts with complex geometry. When the method was first used, plastic materials were studied, but over time this was replaced by metal powders. In addition to metal powders, polymer and composite powders are also used (Bardakçı, 2019). The powders used from the reservoir under the powder bed are laid as a layer on the manufacturing table with a spreader. The average thickness of the laid material is 0.1 mm. The first layer is formed by melting the powder layer with the help of electron beam or laser and the process continues in this order and our 3D part is formed (Yalçın and Ergene, 2017).

2.1.4.1. Selective Laser Melting

It is a fast method fully suitable for the production of parts from metallic materials. It can produce parts with very complex geometries within a few hours, but depending on the difficulty of the part, parts can be delivered between 1 and 2 days. The selective laser melting machine is not suitable for the production of very large parts because of the specific size range. This method requires high prices for some productions, for example, for parts that require mass production and the designs remain the same, this method is very costly. In addition, this method is not suitable for parts that require continuous renewal (Özer, 2020). Although mainly metal materials are preferred, polymer, ceramic and composite materials can also be preferred. The application of the method is that the powder material laid with the help of a roller is adhered to each other using a laser and a layer is formed. The storage of the powder material in the chamber ensures continuous transfer of the material. The process of forming layers continues until our 3D part emerges (URL-5).
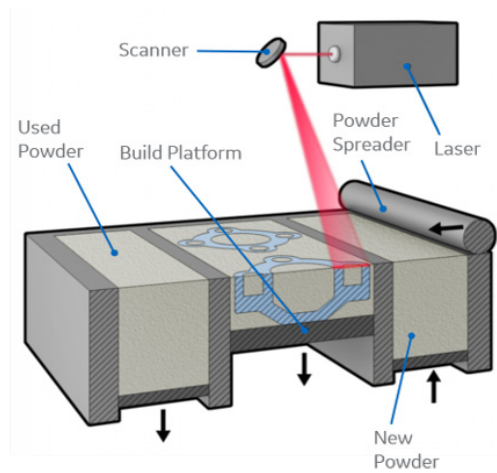
Figure 10. Selective laser melting method application (URL-6)

2.1.4.2. Selective Laser Sintering (SLS)

Polymer material, which is used quite a lot in this method, has been popular because it requires low energy for sintering, but metal powder can also be used. In the SLS method, CO_2 laser is used for sintering plastic materials. The way the method produces the part is similar to selective laser melting. The difference in the production phase is that we do not completely melt our material (Özer, 2020). We store the formed part in a room containing nitrogen, as a result of which its quality is improved. They are then allowed to cool and have a good tolerance.
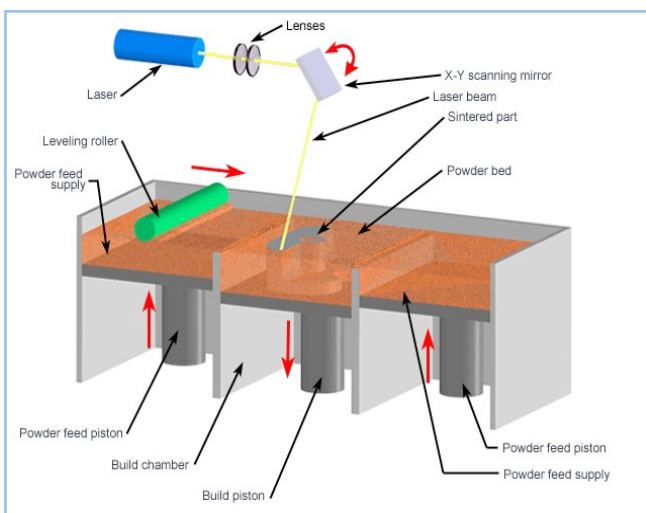
Figure 11. Selective laser sintering method (URL-7)

2.1.4.3. Direct Metal Laser Sintering Method

It is one of the most important methods for the application of metallic materials in additive manufacturing. The research on Direct Metal Laser Sintering method, which started at Texas University in 1989-1990, has continued with the studies of many institutions. The metal sintering machine was developed at Catholic Leuven University in the early 1990s. In 1995, an experimental device of laser sintering, which directly melts metal, was produced at Fraunhofer Institute for Manufacturing Technology. It is one of the most important methods for the application of metallic materials in additive manufacturing. The same steps as in the SLS method are applied using metal powders (Duman and Kayacan, 2017).

2.1.4.4. Electron Beam Melting

The Electron Beam Melting method is one of the non-traditional manufacturing methods, which makes profit from material, time and weight. When we summarize the working sequence of the method in this method, where electrons are used as sources; Electrons with high velocity are sent onto metal dust. In this part, kinetic energy is quickly converted into thermal energy. The temperature increase causes the titanium powder to liquefy above the melting temperature. Smelting machines with Electron Beam have processes that ensure discharge with control panel and turbo molecular pump. Here the trading circle has the loading tank, which includes the controllable trading platform. Two different powder dispensing systems are supplemented and swept with filling hopper and screening system. Electron beam is obtained by heating tungsten wires. The electrons are accelerated to reach 0.1 and 0.4 times the speed of light. The acceleration voltage should be 60 kV. With electromagnetic lenses, electrons are focused and reflected. The electrons hit the dust particles within the processing circle and are converted into thermal energy, taking their kinetic energy. With the help of this heat provided by electrons, the dust particles melt, creating a precise thin layer. It can rise to a maximum beam power of 3500W. In these systems, the spot size is on average 0.1-0.4mm and the maximum structure size is around 200x200x350mm^3. Vacuum pressure of 10^{-4}-10^{-5} mbar is applied in this process. Materials with a conductive structure are used in this method. Often alloys of steel, titanium and cobalt chromium are among the materials used in this method. It is produced layer by piece. The method of Melting with Electron Beam begins with preheating of electron beams with low current high velocity on the powder layer. This step is the light sintering of dust particles. Thus, integrity will be maintained when rays with high power arrive, and the thermal temperature difference between the heated layer and the remaining parts

of the part will be reduced. Subsequently, electron beams will scan the dust particles on the surface according to the defined layer data and the desired model will be given. First, the first layer is heated, the added powder is distributed through the powder funnel, laid with the help of a comb, excess powder is sent. After the first layer is heated and sintered, the second layer is subjected to the same methods and these processes are repeated until the desired thickness and geometry are formed. With the creation of the structure, the part is cooled under vacuum or helium flow. Leftover powders are separated for use in another job.
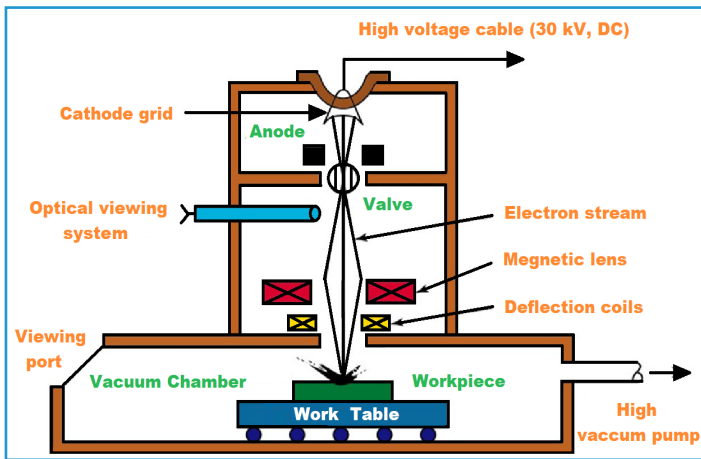
Figure 12. Electron beam melting method (URL-8)

2.1.5. Sheet Lamination Method

The Sheet Lamination Method is one of the first additive manufacturing methods to emerge. Many sheet materials are used, but unlike others, it uses 'paper', which is readily available and cheap. The material used in this method is fed in a position that coincides with the top of the manufacturing table. And a roll or cylinder, which has been previously exposed to heat, is passed over it and glued to the table. Cutting is done with the help of a laser. The cutting process starts by cutting the outer surfaces of the part. The same processes are applied in the next layer and the material is created in 3D (Bardakçı, 2019). In this method, paper is used as material and adhesive. The Sheet Lamination Method utilizes a cross-hatching method during the printing process step to allow for easy removal after construction. Although not ideal for structural use, parts from this production are preferred for aesthetic and visual models.
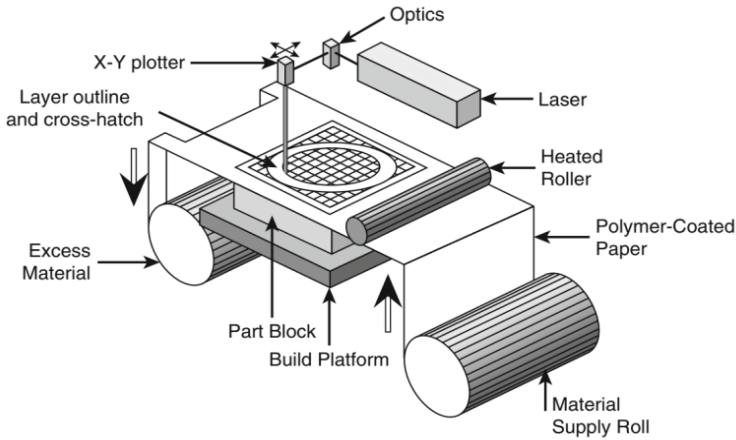
Figure 13. Production Stages of Lamination Method Process (URL-9)

2.1.5.1. Ultrasonic Additive Manufacturing

The Ultrasonic Additive Manufacturing method uses metal sheets that are joined together with the help of ultrasonic welding. The method requires CNC machining of the unbonded metal as a plus. Unlike the lamination method, the formed metal cannot be removed immediately. Machining is required to remove unnecessary material. The metallic tape left over from the material causes less material to be cut. The milling process after each layer can be done after all steps have been applied. This method uses metals such as copper, aluminum, stainless steel and titanium. The distinctive advantages of this method are that it consumes minimum energy because it does not melt the metal and it combines different materials.

2.1.6. Directed Energy Deposition

This method is mostly preferred on metals, but it is also used on polymers and ceramics. Metals are used as powder or wire material. The method is based on the principle of solidification by melting the material. In this method, which uses a laser, electron beam or plasma arc in the melting process, the material is melted and then solidified using a head with multiple axes and movements. Material cooling times are very fast, typically between 1000 - 5000 °C/s. The most commonly used metallics are Cobalt Chrome and Titanium. When we look at the process steps of the method, first of all, the moving and axial head is moved on the fixed part. The material is deposited on the part, provided in the

form of wire or powder. The material is melted using an electron beam or laser, then solidified and the production process continues layer by layer (Yalçın and Ergene, 2017)
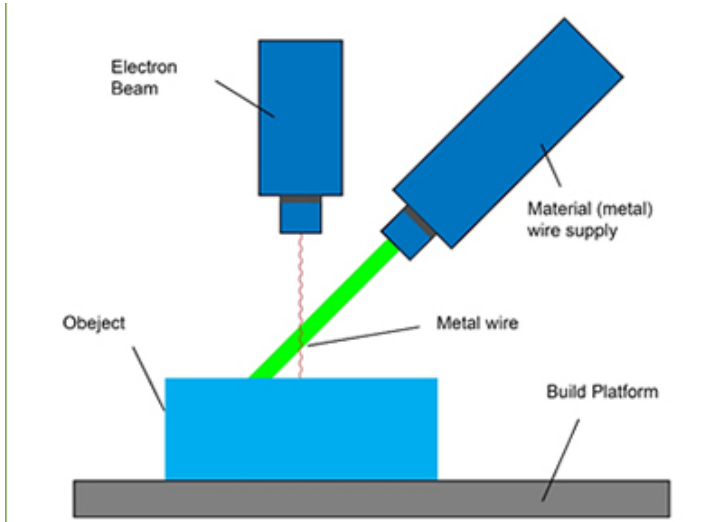
Figure 14. Directed Energy Deposition (URL-10)

2.1.7. Binder Jetting

The foundations of Binder Jetting manufacturing were laid in the 1990s by the Massachusetts Institute of Technology. In its early days, it was called 3D Printer. In 2010, at the time of commercialization, it passed into the literature as "Binder Jetting". In this method, two fundamentally different materials are used for production. The first one is the powder material, which is the main material, and powder materials; ceramic, polymer, composite and metal powders. The metal powders used in model production have recently started to be used. The second material is the liquid binding agent, often called resin, which joins the powdered main material together. The powder of the material forming the part is laid by powder sprinkling method. Similar to a spray printer, the binder material is sprayed onto a layer. At the end of this step, the desired geometry is obtained in two dimensions. Then the same process is repeated with the next layer and the part is three-dimensional. Once the manufacturing process is done, the part is in its raw form. Final processes are applied to the material to increase the mechanical properties of the produced part (Gürgen and Kayacan, 2020).
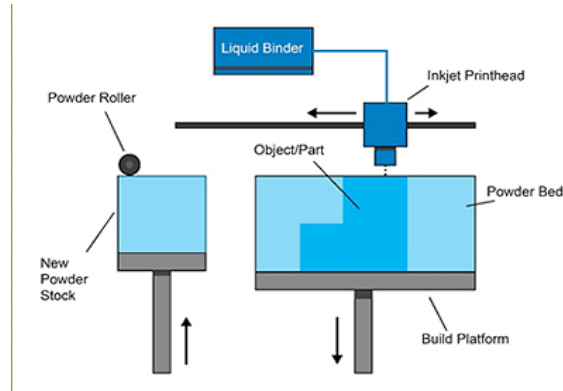
Figure 15. Production principle of binder jetting method (URL-11)

2.1.7.1. Binder Jetted Metal Additive Manufacturing

This method, whose raw material is only metal powder, actively uses cobalt/chromium and tungsten carbide in its devices. Used in advanced engineering technologies, the method has become a favorite in the aerospace, automotive and defense industries. It is also used in other sectors as an aid in the production of complex shapes. In this method, firstly, low-density parts with raw strength are produced. The final processes (curing, sintering, infiltration, etc.) of the produced parts are applied to improve the mechanical properties of the produced part. When we look at the process steps of this method, the first step is to fill the hoppers with powder and binder raw material. Then, thanks to the mechanism for laying the powder taken from the feeding unit, it is laid on the manufacturing table. The binder is sprayed on the necessary parts of the powder laid on the production table. Hardening is applied according to the characteristics of the binder. Until the 3D part is produced, all these processes are repeated from the beginning and layer-by-layer production is also in question here. After the part is produced, it is cleaned from unbound dust and cleaned. The produced part is baked to ensure better fusion and the binder is blown away. And liquid metal is impregnated into these flying hollow parts. The method is mostly preferred for parts such as pumps, turbines, heat exchangers, filtration systems, powertrains, some prostheses, etc. (Gürgen and Kayacan, 2020).

3. Application of Metallic Materials to Additive Manufacturing

After mentioning the additive manufacturing methods using metal powders, it is investigated which of these metal powders are mainly used. Metallic materials

used in additive manufacturing technologies not only produce complex and difficult parts, but also contribute to the design and production of some customized structures by using monolithic, bimetallic or multi-material compositions. The sectors that use additive manufacturing technology using metallic materials are mostly aerospace, automobile and biomedical sectors (Bandyopadhyay et al., 2020). The metal powders to be used in additive manufacturing will directly affect the mechanical properties of the structure to be produced. Apart from this, it will affect the porosity of the produced part, the production of defect-free components, production defects on its surface and its reproducibility in the machine.

3.1. Metallic Powders Used in Additive Manufacturing and Their Properties

3.1.1. Properties Required from Metallic Powders

We have already mentioned that the quality of the resulting product in additive manufacturing technologies depends on part density, surface roughness, production speed and mechanical properties. In order to achieve all these properties, the properties of metal powders and production parameters must be optimized correctly.

We can classify the properties required from metal powders in additive manufacturing technologies as chemical composition, particle size distribution and shape, and packaging.

Chemical Composition: The composition of the metal powder to be used in additive manufacturing technology should be homogeneous and the amount of impurity in its content should be kept at a minimum level.

Particle Size Distribution and Shape: In the additive manufacturing method, it is preferred that the powder particle sizes are between 10 - 100 µm due to the production of 20, 40, 60, 80 µm layer thickness. Since the particle shape of the metal powder will affect the packaging of the powder, manufacturing is started after the irregular particles become smooth. Generally, metal powders with spherical dimensions are preferred in additive manufacturing methods.

Packaging: The packaging feature of the powder directly affects the surface roughness and density of the produced part.

3.1.2. Commonly Used Metallic Materials

Thanks to the availability of metal powders, many types of metallic alloys are used in additive manufacturing processes. The metals mainly used are aluminum alloys, cobalt alloys, titanium alloys, nickel alloys, copper alloys, stainless steels, tool steels and precious metals.

3.1.2.1. Aluminum Alloys

The limited use of different aluminum alloys in additive manufacturing is due to the fact that aluminum, unlike titanium, is easy to machine and the material cost of aluminum parts is slightly lower. For this reason, the use of aluminum alloys in additive manufacturing technology has a lower commercial advantage. Another reason is that several aluminum alloys are known to have low weldability. Performance-efficient alloys generally derive their strength from precipitation hardening (Ozsolak, 2019). The most commonly used aluminum alloys for additive manufacturing are Al-Si and Al-Si-Mg alloys. These alloys contain Si, which improves laser absorption. Research has shown that Al12Si material has a fine microstructure with eutectic Si embedded in the Al matrix, which enhances thermal properties. Another study showed that AlSi10Mg processed by laser-based PBF has outstanding cavitation erosion resistance compared to the same material prepared by casting due to the fine-grained microstructure developed by the AM process (Bandyopadhyay et al., 2020).

3.1.2.2. Steels

Steels, one of the most widely used engineering materials, are the most preferred metal powders in additive manufacturing technology. The use of austenitic stainless steel and tool steel for LMD is also described in the literature. The cross-sectional image of austenitic stainless steel produced in 3 layers with LMD is given and the laser traces formed on the material are also revealed with the cross-sectional image. It is shown in Figure 16.

Figure 16. Sectional image for stainless steel fabricated with lmd in 3 layers (Haghdadi et al., 2021)

3.1.2.3. Titanium Alloys

Titanium (Ti) alloys are one of the most widely studied metallic materials used in additive manufacturing technology. Titanium alloys are the most widely used metallic material in additive manufacturing technology due to their high specific strength and fracture resistance, good formability, excellent corrosion and fatigue resistance as well as good biocompatibility. The microstructure of Ti alloys shows columnar grains due to rapid solidification during additive

manufacturing processing. This type of microstructure is normally found in parts machined by additive manufacturing and shows growth along multiple layers along the build direction. Studies have shown that the morphology of columnar grains results in anisotropic properties in additive manufacturing machined parts. The researchers reported that the needle martensitic α' phase was obtained in Ti6Al4V samples processed by additive manufacturing, which tends to increase the strength and decrease the ductility of Ti6Al4V samples. To improve ductility by decomposing the α' phase into α and β phases, Ti6Al4V parts are usually subjected to final thermal steps. Recent studies also show that complex structures such as porous and lattice structures can be fabricated using additive manufacturing Ti alloys (Bandyopadhyay et al., 2020).

3.1.2.4. Nickel Alloys

Nickel alloys are one of the most popular metal powders due to their unique properties. Applications where nickel alloys are used are usually in conditions of high corrosiveness and high temperature. Nickel alloys are typically difficult to machine. For this reason, although they are processed by traditional methods, their use in additive manufacturing has become more important.

3.1.2.5. Precious Metal Alloys

In addition to metal, additive manufacturing machines can also print with different materials such as gold, silver and bronze. Gold is used especially for the jewelry industry. During the production of gold, a high-resolution printout is first taken with the help of wax. It is then placed in a container with liquid plaster around it. When the wax melts, the remaining liquid becomes a mold. The melted gold is poured into the mold and is expected to harden. After the plaster is broken, the hardened gold is slowly cleaned and polished. Thus, even shapes that are quite complicated to make with traditional methods are obtained (Düzgün and Çetinkaya, 2019).

4. Application Areas of Metal Additive Manufacturing

Due to the advantages of metal additive manufacturing, the materials it uses and the fact that it is a future-oriented technology, it is used in many different fields such as industry, aviation, automotive, biomedical, electronics, fashion and jewelry (Dursun, 2019). Rapid prototyping in the field of industrial design enables a designer to create various geometries and to be financially efficient. It

provides convenience in checking the functional, ergonomic, aesthetic features of a product and making changes during the design phase. Recently, the designer can use these technologies as a manufacturer of the final product as well as rapid prototyping (Seyhan et al., 2021).
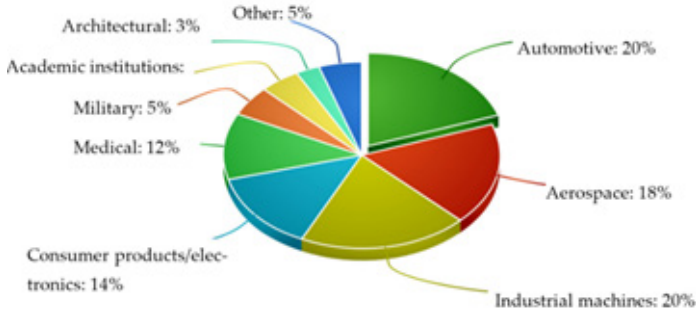
Figure 17. Utilization rates of metal additive manufacturing technology in different industries (Vafadar et al., 2021)

4.1. Aerospace Industry

Additive manufacturing technologies are preferred in the aerospace industry for creating difficult geometries, material control, part classification and lightweight parts. Aviation has produced some parts of the jump engine with this technology. The splash engine fuel nozzle was produced from cobalt chromium with a laser additive manufacturing machine. With this method, it was more efficient in terms of cost, weight and replacement of twenty components. EOS, which uses metal sintering technology, is an important company in the aerospace industry. Engine and turbine parts are produced with the help of additive manufacturing technology. Parts with complex geometries are produced quickly and at low cost (Seyhan et al., 2021).

4.2. Automotive Sector

Additive manufacturing technology is used in the automotive industry for rapid prototyping, rapid product development, production of spare, complex and high productivity parts. This technology does not require expensive parts to produce prototypes and is cost-efficient. In this sector, where metal materials are predominantly used, parts are created with artificial intelligence and then produced in these 3D machines. If we give an example for the future, the Rimac Scalatan concept designed by Max Schneider for the year 2080 offers us a

concept of what our world and the transportation industry might look like in the future. The car is designed with an aerodynamic carbon-nanotube graphene exterior sitting on a generatively designed chassis made of 3D-carboprinted titanium graphite (Seyhan et al., 2021).

One of the purposes of additive manufacturing applications in the automotive field is the production of small and complex parts with tools and molds, functional prototypes; eliminating or reducing the need for molding, welding and assembly processes in the automotive sector. Companies in the sector are expanding and executing 3D printing technology applications with three main objectives. Increasing the quality and added value of products, accelerating the design and production processes of products, and improving supply chain activities (Seyhan et al., 2021).
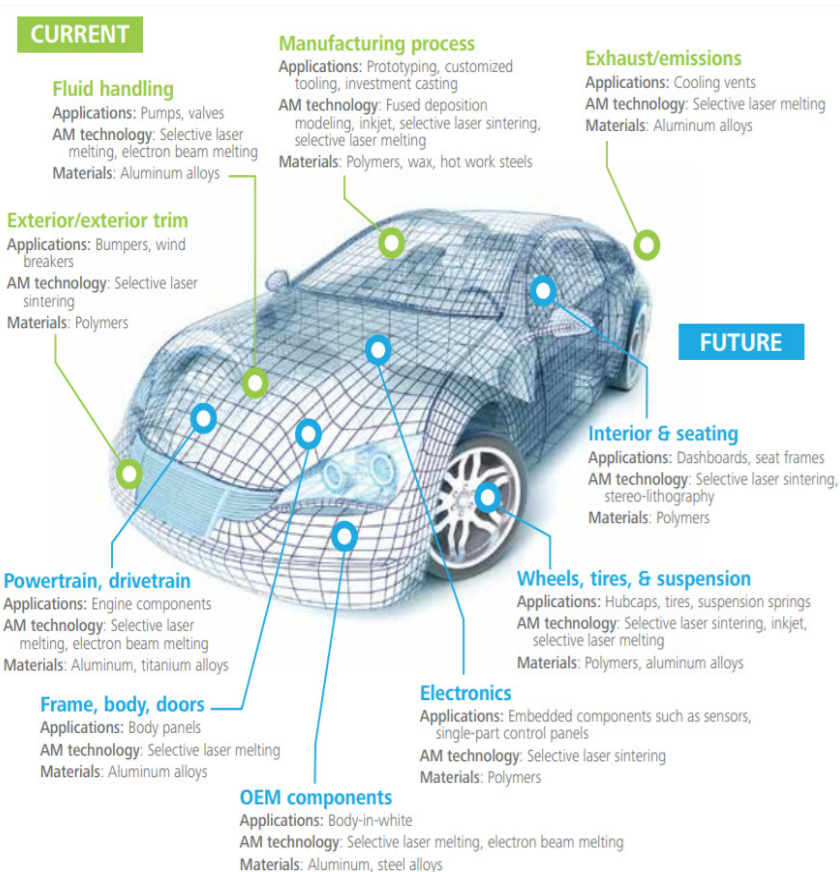
Figure 18. Automotive Parts that can be Produced with Additive Manufacturing (URL-12)

4.3. Health Industry

The use of additive manufacturing technologies in the healthcare sector is increasing rapidly. In particular, the production of medical devices has undergone a radical change with the development of additive manufacturing technologies. It is a promising technology that revolutionizes the production of medical devices and implants. Thanks to this technology, the production time of implants can be dramatically reduced compared to traditional methods. Moreover, since implants can also be manufactured based on the patient's individual anatomy, they can better fit the patient, reducing the possibility of failure, which is common with mass-produced implants. In the dental industry, additive manufacturing processes are used to create precision dental crowns, bridges and implants. The SLM process' ability to produce custom, complex, accurate and fully dense parts makes it suitable for dental applications. The process of creating crowns and bridges consists of scanning a dental impression of the patient's teeth, digital modeling of the part, followed by SLM production. This process offers a competitive market for additive manufacturing that rivals traditional casting and milling production methods. In addition, a similar process is used for artificial teeth made of titanium or cobalt-chromium for the production of personalized dentures. In the medical sector, metal additive manufacturing processes are used because they can produce custom components very quickly. The technology is very useful for producing bespoke medical implants as well as surgical instruments for use in operating theaters. Furthermore, 3D printing techniques are highly suitable for creating objects with a biomimetic structure (Özer, 2020).

4.4 Molding Industry

The value of additive manufacturing technology (AMT) has increased due to the problems such as the loss of material while producing the part in traditional stone manufacturing, the high number of production processes and the high cost compared to AMT in terms of financial aspects. In addition to these, saving time has greatly increased the use of additive manufacturing in the molding industry. Additive manufacturing technology, which can add previously unavailable features to the part and reduce the production process steps, ensures that the molds to be produced have improved cooling channels. Additive manufacturing molds manufactured with molds with cooling channels are long-lasting because they allow the designer to reduce the temperature stress load experienced by the designer. Production tools made with additive manufacturing offer many advantages. For example, low material cost and

short production time. But most importantly, parts produced using additive manufacturing improve the performance of the end product. For more general applications of additive manufacturing, some challenges remain. For example; the need for a wider variety of available materials, a workforce specialized in additive manufacturing design and production with much higher manufacturing numbers, and improvements in financial competitiveness (Özer, 2020).

4.5. Nano-Manufacturing

Additive manufacturing technologies have been combined with nanotechnology to produce products from nano-composites in next generation manufacturing. The main benefit of using nano materials in AMT is to improve the material properties of the manufactured parts. Thus, parts with superior optical, thermal, electrochemical and mechanical properties have been obtained. In recent years, a wide variety of nano-materials have been used in additive manufacturing machines, including carbon nanotubes, nanowires, metal nanoparticles and nano-graphene. Additive manufacturing at the nanoscale plays a crucial role in fabricating metal parts with nanopores, thus eliminating or minimizing the formation of pores and voids (Özer, 2020).

5. Design of Metal Materials on Additive Manufacturing

Compared to traditional manufacturing methods, additive manufacturing technology gives us a great deal of freedom in design. Additive manufacturing, which has a production with the method of adding on top of each other, reveals the part without using molds in powder or wire form. It is low-budget and easier to make multifunctional products with the additive manufacturing machine that creates the part by layered production. The budget spent for molds and design stages used in traditional methods is eliminated in additive manufacturing. In additive manufacturing, it is possible to make changes after the part is produced. After the separation of the support parts from the product at the stage of removing the product from the layered production platform, milling, drilling, polishing processes on the part as well as surface cleaning with chemical fluid abrasives on the inner surfaces are possible. Heat treatment is applied at the last stage of the layered production process to improve mechanical properties and reduce internal stresses (Altuncu, 2020).

5.1. Spiral Part Design

A spiral part was drawn with Solidworks program using steel material. This part can be produced on additive manufacturing machines. Thanks to the

layer-by-layer production, the additive manufacturing machine can realize 3D production in one go. It will be more economical in terms of time and cost than the traditional method.
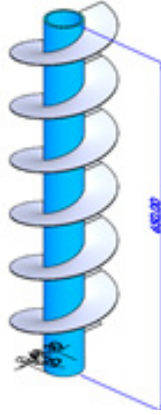
Figure 19. Solidworks spiral part design

Figure 20. Spiral Part Produced in Additive Manufacturing Machine (Altuncu, 2020)

5.2. Gear Wheel Design

Gear wheels, which are widely used and needed in the market and have become a favorite in the industry with the advantage of the power transmission feature they provide, are used in wind turbines, air and space vehicles and electromechanical systems. The production of gear wheels in additive manufacturing machines is easier to produce than traditional methods and can minimize material waste. Looking at the literature, many gear wheels have been produced with additive manufacturing technology. For the production of less than 1000 gear wheels, additive manufacturing technology is preferred (Doğan and Kamer, 2021).
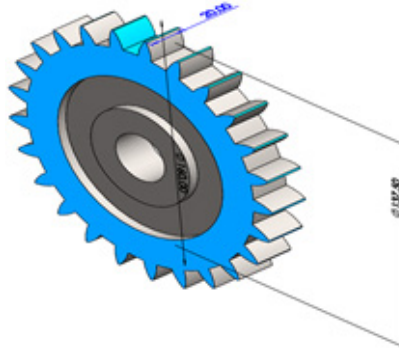
Figure 21. Gear wheel design
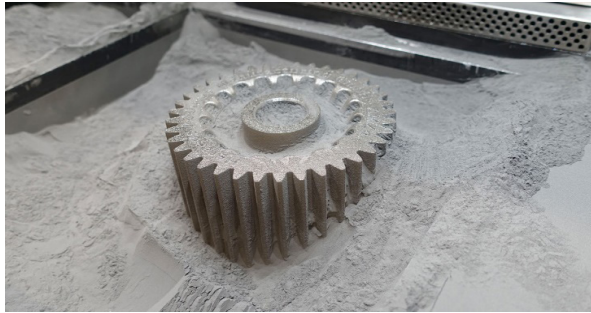
Figure 22. Additive manufactured gear wheel (URL-13)

6. Conclusion

Additive manufacturing technology, which I will talk about in my study, is a very important technology that has gained a lot of value today and will be mentioned even more in the future. With this period when 3D printers are highly needed, the need for additive manufacturing technology increases at the same rate. The working principle of additive manufacturing technology is similar to the 3D printer logic. Additive manufacturing enables a 3D part drawn in a PC program to be produced concretely by combining the material in layers. It has enabled the production of highly complex and porous parts. Additive manufacturing technology enables the production of parts made of many materials, for example; metal, ceramic and polymer parts by combining layer by layer. Today, additive manufacturing is used in the aerospace and aviation, health and construction sectors, automotive, defense industry and energy sectors, which are important areas of industry. Additive manufacturing technology is also an important part of Industry 4.0. The use of additive manufacturing technology with metallic materials is a new and emerging industry. Additive manufacturing

technology has started to be used on metallic materials after providing strength, energy and financial savings while starting production.

References

Altuncu, E. (2020). Katmanlı İmalat İle Üretilen Parçalara Uygulanan Yüzey İşlemler. Sakarya Uygulamalı Bilimler Üniversitesi – SUMAR.

Ayan , Y., Kahraman, N. (2018). Metal Eklemeli İmalat: Tel Ark Yöntemi ve Uygulamaları. International Journal of 3D Printing Technologies and Digital Industry,2:3(2018), 74-84.

Bandyopadhyay, A., Zhang, Y., Bose, S. (2020). Recent Developments in Metal Additive Manufacturing. Curr Opin Chem Eng. 2020 Jun;28:96-104. doi: 10.1016/j.coche.2020.03.001. Epub 2020 Apr 29.

Bardakçı, Y.S. (2019). Bağlayıcı Püskürtmeli Metal Eklemeli İmalat Cihazı Tasarımı ve Prototip İmalatı. Yüksek Lisans Tezi, Süleyman Demirel Üniversitesi Fen Bilimleri Enstitüsü. Isparta.

Bozkurt, Y., Gülsoy,H.Ö., Karayel,E. (2021). Eklemeli İmalat Teknolojilerinin Tıbbi Ekipmanlarının Üretiminde Kullanımı. El-Cezeri Fen ve Mühendislik Dergisi, Cilt 8, No:2, (962-980).

Çelik , K., Özkan, A. (2017). Eklemeli İmalat Yöntemleri İle Üretim ve Onarım Uygulamaları. Düzce Üniversitesi Bilim ve Teknoloji Dergisi, 5 (2017) 107-121.

Doğan , O., Kamer , M.S. (2021). Eklemeli İmalat Yöntemi ile Optimum Düz Dişli Çark Tasarımı ve Üretimi. BEÜ Fen Bilimleri Dergisi, 10 (3), 1093-1103.

Duman, B., Kayacan, M.C. (2017). Doğrudan Metal Lazer Sinterleme/Ergitme Yöntemi ile İmal Edilecek Parçanın Mekanik Özelliklerinin Tahmini. Süleyman Demirel Üniversitesi Teknik Bilimler Dergisi, Cilt 7, Sayı 1, Sayfa 12-28.

Dursun, A.M. (2019). Değişken Gözenekli Hücresel Yapıların Metal Eklemeli İmalat İçin Tasarımı ve Üretilen Yapıların Tasarım İle Uyumluluğunun Araştırılması. Gazi Üniversitesi Fen Bilimleri Enstitüsü, Yüksek Lisans Tezi.

Düzgün, D.E., Çetinkaya, K. (2019). Moda Alanında 3 Boyutlu Baskı Teknolojilerinin Kullanılması. International Journal of 3D Printing Technologies and Digital Industry , 3:1(2019), 19-31.

Gay, P., Blanco, D., Pelayo, F., Noriega, A., & Fernández, P. (2015). Analysis of factors influencing the mechanical properties of flat PolyJet manufactured parts. Procedia Engineering, 132, 70-77.

Gürgen , M., Kayacan, M.C. (2020). Bağlayıcı Püskürtmeli Metal Eklemeli İmalatta Kullanılan Parametreler. Uluborlu Mesleki Bilimler Dergisi, 3:1, 19-27.

Haghdadi, N., Laleh, M., Moyle, M., & Primig, S. (2021). Additive manufacturing of steels: a review of achievements and challenges. Journal of Materials Science, 56, 64-107.

Konta, A. A., García-Piña, M., & Serrano, D. R. (2017). Personalised 3D printed medicines: which techniques and polymers are more successful? Bioengineering, 4(4), 79.

Lang, A., Gazo, C., Segonds, F., Mantelet, F., Jean, C., Guegan, J., & Buisine, S. (2019). A proposal for a methodology of technical creativity mixing TRIZ and additive manufacturing. In New Opportunities for Innovation Breakthroughs for Developing Countries and Emerging Economies: 19th International TRIZ Future Conference, TFC 2019, Marrakesh, Morocco, October 9–11, 2019, Proceedings 19 (pp. 106-116). Springer International Publishing.

Özer, G. (2020). Eklemeli Üretim Teknolojileri Üzerine Bir Derleme. Niğde Ömer Halisdemir Üniversitesi Mühendislik Bilim Dergisi, 9(1),606-621.

Özsoy, K., Duman, B. (2017). Eklemeli İmalat (3B Boyutlu Baskı) Teknolojilerinin Eğitimde Kullanılabilirliği. International Journal of 3D Printing Technologies and Digital Industry, 1:1(2017) 36-48.

Özsolak, O. (2019). Eklemeli İmalat Yöntemleri ve Kullanılan Malzemeler. International Journal of Innovate Engineering Applications 3,1(2019), 9-14.

Seyhan , M., Bayram , G., Toğay, A. (2021). Hızlı Prototipleme ve Endüstriyel Tasarım İlişkisinin Sektörel Üretim Süreçlerinde Mevcut Durum Tartışması. International Journal of 3D Printing Technologies and Digital Industry, Cilt: 5,Sayı: 2.

URL-1. 2023. https://arge.ssb.gov.tr/Documents/Eklemeli_Imalat%20_Teknolojileri_OTAG_Sonuc_Raporu.pdf

URL-2. 2023. https://www.rapiddirect.com/blog/additive-vs-subtractive manufacturing/

URL-3. 2023. https://manufactur3dmag.com/stereolithography-sla-3d-printing-works

URL-4. 2023. https://www.3dprinting.lighting/3d-printing-technologies/digital-light-processing/

URL-5. 2023. http://www.icme.unina.it/ICME%2014/CIRP%20ICME%2014_Plenary%20Session%20Presen_LEVY.pdf

URL-6. 2023. https://3dprintingcenter.net/3d-printing-applications-for-tool-steel/

URL-7. 2023. https://www.custompartnet.com/wu/selective-laser-sintering

URL-8. 2023. https://www.theengineeringprojects.com/2021/06/what-is-3d-printing-definition-technology-and-applications.html

URL-9. 2023. https://engineeringproductdesign.com/knowledge-base/sheet-lamination/)

URL-10. 2023. https://www.lboro.ac.uk/research/amrg/about/the7categoriesofadditivemanufacturing/directedenergydeposition/)

URL-11. 2023. https://www.lboro.ac.uk/research/amrg/about/the7categoriesofadditivemanufacturing/binderjetting/

URL-12. 2023. https://www.linkedin.com/pulse/additive-manufacturing-automotive-industry-saenitk

URL-13. 2023. https://www.3printr.com/milestone-additive-manufacturing-worlds-largest-amorphous-metal-component-automate-2019-2951554/

Vafadar, A., Guzzomi, F., Rassau, A., & Hayward, K. (2021). Advances in metal additive manufacturing: a review of common processes, industrial applications, and current challenges. Applied Sciences, 11(3), 1213.

Yalçın, B., Ergene, B. (2017). Endüstride Yeni Eğilim Olan 3-B Eklemeli İmalat Yöntemi ve Metalürjisi. Süleyman Demirel Üniversitesi Teknik Bilimler Dergisi, Cilt 9, Sayı 3.

FREE VIBRATION ANALYSIS OF SINGLE STEP TAPERED BEAMS WITH MULTIPLE CRACKS

Mehmet HASKUL[1]& Murat KISA[2]

[1](Assoc. Prof. Dr.), Şırnak University, *Faculty of Engineering,*
Department of Mechanical Engineering,
E-mail:mehmethaskul@sirnak.edu.tr
ORCID: 0000-0001-8671-4597

[2](Prof. Dr.), Harran University, Faculty of Engineering,
Department of Mechanical Engineering,
E-mail:mkisa@harran.edu.tr
ORCID: 0000-0001-7015-2198

1. Introduction

Examining the vibration behavior of a system or structural element without the influence of an external force or movement is called free vibration analysis. This analysis is frequently used in structural design and dynamic analysis in engineering applications. Free vibration analysis is typically performed using differential equations, mathematical models, or numerical modeling methods. The main goal of vibration modeling of structures is to find the dynamic characteristics of the system, such as the natural frequency and mode shapes. This data can be used in many engineering applications, including structural durability, vibration-based predictive maintenance, vibration-induced noise control and design optimization.

Finite element technique is one of the popular numerical solution methods used in the analysis of engineering problems. This method divides complex structures into smaller, simpler elements and aims to reach a general solution by solving mathematical models in these elements. It is generally used in various

fields such as engineering design and analysis, heat conduction, fluid dynamics, electrical fields.

In this section, free vibration modeling of a single-stepped, tapered beam with multiple cracks was carried out. Mass and stiffness matrices were found for a beam element whose cross section varies linearly. The cracks in the beam were considered as massless springs, and the stiffnesses induced by the cracks were estimated using linear fracture mechanics principles. Element stiffnes, mass and crack-induced stiffness matrices of the tapered-cracked beam were included in a computer program developed to perform free vibration analysis and targeted analyses were carried out. In the calculations, the finite element method was used. The natural frequencies and mode shapes of the cracked beam were obtained by various the crack depth ratios, crack locations, and taper ratios. The effects of crack locations and crack depth ratios and taper ratios on the dynamic characteristics of the structure were clearly seen in the graphs.

Many studies on vibration analysis of beams, columns, and frame structures with uniform and variable cross-sections containing single or multiple cracks have been published in the literature. (Salawu 1997, Dimarogonas 1996, Wauer 1990, Gasch 1993, Krawczuk and Ostachowicz 1996, Jassim et al. 2013, Kisa 2004, Kisa 2011, 2012, Kisa and Gürel 2006, 2007, Kisa et al. 1998, Kisa and Brandon 2000a, 2000b, Haskul and Kisa 2021a, 2021b). Lee (2015) used the Chebyshev-tau method to analyze the free vibration of stepped Euler-Bernoulli and Timoshenko beams. Lu et al. (2009) developed a new approach for analyzing the free and forced vibrations of beams subjected to single or multi-step variations. Mao and Pietrzko (2010) and Mao (2011) examined the free vibrations of the stepped and multi-stepped Euler-Bernoulli beam using the Adomian decomposition method (ADM). Wang and Wang (2013) used the differential quadrature element method (DQEM) to analyze the free vibration problem of multi-step beams. Attar (2012) proposed an analytical approach to find the dynamic characteristics of a stepped beam containing multiple edge cracks. Duan and Wang (2013) used the modified discrete singular convolution (DSC) method for free vibration analysis of multi-step beams. Su et al. (2018) proposed a formulation to analyze the modal analysis of multi-step Timoshenko beams with well-known boundary conditions. Vaz and Lima Junior (2016) investigated the natural frequencies and mode shapes of Euler-Bernoulli stepped beams with elastic end supports. Šalinić et al. (2018) conducted vibration analysis of tapered, stepped and continuously section AFG bars and EulerBernoulli beams. Wattanasakulpong and Chaikittiratana (2016) applied the Adomian mode decomposition method to solve the large-amplitude vibration analysis of stepped beams with various general and elastic boundary conditions.

Jaworski and Dowell (2008) theoretically examined the analysis of free vibration of a multi step cantilever beam and conducted an experimental study to verify the results they found.

In this section, a method has been developed for the free vibration analysis of a single-stepped tapered beam with multi cracks and different boundary conditions. Natural frequencies and mode shape values were obtained for different crack depth ratios, various crack locations and different taper ratios, and then the effects of these parameters on the dynamic properties of the structure were revealed.

2. Material and Method

The problem was modelled in this section depicted in Figure 1. The finite element method was used to divide the beam into elements (see Figure 2). These elements have two nodes and three degrees of freedom at each node, including the crack sections. Taking these conditions into account, the stiffness and mass matrices of the beam with single step tapered multi-cracked beams were obtained.
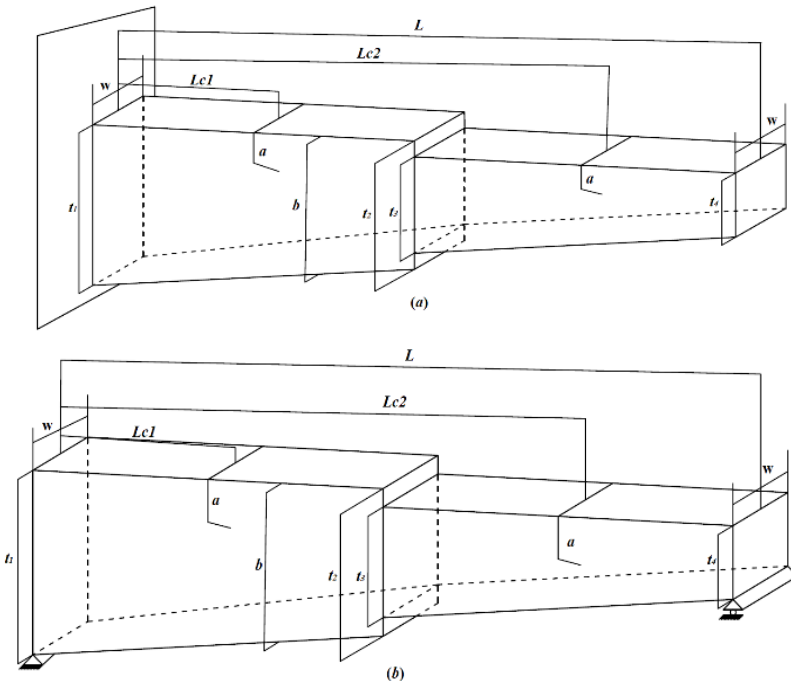
Figure 1. Sketch of single-stepped tapered multi-cracked beam
(a) fixed-free ends and, (b) pinned-pinned ends

first crack section

second crack section

(a)
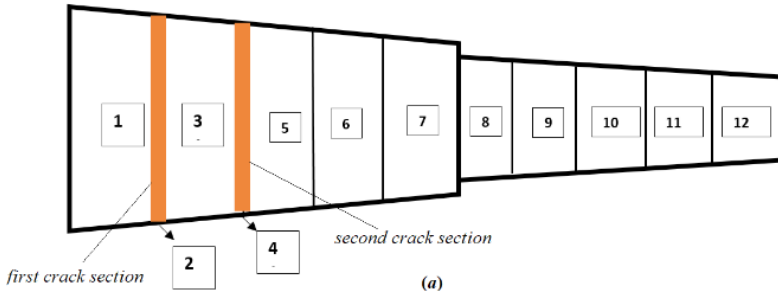
Figure 2. Finite element modelling of the single-step
tapered beam with multiple cracks

For the beam at x distance from the left end, the equations $EI_{zz}(x)$ and $EA(x)$ are as follows:

$$EI_{zz}(x) = EI_{zz1}\left(1 + \alpha\left(\frac{x}{L}\right)\right)^3 \tag{1}$$

$$EA(x) = EA_1\left(1 + \alpha\left(\frac{x}{L}\right)\right) \tag{2}$$

where I_{zz1} and A_1 represent the left end's area moment of inertia and cross-sectional area, respectively. α for single stepped beam is given as following:

$$\alpha = \frac{t_2 - t_1}{t_1} = \frac{t_4 - t_3}{t_3} \tag{3}$$

The stiffness matrix of a variable cross-section beam element is given by (Haskul 2010):

$$K = \begin{bmatrix} \frac{1}{C} & 0 & 0 & \frac{-1}{C} & 0 & 0 \\ 0 & \frac{A_1}{D_1} & \frac{A_2}{D_1} & 0 & \frac{-A_1}{D_1} & \frac{A_1L - A_2}{D_1} \\ 0 & \frac{A_2}{D_1} & \frac{A_3}{D_1} & 0 & \frac{-A_2}{D_1} & \frac{A_2L - A_3}{D_1} \\ \frac{-1}{C} & 0 & 0 & \frac{1}{C} & 0 & 0 \\ 0 & \frac{-A_1}{D_1} & \frac{-A_2}{D_1} & 0 & \frac{A_1}{D_1} & \frac{A_2 - A_1L}{D_1} \\ 0 & \frac{A_1L - A_2}{D_1} & \frac{A_2L - A_3}{D_1} & 0 & \frac{A_2 - A_1L}{D_1} & \frac{A_1L^2 - 2A_2L + A_3}{D_1} \end{bmatrix} \tag{4}$$

where A_1, A_2, A_3, D_1 and C are:

$$A_i = \int_0^L \frac{x^{(i-1)}}{EI_{zz}(x)}\,dx, \quad i = 1,2,3, \tag{5}$$

$$D_1 = A_1.A_3 - A_2^2 \tag{6}$$

$$\frac{1}{C} = \frac{EA_1}{L}\left[\frac{\alpha}{\ln(\alpha+1)}\right] \tag{7}$$

The mass matrix of a beam element with variable cross section is given as follows (Haskul 2010):

$$[M] = \begin{bmatrix} m_{11}^A & 0 & 0 & m_{12}^A & 0 & 0 \\ 0 & m_{11}^B & m_{12}^B & 0 & m_{13}^B & m_{14}^B \\ 0 & m_{21}^B & m_{22}^B & 0 & m_{23}^B & m_{24}^B \\ m_{21}^A & 0 & 0 & m_{22}^A & 0 & 0 \\ 0 & m_{31}^B & m_{32}^B & 0 & m_{33}^B & m_{34}^B \\ 0 & m_{41}^B & m_{42}^B & 0 & m_{43}^B & m_{44}^B \end{bmatrix}_{6x6} \tag{8}$$

where m^A_{ij} and m^B_{ij} are:

$$[m]^A = \begin{bmatrix} \dfrac{1}{12}\rho A_1 L(4+\alpha) & \dfrac{1}{12}\rho A_1 L(2+\alpha) \\ \dfrac{1}{12}\rho A_1 L(2+\alpha) & \dfrac{1}{12}\rho A_1 L(4+3\alpha) \end{bmatrix} \tag{9}$$

$$[m]^B = \begin{bmatrix} \frac{1}{35}\rho A_1 L(13+3\alpha) & \frac{1}{420}\rho A_1 L^2(22+7\alpha) & \frac{9}{140}\rho A_1 L(2+\alpha) & -\frac{1}{420}\rho A_1 L^2(13+6\alpha) \\ & \frac{1}{840}\rho A_1 L^3(8+3\alpha) & \frac{1}{420}\rho A_1 L^2(13+7\alpha) & -\frac{1}{280}\rho A_1 L^3(2+\alpha) \\ & & \frac{1}{35}\rho A_1 L(13+10\alpha) & -\frac{1}{420}\rho A_1 L^2(22+15\alpha) \\ \textit{Symmetric} & & & \frac{1}{840}\rho A_1 L^3(8+5\alpha) \end{bmatrix} \tag{10}$$

For plane strain, the strain energy release rate J is equal to the amount of energy required per unit strain occurring in front of the crack. J is (Tada et al. 1985):

$$J = \frac{1-v^2}{E}K_I^2 + \frac{1-v^2}{E}K_{II}^2 + \frac{1+v}{E}K_{III}^2 \tag{11}$$

where E is the modulus of elasticity, v is Poisson's ratio, and K_I, K_{II} and K_{III} are modes of deformation. The strain energy release rate is always positive and consists of three different strain modes. If J is re-expressed using the principle of superposition, the following expression is obtained:

$$J = \frac{1-v^2}{E}\left(K_{I1} + K_{I2} + ... + K_{In}\right)^2 + \frac{1-v^2}{E}\left(K_{II1} + K_{II2} + ... + K_{IIn}\right)^2$$
$$+ \frac{1+v}{E}\left(K_{III1} + K_{III2} + ... + K_{III3}\right)^2 \tag{12}$$

Cracks in the structure cause local flexibility, and in this study, Castigliano's theorem and stress intensity factors were used to find these local flexibilty coefficients. Simultaneously, if the amount of strain energy released is taken into account according to the Griffth-Irwin theory (Irwin, 1960), the flexibility coefficients are as follows:

$$c_{ij} = \frac{\partial u_i}{\partial P_j} = \frac{\partial^2}{\partial P_i \partial P_j} \int_A J\left(P_i, A\right) dA \tag{13}$$

Flexibility coefficients c_{11}, c_{13}, c_{22} and c_{33} are as follows:

$$\left. \begin{array}{l} c_{11} = \dfrac{2\pi}{E^* b^2 d} \displaystyle\int_0^a \xi F_1^2\left(\dfrac{\xi}{b}\right) d\xi \\[2em] c_{13} = c_{31} = \dfrac{12\pi}{E^* b^3 d} \displaystyle\int_0^a \xi F_1\left(\dfrac{\xi}{b}\right) F_2\left(\dfrac{\xi}{b}\right) d\xi \\[2em] c_{22} = \dfrac{2\pi\kappa^2}{E^* b^2 d} \displaystyle\int_0^a \xi F_2^2\left(\dfrac{\xi}{b}\right) d\xi \\[2em] c_{33} = \dfrac{72\pi}{E^* b^4 d} \displaystyle\int_0^a \xi F_3^2\left(\dfrac{\xi}{b}\right) d\xi \end{array} \right\} \tag{14}$$

The stiffness matrix for a node's crack is provided by:

$$[C]^{-1} = \begin{bmatrix} \dfrac{c_{33}}{-c_{13}^2 + c_{11}c_{33}} & 0 & \dfrac{c_{13}}{c_{13}^2 - c_{11}c_{33}} \\[1.5em] 0 & \dfrac{1}{c_{22}} & 0 \\[1.5em] \dfrac{c_{13}}{c_{13}^2 - c_{11}c_{33}} & 0 & \dfrac{c_{11}}{-c_{13}^2 + c_{11}c_{33}} \end{bmatrix}_{3x3} \tag{15}$$

The stiffness matrix for the crack is given below:

$$K_e = \begin{bmatrix} [C]^{-1} & -[C]^{-1} \\ -[C]^{-1} & [C]^{-1} \end{bmatrix}_{(6x6)} \tag{16}$$

where K_{cr} indicates the stiffness matrix occured due to cracks in the beam.

It is well known that cracks inside the structure reduce stiffness (Irwin, 1960). The matrix of stiffness for beam with crack, $[K]_{wcr}$ is given as:

$$[K]_{wcr} = [K] - [K]_{cr} \tag{17}$$

Where the elements of the K_{cr}, the stiffness matrix resulting from the crack, are substracted from the general stiffness matrix acording to the relevant degrees of freedom. In case there is more than one crack, the stiffness matrix elements resulting from each crack are substracted from the general stiffness matrix.

The free vibration equation is given below in matrix format:

$$\left\| [K]_{wcr} - \lambda [M] \right\| \varphi = 0 \tag{18}$$

Using Equation 18, the dynamic properties of a single-stepped varying cross-section beam with multi-crack were obtained.

3. Numerical Results

The results of free vibration analysis for multi-cracked single-stepped tapered beams were obtained and interpreted in this section. By using finite element, a computer program was written for analysis of beams vibration, via this program natural frequencies and mode shapes of the beam were determined for various cracks location and cracks depth ratios, as well as the beam's taper ratio $t_2/t_1=0.7$.

The beam's geometric properties are expected to be the beam's length $L=0.2$m, the beam's thickness $t_1=0.025$m, and the beam's width 0.0078m, with the thickness ratio of the beam ($t_2/t_1 = t_4/t_3$) varying linearly. The mechanical properties are taken as Young's modulu $E=216$GPa, Poisson ratio $v=0.3$ and density $\rho=7850$ kg/m^3.

The findings of these analyses are presented in the following section of the text.

3.1. Fixed-free Single-Stepped Beam with Tapered Cross-Section and Multiple Cracks

In this section; a free vibration analysis was analyzed on a fixed-free single-stepped beam with tapered cross-section and multiple cracks.
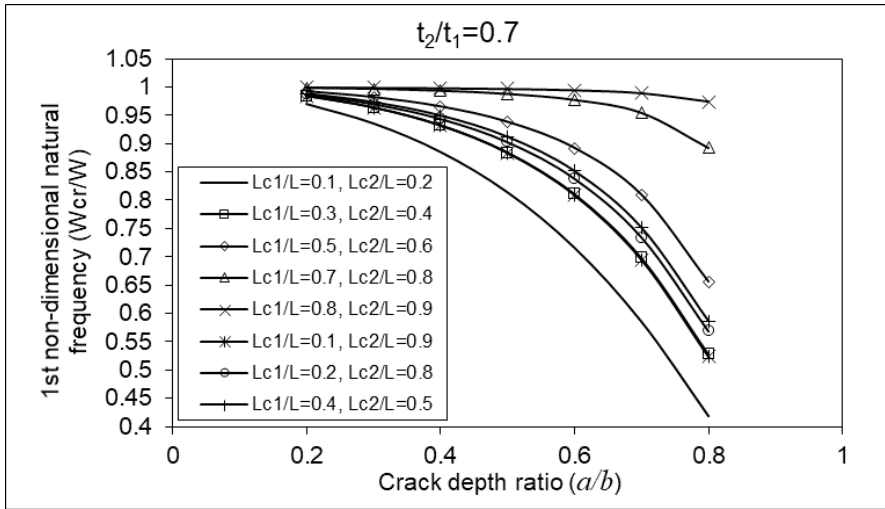
Şekil 3. *First non-dimensional natural frequencies of single-stepped beam with fixed–free ends for multiple crack locations and taper ratio $t_2/t_1=0.7$ depending on crack depth ratios a/b=0.2–0.8*
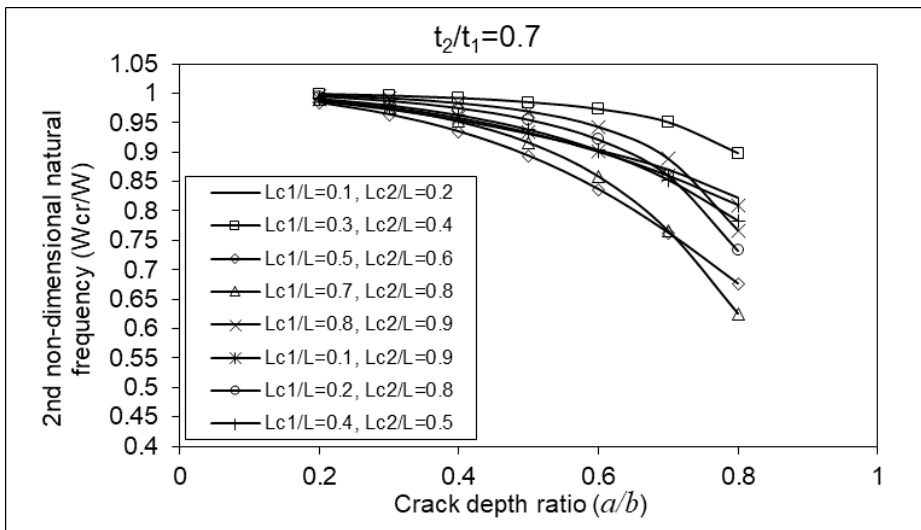
Şekil 4. *Second non-dimensional natural frequencies of single-stepped beam with fixed–free ends for multiple crack locations and taper ratio $t_2/t_1=0.7$ depending on crack depth ratios a/b=0.2–0.8*
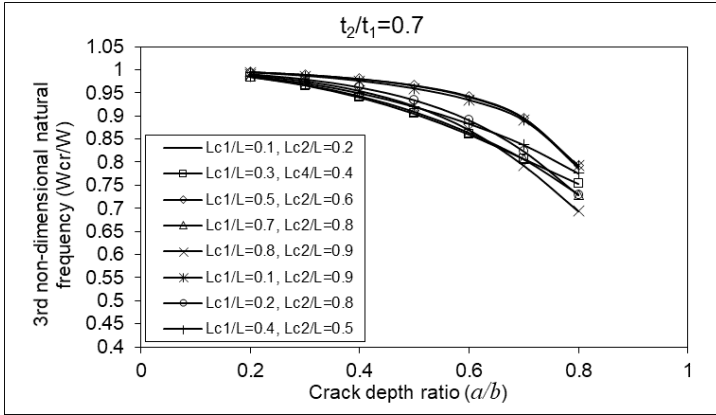
Şekil 5. *Third non-dimensional natural frequencies of single-stepped beam with fixed–free ends for multiple crack locations and taper ratio t_2/t_1=0.7 depending on crack depth ratios a/b=0.2–0.8*

Figures 3, 4, and 5 show the first, second, and third dimensionless natural frequencies of the fixed-free single-stepped beam with a taper ratio t_2/t_1=0.7 and various of crack locations according to the crack depth ratios (a/b=0.2–0.8). As illustrated by the figures, the maximum decrease in the first natural frequency occurred when the cracks were located close to the fixed end Lc1/L=0.1 and Lc2/L=0.2. The second and third natural frequencies showed maximum decreases when the cracks were at Lc1/L=0.7, Lc2/L=0.8, and Lc1/L=0.8, Lc2/L=0.9, respectively. These frequency drops in the beam are caused by significant energy losses in the crack section.
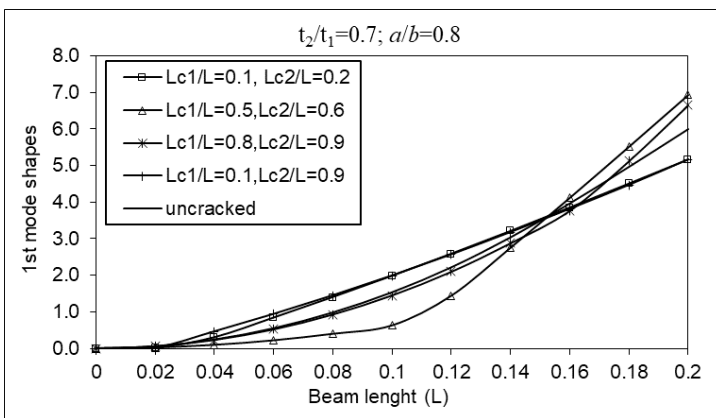
Figure 6. *First mode shapes of fixed-free single-stepped beam with multiple cracks for crack depth ratio a/b=0.8 and taper ratio t_2/t_1=0.7*
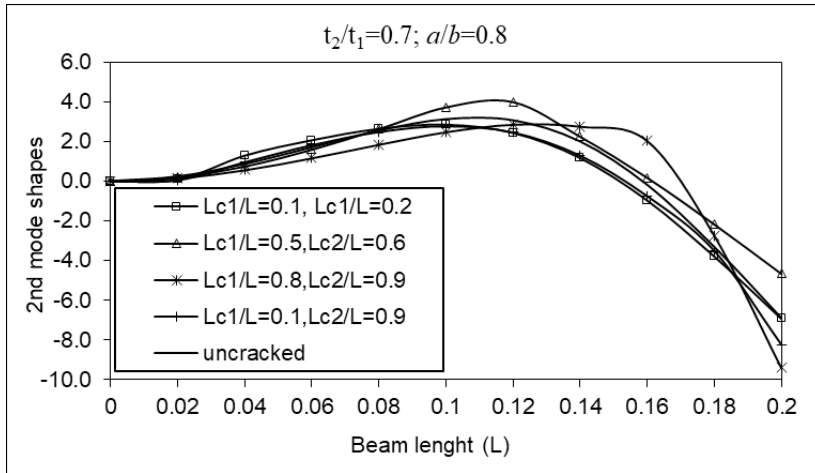
Figure 7. *Second mode shapes of fixed-free single-stepped beam with multiple cracks for crack depth ratio a/b=0.8 and taper ratio t_2/t_1=0.7*
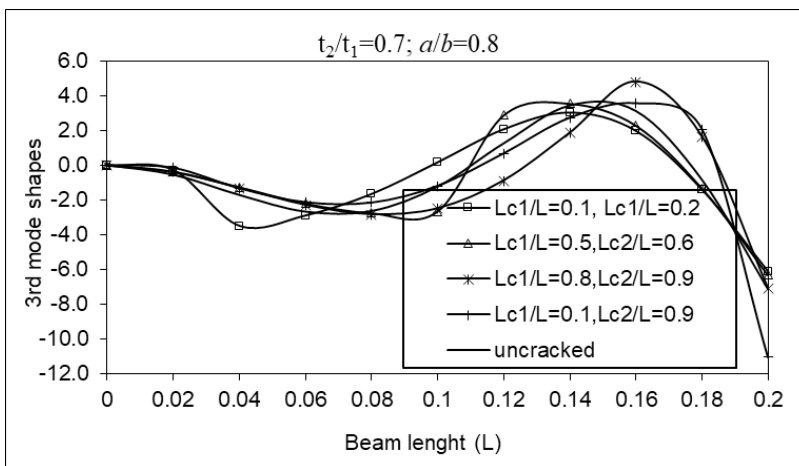
Figure 8. *Third mode shapes of fixed-free single-stepped beam with multiple cracks for crack depth ratio a/b=0.8 and taper ratio t_2/t_1=0.7*

Figures 6, 7, and 8 show the first, second and third mode shape variations depending on the crack locations for the taper ratio t_2/t_1=0.7 and the crack depth ratio *a/b=0.8*. The changes in the mode shapes are seen to vary depending on the location of the cracks in the beam. Because the cracks are in different locations, the mode shapes exhibit a variety of oscillatory movements. The graphs clearly show these oscillatory movements.

3.2. Pinned-pinned Single-Stepped Beam with Tapered Cross-Section and Multiple Cracks

In this section; a free vibration analysis was performed on a pinned-pinned single-stepped beam with tapered cross-section and multiple cracks.
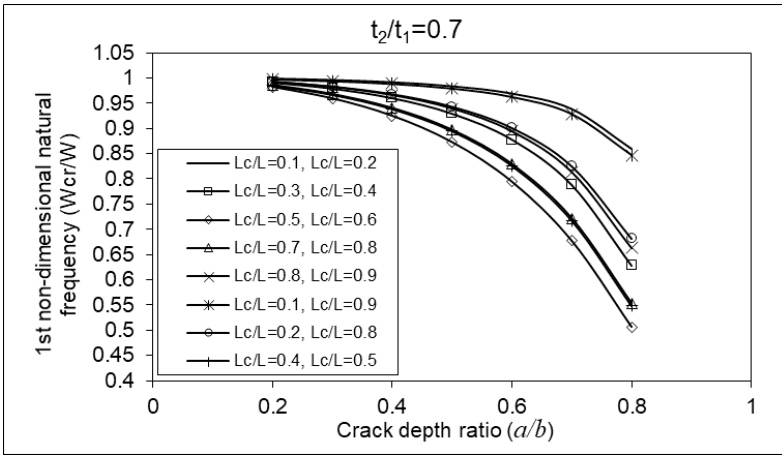
Figure 9. *First non-dimensional natural frequencies of single-stepped cracked beam with pinned-pinned ends for multiple crack locations and taper ratio $t_2/t_1=0.7$ depending on crack depth ratios a/b=0.2–0.8*
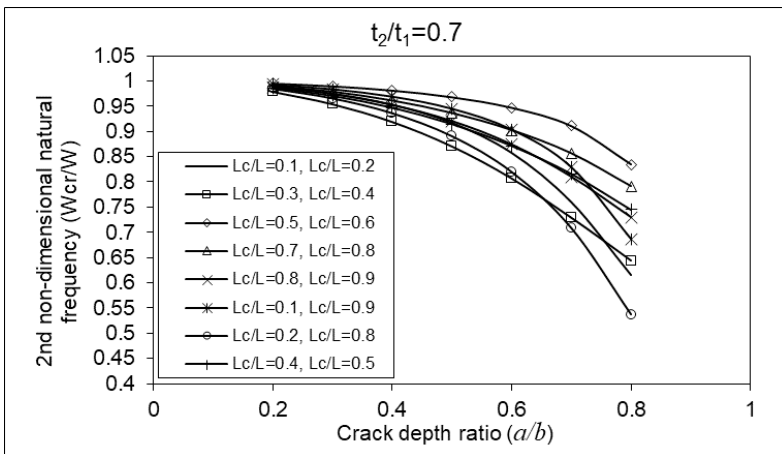
Figure 10. *Second non-dimensional natural frequencies of single-stepped beam with pinned-pinned ends for multiple crack locations and taper ratio $t_2/t_1=0.7$ depending on crack depth ratios a/b=0.2–0.8*
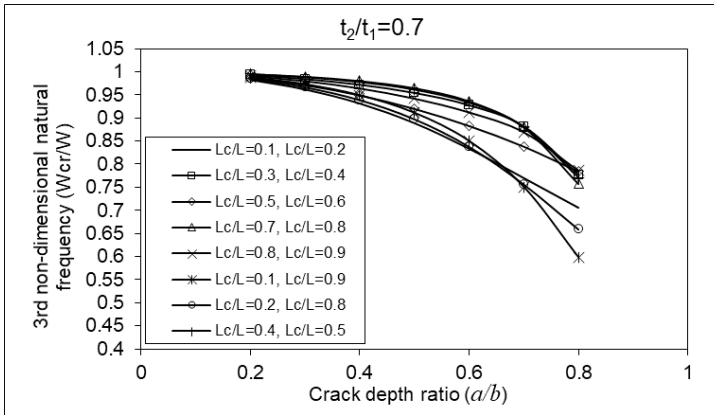
Figure 11. *Third non-dimensional natural frequencies of single-stepped beam with pinned-pinned ends for multiple crack locations and taper ratio $t_2/t_1=0.7$ depending on crack depth ratios a/b=0.2–0.8*

Figures 9, 10, and 11 show the first, second, and third dimensionless natural frequencies of the pinned-pinned single-stepped beam with taper ratio $t_2/t_1=0.7$ and the various multiple crack locations depending on crack depth ratios (*a/b*=0.2–0.8). As illustrated by the figures, when the location of the cracks were at *Lc1/L*=0.5, *Lc2/L*=0.6, the first natural frequency decreased to its maximum. The location of the cracks at *Lc1/L*=0.2, *Lc2/L*=0.8 and *Lc1/L*=0.1, *Lc2/L*=0.9, respectively, resulted in the largest reductions in the second and third natural frequencies.
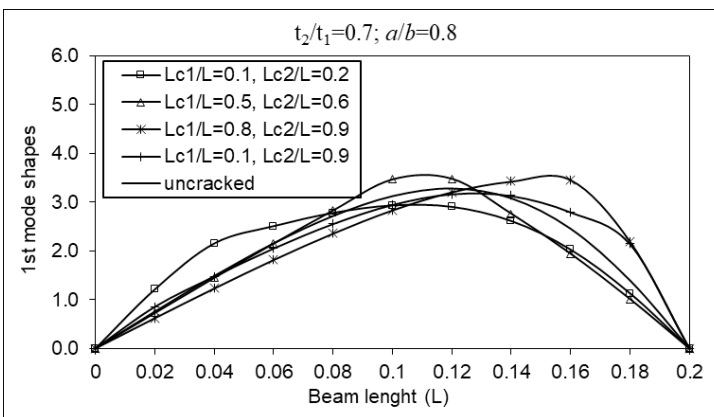
Figure 12. *First mode shapes of pinned-pinned single-stepped beam with multiple crack for crack depth ratio a/b=0.8 and taper ratio $t_2/t_1=0.7$*
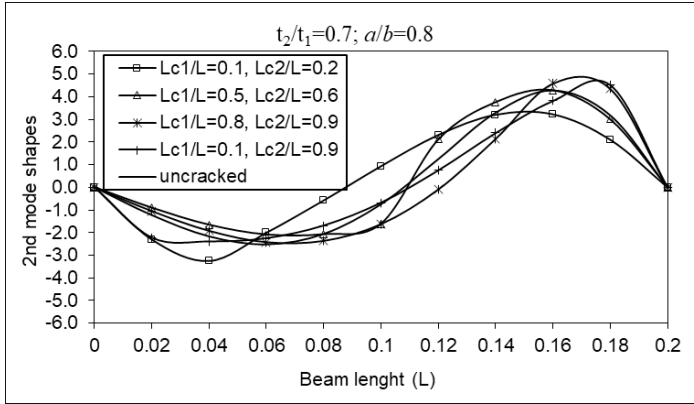
Figure 13. *Second mode shapes of pinned-pinned single-stepped beam with multiple crack for crack depth ratio a/b=0.8 and taper ratio $t_2/t_1=0.7$*
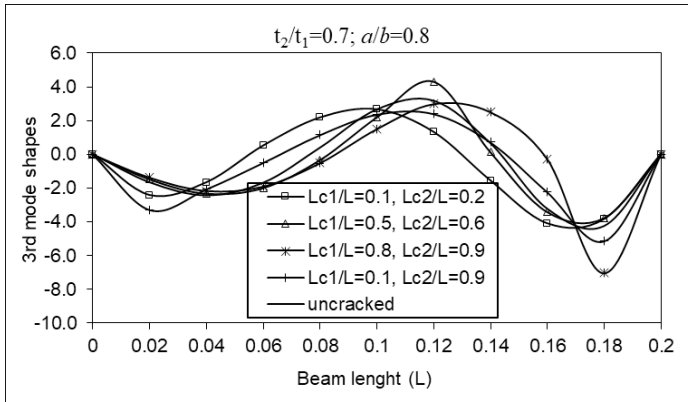
Figure 14. *Third mode shapes of pinned-pinned single-stepped beam with multiple crack for crack depth ratio a/b=0.8 and taper ratio $t_2/t_1=0.7$*

Figures 12, 13, and 14 show the first, second and third mode shapes variations depending on multiple crack locations for the taper ratio $t_2/t_1=0.7$ and the crack depth ratio *a/b=0.8*. The figures clearly show how mode shapes are affected by the location of cracks. Larger energy losses and significant changes in the relevant mode shapes will result from cracks located in the vicinity of the relevant mode's maximum bending moment.

4. Conclusion

In this section, single-stepped tapered beam with multiple cracks and different ends were studied for free vibration analysis. To solve the vibration problem, a

computer programme was built utilising the finite element method. The cracks in the beam are considered as a massless springs. The element stiffness, mass, and crack-induced stiffness matrices obtained for the tapered cracked beam were integrated into the written finite element code, and the beam was subjected to free vibration analysis. Natural frequencies and mode shapes were calculated using the computer program for various crack depth ratios, multiple crack locations, and taper ratios. Natural frequency and mode shape changes provide important details on the crack's position and depth, contributing significantly to non-destructive predictive maintenance.

While the maximum decreases and variations in the first natural frequencies and mode shapes occur when the cracks were located close to the fixed end of the fixed-free beam ($Lc1/L$=0.1, $Lc2/L$=0.2), the maximum decrease in the first natural frequencies and mode shapes occur when the cracks were in the middle of the pinned-pinned beam ($Lc1/L$=0.5, $Lc2$=0.6). The maximum decreases and variations in the second and third natural frequencies and mode shapes occurred when the cracks were at $Lc1/L$=0.7, $Lc2/L$=0.8, and $Lc1/L$=0.8, $Lc2/L$=0.9 for fixed-free beam, and $Lc1/L$=0.2, $Lc2/L$=0.8 and $Lc1/L$=0.1, $Lc2/L$=0.9 for pinned-pinned beam for taper ratio t_2/t_1=0.7, respectively.

The magnitude of energy loss caused by cracks depend on their sizes and locations. The bending moment in the beam section varies with the boundary and loading conditions along the beam. A crack in a section of the beam where the bending moment is greatest will result in significant energy loss and will also affect the beam's dynamic behavior. This study clearly demonstrated all of these findings.

References

Salawu, O. S. (1997). Detection of structural damage through changes in frequency: a review. *Engineering structures*, *19*(9), 718-723.

Dimarogonas, A. D. (1996). Vibration of cracked structures: a state of the art review. *Engineering fracture mechanics*, *55*(5), 831-857.

Wauer, J. R. (1990). On the dynamics of cracked rotors: a literature survey. *Applied Mechanics Reviews* 43 (1) 13–17.

Gasch, R. (1993). A survey of the dynamic behaviour of a simple rotating shaft with a transverse crack. *Journal of sound and vibration*, *160*(2), 313-332.

Krawczuk, M., & Ostachowicz, W. (1996). Damage indicators for diagnostic of fatigue cracks in structures by vibration measurements–a survey. *Journal of Theoretical and Applied Mechanics*, *34*(2), 307-326.

Jassim, Z. A., Ali, N. N., Mustapha, F., & Jalil, N. A. (2013). A review on the vibration analysis for a damage occurrence of a cantilever beam. *Engineering Failure Analysis*, *31*, 442-461.

Kisa, M. (2004). Free vibration analysis of a cantilever composite beam with multiple cracks. *Composites Science and Technology*, *64*(9), 1391-1402.

Kisa, M. (2011). Vibration and stability of multi-cracked beams under compressive axial loading. *International Journal of the Physical Sciences*, *6*(11), 2681-2696.

Kisa, M. (2012). Vibration and stability of axially loaded cracked beams. *Structural engineering and mechanics: An international journal*, *44*(3), 305-323.

Kisa, M., & Gurel, M. A. (2006). Modal analysis of multi-cracked beams with circular cross section. *Engineering Fracture Mechanics*, *73*(8), 963-977.

Kisa, M., & Gurel, M. A. (2007). Free vibration analysis of uniform and stepped cracked beams with circular cross sections. *International Journal of Engineering Science*, *45*(2-8), 364-380.

Kisa, M., Brandon, J., & Topçu, M. (1998). Free vibration analysis of cracked beams by a combination of finite elements and component mode synthesis methods. *Computers & structures*, *67*(4), 215-223.

Kisa, M., & Brandon, J. A. (2000). Free vibration analysis of multiple open-edge cracked beams by component mode synthesis. *Structural engineering and mechanics: An international journal*, *10*(1), 81-92.

Kisa, M., & Brandon, J. (2000). The effects of closure of cracks on the dynamics of a cracked cantilever beam. *Journal of sound and vibration*, *238*(1), 1-18.

Haskul, M., & Kisa, M. (2021). Free vibration of the double tapered cracked beam. *Inverse Problems in Science and Engineering*, *29*(11), 1537-1564.

Haskul, M., & Kisa, M. (2021). Free-vibration analysis of cracked beam with constant width and linearly varying thickness. *Emerging Materials Research*, *11*(1), 125-137.

Lee, J. (2015). Application of Chebyshev-tau method to the free vibration analysis of stepped beams. *International Journal of Mechanical Sciences*, *101*, 411-420.

Lu, Z. R., Huang, M., Liu, J. K., Chen, W. H., & Liao, W. Y. (2009). Vibration analysis of multiple-stepped beams with the composite element model. *Journal of Sound and Vibration*, *322*(4-5), 1070-1080.

Mao, Q., & Pietrzko, S. (2010). Free vibration analysis of stepped beams by using Adomian decomposition method. *Applied Mathematics and computation*, *217*(7), 3429-3441.

Mao, Q. (2011). Free vibration analysis of multiple-stepped beams by using Adomian decomposition method. *Mathematical and computer modelling*, *54*(1-2), 756-764.

Wang, X., & Wang, Y. (2013). Free vibration analysis of multiple-stepped beams by the differential quadrature element method. *Applied Mathematics and Computation*, *219*(11), 5802-5810.

Attar, M. (2012). A transfer matrix method for free vibration analysis and crack identification of stepped beams with multiple edge cracks and different boundary conditions. *International Journal of Mechanical Sciences*, *57*(1), 19-33.

Duan, G., & Wang, X. (2013). Free vibration analysis of multiple-stepped beams by the discrete singular convolution. *Applied Mathematics and Computation*, *219*(24), 11096-11109.

Su, Z., Jin, G., & Ye, T. (2018). Vibration analysis of multiple-stepped functionally graded beams with general boundary conditions. *Composite Structures*, *186*, 315-323.

Vaz, J. D. C., & de Lima Junior, J. J. (2016). Vibration analysis of Euler-Bernoulli beams in multiple steps and different shapes of cross section. *Journal of Vibration and Control*, *22*(1), 193-204.

Šalinić, S., Obradović, A., & Tomović, A. (2018). Free vibration analysis of axially functionally graded tapered, stepped, and continuously segmented rods and beams. *Composites Part B: Engineering*, *150*, 135-143.

Wattanasakulpong, N., & Chaikittiratana, A. (2016). Adomian-modified decomposition method for large-amplitude vibration analysis of stepped beams with elastic boundary conditions. *Mechanics Based Design of Structures and Machines*, *44*(3), 270-282.

Jaworski, J. W., & Dowell, E. H. (2008). Free vibration of a cantilevered beam with multiple steps: Comparison of several theoretical methods with experiment. *Journal of sound and vibration*, *312*(4-5), 713-725.

Haskul, M. (2010). *Çatlak içeren değişken kesitli kirişlerde titreşim probleminin sonlu elemanlar metoduyla modellenmesi/Finite element method for the vibration of cracked beams with varying cross section (Harran Üniversitesi, Fen bilimleri Enstitüsü).*

Tada, H., Paris, P. C., & Irwin, G. R. (1973). The stress analysis of cracks. *Handbook, Del Research Corporation*, *34*(1973).

Irwın, G. (1960). Fracture Mechanics, Editors JN Goodier and NJ Hoff

STRUCTURAL STRENGTH ANALYSIS WITH FINITE ELEMENT METHOD IN PIPE-CLAMP CONNECTIONS

Sümeyye ERDEM[1] & Yusuf DİLAY[2]

[1](Lecturer), Karamanoğlu Mehmetbey University
Vocational School of Technical Sciences, Department of
Mechanical and Metal Technologies, Karaman, Turkey
E-mail: sumeyyeerdem@kmu.edu.tr
ORCID: 0000-0002-5518-2716

[2](Asst. Prof. Dr), Karamanoğlu Mehmetbey University
Vocational School of Technical Sciences, Department of
Mechanical and Metal Technologies, Karaman, Turkey
E-mail: ydilay@kmu.edu.tr
ORCID: 0000-0002-5365-5137

1. Introduction

Closed paths used for the controlled transportation of fluids (water, oil, air and fuel) from one place to another in the desired way are called pipes. Pipes used in the transmission lines of hydraulic systems can be exposed to various stresses. If the system passes through a place subject to movement and vibration, flexible or ring pipes are used in the system, and straight pipes are used in places that do not encounter any stress. These pipes are generally made of aluminium and stainless steel. Aluminium pipes are generally used in aircraft systems at pressures up to 1500 PSI due to their light weight and ease of processing. However, since the materials used in their alloy are different, not all aluminium pipes can be used under 1500 PSI pressure, and the hard alloyed ones can be used under high pressure such as 3000 PSI. Pipes made of stainless steel are used in high pressure lines and at points exposed to external influences (attack edges). It is expensive and requires special equipment for

processing due to its hardness. This means that the piping must be supported. If appropriate supports are used to accommodate expansion and contraction due to environmental conditions, the life of the system and the pipe will be extended. Stresses affecting the pipe support are the mass (weight) of the piping system and the type of fluids it carries, thermal expansion and contraction, vibration and installation stresses (Anonymous, 2013).

Piping systems can have a significant mass to support. This factor is an important consideration in the design of the piping system. For example, the widespread use of butt weld piping systems to reduce mass is a major reason for this. Piping that is not properly supported will sag and cause pockets of liquid that cannot be drained from the pipe. Small diameter pipes sag more easily than larger diameter pipes and therefore require more support. Due to the high cost of pipe support, it is sometimes cheaper to use a larger diameter pipe than a small diameter pipe with support.

Temperature changes in the piping system due to changes in ambient temperature or changes in the temperature of the transported fluids cause changes in the length of the piping system. The changes in length depend on the change in temperature and the coefficient of expansion of the pipe material.

Piping systems and pipe supports should be designed with thermal expansion in mind. Piping systems that are too rigid can create excessive expansion and/or contraction forces on nozzles, flanges, couplings, etc.

Vibration, in combination with other stresses, can significantly increase fatigue failure of piping systems. Where piping and equipment are subjected to load and vibration, the transferred load and vibration should be minimized.

The Finite Element Method (FEM) is a mathematical model that can perform stress analysis of complex geometrically shaped bodies and such bodies under static and dynamic loads (Makange et al., 2015). With the help of FEM, it is possible to prevent incorrect construction and material use in manufacturing, and it is possible to design machines or parts that work longer and more efficiently (Altuntaş et al., 2018). Strength calculations have been carried out by different researchers using the finite element method. Değirmencioğlu et al. (1998), stress analysis of plough roofs using finite element method, Gürsel et al. (2005), Gürsel et al. (2006), Yurdem et al. (2019), stress analysis of three-stemmed ploughs using finite element method, Çelik et al. (2007), strength analysis of structural and functional elements of the boot using finite element method. Şahin et al. (2018), determined the strength properties of cultivator crowbar end irons using finite element method (FEM). Zeytinoğlu (2006) performed the stress analysis of the towing ring of a 3.5-ton single-axle agricultural cart by finite element

method. Kalkan (2007) studied the investigation of static loading tests of tractor safety cab with finite element method. Soncu et al., (2010) performed thermal analysis of St 37 material welded by cornice method using finite element method. Arefi et al., (2022), Draught force prediction from soil relative density and relative water content for a non-winged chisel blade using finite element modelling. Naderi-Boldaji et al., (2023), Investigation of the predictability of mouldboard plough draught from soil mechanical strength (cone index vs. shear strength) using finite element modelling. Nazemosadat et al., (2022), Structural analysis of a mounted mouldboard plough using the finite element simulation method. Topakci et al. (2008), performed stress analysis of group gears used in rotovator with the help of finite elements.

In this study, three-dimensional solid modelling of the pipe-clamp connection was carried out, stress, displacement and fatigue analyses of the modelled pipe-clamp connection under normal conditions were simulated using the finite element method and the safety factor of the pipe-clamp connection was calculated.

2. Materials and Method

The research material considered in the study is the pipe-clamp connection. The technical dimensions of the solid modelling of the analysed pipe-clamp connection prepared using SolidWorks program are given in Figure 1. Pipe-clamp fittings, which consist of a large number of parts, can be used to improve the design or directly intervene in the design. The pipe-clamp connection considered in the research consists of pipe, clamp, bolt and nut elements. The pressure value applied to the pipe-clamp connection was taken from the manufacturer's catalogues. During the analysis, the side surfaces of the head parts of the pipe were kept constant and a pressure of 10 MPa was applied to the inner surface of the pipe. The materials used in the pipe-clamp connection were ASTM 304 for the pipe, ASTM 304 for the clamp, St 50 for the bolt and St 50 for the nut. Some technical properties of the materials are given in Table 1-4.

Table 1. Material properties of the pipe element

Pipe (ASTM 304)	Properties
Modulus of Elasticity	193 GPa
Yield Strength	215 MPa
Poisson Ratio	0,3
Tensile Strength	505 MPa

Table 2. Material properties of the clamp element

Clamp (ASTM 304)	Properties
Modulus of Elasticity	193 GPa
Yield Strength	215 MPa
Poisson Ratio	0,3
Tensile Strength	505 MPa

Table 3. Material properties of the bolt element

Bolt (St 50)	Properties
Modulus of Elasticity	211 GPa
Yield Strength	295 MPa
Poisson Ratio	0,3
Density	7,8 g/cm³

Table 4. Material properties of the nut element

Nut (St 50)	Properties
Modulus of Elasticity	211 GPa
Yield Strength	295 MPa
Poisson Ratio	0,3
Density	7,8 g/cm³
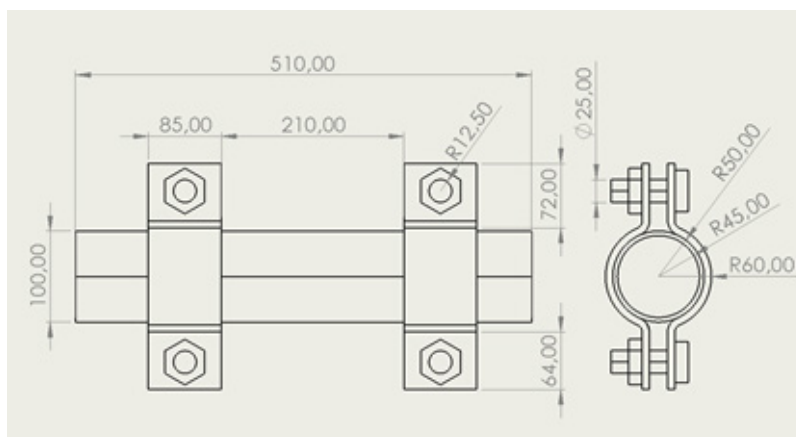
Figure 1. Technical drawing of pipe-clamp connection

The study started with solid modelling of the pipe-clamp connection with Solidworks software (Figure 2). Then, the stress distributions occurring on the pipe-clamp connection were made with the help of finite element package software Ansys Workbench. Thus, simulations of operation under different loads and operating environments were obtained. The analyses were carried out as three-dimensional and linear static. The obtained strength analysis results are given as outputs of Ansys Workbench package software. The pipe-clamp connection was evaluated and simulated considering the application conditions.
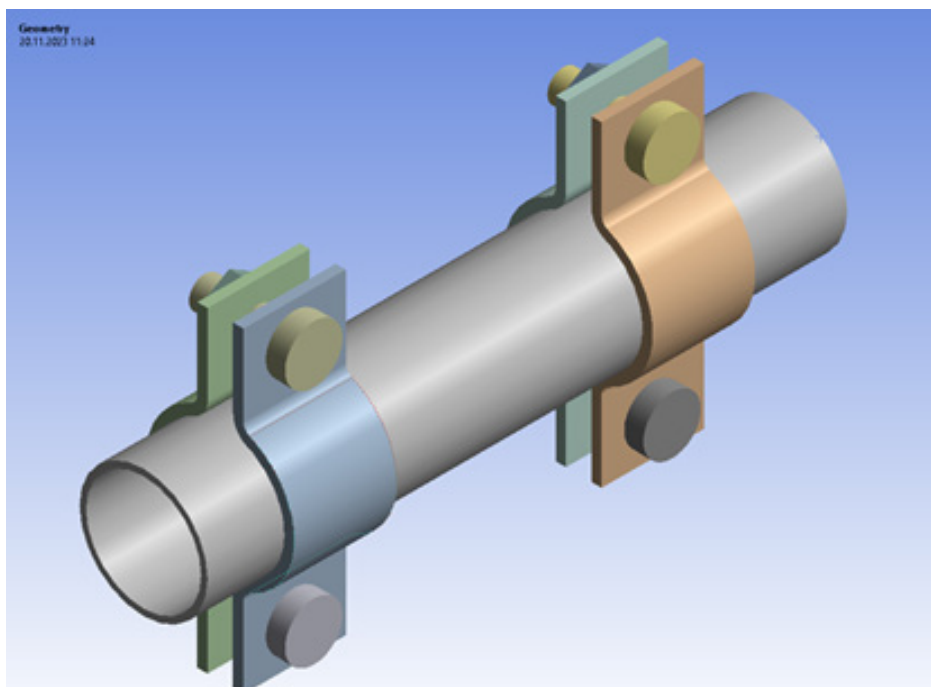
Figure 2. Solid model drawings of pipe-clamp connection

In the first step of the analysis process performed in the simulation environment with the finite element method, the meshing of the pipe-clamp connection model, in other words, the separation of the model into the most appropriate small parts, was performed (Figure 3). The "meshing" functions of Ansys Workbench software were utilized to create the finite element structure of the pipe-clamp connection. A total number of 208,144 elements and 496,382 total nodes were obtained for the pipe-clamp connection.
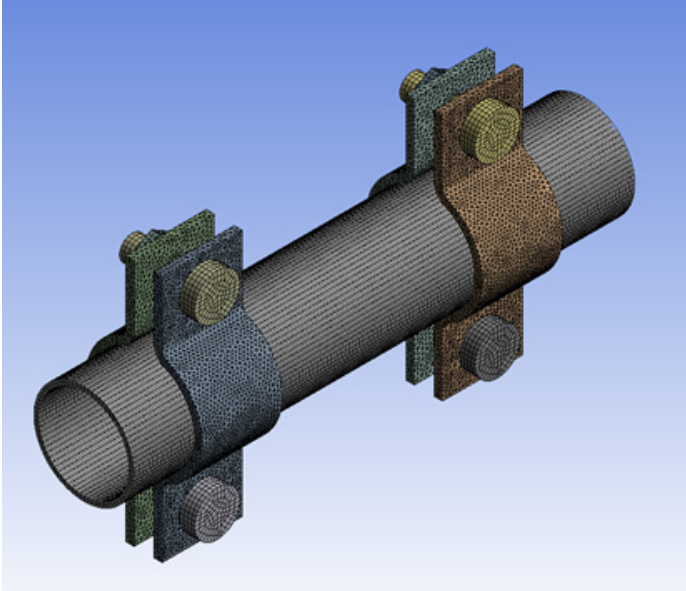
Figure 3. Finite element structure of the pipe-clamp connection model

In the pipe-clamp connection, the side surfaces of the heads of the pipe were kept stationary and a pressure of 10 MPa was applied to the inner surface of the pipe (Makhutov et al., 1991) using the literature (Figure 4).
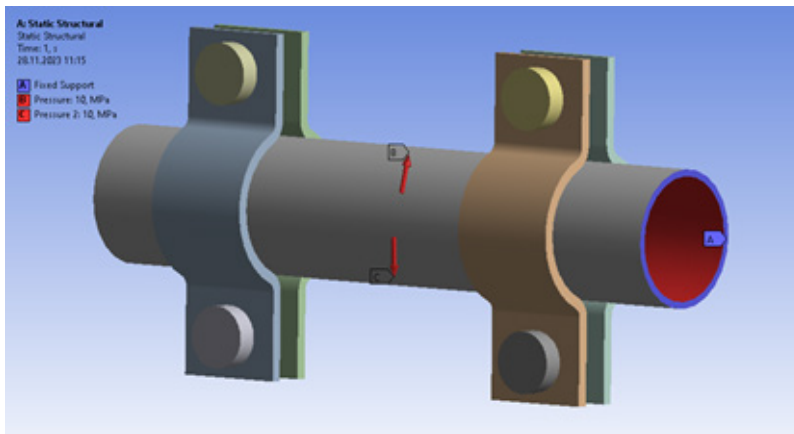
Figure 4. Defining boundary conditions and pressure

3. Research Findings and Discussion

After the strength analysis solution process, the stress distributions occurring on the pipe-clamp connection are given in Figure 5. When the pipe-

clamp structure is examined, it is seen that the maximum equivalent stress is on the side inner surfaces of the head parts of the pipe. The maximum stress value is 145.87 MPa. When this value is evaluated in terms of material, it is below the yield strength. When the stresses on the other structural elements were examined (Figure 6-9), it was determined that the stress distribution under the applied loads remained within the yield strength limits of the material. The maximum equivalent stress and the safety coefficients obtained according to the yield strength of the material for Figures 6-9 are given in Table 5. When the equivalent stress values of all structural elements are analysed, it is seen that the pipe-clamp connection works safely without damage under the application conditions.
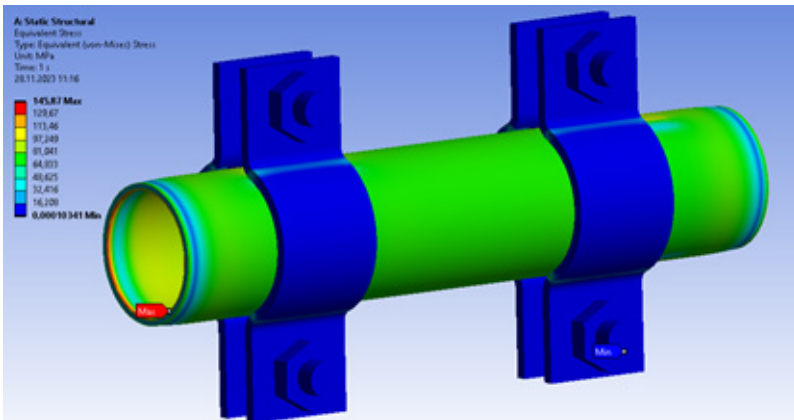
Figure 5. Distribution of equivalent stresses for the whole structure
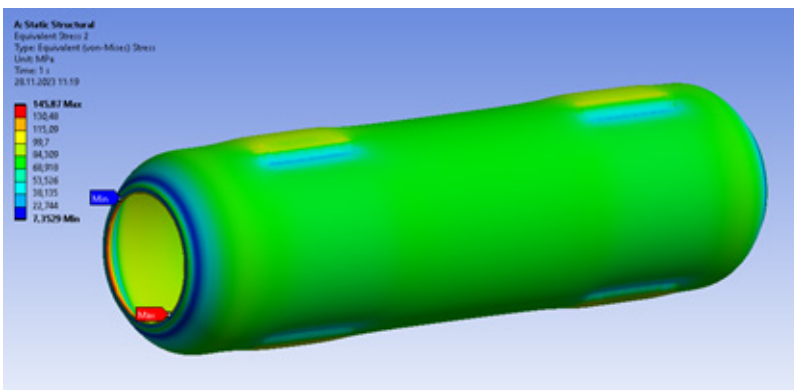
Figure 6. Equivalent stress distributions for pipe
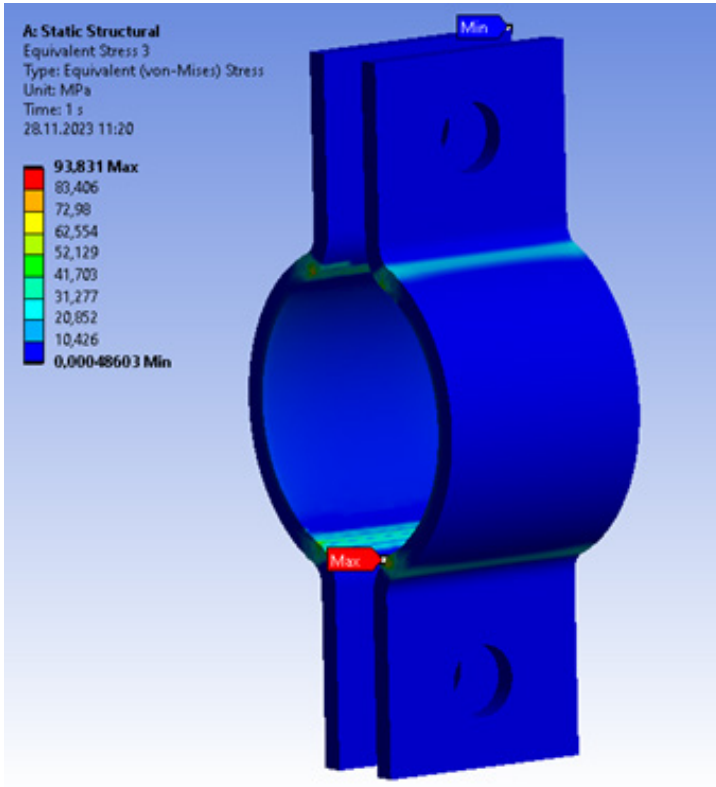
Figure 7. Equivalent stress distributions for clamp
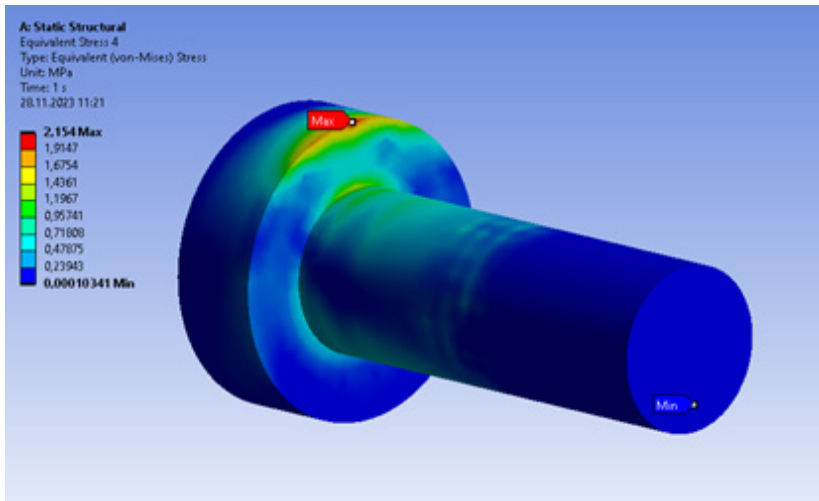
Figure 8. Equivalent stress distributions for bolt
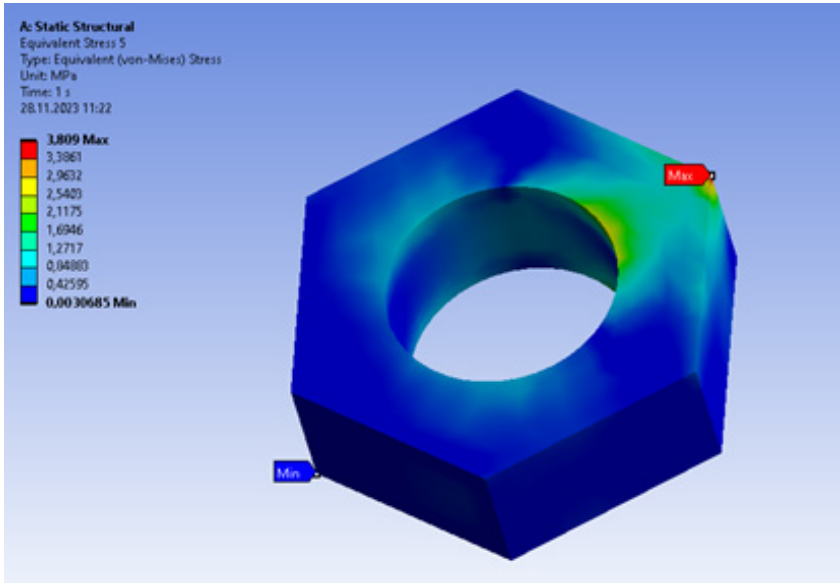
Figure 9. Equivalent stress distributions for nut

Table 5. Working safety coefficients calculated for pipe-clamp connection

Pipe-clamp fittings	Material yield strength [σ_{yield}][MPa]	Max. equivalent stress [σ_{eq}] [MPa]	Safety factor [k_s]=[$\sigma_{yield}/\sigma_{eq}$]
Pipe	215	145,87	1,473
Clamp	215	93,831	2,291
Bolt	295	2,154	136,954
Nut	295	3,809	77,448

In the research, displacement analysis was performed under the effect of pressure applied to the pipe-clamp connection. After the analysis, the total displacement value occurring on the pipe-clamp connection is given in Figure 10. When the structure of the pipe-clamp connection is examined, it is seen that the total displacement value is at the bolt. The total displacement value is 0.43315 mm. Displacement values were also calculated on other structural elements (Figure 11-14). The values obtained according to the displacement analysis for Figure 11-14 are given in Table 6.
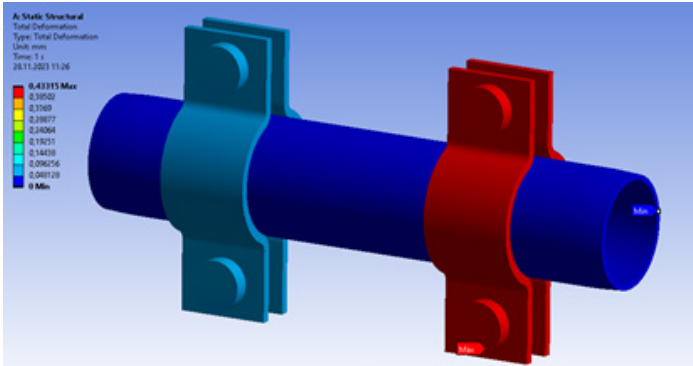
Figure 10. Maximum total displacement distribution in pipe-clamp connection
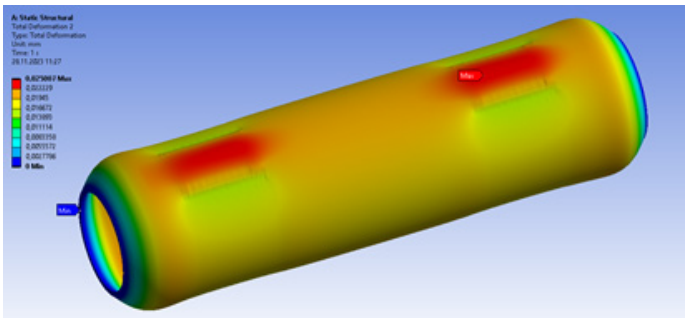
Figure 11. Displacement distributions for pipe
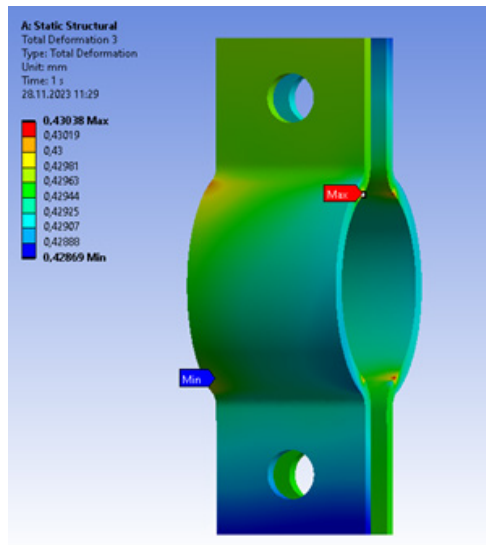
Figure 12. Displacement distributions for clamp
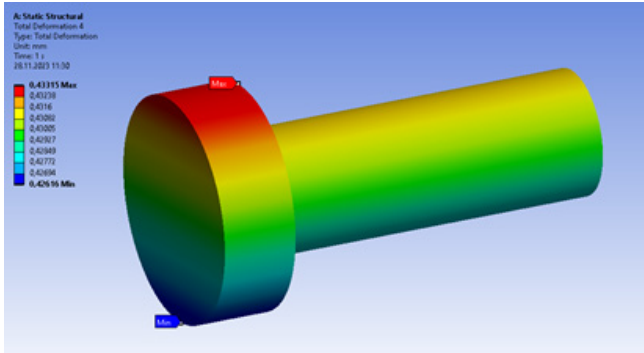
Figure 13. Displacement distributions for bolt
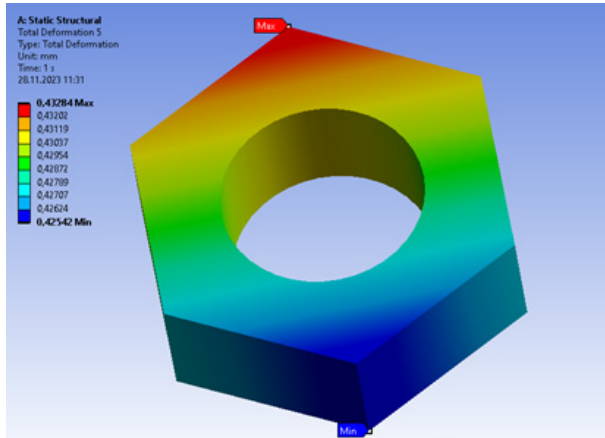
Figure 14. Displacement distributions for nut

Table 6. Calculated displacement values for pipe-clamp

Pipe-clamp fittings	Displacement Values (mm)
Pipe	0,025007
Clamp	0,43038
Bolt	0,43315
Nut	0,43284

After the analysis, the safety factor value on the pipe-clamp connection was calculated and given in Figure 15. The blue colour indicates the maximum safety factor and the red colour indicates the minimum safety factor value on the pipe-clamp connection. The maximum safety factor value of the pipe-clamp connection is 15 and the minimum value is 0.
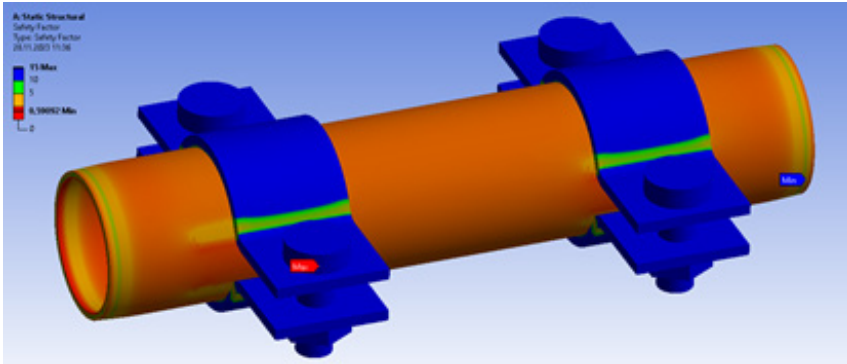
Figure 15. Safety factor of pipe-clamp connection

4. Conclusion

In this study, three-dimensional solid modelling of the pipe-clamp connection was performed, stress, displacement and fatigue analysis of the modelled pipe-clamp connection under normal conditions were simulated and the safety factor of the pipe-clamp connection was calculated. The results obtained as a result of the analyses are given below.

a. For the whole pipe-clamp connection construction, the maximum equivalent stress value was found to be on the side inner surfaces of the pipe heads. The maximum stress value is 145.87 MPa.

b. The maximum equivalent stress value is 145.87 MPa in the pipe element, 93.831 MPa in the clamp element, 2.154 MPa in the bolt element and 3.809 MPa in the nut element.

c. The maximum total displacement for the pipe-clamp connection was found to be 0.43315 mm in the bolt element.

d. The displacement value was determined as 0.025007 mm for the pipe element, 0.43038 mm for the clamp element, 0.43315 mm for the bolt element and 0.43284 mm for the nut element.

e. Safety factor values were calculated for pipe-clamp connection. The maximum safety factor value was found to be 15 on the side surface of the pipe head. The minimum safety factor value was found to be 0 at the pipe element.

f. In the simulation, no damage was found in the pipe-clamp connection construction. It was determined that the pipe-clamp connection element and structural elements carried the forces at different points applied within the elastic deformation limits of the materials used.

The maximum equivalent stress value, maximum total displacement and safety factor values calculated as a result of the research were similar to the literature.

Due to the time-consuming and costly nature of real tests, the strength analysis of the products to be designed with 3D solid modelling techniques and finite element method will minimize unnecessary time loss. In this context, the data obtained in the virtual environment should be interpreted very well before manufacturing and experimental studies should be directed where necessary.

References

Altuntaş, E., Şahin, A., & Güleç, U. (2018). Determination of deformation behaviour of the cultivator narrow shares manufactured by the different firms under various loading conditions by means of finite element analysis. *Anadolu Journal of Agricultural Sciences*, *33*(2), 131-141.

Anonymous, (2013). Pipe Fabrication Materials, Drawing and Fabrication Methods Metals and Engineering. ENG 2068. https// www.dtwd.wa.gov.au

Arefi, M., Karparvarfard, S. H., Azimi-Nejadian, H., & Naderi-Boldaji, M. (2022). Draught force prediction from soil relative density and relative water content for a non-winged chisel blade using finite element modelling. *Journal of Terramechanics*, *100*, 73-80.

Çelik H K, Topakçı M, Yılmaz D, Akıncı İ (2007). Strength analysis of the structural and functional elements of the boot by finite element method, *Journal of Agricultural Machinery Science*, 3(2): 111-116.

Değirmencioğlu, A., Çakır, E., Gülsoylu, E., Keçecioğlu, G., (1998). Stress Analysis of Plough by Finite Element Method. 18th National Agricultural Mechanization Congress, Proceedings, S. 283-289, Tekirdağ.

Gürsel, K. T., & Köftecioğlu, E. Y. (2006). Structural Analysis of Elements of Two-Bottom Mouldboard Plough. *Sigma*, 3.

Gürsel, K.T., Kılıç, A., Değirmencioğlu, A., (2005). Strength Analysis of a Theree- Bottom Moldboard Plough Using Finite Element Method. 9th. International Congress on Mechanization and Energy in Agricultural. İzmir.

Kalkan, E. (2007). *Traktör güvenlik kabini statik yükleme deneylerinin sonlu elemanlar yöntemi ile incelenmesi* (Doctoral dissertation, Sakarya Universitesi (Turkey)).

Makange, N. R., Parmar, R. P., & Tiwari, V. K. (2015). Stress analysis on tyne of cultivator using finite element method. *Trends in Biosciences*, *8*(15), 3919-3923.

Makhutov, N.A., Serikov, S.V. & Kotousov, A.G., (1991). Increasing the design strength of piping fittings. *Strength Mater* 23, 468–472. https://doi.org/10.1007/BF00771978.

Naderi-Boldaji, M., Karparvarfard, S. H., & Azimi-Nejadian, H. (2023). Investigation of the predictability of mouldboard plough draught from soil mechanical strength (cone index vs. shear strength) using finite element modelling. *Journal of Terramechanics*, *108*, 21-31.

Nazemosadat, S. M. R., Ghanbarian, D., Naderi-Boldaji, M., & Nematollahi, M. A. (2022). Structural analysis of a mounted moldboard plow using the finite element simulation method. *Spanish Journal of Agricultural Research*, *20*(2), e0204-e0204.

Şahin, A., Altuntaş, E., & Güleç, U. (2018). Determination of the Strength Analysis of the Cultivator Duckfoot Shares with Finite Element Methods. *Selcuk Journal of Agriculture and Food Sciences*, *32*(3), 257-265.

Topakci M, Celik H K, Yılmaz D, Akıncı I (2008). Strees analysis on transmission gears of a rotary tiller using finite element method. *Akdeniz University Journal of Faculty of Agriculture*, 21(2): 155-160.

Yurdem, H., Degirmencioglu, A., Cakir, E., & Gulsoylu, E. (2019). Measurement of strains induced on a three-bottom moldboard plough under load and comparisons with finite element simulations. *Measurement*, *136*, 594-602.

Zeytinoğlu, M. (2006). Stress analysis of the towing ring of a 3.5 ton single axle agricultural cart using finite element method. *Journal of Uludag University Faculty of Agriculture*, *2*(21), 21-24.

EFFECTS ON MECHANICAL PROPERTIES OF MG ADDED TO AL-FE ALLOY AND HOMOGENIZATION PROCESS

Yunus TÜREN[1] & Hayrettin AHLATCI[2] &Fatma MEYDANERİ TEZEL[3]

[1](Assoc. Prof. Dr.), Necmettin Erbakan University, Faculty of Engineering, Department of Mechanical Engineering, 42090, Konya, Türkiye. E-mail: yunus.turen@erbakan.edu.tr,
ORCID:0000-0001-8755-1865

[2](Prof. Dr.), Karabük University, Faculty of Engineering, Department of Metallurgy and Materials Engineering, 78050, Karabük, Türkiye. E-mail: hahlatci@karabuk.edu.tr,
ORCID: 0000-0002-6766-4974

[3](Prof. Dr.), Karabük University, Faculty of Engineering, Department of Metallurgy and Materials Engineering, 78050, Karabük, Türkiye. E-mail: fatmameydaneri@karabuk.edu.tr,
ORCID: 0000-0003-1546-875X

1. Introduction

Aluminum is one of the most abundant elements in nature, and is the most used metal in engineering structures after steel. Aluminum and aluminum alloys in today's industry; they are an important material for engineers and designers due to their lightness, good thermal and electrical conductivity, increased strength properties and resistance to corrosion. Aluminum and its alloys have many excellent properties such as low density, good corrosion resistance, machinability and electrical conduction compared to other materials, so they are widely used in the aircraft and automotive industries (Que et al., 2021). Aluminum alloys contain 1-3% Mg and have higher hardness and strength than other aluminum alloys, making them ideal materials for the

aircraft, space and automotive industries. Since magnesium is highly soluble in aluminum, precipitation strength is increased (Liu et al., 2021). In the manufacturing of air and space vehicles, high-performance materials that are both very durable and lightweight must be used.

By adding alloying elements to aluminum, many properties such as mechanical properties, structural, electrical, thermal and corrosion have been improved. Studies have shown that different compositions of alloys, different compositions and heat treatments applied to alloys improve their existing properties. For example, some aluminum alloys can match or even exceed the strength of building steel. Compared to cast iron and non-ferrous alloys, it has been shown to have superior properties such as higher strength, castability, formability and recyclability. Aluminum alloys are economical in many applications such as the automotive industry, aerospace industry, in the construction of machines and devices, as cooking vessels, housings of electronic devices, pressure vessels, cryogenic applications etc.(Wang et al., 2020).

Previous studies have shown that alloying can increase the high strength of Al and Al alloys. Karabay studied the combination of Al-boron alloy addition with artificial aging to simultaneously improve the electrical conductivity and strength of 6201 Al alloy (Karabay, 2006). Recently, numerous studies have been conducted to investigate the effect of rare earths on the electrical conductivity and tensile strength of Al alloys (Zheng et al, 2020; Qiu et al, 2013; Li et al., 2015; Barrirero et al., 2019; Pandee et al., 2018; Feng et al., 2018; Li et al., 2018; Sun et al, 2017), and the results have shown that rare earths have excellent potential in the modification of microstructure and properties. However, the opposite results were generally obtained. For example, Jiang et al. (Jiang et al., 2014) thought that the max. tensile strength, yield strength and elongation of A357 alloy could be improved by adding 0.2 wt.% mischmetal. The results of Yuan et al. (Yuan et al., 2012) showed that the tensile strength of the Al-Mg-Si-Zr alloy decreased with the addition of 0.2 wt.% La. Zhao et al. (Zhao et al., 1995) emphasized that the addition of Ce or La to the Al-Mg-Si alloy is suitable for strengthening its electrical conductivity, while Gao et al. (Gao et al., 1992) found that the addition of Ce reduces the electrical conductivity of pure Al. Such controversial results have shown that it is very important to investigate the effects of rare elements on the microstructure and properties of Al alloys (Jiang et al., 2020).

Iron is a well-known impurity in aluminum alloys, and iron causes the formation of iron-rich intermetallics on complex shapes and morphologies

(Zhang et al., 2013). The types of these iron-rich intermetallics depend on the degree of solidification and iron level (Zhang et al., 2013; Osawa et al., 2007). Normally; β phase, Chinese script α phase and polyhedral α phase are formed in Al-Si alloys (Taghaddos et al., 2009; Phongphisutthinan et al., 2012). Considering that the effect of Fe content on the microstructure and mechanical properties of Al alloys is quite important, various studies have been carried out to determine the structure (Gustafsson et al., 1986) and morphologies (Dinnis et al., 2005) of Fe-IMCs. As the volume fraction of the secondary phase increases, the strength and elongation decrease (Kobayashi, 2000). The random shape and morphology of Fe-IMCs significantly affect the mechanical properties such as ductility of these alloys (Sato and Tezuka, 2006; Cao and Campbell, 2006). In other words, iron is an element that can be useful in recycled materials. It is very important that these intermetallics meet the demands for recycling of scrap materials (Kumari et al., 2007; Umezawa et al., 2005). Recently, Sato et al. (Sato and Tezuka, 2006; Aoki et al., 2014) demonstrated that high strength and ductility properties can be obtained in Al-Mg-Si and Al-Zn-Mg alloys containing 1% Fe under deformation-semi-solid forming. This deformation-semi-solid forming triggers tension within the Al matrix and is an effective method to break down of Fe-IMCs (Kim et al., 2019). According to the Al-Fe and Mg-Fe binary phase diagrams, while the formation of compounds between Mg and Fe is limited for all ranges of composition, on the other hand, various compounds allow formation between Al and Fe. Therefore, the microstructure of the Al-Mg-Fe alloy is expected to form fine grains due to the presence of Mg-rich Al matrix and Al/Fe compounds caused by the chemical immobility between Mg and Fe. The effects of solute entrainment and grain boundary shifting can be expected from these types of alloy, possibly leading to an improvement in superplasticity (Kim and Shin, 1998).

The effects of Mg on intermetallic compounds, especially on intermetallic compounds containing Fe and the heterogeneous nucleation of α-Al, have been studied very little. Addition of Fe to Al alloys has some advantages such as improving the strength of the final forged product or the machinability of the alloy (Jinta et al., 2000; Toros et al., 2008). However, due to the very low solid solubility of Fe in Al, especially at low temperatures, the main problem with Fe-containing Al alloys is that Fe-rich intermetallic compounds damage the mechanical properties of Al alloys and always form as large particles. However, Fe is considered to be a useful element for strengthening Al-Mg and Al-Mg-Mn casting alloys (Zhu et al., 2018). These iron-rich needle intermetallics often

induce high local stress and therefore cause damage to mechanical properties. Their damage effects depend on the size, morphology, extent of particle litter and amount within the alloy (Zhu et al., 2018; Ji et al., 2013; Wang et al., 2003). Puncreobutr et al. (Puncreobutr et al., 2014) explained that β-Al5FeSi iron-rich intermetallics facilitate pore formation and tend to block interdendritic channels, thus increasing hot tear sensitivity. Bjurenstedt and his colleagues (Bjurenstedt et al., 2019) examined the effects of iron-rich intermetallics such as size, orientation and accumulation/clustering in the crack initiation area in casting alloys. The results showed that the iron-rich intermetallics in these accumulations likely triggered the formation of more cracks.

In recent years, the effects of additive elements and heat treatment have been investigated in order to improve the mechanical and physical properties of commercially important alloys. In this study, mechanical properties were examined by adding Mg to the Al-Fe alloy and applying homogenization heat treatment.

2. Materials and Method

Al plates, coarse pure Fe particles and pure Mg plates were used to casting of the Al-21.1 wt.% Fe and Al-Fe-xMg (x=1, 2, 3 wt.%) alloys examined in this study. From the phase diagrams, the composition of the Al-Fe alloy was determined and the mass ratios of the elements were calculated and the casting phase was started. Casting of the alloys was carried out in an induction casting furnace. During the production, pure Al was first melted at 750 °C and Fe particles were added into the liquid melt at approximately 850 °C. The dissolution of Fe particles in molten Al was controlled by stirring with the help of graphite rods. The mixing process lasted half an hour, and after adding the determined amount (1,2,3 wt.%) of pure Mg into the melt that reached a temperature of 750 °C, casting was carried out in permanent molds. The casting samples and samples that would be subjected to 5-hour homogenization annealing at 500 °C were grouped into 4 groups.

In the first stage, the samples were cut on the Discotom 100 cutting device, bakelite was taken with the Cito Press 10 brand device, and polished with 6, 3, 1 micron diamond suspensions in the Tegramin 30 brand polishing device, respectively. They were etched with Keller solution (2.5 ml HNO_3+ 1.5 ml HCl + 1.0 ml HF + 95 ml H_2O) then ultrasonic polishing was followed, and then the surface morphologies were visualized under an optical microscope.

Matrix phase, microstructural examinations such as distribution and shapes of intermetallic phases, grain boundaries and casting defects etc. were carried out. In the second stage, elemental mapping of the formed phases was obtained with the CARL ZEISS ULTRA PLUS GEMINI brand FESEM device by EDX analysis of the samples. In the third stage, Zwick/Roell Z600 Universal testing device and Q10 A+ QNESS brand Vickers microhardness device were used to determine the strength properties by compression test and microhardness of the samples, respectively. The morphology of the fractured surfaces obtained as a result of the compression test and the elemental mapping of the phases were examined with FESEM. The morphology of the fractured surfaces obtained as a result of the compression test were examined with FESEM.

3. Results and Discussion

3.1. Surface Morphologies and Composition Analysis

Matrix phase, microstructural examinations such as distribution and shapes of intermetallic phases, grain boundaries and casting defects were imaged. The cast state of the samples and the optical microscope images of the samples homogenized at 500 °C are given in Figure 1. θ-$Al_{13}Fe_4$+α-Al eutectic phase was formed within the white α-Al matrix phase in both Al-21.1 wt.% Fe samples that were cast and homogenized annealed. With this annealing, the structure of the eutectic lamellae in the white α-Al phase increased and became thinner. In addition, intermetallic θ-$Al_{13}Fe_4$ phase with the long and thick body structure is separated by α-Al phases, and is divided into two according to their sizes. The first one has a coarse structure, and the second one has a small fine structure surrounded by α-Al phase. The Fe phase, which is insoluble in the structure, appears as small dots on the edges of the long and thick/rough-bodied intermetallic θ-$Al_{13}Fe_4$ phase and inside the α-Al phase. When the Al-Fe-xMg (x=1, 2, 3 wt.%) casting samples are examined, as the amount of Mg added to the structure increases and the amount of Fe decreases, the eutectic (θ-$Al_{13}Fe_4$ +α-Al) phase within the α-Al white phase decreases, and the sizes of primary plate-like coarse-structured Fe-rich intermetallic phases also decrease. As the amount of Mg increases and the amount of Fe decreases and with homogenization annealing, while the intermetallic structure with long-thick body begins to thin and turns into a small needle-like structure, medium-sized spherical structures and dendrite arms will continue to grow further. These are binary eutectic intermetallic phases and have flake-like and spherical shapes that are smaller in

size than the primary iron-rich intermetallic phases (Figure 1). Also, the EDX mapping of the cast and homogenization annealed samples is given in Figures 2 and 3, respectively.
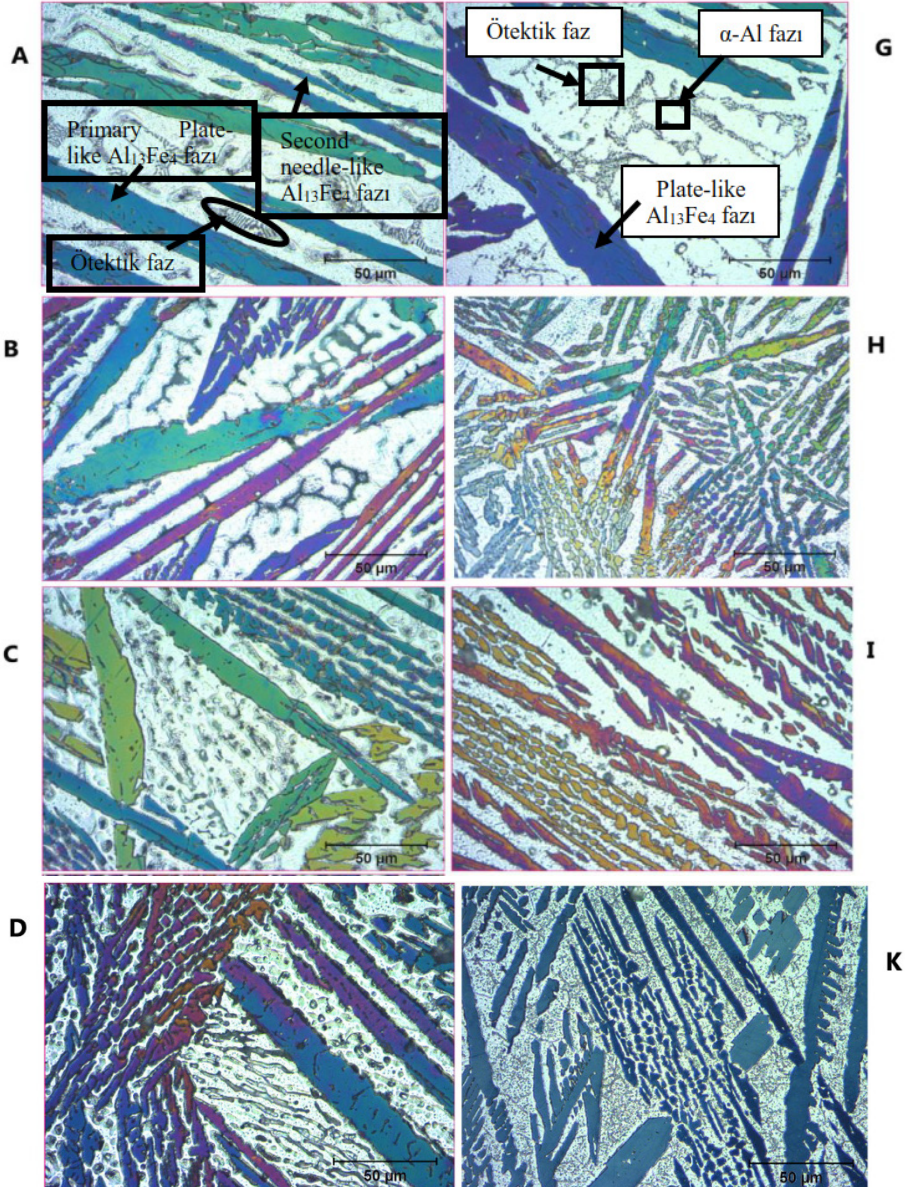
Figure 1. Optical microscope images of A, B, C, D casting samples and G, H, I, K homogenization annealed samples of Al-Fe and Al-Fe-xMg (x=1, 2, 3) alloys, respectively.
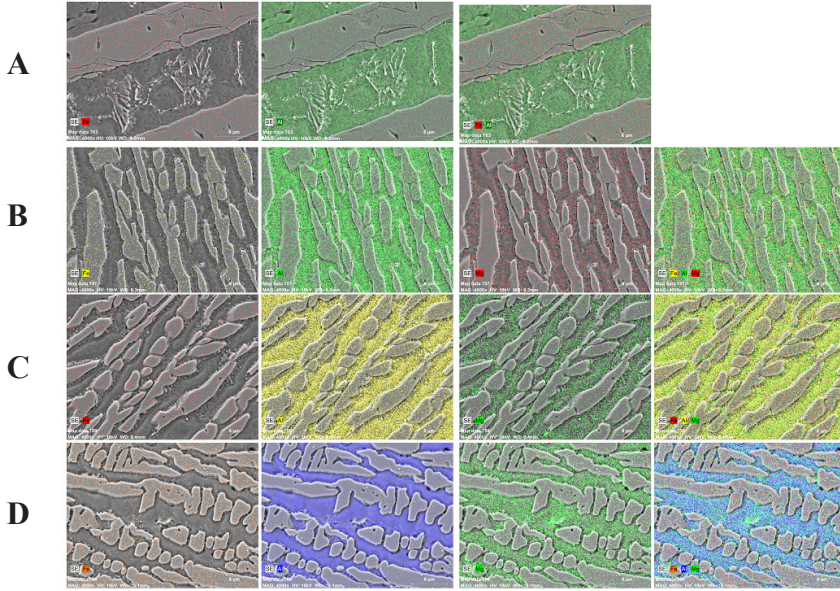
Figure 2. The elemental Al, Mg, Fe EDX mapping analyzes of casting samples of Al-Fe and Al-Fe-xMg (x=1, 2, 3) alloys, (A,B,C,D row) respectively.
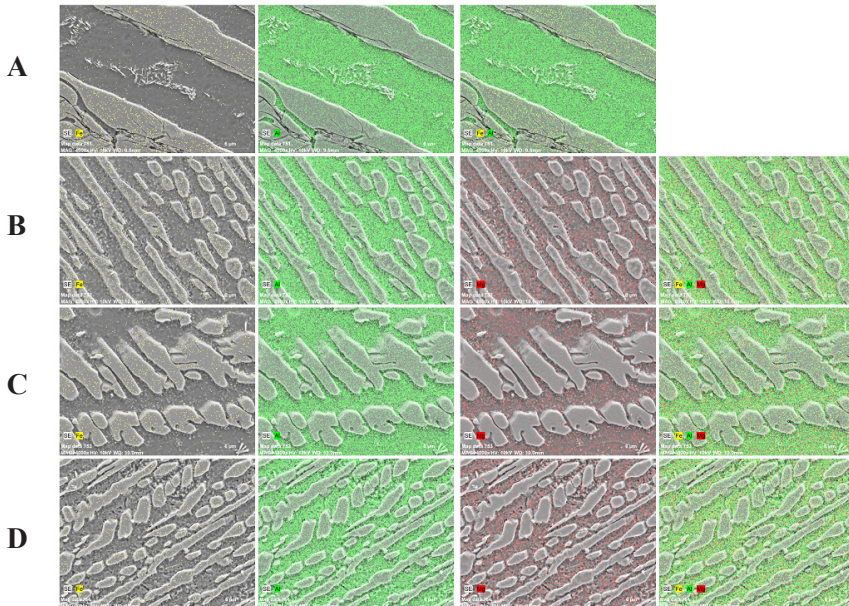
Figure 3. The elemental Al, Mg, Fe EDX mapping analyzes of samples of homogenization annealed samples at 500 °C for Al-Fe and Al-Fe-xMg (x=1, 2, 3) alloys, (A,B,C,D row) respectively.

3.2. Mechanical Properties

Compression tests were performed on a ZwickRoell 600 kN universal testing device and the compression speed was selected as 1 mm/min. In MARGEM (Karabuk University), two compression tests were applied for each composition and the compression test results are given in Table 1 and the graphs are given in Figure 4. Accordingly, the average Poisson ratio is 3.26 and the average deformations are around 7 mm.

Table 1. Compression test results of casting and homogenized annealed samples at 500 °C for Al-Fe and Al-Fe-xMg(x=1, 2, 3) alloys.

Alloys	h_0 (mm)	d_0 (mm)	S_0 (mm^2)	F_{max} (N)	σ_b (N/mm^2)	W (N.mm)
Al-Fe-Casting	8.72	7.95	49.65	64300	1295.0655	142092.22
Al-Fe-1Mg- Casting	8.25	7.90	49.02	74800	1525.9078	153228.24
Al-Fe-2Mg- Casting	8.20	7.84	48.27	93900	1945.3076	205224.19
Al-Fe-3Mg- Casting	8.60	7.97	49.89	71300	1429.1441	126279.96
Al-Fe-Homogenized	8.50	7.83	48.15	41200	855.6594	85422.17
Al-Fe-1Mg-Homogenized	8.48	8.22	53.07	85100	1603.5425	193905.98
Al-Fe-2Mg-Homogenized	8.20	7.90	49.02	113000	2305.1816	244350.23
Al-Fe-3Mg-Homogenized	8.25	8.07	51.15	52800	1032.2581	104017.52
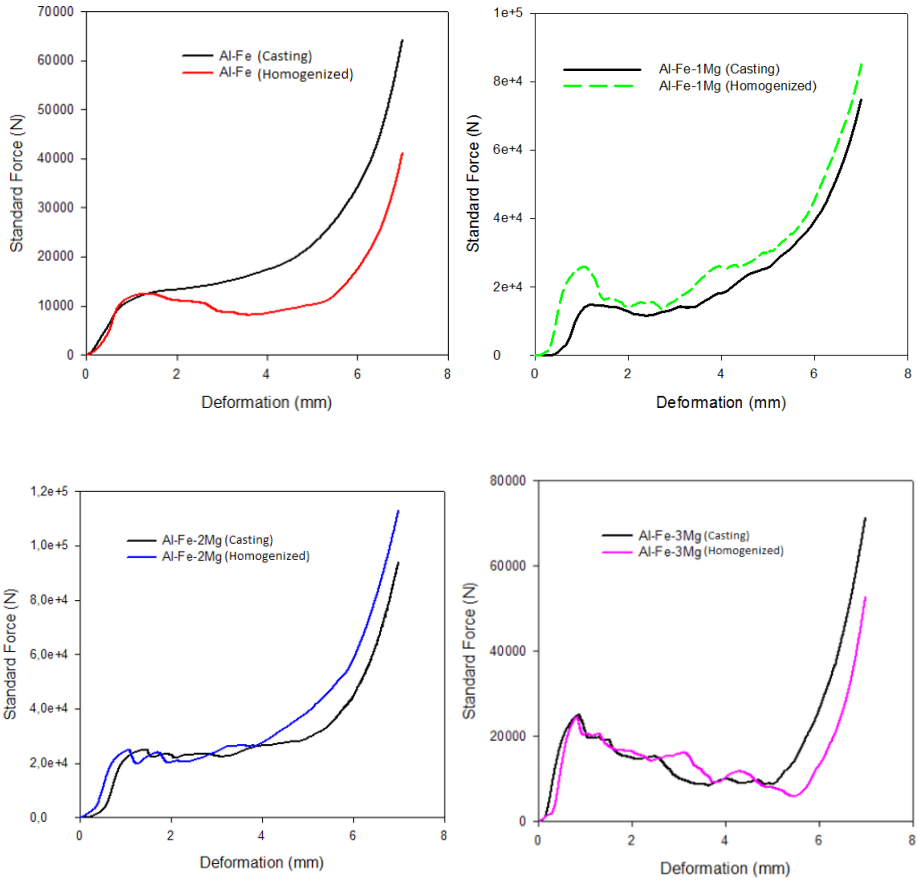
Figure 4. Compression test graphs of casting and homogenized annealed samples at 500 °C for Al-Fe and Al-Fe-xMg(x=1, 2, 3) alloys.

The maximum compressive strength values of the examined alloys tended to increase with Mg content. With the addition of Mg to the alloy, the thinning of the thick plate-shaped long $Al_{13}Fe_4$ intermetallics, the disappearance of the dendritic arms formed at the edges of the $Al_{13}Fe_4$ intermetallics with the homogenization heat treatment, the sphericalization of the plates along with their thinning, and the increase of the Al_3Mg_2-Al binary eutectics led to the improvement of the compressive strength of the Al-Fe-xMg alloy. The change curves of the maximum compressive strength of Al-Fe-xMg alloys with Mg content are given in Figure 5. FESEM images and EDX mapping analyzes of the broken surfaces resulting from compression of Al-Fe and Al-Fe-xMg

(x=1, 2, 3) alloys as casting and homogenized annealed at 500 °C are given in Figures 6 and 7, respectively.
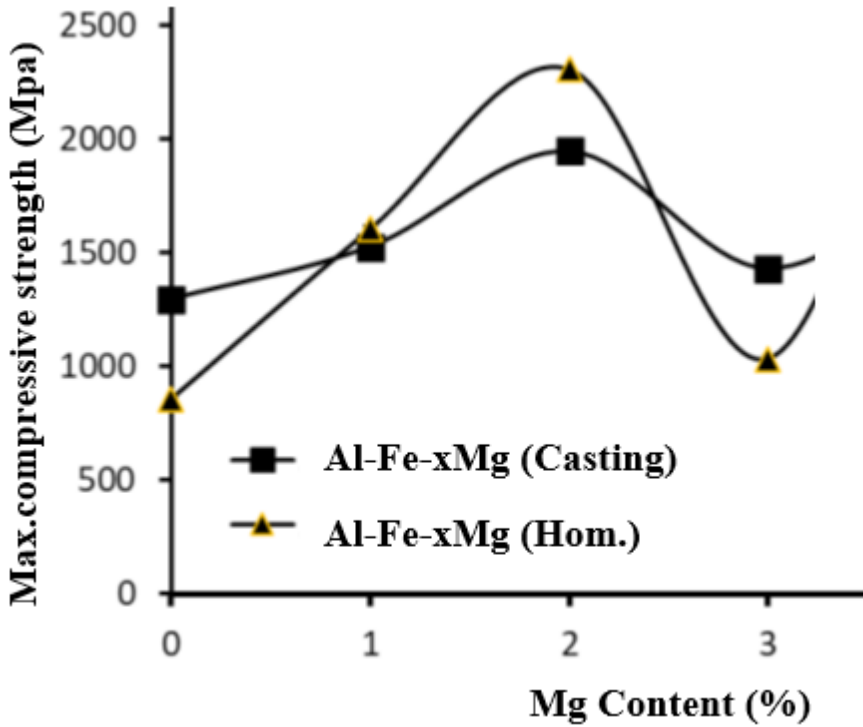
Figure 5. Change curves with Mg content of maximum compressive strength of the examined Al-Fe-xMg alloys.
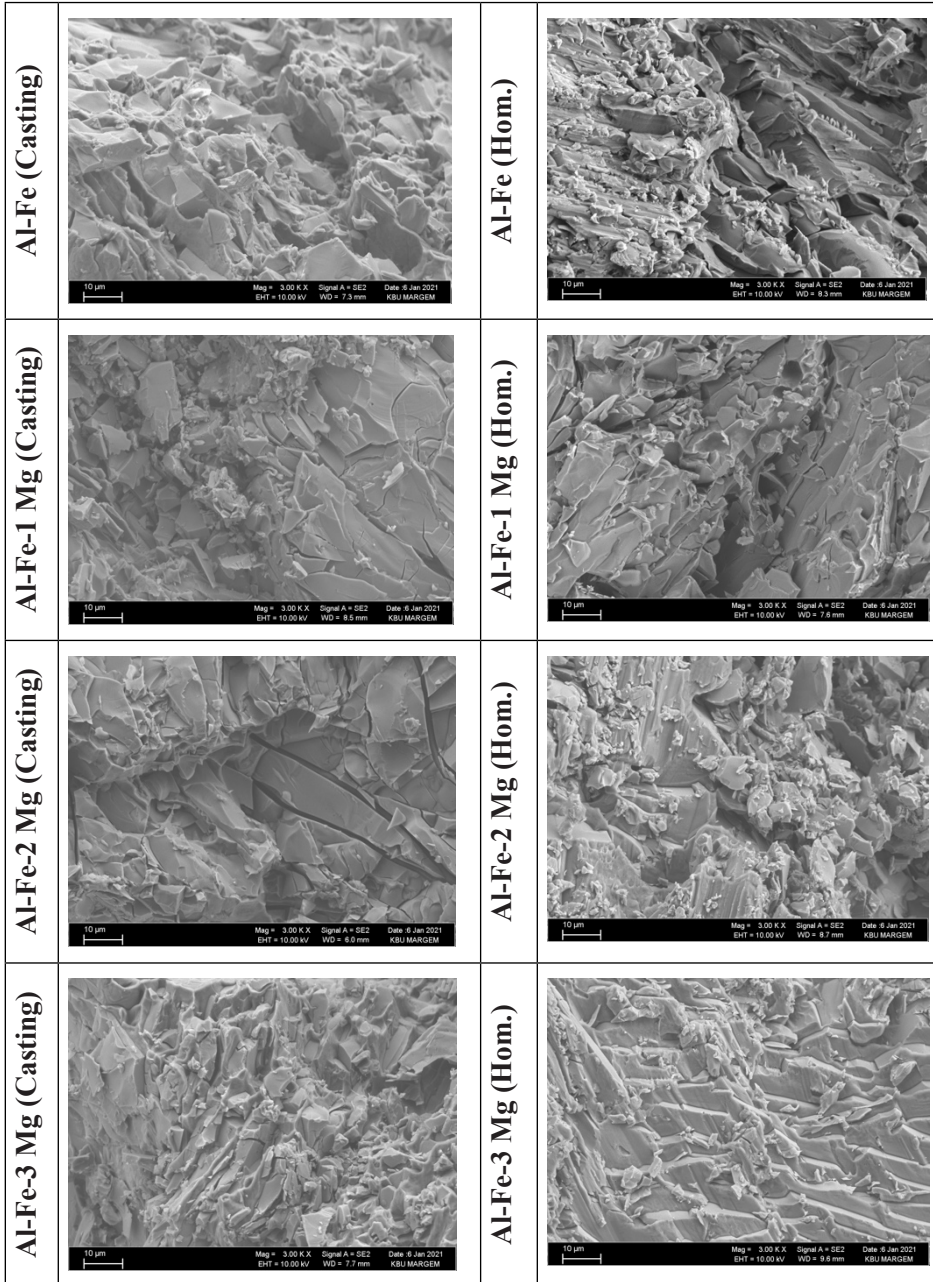
Figure 6. FESEM images of the broken surfaces for Al-Fe and Al-Fe-xMg(x=1, 2, 3) alloys as casting and homogenized annealed at 500 °C.
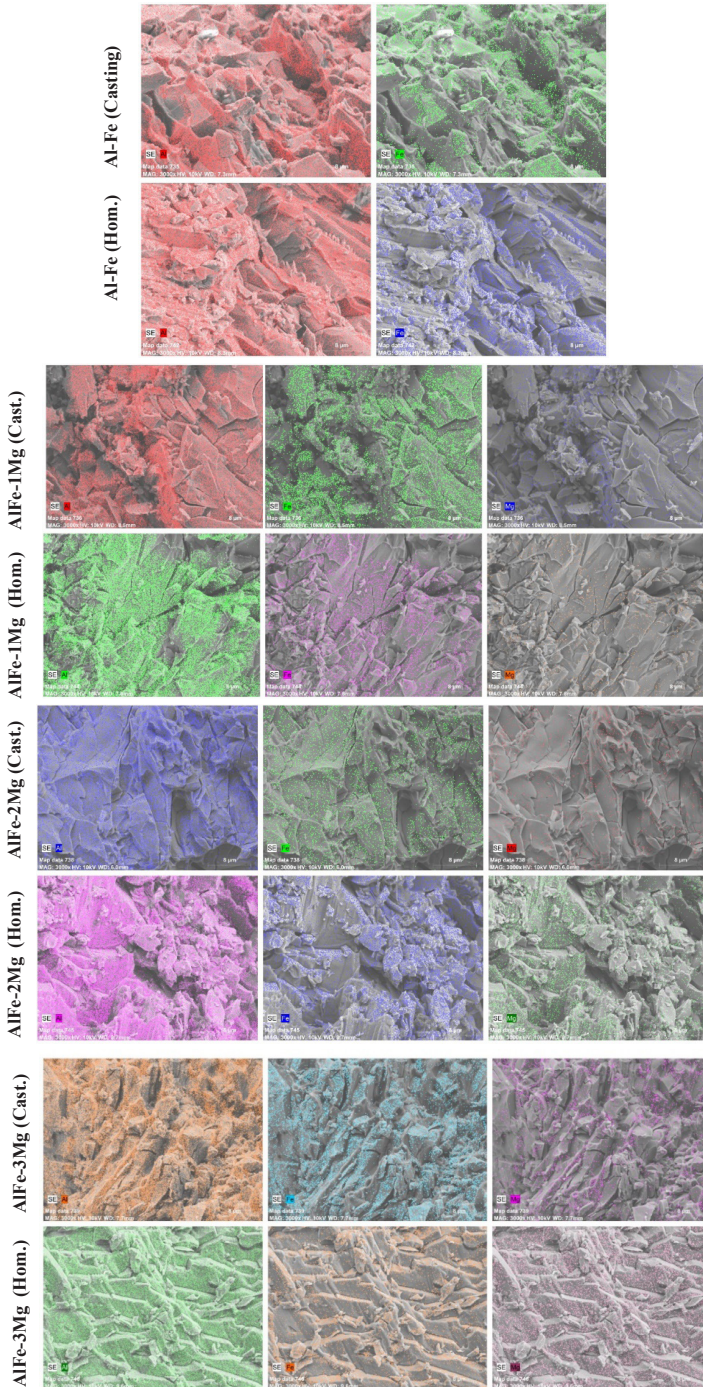
Figure 7. EDX mapping analyzes of the broken surfaces for Al-Fe and Al-Fe-xMg(x=1, 2, 3) alloys as casting and homogenized annealed at 500 °C.

Since the thick plate-shaped Fe-containing $Al_{13}Mg_4$ intermetallics in the microstructure of the Mg-free Al-Fe alloy cause flat-surface brittle fracture (Figure 5), the strength of this alloy is low. Figure 6 shows that with the addition of Mg to the alloy, the fracture surface becomes rougher than the smooth appearance, and Figure 7 shows that the EDX map regions containing Al and Mg increase.

3.3. Brinell Hardness Results

Brinell Hardness values of the Al-Fe-xMg alloys examined under 2.5 mm ball and 187.5 kg load are plotted in Figure 8, depending on the Mg composition. As the Mg content of the alloy increased, the hardness value increased, exhibiting two regions. While the hardness value increased rapidly in the initial region up to 1% Mg content, the change in hardness in the second region occurred at a steady-state rate. The change in the hardness of the Al-Fe alloy with the addition of Mg can be attributed to the formation of the $Al-Al_3Mg_2$ binary eutectic. This situation can be better understood from the Al, Fe and Mg EDX composition maps taken on the broken surfaces after the compression test. As the Mg content of the alloy increases, the Al and Mg EDX composition map density regions expand.
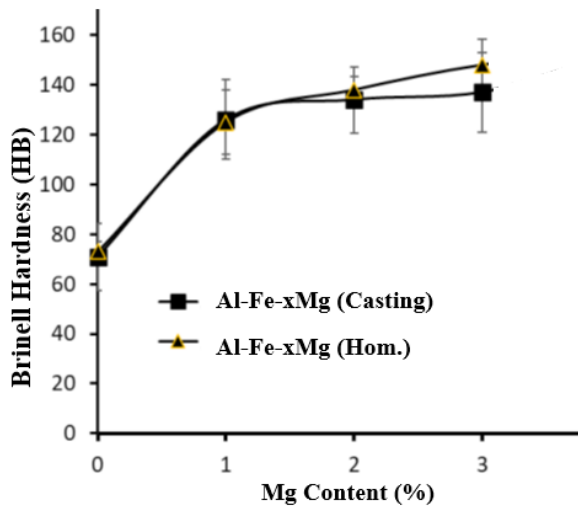
Figure 8. Change curves of Brinel hardness of the examined Al-Fe-xMg alloys with Mg content.

4. Conclusion

In this study, mechanical and microstucture properties were examined for the Al-21.1 wt% Fe and Mg-doped Al-Fe-xMg (x=1,2,3 wt.%) alloys as casting

and homogenized annealed at 500 °C. With this annealing, the structure of the eutectic lamellae in the white α-Al phase increased and became thinner. Also, intermetallic θ-$Al_{13}Fe_4$ phase with the long and thick body structure is separated by α-Al phases. When the Al-Fe-xMg (x=1, 2, 3 %wt.) casting samples are examined, as the amount of Mg added to the structure increases and the amount of Fe decreases, the eutectic (θ-$Al_{13}Fe_4$ +α-Al) phase within the α-Al white phase decreases, and the sizes of primary plate-like coarse-structured Fe-rich intermetallic phases also decrease. As the amount of Mg increases and the amount of Fe decreases and with homogenization annealing, while the intermetallic structure with long-thick body begins to thin and turns into a small needle-like structure, medium-sized spherical structures and dendrite arms will continue to grow further. The hardness and maximum compressive strength of the examined Al-Fe-xMg alloys increased significantly with the increase in Mg content. This is due to the formation of the Al-Mg_3Al_2 binary eutectic phase in the structure with the addition of Mg to the alloy and the thinning of the plate-shaped $Al_{13}Fe_4$ lamellaes. Applying homogenization heat treatment to the alloy causes to disappear of the dendritic structure, to become thinner of the plate-shaped lamellaes and to become spherical at the same time, and its mechanical properties are slightly improved.

5. Acknowledge

REFERENCES

Aoki, T., Kobayashi, E., Sone, M., & Sato, T. (2014, July). Microstructure and Mechanical Properties of D-SSF Processed Al-Zn-Mg Alloys with High Fe Content. In Materials Science Forum (Vol. 794, pp. 1109-1114). Trans Tech Publications Ltd.

Barrirero, J., Pauly, C., Engstler, M., Ghanbaja, J., Ghafoor, N., Li, J., ... & Mücklich, F. (2019). Eutectic modification by ternary compound cluster formation in Al-Si alloys. Scientific reports, 9(1), 5506.

Bjurenstedt, A., Ghassemali, E., Seifeddine, S., & Dahle, A. K. (2019). The effect of Fe-rich intermetallics on crack initiation in cast aluminium: An in-situ tensile study. Materials Science and Engineering: A, 756, 502-507.

Cao, X., & Campbell, J. (2006). Morphology of β-Al5FeSi phase in Al-Si cast alloys. Materials Transactions, 47(5), 1303-1312.

Dinnis, C. M., Taylor, J. A., & Dahle, A. K. (2005). As-cast morphology of iron-intermetallics in Al–Si foundry alloys. Scripta materialia, 53(8), 955-958.

Feng, J., Ye, B., Zuo, L., Qi, R., Wang, Q., Jiang, H., ... & Wang, C. (2018). Effects of Zr, Ti and Sc additions on the microstructure and mechanical properties of Al-0.4Cu-0.14Si-0.05Mg-0.2Fe alloys. Journal of Materials Science & Technology, 34(12), 2316-2324.

Gao, G. Z., He, Y. W., & Chen, J. Z. (1992). Chin: Effect of rare earth on conductivity of the aluminum wire. Chin. J. of Nonferrous Met., 2(1), 78.

Gustafsson, G., Thorvaldsson, T., & Dunlop, G. L. (1986). The influence of Fe and Cr on the microstructure of cast Al-Si-Mg alloys. Metallurgical Transactions A, 17, 45-52.

Ji, S., Yang, W., Gao, F., Watson, D., & Fan, Z. (2013). Effect of iron on the microstructure and mechanical property of Al–Mg–Si–Mn and Al–Mg–Si diecast alloys. Materials Science and Engineering: A, 564, 130-139.

Jiang, H., Li, S., Zheng, Q., Zhang, L., He, J., Song, Y., ... & Zhao, J. (2020). Effect of minor lanthanum on the microstructures, tensile and electrical properties of Al-Fe alloys. Materials & Design, 195, 108991.

Jiang, W., Fan, Z., Dai, Y., & Li, C. (2014). Effects of rare earth elements addition on microstructures, tensile properties and fractography of A357 alloy. Materials Science and Engineering: A, 597, 237-244.

Jinta, M., Sakai, Y., Oyagi, M., Yoshizawa, S., Matsui, K., & Noda, K. (2000). Press forming analysis of aluminum auto body panel: wrinkle behavior in 5000 and 6000 series aluminum alloy sheet forming. JSAE review, 21(3), 407-409.

Karabay, S. (2006). Modification of AA-6201 alloy for manufacturing of high conductivity and extra high conductivity wires with property of high tensile stress after artificial aging heat treatment for all-aluminium alloy conductors. Materials & design, 27(10), 821-832.

Kim, D., Kim, J., & Kobayashi, E. (2019). Microstructure characterization of rolled Al-Si-Mg-Fe alloy by three-dimensional tomography. Materials Science and Engineering: A, 768, 138449.

Kim, J. K., Shin, D. H., & Kim, W. J. (1998). High-strain-rate superplastic behavior of ingot-processed Al-Mg-Fe alloy. Scripta materialia, 38(6), 991-998.

Kobayashi, T. (2000). Strength and fracture of aluminum alloys. Materials Science and Engineering: A, 280(1), 8-16.

Kumari, S. S., Pillai, R. M., Rajan, T. P. D., & Pai, B. C. (2007). Effects of individual and combined additions of Be, Mn, Ca and Sr on the solidification behaviour, structure and mechanical properties of Al7Si–0.3Mg–0.8Fe alloy. Materials science and engineering: A, 460, 561-573.

Li, J. H., Wang, X. D., Ludwig, T. H., Tsunekawa, Y., Arnberg, L., Jiang, J. Z., & Schumacher, P. (2015). Modification of eutectic Si in Al–Si alloys with Eu addition. Acta Materialia, 84, 153-163.

Li, Z., Jiang, H., Wang, Y., Zhang, D., Yan, D., & Rong, L. (2018). Effect of minor Sc addition on microstructure and stress corrosion cracking behavior of medium strength Al–Zn–Mg alloy. Journal of Journal of Materials Science & Technology, 34(7), 1172-1179.

Liu, C., Jiao, X., Nishat, H., Akhtar, S., Wiesner, S., Guo, Z., & Xiong, S. (2021). Characteristics of Fe-rich intermetallics compounds and their influence on the cracking behavior of a newly developed high-pressure die cast Al–4Mg–2Fe alloy. Journal of Alloys and Compounds, 854, 157121.

Osawa, Y., Takamori, S., Kimura, T., Minagawa, K., & Kakisawa, H. (2007). Morphology of intermetallic compounds in Al-Si-Fe alloy and its control by ultrasonic vibration. Materials Transactions, 48(9), 2467-2475.

Pandee, P., Gourlay, C. M., Belyakov, S. A., Patakham, U., Zeng, G., & Limmaneevichitr, C. (2018). AlSi$_2$Sc$_2$ intermetallic formation in Al7Si-0.3Mg-xSc alloys and their effects on as-cast properties. Journal of Alloys and Compounds, 731, 1159-1170.

Phongphisutthinan, C., Tezuka, H., Sato, T., Takamori, S., & Ohsawa, Y. (2012). Caliber rolling process and mechanical properties of high Fe-containing Al–Mg–Si alloys. Materials Transactions, 53(5), 885-892.

Puncreobutr, C., Lee, P. D., Kareh, K. M., Connolley, T., Fife, J. L., & Phillion, A. B. (2014). Influence of Fe-rich intermetallics on solidification defects in Al–Si–Cu alloys. Acta Materialia, 68, 42-51.

Qiu, H., Yan, H., & Hu, Z. (2013). Effect of samarium (Sm) addition on the microstructures and mechanical properties of Al–7Si–0.7Mg alloys. Journal of Alloys and Compounds, 567, 77-81.

Que, Z., Zhou, Y., Wang, Y., Mendis, C. L., & Fan, Z. (2021). Effects of Mg addition on the Al6 (Fe, Mn) intermetallic compounds and the grain refinement of α-Al in Al-Fe-Mn alloys. Materials Characterization, 171, 110758.

Sato, T., & Tezuka, H. (2006). A new deformation-semi-solid casting process of highly concentrated Fe containing Al-Si-Cu-Fe cast alloys. Solid State Phenomena, 116, 247-250.

Sun, F., Nash, G. L., Li, Q., Liu, E., He, C., Shi, C., & Zhao, N. (2017). Effect of Sc and Zr additions on microstructures and corrosion behavior of

Al-Cu-Mg-Sc-Zr alloys. Journal of Materials Science & Technology, 33(9), 1015-1022.

Taghaddos, E., Hejazi, M. M., Taghiabadi, R., & Shabestari, S. G. (2009). Effect of iron-intermetallics on the fluidity of 413 aluminum alloy. Journal of Alloys and Compounds, 468(1-2), 539-545.

Toros, S., Ozturk, F., & Kacar, I. (2008). Review of warm forming of aluminum–magnesium alloys. Journal of materials processing technology, 207(1-3), 1-12.

Umezawa, O., Nakamoto, M., Osawa, Y., Suzuki, K., & Kumai, S. (2005). Microstructural Refinement of Hyper-Eutectic Al–Si–Fe–Mn Cast Alloys to Produce a Recyclable Wrought Material. Materials transactions, 46(12), 2609-2615.

Wang, Q. G., Caceres, C. H., & Griffiths, J. R. (2003). Damage by eutectic particle cracking in aluminum casting alloys A356/357. Metallurgical and Materials Transactions A, 34, 2901-2912.

Wang, W., Takata, N., Suzuki, A., Kobashi, M., & Kato, M. (2020). Formation of multiple intermetallic phases in a hypereutectic Al–Fe binary alloy additively manufactured by laser powder bed fusion. Intermetallics, 125, 106892.

Yuan, W., Liang, Z., Zhang, C., & Wei, L. (2012). Effects of La addition on the mechanical properties and thermal-resistant properties of Al–Mg–Si–Zr alloys based on AA 6201. Materials & Design, 34, 788-792.

Zhang, Z., Tezuka, H., Kobayashi, E., & Sato, T. (2013). Effects of the Mn/Fe ratio and cooling rate on the modification of Fe intermetallic compounds in cast A356 based alloy with different Fe contents. Materials Transactions, 54(8), 1484-1490.

Zhao, N. Q., Yao, J. X., & Yang, X. J. (1995). Effect of rare earth on microstructure and properties of 6063 aluminum alloy. J. Tianjin Univ, 28(3), 375.

Zheng, Q., Zhang, L., Jiang, H., Zhao, J., & He, J. (2020). Effect mechanisms of micro-alloying element La on microstructure and mechanical properties of hypoeutectic Al-Si alloys. Journal of Materials Science & Technology, 47, 142-151.

Zhu, X., Blake, P., Dou, K., & Ji, S. (2018). Strengthening die-cast Al-Mg and Al-Mg-Mn alloys with Fe as a beneficial element. Materials Science and Engineering: A, 732, 240-250.

USE OF ASPHALT LAYER INSTEAD OF GRANULAR SUB-BALLAST LAYER IN RAILWAY TRACK

Cahit GÜRER[1]

[1](Prof. Dr.), Afyon Kocatepe University
Engineering Faculty, Department of Civil Engineering,
03200, Afyonkarahisar, Turkiye
E-mail: cgurer@aku.edu.tr
ORCID: 0000-0003-1413-2357

1. Introduction

Asphalt mixture subballast layer is widely used in many countries. It is used on high-speed and traditional railway lines of countries such as the USA, Italy, Japan, Austria, France and Spain. In sub-ballast layers, the asphalt layer is generally applied with a thickness of 12–15 cm and consists of a dense graded asphalt mixture with a maximum aggregate size of 22–25 mm (Rose and Bryson 2009). The asphalt mixture is generally designed to have the same properties as that used on highways, but for subballast application the bitumen content is increased by 0.5% compared to the optimum value used for highways. Additionally, the void percentage is reduced to 1-3% to be used as an impermeable layer that can prevent rutting deformation problems as pressure is applied over a large area throughout the ballast (Rose et al. 2011).

In general, factors such as geographical structure, economic conditions, usage and maintenance life have created a need for alternative load carrying layers in developed countries where railway transportation is frequently preferred. Research on this subject supports the idea that asphalt mixtures can be used as load carrying layers (Yang 2015, Gürer et al. 2021). For example; In Germany, various researches have been carried out to solve problems such as breakage and wear caused by high speed during travel on high-speed railway lines and, and the use of asphalt layer in rail tracks has become widespread

in the country In Italy, asphalt mixture layers have been used in the railway track of more than 2250 km of high-speed train lines, especially to increase travel comfort. In Japan, which is at the forefront in high-speed railway line technology, the use of asphalt mixture is preferred to create a strong foundation to reduce both the irregularities on the line and the effect of the loads transmitted to the lower layers, while in countries such as the USA, France and Spain due to improve the existing line and to reduce the layer thickness in the rail line, the use of asphalt mixture materials is increasing day by day.

2. Use of Asphalt Layer in Railway Tracks

Objects that conduct electricity and heat are called conductive materials. The railway track technique, consisting of two parallel rails placed on wooden parallel sleepers on natural ground, was first developed in the 1830s. After a while, it became clear that the quality of the support materials under the sleepers needed to be improved. It was deemed necessary to place natural stone aggregate (known as ballast) around and under the sleepers to limit excessive horizontal and vertical movements and displacements, providing an improved railway track. Thus, completely granular material supported railway track was defined and later became the term ballasted railway track (Rose and Souleyrette 2015).

As wheel loads, train frequencies and speeds increased, emphasis has been placed on determining larger rail sizes, selecting larger size sleepers with closer spacing, and ensuring that the ballast around and under the sleepers is of a certain quality and thickness. The ultimate goal is to reduce the applied loads to the bearing capacity of the natural subgrade material, thus providing equally strong support. It was recognized that drainage is very important because most subgrade materials tend to lose significant bearing capacity when wet or saturated. Therefore, removing surface water from the railway track and draining the water from the railway track as quickly as possible were the most important issues.

Further improvement of the support structure is the addition of a "subballast" layer consisting of granular material of a certain grain diameter between the ballast and the subgrade layers. Typically, this is a locally available aggregate material containing significantly finer sized particles with smaller size than conventional ballast material. It is a very compact, low permeability material with a very low void content and is similar to the aggregate base material commonly used in highway construction. Their main function is to provide support to the ballast, further distribute the loads and provide a certain level of waterproofing for the

subgrade underneath. This improves the quality and load-carrying capacity of the railway track. This railway track design is known as "All Granular" as no additional cementing or binding material is incorporated into the various support materials and layers. Figure 1 shows the classic or traditional "Fully Granular" railway track. In railway tracks on high-speed lines, the quality of the materials and the relative dimensions of the materials and layers are specifically selected and determined. It is assumed that surface drainage is provided to minimize the possibility of water leaking into the railway track, thus minimizing weakening of the subballast or subgrade. High-traffic mainline railway track requires higher quality and thicker ballast and sub-ballast layers to resist loads and effectively distribute loads to the underlying subgrade layer. Variations of this design have been common on most railway tracks and the most distinctive design of railway tracks worldwide. Over the past 30 years, additional designs incorporating asphalt layers have attracted the attention of design engineers for special applications, instead of the classical granular design.
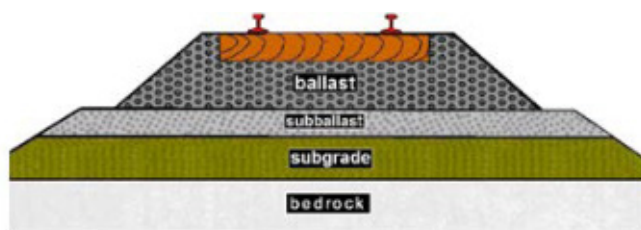
Figure 1. Typical railway track that consist from granular
ballast layers (Rose et al. 2011)

Since the early 1980s, the US railway industry has selectively used hot mix asphalt as a support layer in railway track. Such practices are increasing in other countries as well. An asphalt layer, similar to that generally used for road construction, distinguishes railway track from all conventional granular railway tracks. This development responds to the challenges of providing higher quality and more durable railway track and support structures to accommodate the unprecedented growth in rail traffic volumes, ton-mile capacities, axle loadings and tonnages being experienced worldwide. Priority is given to the development and evaluation of asphalt pavement technology for heavy-tonnage railroads in the United States and high-speed passenger rail lines in other countries.

Three basic types of asphalt layers are used. Two of them combine the traditional ballast layer as part of the support. The "Asphalt Pavement" pavement

layer is similar to the classic granular pavement layer; The only difference is that the asphalt layer is used for the granular sub-ballast layer. A typical cross-section is shown in Figure 2 "Asphalt Combination" pavement includes both the asphalt layer and the granular subballast layer. The asphalt layer thickness can be reduced somewhat as a relatively thick sub-ballast layer lies below.
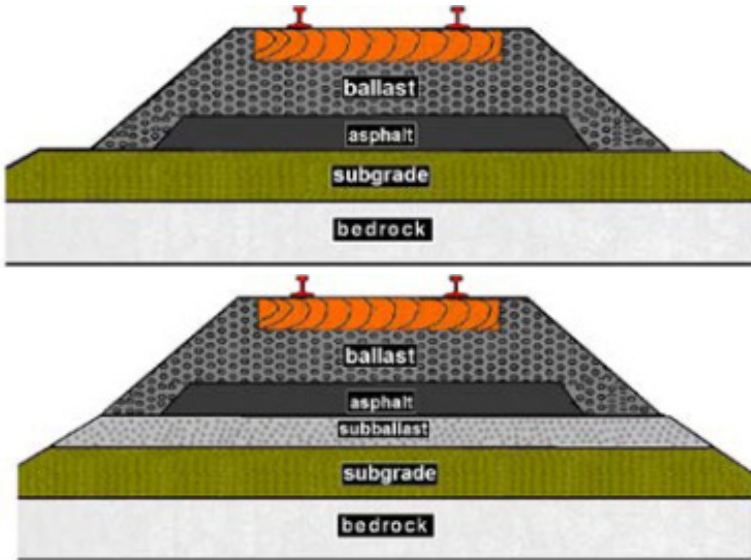
Figure 2. Railway track using a asphalt layer combination in the subballast layer (Rose et al. 2011)

The "Ballastless Asphalt Combination" railway track bed consists of sleepers or slab track placed on a relatively thick asphalt layer and granular subballast in the lower layer. These thickened sections compensate for the absence of a ballast layer. The exact design and configuration of the sleepers, mono block or twin-block, the form of slab used, the sleepers and the asphalt surface profile vary significantly as a function of the preferred properties. According to Esveld (2001), softening of the subgrade can cause major problems, especially with vibration. For this reason, in high-speed lines in Japan and Italy, a 5 to 8 cm thick waterproof asphalt layer is used on the subgrade. In order to distribute and thus reduce the stresses on the subgrade, the asphalt concrete layer can be increased up to 15-20 cm (Figure 3) (Int. Reference 5). With this type of asphalt layer applications, period heavy maintenance of the railway track is expanded.
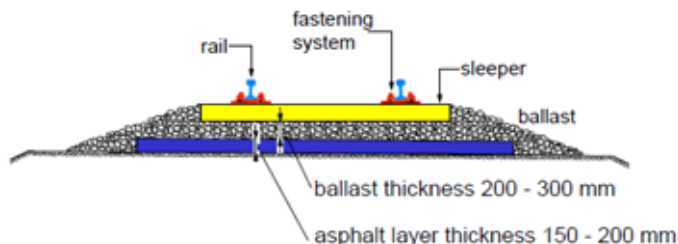
Figure 3. Railway track reinforced with asphalt layer (Esveld 1997)

Asphalt layers can offer great advantages in the construction of new railway track designed for relatively high axle loads and high gross tonnages. In addition, the use of reinforcement layers in conventional railway tracks designed for passenger services ensures the preservation of track geometry and reduces maintenance.

Italian High Speed Railway is a multi-layer system consisting of an embankment, super compacted substrate, asphalt subballast, ballast, fasteners, sleepers and rail. Its cross-sectional profile is shown in Figure4.
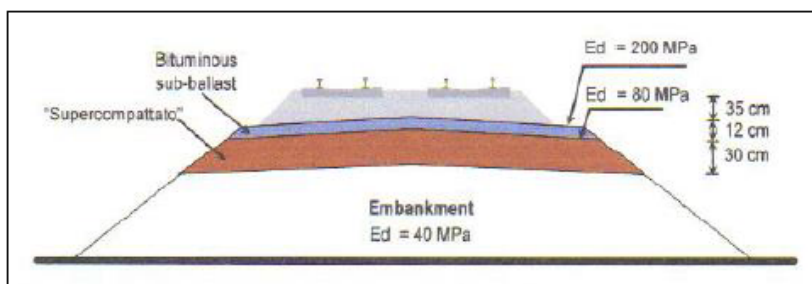
Figure 4. Cross-section profile of Italian high-speed rail track
(Rose et al. 2015)

Construction practices place a heavy emphasis on the placement of these layers to maintain proper geometric alignment in high-speed track operations. The lower portion of the embankment must provide a minimum bearing capacity of 40 MPa (5,800 psi) and is constructed of a water-free material not exceeding 50 cm (20 in) in thickness. The material is compacted using static and vibratory compaction methods. To ensure proper compaction, Italian quality control mandates that 2,000 m2 (2,390 yd2) of the embankment must be tested. A 30 cm (12 in) super compacted layer with a minimum subgrade modulus of 80 MPa (11,600 psi) is placed on the backfill. The super compacted layer consists of a sand /

gravel mixture and is constructed with a slope of 3.5%. This layer has the ability to withstand the repeated loads of high-speed trains and acts as an impermeable layer to help divert surface water. The asphalt subballast layer is placed on top of the super compacted layer. It consists of a asphalt mixture with a maximum aggregate size of 25 mm (1 inch). This layer has a thickness of 12 cm (5 in) and is applied to the entire pavement cross-section for a total of 14 m (46 ft). The asphalt subballast layer must provide a minimum modulus of elasticity of 200 MPa (29,000 psi) to withstand repeated wheel loads and reduce stress to the backfill. Asphalt has multiple advantages according to traditional granular subballast. These;

- decreased vibration and noise levels,
- decreased sectional thickness,
- decreased lifecycle costs in infrastructure due to decreased subgrade fatigue,
- homogenization of railway track carrying capacity and better ballast retention,
- less ballast fouling due to improved drainage and
- increased structural reliability and safety due to increased modulus and homogeneity.

Standard asphalt paving machines are used to construct asphalt subballast (Figure 5). It is then compacted to 98% of its maximum density using vibrating rollers. Asphalt mixtures comply with all Marshall design standards. Verification tests are performed every 10,000 m3 (13,000 y3) to ensure mixtures comply with specifications. Falling weight deflectometer test is used to verify the dynamic response with three tests per 100 m (330 ft) of railway line section. For the last 20 years, all Italian railways were built using this method. Following the completion of the North-South and East-West high-speed passenger lines, the Italian High-Speed rail network consists of more than 1,200 km (745 mi) of asphalt sub-ballast railway track.

Figure 5. Paving of asphalt pavement layer on Italian high-speed railway line (Rose et al. 2015)

The French National Railway Administration (SNCF) was carried out studies on the use of asphalt in railway track construction. Asphalt is considered an attractive building material because it can reduce the thickness of sub ballast layers, allowing easy placement of railway track and railway equipment and optimizing maintenance costs. In 2000, a feasibility study was conducted by SNCF & Colas to measure the impact of using asphalt on a high-speed line. A section with 3 km length of the European High Speed line between Paris and Strasbourg was chosen as the test area. This railway section consists of various railway track features, including cuts and bridges, which in many cases provide detailed visualization of asphalt performance. A conventional granular railway track cross-section consists of a 35 cm (14 in) thick ballast on a 20 cm (8 in) thick gravel subballast. Both are on a 50 cm (20 in) thick layer of capping. For the works, SNCF used a 35 cm (14 in) thick ballast layer over a 15 cm (6 in) layer of asphalt mixture, all resting on a 35 cm (14 in) thick capping layer. This decreases the total section thickness by 20 cm (8 in), which significantly reduces the amount of material required to create railway track. The asphalt test section was built in 2004 using machines designed for road construction (Figure 6). To collect continuous data, thermometers were placed in the test area, accelerometers and pressure sensors were placed on the sleepers, and expansion gauges were placed at the base of the asphalt layer. Figure 6 shows the instrument placement in the test area.

Figure 6. Laying of the asphalt layer of the SNCF test section and instrument layout plan in the test area (Wikizero 2019)

According to the comparative results of the study on the use of asphalt layer instead of traditional granular railway track as in Figure 6;

- average section thickness can be decrease by 36 cm (Figure 7),
- the amount of filling material can be decreased by 5,000 m3 / km,
- the pressures under the asphalt layer in the railway track reach half of the pressure measured under the granular layer in conventional railway track,

- deformations of the railway track with asphalt subballast reach only one third of the maximum permissible deflections.
- No significant difference was observed in the accelerations of the sleepers in both conventional and asphalt layered railway track,
- changes in railway track stiffness are 40% lower,
- railway track degradation rate is lower depending on surface determination requirements and
- asphalt railway track requires less maintenance; several more layers can be planned due to the superior performance of the asphalt railway track.
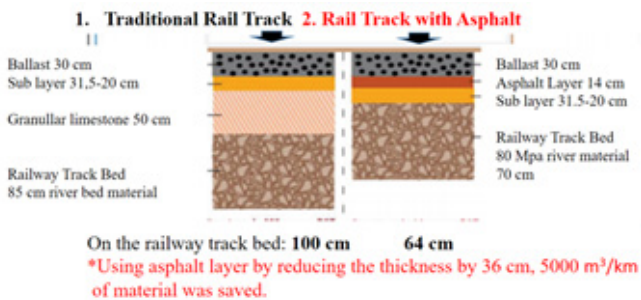
Figure 7. Comparison of the use of granular and asphalt subballast layer in France (Rose et al. 2015)

- The research results showed that the asphalt reinforced subgrade surface achieved the purpose of reducing the fluctuation of water content in the subgrade, improving the load distribution, and reinforcing the ballast layer (Yang 2015).

Yang et al. (2015) investigated the using asphalt concrete for high-speed railway ınfrastructure. To apply the railway asphalt concrete (RAC) effectively to high-speed railway infrastructures, modified highway asphalt pavement material tests are conducted to verify mixture parameters. To verify the performance and analyze the mechanistic response of RAC infrastructure, full-scale laboratory dynamic models are established under different environmental temperatures and loading levels. Based on model testing, the reinforced RAC foundation with a 12 cm deep graded gravel layer replaced by RAC-25 shows much better performance compared with the traditional design. In railway track with asphalt concrete, the surface deformation was reduced by 52%. According to the researcher RAC material also can be used to reduce the vibration of a high-speed railway structure.

Gürer et al. (2021) investigated the differences by performing finite element modeling for the railway track consisting of asphalt and granular layer. It was determined that the maximum displacement was 2.68 mm when asphalt material was used in the subballast layer, and 3.06 mm when granular material was used (Figure 8).
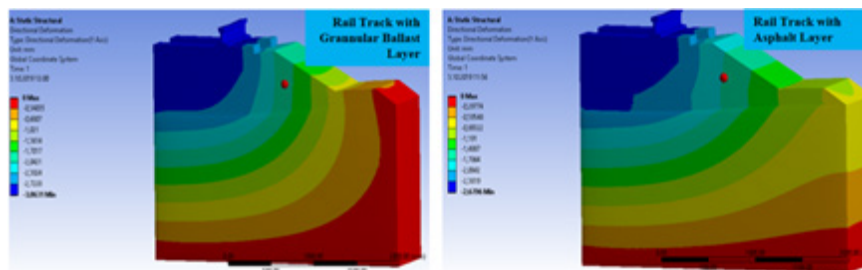
Figure 8. Variation of vertical displacements of granular material and asphalt materials used in the 150 mm subballast layer (Gürer et al. 2021)

Sowmiya et al. (2010) reported a deformation value of 1.68 mm in the subgrade as a result of SEM analysis. Sol-Sánchez et al. (2015) investigated the use of asphalt subballast in railway infrastructure and similarly obtained lower displacement values in the asphalt subballast layer.

4. Asphalt Mixture Properties to be Used in Railway Track's Subballast Layer

Asphalt layered sub-ballast consists from dense grade bituminous mixture with a maximum aggregate size of 22-25 mm, similar to the base layer in highway pavements. The amount of bitumen in the sub-ballast is normally increased by 0.5% compared to the base layer and air voids % are reduced to 1-3% to preventing permeability of the layer. This results in a mixture characterized by moderate permanent deformation resistance. Unlike highway pavements, rut deformation does not represent a significant type of deterioration in the railway bed because the presence of ballast layer allows axle loads to apply pressure over a larger area. Similarly, bleeding and bitumen rising do not any problems because the wheels do not come into direct contact with the asphalt sub-ballast layer and excessive temperatures in the depth of the railway track bed are minimized. Although the sub-ballast layer composition is similar to the asphalt base layer mixture used in road pavements, its configuration is different in terms of system requirements and temperature profile. Therefore, different

mixture design systems and approaches should be adopted to optimize asphalt mixtures when used in railway sub-ballast layers (Fernando and Gaetano 2017). Recommended hot mix asphalt (HMA) specifications, railway layer designs and applications have evolved over the years. The HMA mixture with the best properties for railway track is a mixture with a design void of 1 to 3%. The mixture is easily compacted in place with less than 5 % air void. A local densely graded highway base course mix with a minimum aggregate size of 25 to 37 mm is generally used. Long-term monitoring and test results of railway pavements consist from asphalt sub-ballast layer have shown that, due to these low voids, the mixture is impermeable and is minimally affected by the effects of air and water. The mixture provides a layer with reasonably constant stiffness in hot weather, but is somewhat flexible in cold weather. In addition, the mixture's tendency to rut deformation, bleeding in hot weather and cracking in cold weather conditions is significantly reduced, thus providing a long fatigue life for the mixture. Tests conducted on subgrade / roadbed samples obtained directly under the HMA layer have shown that the in situ moisture content is very close to optimum values at the maximum density of the materials (Asphalt 2019).

5. Conclusions

The following conclusions can be drawn from this research study:

- In railway track construction, it is known that the use of asphalt material instead of granular material in the subballast layer reduces the stresses on the subgrade. Yang et al. (2015) reported that surface deformations occurring after 100,000 loadings on asphalt railway tracks were 52% less.

- Since the subballast layer will be covered with other layers, changes in elastic modulus during seasonal transitions are very limited. Therefore, it is thought that changes in asphalt carrying capacity will be limited during the summer period (Gürer et al. 2021).

- The use of asphalt layer instead of subballast will prevent water leakage into the subgrade and will contribute significantly to the reduction of deformations and safety of movement on high-speed lines.

- Considering that rocks such as basalt and granite are used especially for granular ballast and subballast layers and that the reserves of volcanic rock are very limited all over the world, the use of asphalt in layers such as subballast layer will both ensure the stability of the railway line and eliminate the high transportation costs of this type of rocks.

• It is known that the construction cost of granular ballast is lower than asphalt. However, asphalt material has a longer lifespan and will reduce maintenance costs as it protects the upper ballast and other track component compared to granular material. When the reasons are assessed, asphalt layer will be more advantageous and economical in the medium and long term compared to granular sub-ballast material.

• According to the researchers (Rose and Bryson 2009, Sol-Sánchez et al. 2015, Gürer et al. 2021), more comprehensive studies are needed to provide a basis for future design and construction guidelines of railway track with asphalt layer structures especially in high-speed rail.

References

Asphalt. (2019). Retrieved from http://www.asphaltmagazine.com

Esveld C. (2001). Modern Railway Track. 2nd edition, Delft University of Technology, Netherlands.

Fernando M.S., Gaetano D.M. (2017). Optimization of the Mix-Design System for the Sub-ballast Railroad. Journal of Traffic and Transportation Engineering. 5, 246-259.

Gürer C., Akıllı Törer, T., Aslantaş K. (2021). Investigation of using bituminous mixture ınstead of granular sub-ballast layer in high-speed rail tracks with finite element method. Railway Engineering. 14, 39-48.

Gürer, C. (2018). Railway Engineering. Unpublished Lecture Notes, Afyon Kocatepe Üniversity, Dpartment of Civil Engineering. Afyonkarahisar, Turkiye.

Rose J.G., Bryson L.S. (2009). Hot mix asphalt railway trackbeds: trackbed materials, performance evaluations, and significant implications. International Conference on Perpetual Pavements. Columbus, Ohio, USA.

Rose J.G., Souleyrette R.R. (2015). Asphalt railway trackbeds: recent designs,applications and performances. AREMA.

Rose J.G., Uzarski D.R. (2011). Performance-based trackbed structural design and analysis utilizing KENTRACK. Urbana, Illinois, USA.

Sol-Sánchez M., Pirozzolo L., Moreno-Navarro F., Rubio-Gámez M.C. (2015). Advanced characterisation of bituminous sub-ballast for its application in railway tracks: The influence of temperature. Construction and Building Materials. 101, 338-346, doi.org/10.1016/j.conbuildmat.2015.10.102

Sowmiya L.S., Shahu J.T., Gupta K.K. Three-dimensional finite element analysis of railway track. Indian Geotechnical Conference, IGS, Mumbai, Chapter & IIT Bombay, 2010, pp.909-912

Wikizero. (2019). Retrieved from http://www.educational-psychologist. org.uk/behaviour.html

Yalçın, N. S, Erel, A. (2007). Yüksek hızlı demiryollarında altyapının önemi ve tasarım ilkeleri. 7th Ulaştırma Kongresi. İstanbul (in Turkish).

Yang E., Kelvin C.P., Wang M., Qiu Y., Luo Q. (2015). Asphalt concrete for high-speed railway infrastructure and performance comparisons. Journal of Materials in Civil Engineering.

EVALUATION OF WASTEWATERS FROM CARBON BLACK PRODUCTION PROCESS USING A SIMPLE AND LOW COST PHYTOTOXCICITY TEST METHOD

Süheyla TONGUR

(Assoc. Prof. Dr.), Konya Technical University, Engineering and Natural Science Faculty, Environmental Engineering Department Konya, Turkey, E-mail: stongur@ktun.edu.tr, ORCID: 0000-0002-8647-6338

1. Introduction

Lepidium sativum, also known as garden cress or watercress, is a plant species that stands out as a model organism used for assessing biological diversity and conducting toxicity tests. Toxicity tests involving Lepidium sativum evaluate the plant's responses when exposed to various environmental conditions, chemicals, or toxic substances(Shama Adam, 2011). These tests are conducted with the aim of determining the effects of the tested substances on the growth, development, root length, seed production, and other biochemical parameters of watercress. Such tests provide a significant tool for identifying environmental impacts and assessing potential risks. However, the specific details and protocols of a test often vary depending on the methodology employed and the specific objectives of the test(Aydin et al., 2015). The rapid industrial development and urbanization bring about social, political, and economic problems in many countries. These processes negatively affect critical resources such as forests, freshwater sources, seas, and marine life. As a result of industrial activities and urbanization, adverse effects are observed in the growth, development, root length, seed production, and other biochemical parameters of watercress. These negative impacts lead to environmental problems and potential risks. Particularly, lakes, rivers, beaches, and recreational areas are

exposed to excessive pollutants originating from industries and extensive urbanization, sometimes leading to the complete cessation of positive uses of these resources(Aydın M. E., 2006).

Wastewaters generated during industrial activities in industrial facilities are referred to as "industrial wastewater." These wastewaters can arise from processes such as washing, cooking, heating, extraction, reaction products, separation, transportation, and quality control. Water pollution occurs due to the potential amount of pollutants that can cause undesirable changes in

water quality. Industrial wastewaters include not only pollutants from industrial activities but also domestic waters from facilities such as employee bathing, housing, and cafeterias.

The sources of industrial wastewater generation include industrial production processes, equipment cleaning, and on-site floor cleaning waters, water-cooling processes, sanitary water uses, raw material and product storage (open) areas, rain drainage channels, and air pollution control operations (wet treatment)(Gutiérrez, Etxebarria, & de las Fuentes, 2002).

The pollution status and content of wastewaters vary significantly according to different types of industries. In assessing wastewater quality, toxicity measurements are crucial since traditional parameters like COD and BOD may not be sufficient for some wastewater types. The uncontrolled discharge of industrial wastewaters into the environment can result in the transfer of pollution factors to soils and their reaching humans through the food chain. Therefore, studies assessing the effects of industrial wastewaters are important. The discovery of carbon blacks as a reinforcing pigment was made in 1904 by Mote, Mathews, and other scientists in the United Kingdom. This significant development, entering the production of automobile tires in 1910, extended the lifespan of tires. A large portion of globally produced carbon black (95%) is consumed by the rubber industry. Outside of rubber, it is used as a material in plastics, pigments for paints, printing inks, and as an adsorbent substance. Carbon blacks are used in rubber compounds to enhance mechanical properties, increase hardness, and achieve a black color(Seher, 2007).

Known colloquially as "lampblack," carbon blacks are finely dispersed structural carbon particles resembling graphite, obtained through the partial combustion or thermal decomposition of carbonaceous hydrocarbons in gas or liquid form. This material is commonly produced through the incomplete combustion of natural gas, crude oil, tar, and unfinished combustion of residual oils. Carbon blacks serve as an active filler material to improve the mechanical

properties of rubber. Additionally, they are used as an additive in other polymers, apart from rubber, for coloration (black), protection against UV rays, and to enhance conductivity(Grigoryan K.V., 1979).

2. Materyal Method

2.1. Industrial Facility Supplying Carbon Black Wastewater Sample

The facility is located in the Organized Industrial Zone and is involved in the production of carbon black and industrial aromatic, olefinic, and aliphatic compounds from rubber, plastic, and tires in various sizes or granulated f orms, which are procured from the market as finished or semi-finished products. In the facility, rubber, plastic, and tires are processed, resulting in carbon black and industrial liquids (light, medium, heavy fractions).
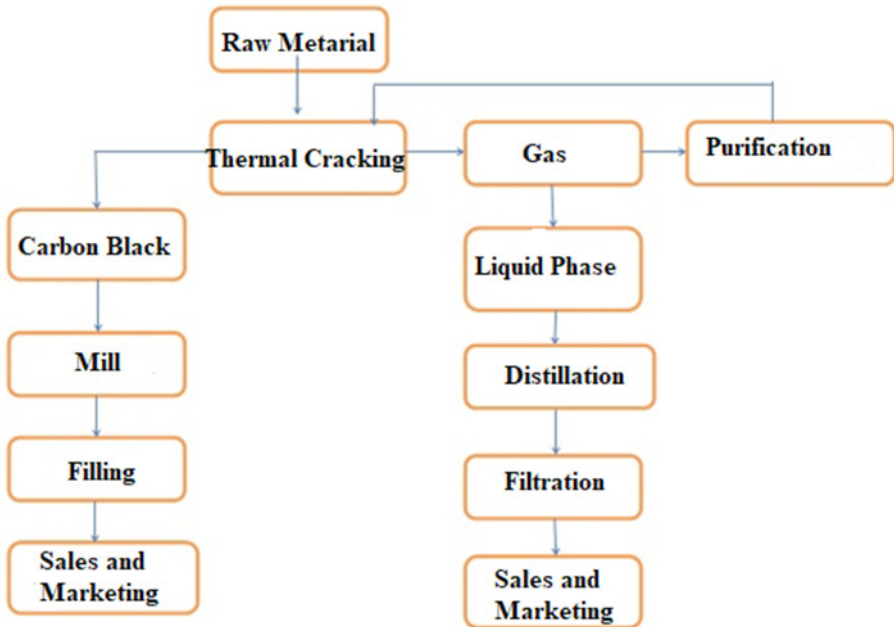
Figure 1. Carbon Black Industry Process Flowchart

2.2. Generated Wastes in the Facility

The facility has two furnaces, Each furnace operates for one day, and the other stages of production also take one day. 40% of the production is Liquid Plasticizer, 30% is Carbon Black, 15% is gas, and 15% is calculated as waste.

The generated gas undergoes washing and combustion processes, contributing either to the product or to the energy needs of the system when burned.1% of the waste amount constitutes filter cake, and the remaining part (liquid waste) is calculated as distillation waste. The categorization of liquid wastes is done to classify them as mineral oil (recycling), solvent (recycling), or asphalt (disposal).

2.3. Wastewaters Obtained from Carbon Black Industry

Sample A = Wastewater sample taken after ground cleaning (containing liquid plasticizer spills, carbon black, dust from the ground, etc.)

Sample B = Wastewater sample resulting from the washing of tanks where the product (liquid plasticizer) is stored

2.3.1. Wastewater Characterization

2.3.1.1. Chemical Oxygen Demand (COD)

Chemical Oxygen Demand (COD) is a parameter used to determine the degree of pollution in domestic and industrial wastewaters. Unlike biochemical oxygen demand, it is based on the oxidation of organic matter through redox reactions rather than biochemical reactions. While biochemical oxidation can occur rapidly for some organic substances, it may proceed very slowly for others. In contrast, in chemical oxidation, all organic substances oxidize regardless of whether they undergo biological decomposition and the rate of decomposition.

The COD test is widely used to examine changes in the concentrations of known components in water and wastewater. COD tests are valuable for detecting toxic conditions and determining non-biologically reducible organic substances. COD is an important and rapidly yielding parameter in the analysis of water, domestic, and industrial wastewaters(American Public Health, Eaton, American Water Works, & Water Environment, 2005).

2.3.1.2. Suspended Solids (SS)

It is determined by drying and weighing the materials remaining on filter paper in used water. The determination of suspended solids in wastewater is crucial.

Total suspended solids are the sum of settleable and non-settleable solid materials in a water sample. Generally, they consist of sediment materials, rock particles, mud or clay minerals, colloidal organic matter particles, and plankton. Human activities can increase the amount of suspended solids in surface waters.

Also, erosion occurring in agricultural areas increases the amount of suspended solids(American Public Health et al., 2005).

Total suspended solids usually cause physical pollution of water after a certain amount, leading to the cloudiness, density, and potential toxicity of water. It can also harm aquatic organisms by reducing light transparency and oxygen levels as they settle on fauna and flora. The impact of suspended solids depends on the type and quantity of these substances and the species and size of aquatic organisms(American Public Health et al., 2005).

2.3.1.3. pH

pH is a term indicating the strength of a solution's acidity or basicity, showing the concentration of H+ ions in the solution and, more precisely, the activity of hydrogen ions. This parameter is crucial in Environmental Engineering applications(American Public Health et al., 2005).

2.3.1.3.Conductivity

Conductivity is a numerical expression of the ability of an aqueous solution to conduct electricity. The conductivity of water depends on the total and relative concentrations, mobility, valence, and measurement temperature of ions in water. Although conductivity is directly proportional to the ion amount, for some ions such as chloride, sulfate, calcium, and magnesium, this ratio is not the same.

By measuring the conductivity of water, the approximate amount of ions in the water can be determined. Thus, without conducting any analysis, the product of the conductivity value multiplied by 0.6 – 0.75 can provide an idea about the total salinity of the water(American Public Health et al., 2005).

2.3.2 Phytotoxicity (Lepidium sativum) test method

To assess the toxicity of Carbon Black wastewater samples on Lepidium sativum, dilutions were prepared at rates of 6.25%, 12,5%, 25%, 50%, and 100%. These same dilution ratios were applied to two different wastewater samples. Six control groups were established for each wastewater sample. Two 90 mm diameter Whatman filter papers were placed in 9 cm glass Petri dishes. For the control group, 5 ml of distilled water was applied to one filter paper, while 5 ml of wastewater sample with varying dilutions was applied to the other filter paper in the sample Petri dishes. Careful measures were taken to remove air bubbles from the filter paper. Each Petri dish contained 25 Lepidium sativum seeds

evenly spaced; the lids were closed, and the dishes were incubated in the dark at 25°C for 72 hours. Afterward, the 20 seeds in each Petri dish that exhibited the fastest growth were selected to measure their root and stem lengths. The root and stem length measurements from the control Petri dishes were compared with the mean values obtained from well-grown Lepidium sativum seeds. Inhibition rates in percentage (%) and EC_{50} values were calculated based on the measured lengths. The EC_{50} values were then utilized to determine toxic-unit values(Persoone & Janssen, 1997; D. T. Sponza, 2002; S. Y. Süheyla Tongur, Rıfat Yıldırım, 2019).

Additionally, reference tests were conducted at six different dilution concentrations using potassium dichromate. The purpose of these tests is to eliminate the presence of any adverse effects arising from laboratory or environmental conditions or from the seeds. The results obtained from both the reference tests and wastewater samples were presented comparatively in the results section through graphs(S. Y. Süheyla Tongur, 2020; Tongur & Yildirim, 2015).

Figure 2. Lepidium sativum phytotoxicity test

2.4. Toxicity Classification of Samples

Samples are classified for toxicity based on the "Toxic Unit" (TU) value, which is derived from either the percentage inhibition rates or the EC50 figures calculated during the toxicity tests. The toxic-unit value, represented by the symbol 'TU,' is a key indicator for interpreting the obtained results. The formula (Equation 1) for toxic-unit calculation based on EC50 values is utilized:

$$TU = \lceil 1/L(E)C_{50} \rfloor *100 \qquad \text{Equation (1)}$$

In their study, Persoone and Janssen (1997) provided a classification for toxicity levels as follows: TU=0 indicates non-toxicity, 0<TU<1 is considered slightly toxic, 1<TB<10 is classified as toxic, 11<TB<100 is categorized as

highly toxic, and TB>100 is labeled as very highly toxic(Persoone & Janssen, 1997; D. T. Sponza, 2002; Delia Teresa Sponza, 2003, 2006; Delia Teresa Sponza & Oztekin, 2010).

3. Results and Discussion

The wastewater from the carbon black industry is currently untreated within the facility and is discharged directly into the sewage system. This practice significantly increases the pollution load on the treatment plant connected to the sewage system. For sample A, it is evident from the Industrial Effluent Control Regulation that the values of COD (Chemical Oxygen Demand) and TSS (Total Suspended Solids) do not comply with the specified limit values for the industry. Since COD is a parameter indicating the degree of pollution, it can be inferred that these waters are rich in terms of organic pollution. Additionally, the conductivity value in the sample is measured as 1880 µS/cm. The ion concentrations in the wastewater are directly proportional to salinity and exceed the limit values. Furthermore, the conductivity results at these levels also contribute to the increase in COD.

For sample B, COD and TSS analysis values are observed to be significantly higher than the limit values. Unlike sample A, the pH value for sample B is highly acidic and falls outside the specified limit values. This explains why sample B is identified as more toxic than sample A. Additionally, the conductivity value is very high. When looking at the COD value, it is observed that it increases in parallel with the conductivity value.

In conclusion, both samples have exceeded the limit values. Sample B is identified as more 'toxic' compared to sample A.

Table 1. The Average Values for Physicochemical Parameters of Wastewaters from the Carbon Black Industry

Sample Name	COD(mg/L)	SS (mg/L)	pH	Conductivity (µS/cm)
Carbon Black Industry A	768	344	6,2	1880
Carbon Black Industry B	2688	714	2,09	5910

Table 2. The Limit Values specified for Wastewaters from the Carbon Black Industry in Water Pollution Control Regulations

Sample Name	COD(mg/L)	SS (mg/L)	pH
Composite Sample(2 hour)	200	65	6-9
Composite Sample(24 hour)	100	45	6-9

3.1. Phytotoxicity Test Results

In the graphs below, the percent inhibition values obtained as a result of Lepidium sativum exposure to industrial wastewater from carbon black production are displayed (Figure 3; Figure 4).Formun Üstü
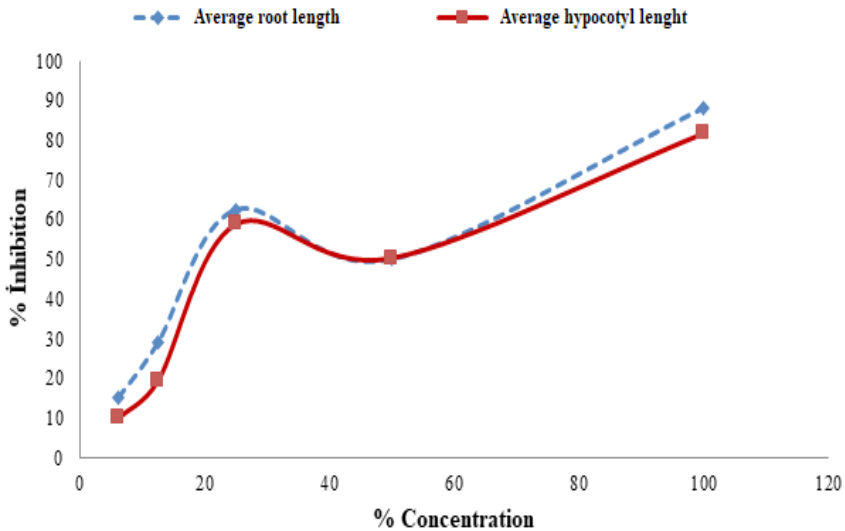
Figure 3. Comparative graph of average root and hypocotyl lengths for Sample A
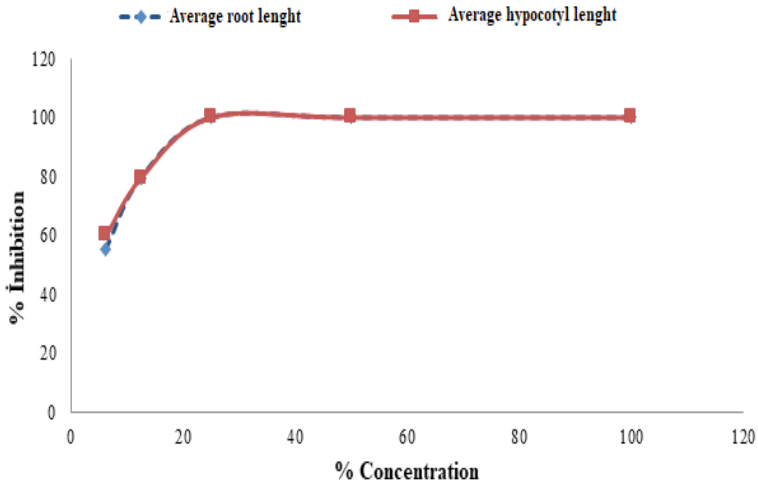
Figure 4. Comparative graph of average root and hypocotyl
lengths for Sample B

According to these values, it is evident that inhibition increases with rising
concentration percentages for both types of samples. As clearly observed from
the graphs, the increase in concentration has a toxic effect on both the roots and
shoots, hindering growth. The results were also calculated as a Toxic Unit value,
and the levels of toxicity were determined. The findings are expressed in Table
3 and Table 4 in terms of EC_{50} and toxic units.
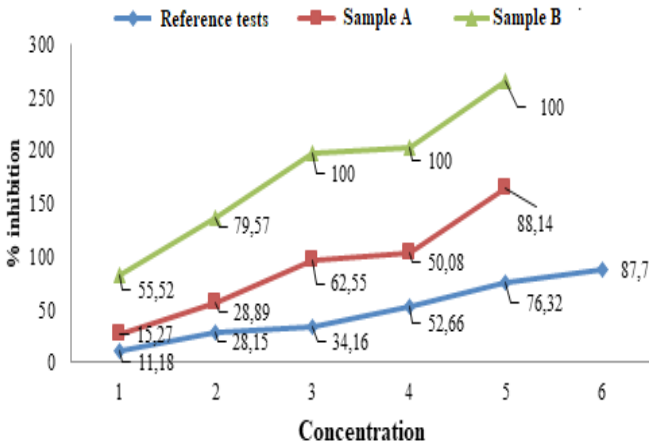
Figure 5. Inhibition rates of average root lengths obtained for sample A,
sample B and Reference tests
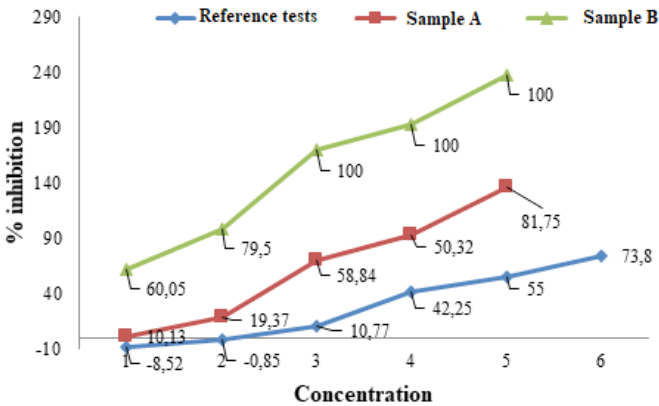
Figure 6. Inhibition rates of average hypocotyl lengths obtained for sample A, sample B and Reference tests

The results obtained from the reference tests and those from Samples A and B have been compared in the above graphs, clearly demonstrating the presence of toxicity in both A and B samples. As depicted in the graph, based on the data obtained from Figure 5 and Figure 6 is evident that Sample B is more toxic than Sample A. The graphs generated from the obtained data and the quantities from our analysis of COD, BOD, pH, and conductivity in the wastewater further support that Sample B exhibits a higher level of toxicity than Sample A, accompanied by reduced growth.

3.2. Toxic Unit Assessment

Table 3. Toxic Unit Results for Root Lengths

Sample Name	EC_{50}	Toxic Unit	Classification
Carbon Black Industry A	51,460	1,943	Toxic
Carbon Black Industry B	7,140	14,00	Highly Toxic

* EC_{50}: The concentration at which the current population is impacted by 50%.

Table 4. Toxic Unit Results for Hypocotyl Lengths

Sample Name	EC_{50}	Toxic Unit	Classification
Carbon Black Industry A	64,090	1,560	Toxic
Carbon Black Industry B	3,230	30,959	Highly Toxic

* EC_{50}: The concentration at which the current population is impacted by 50%..

Wastewaters generated during carbon black production are classified as industrial wastewater. The chemical and biological pollutants present in these wastewaters can adversely affect water quality when discharged into water sources. Organic substances, toxic chemicals, and other waste components can harm aquatic ecosystems(Seher, 2007). The Lepidium sativum toxicity test holds critical importance in assessing the toxic effects of carbon black industrial wastewaters. This test is utilized to determine potential toxic effects in wastewaters, aiding in the evaluation of environmental risks and potential harm. Lepidium sativum, chosen as a sensitive model plant for its susceptibility to plant growth and development processes, provides a reliable method to assess the effects of chemicals in wastewaters on plant life(Häder, 2018; D. T. Sponza, 2002). The toxicity test meticulously evaluates the impacts of pollutants present in carbon black industrial wastewaters on Lepidium sativum. The results of the test, used to identify the adverse effects of wastewaters on plant development, offer crucial insights for environmental sustainability and ecosystem health. Thus, the conducted study establishes the Lepidium sativum toxicity test as an effective tool for assessing and managing the environmental impacts of carbon black industrial wastewaters. The physicochemical analyses and phytotoxicity test conducted in the study demonstrate that wastewater from the carbon black industry possesses a toxic nature. These findings underscore the necessity of not discharging the wastewater into the sewage system without proper pretreatment.

5. Conclusions

Wastewaters originating from carbon black production industry can contain various chemical and organic components. These pollutants vary depending on industrial processes, material usage, and production methods. Wastewaters may contain toxic metals such as zinc, lead, and chromium. These metals can accumulate in aquatic ecosystems, negatively impacting biological diversity and posing risks to human health(Aydın M. E., 2006; Kim & Farnazo, 2017; Mahfooz et al., 2020; Mustafa, Valente, & Vinggaard, 2023). Wastewaters can include organic components such as dissolved organic matter, oils, hydrocarbons, and other organic wastes. These pollutants can decrease water quality and induce toxic effects on aquatic organisms(Cēbere, Faltiņa, Zelčāns, & Kalniņa, 2010). Chemical compounds like phenols, generated during carbon black production, can be found in wastewaters. These substances can be harmful to aquatic life. Various dissolved salts may be present in wastewaters due to the chemicals

used in carbon black production. These salts can negatively impact water quality and contribute to soil salinity. Wastewaters from industrial processes can be acidic or basic. This condition can disrupt the pH balance in aquatic ecosystems, leading to adverse effects on organisms. The types of pollutants present in these wastewaters can vary based on the specific details of carbon black production processes. The analysis of wastewaters is crucial for assessing environmental impacts and determining appropriate treatment methods. In conclusion, the proper disposal and treatment of wastewater from the carbon black industry promote an environmentally friendly approach and contribute to the conservation of water resources. Implementing waste management practices that align with local regulations and are sustainable is a critical step in minimizing the environmental impacts of these wastewaters.Formun Üstü

References

American Public Health, A., Eaton, A. D., American Water Works, A., & Water Environment, F. (2005). *Standard methods for the examination of water and wastewater* (21st ed ed.). Washington, D.C.: APHA-AWWA-WEF Washington, D.C.

Aydın M. E., K. G. (2006). Toxicity of Organized Industrial Wastewater. *Selcuk University Eng. Architect. Faculty, 36(22)*, 2825-2834.

Aydin, M. E., Aydin, S., Tongur, S., Kara, G., Kolb, M., & Bahadir, M. (2015). Application of simple and low-cost toxicity tests for ecotoxicological assessment of industrial wastewaters. *Environ Technol, 36*(22), 2825-2834. doi: 10.1080/09593330.2015.1049216

Cēbere, B., Faltiņa, E., Zelčāns, N., & Kalniņa, D. (2010). Toxicity Tests for Ensuring Succesful Industrial Wastewater Treatment Plant Operation. *Environmental and Climate Technologies, 3*(3), 41-47. doi:doi:10.2478/v10145-009-0005-8

Grigoryan K.V., G. A. S. H. (1979). Effect of Irrigation Water Polluted with Industrial Waste on the Enziymatic Activity of Soils. *Soviet soil science, 11*(11), 220-228.

Gutiérrez, M., Etxebarria, J., & de las Fuentes, L. (2002). Evaluation of wastewater toxicity: comparative study between Microtox® and activated sludge oxygen uptake inhibition. *Water Research, 36*(4), 919-924.

Häder, D.-P. (2018). 18 - Ecotoxicological monitoring of wastewater. In D.-P. Häder & G. S. Erzinger (Eds.), *Bioassays* (pp. 369-386): Elsevier.

Kim, Y., & Farnazo, D. M. (2017). Toxicity characteristics of sewage treatment effluents and potential contribution of micropollutant residuals.

Journal of Ecology and Environment, 41(1), 39. doi:10.1186/s41610-017-0057-9

Mahfooz, Y., Yasar, A., Guijian, L., Islam, Q. U., Akhtar, A. B. T., Rasheed, R., Naeem, U., (2020). Critical risk analysis of metals toxicity in wastewater irrigated soil and crops: a study of a semi-arid developing region. *Scientific Reports, 10*(1), 12845. doi:10.1038/s41598-020-69815-0

Mustafa, E., Valente, M. J., & Vinggaard, A. M. (2023). Complex chemical mixtures: Approaches for assessing adverse human health effects. *Current Opinion in Toxicology, 34*, 100404.

Persoone, G., & Janssen, C. R. (1997). Freshwater Invertebrate Toxicity Tests *Handbook of Ecotoxicology* (pp. 51-65).

Seher, E. (2007). *Karbon Siyahı/Yağ ve Karbon Siyahı/Dolgu Maddesi Oranının Farklı Vulkanizasyon Sistemlerinde Epdm, Nbr ve Sbr Elastomerlerinin Fiziko-Mekaniksel Özellikleri Üzerine Etkisi.* (Yüksek Lisans Tezi), Çukurova Üniversitesi Fen Bilimleri Enstitüsü (178503)

Shama Adam, W. A. (2011). In vitro Antimicrobial Assessment of Lepidium sativum L. Seeds Extracts. *Asian Journal of Medical Sciences, 3*(6), 261-266.

Sponza, D. T. (2002). Incorporation of Toxicity Tests into the Turkish Industrial Discharge Monitoring Systems. *Archives of Environmental Contamination and Toxicology, 43*(2), 186-197. doi:10.1007/s00244-002-1150-2

Sponza, D. T. (2003). Application of toxicity tests into discharges of the pulp-paper industry in Turkey. *Ecotoxicology and Environmental Safety, 54*(1), 74-86. Sponza, D. T. (2006). Toxicity studies in a chemical dye production industry in Turkey. *Journal of Hazardous Materials, 138*(3), 438-447.

Sponza, D. T., & Oztekin, R. (2010). Removals of PAHs and acute toxicity via sonication in a petrochemical industry wastewater. *Chemical Engineering Journal, 162*(1), 142-150.

Süheyla Tongur, S. Y. (2020). Toxicological evaluation of carbamazepine active pharmaceutical ingredient with Lepidium sativum, Daphnia magna and Vibrio fischeri toxicity test methods. *DESALINATION AND WATER TREATMENT, 201*, 438-442.

Süheyla Tongur, S. Y., Rıfat Yıldırım. (2019). Bazı İlaç Gruplarının Su Ortamına Olan Etkilerinin Akut Toksisite Testleri ile Değerlendirilmesi. *Süleyman Demirel Üniversitesi Fen Bilimleri Enstitüsü Dergisi, 23*, 74-75.

Tongur, S., & Yildirim, R. (2015). Acute Toxicity Assessment of Antibiotics in Water by Luminiscence Bacteria and Lepidium Sativum. *Procedia Earth and Planetary Science, 15*, 468-473.

INVESTIGATION THE EFFECTS OF FILTERING ALGORITHMS TO DTM PRODUCTION FROM AIRBORNE LIDAR DATA ON STEEP SLOPES WITH DENSE VEGETATION

Lütfiye KARASAKA[1] & Sultan Hilal KELEŞ[2]

[1](Assist. Prof. Dr.) Konya Technical University, Faculty of Engineering and Natural Sciences, Department of Geomatics Engineering, Konya, TURKEY
E-mail:lkarasaka@ktun.edu.tr
ORCID: 0000-0002-2804-3219

[2](MSc.) Konya Technical University, Faculty of Engineering and Natural Sciences, Department of Geomatics Engineering, Konya, TURKEY
E-mail: sultanhilalkeless@gmail.com
ORCID: 0000-0001-5262-5238

1. Introduction

Today, one of the methods that have begun to be used to produce three-dimensional digital models of the earth is the LiDAR (Light Detection and Ranging) scanning technology. Airborne Light Detection and Ranging, a remote sensing method, allows for an effective and accurate acquisition of three-dimensional coordinate information regarding ground and above-ground objects. This technology, which was developed in late 20th century, is widely used in various activities by many countries and terrestrial analyses are performed successfully. Compared to traditional methods, the LiDAR technology stands out with the high advantages it possesses. The fact that the method is significantly more advantageous and practical compared to the aerial photogrammetry method, particularly in the production of the Digital Terrain Model (DTM), is the most important factor in the selection of this

method. LiDAR systems use thousands of laser signals per second, providing point density, which is important for various models, analyzes and classifications. The data collected in LiDAR includes all artificial and natural terrestrial objects (Doğruluk, Aydın, & Yanalak, 2018). Due to the dense point data it generates, the LiDAR technology is used for many purposes involving agriculture, forest volume and tree classification, development of risk maps in various natural events, flood analyses and flow modeling studies, underwater modeling, coast monitoring, classification of natural life, transportation, modeling of power transmission lines, mining, building modeling, archeology, and monitoring precise changes in objects (Cateanu & Ciubotaru, 2021; Cheng, Tong, Wang, & Li, 2014; Cobby, Mason, Horritt, & Bates, 2003; Cunningham, Grebby, Tansey, Gosar, & Kastelic, 2006; Estornell, Hadas, Mart, & Lopez-Cortes, 2021; Guyot et al., 2019; Hancock, Anderson, Disney, & Gaston, 2017; Lang, Guild, Valenta, Carr, & Zutty, 2021; Matikainen et al., 2016; Paine, Collins, & Costard, 2018; Popescu, Wynne, & Nelson, 2002; Shaker, Yan, & LaRocque, 2019; Stumpf, Malet, Allemand, Pierrot-Deseilligny, & Skupinski, 2015; Thuestad, Risbol, Kleppe, Barlindhaug, & Myrvoll, 2021; Tulldahl, Vahlberg, Axelsson, Karlsson, & Jonsson, 2007; Yastikli & Cetin, 2017; Yu, Lu, Ge, & Cheng, 2010). Using traditional methods to identify the number of individual trees and tree features in large and dense wooded areas is a time-consuming process, particularly when determining the structural aspects of forests and conducting vegetation analyses. Automatic tree detection using point clouds is a subject that has been studied recently. In the LiDAR point cloud, DTM is derived from the points reflected from the ground, while Digital Surface Model (DSM) is generated from the top points. By subtracting these two surfaces, a tree height model is generated that depicts the regional distribution of tree heights. Accurate analysis and classification of airborne LiDAR data is an important process in the conduction of these studies, as well. In order to generate outcomes that are useful for a variety of uses from dense point data acquired from LiDAR systems, it is necessary to separate ground points from object points (Sanchez et al., 2019). Separating ground points from point cloud data containing thousands or millions of data manually is a very time-consuming and complex task. Additionally, a powerful software is also required to process big data containing a lot of information. Classification in the point cloud that is irregularly distributed to all objects refers to the assignment of the point to the object group it belongs to. The filtering process, on the other hand, performs classification in the form of separating ground points from other points (Karasaka & Keleş, 2020; Soycan,

Tunalıoğlu, Öcalan, Soycan, & Gümüş, 2011). Many filtering algorithms and methods that can differentiate ground and object points currently exist or are under development (Ali, Taha, Mohamed, & Mandouh, 2021). Based on their working principles, the existing filtering methods can be classified into five as slope-based, morphology-based, interpolation-based, segmentation-based and machine learning-based algorithms (Chen, Guo, Wu, Li, & Shi, 2021). The slope-based filtering method was first developed by (Vosselman, 2000). This method is based on the observation that a substantial height difference between two points close to each other is less likely to be caused by a steep slope in the terrain. The method was developed with the studies conducted by (Chen, Chang, Li, & Shi, 2021; Meng, Wang, Silvan, & Currit, 2009; Susaki, 2012). In the morphology-based filtering method, morphological operators transform the raw point cloud to a raster at a specified window size. Points with height differences greater than the threshold value are filtered out as non-ground points (Meng et al., 2019). The performance of morphology-based filters is dependent on window size and height differences. While small window sizes are effective at filtering out small objects, large window sizes tend to soften details such as mountains and hills (Zhang et al., 2016). For this reason, progressive morphological filters were proposed by (Pingel, Clarke, & McBride, 2013; Zhang et al., 2003). Interpolation-based filters use floating windows slightly larger than the maximum object size to select starting points and subject them to interpolation. When the vertical distance to the interpolated surface is lower than the threshold value, new ground points are detected (Chen, Guo, et al., 2021). The Adaptive Triangulated Irregular Network (ATIN) is an interpolation-based filtering method proposed by (Axelsson, 2000). In the segmentation-based filtering method, each measurement is labeled in the point cloud. This way, similar points belonging to the same region are assigned the same label (Chen et al., 2016). The success of the method depends on segmentation, and it may produce more reliable results in terms of classification as geometric and topological information are taken into consideration (Vosselman, Coenen, & Rottensteiner, 2017). With the advancement of computer hardware's ability to process large amounts of data in recent years, studies utilizing machine learning-based filtering methods have garnered considerable attention. Particularly the image classification studies carried out with convolutional neural networks (CNN), a sub-branch of machine learning, can be given as an example. In the study conducted by (Varlik & Uray, 2021), the FCN-based U-net architecture PixU-net is proposed for ALS point cloud segmentation. (Trier, Reksten, & Løseth, 2021) investigated the

suitability of high-resolution airborne LiDAR data in the semi-automated detection of different cultural heritage objects. In the study conducted by (Li et al., 2021), the researchers proposed a new workflow for the automated generation of a Digital Terrain Model (DTM) from ALS point clouds based on a convolutional neural network (CNN). The researchers classified ground and non-ground objects using ResNet models and compared the results with two different traditional filtering methods, Progressive Morphological Filtering (PMF) and Progressive Triangulated Irregular Network Densification (PTD). In recent studies, it is observed that certain filtering algorithms are developed with the combination of different methods, as well. In relation this, in the study conducted by (Meng et al., 2019), the Multilevel Adaptive Filter (MAF) filtering algorithm was tested in two different study areas. Selecting terrains of different types, the researchers emphasized the importance of the possibility that the fixed threshold value generally found in filtering parameters may have a negative effect on filtering results in areas with terrain fluctuation. For this reason, the Multilevel Adaptive Filter (MAF), a combination of the Morphological Reconstruction and multi-layer Thin Plate Spline (TPS) interpolation, in order to overcome the classifications in a single algorithm and increase the accuracy of filtering. In general terms, while TPS interpolation tends to create a continuous surface that involves all control points, Morphological Reconstruction extracts ground pixels by producing DSM in every iteration and is updated with threshold value terrain slope. Filtering algorithms are included in commercial and open-source software that users can easily download over the internet. Each software involves various algorithms and their parameters in their content. It is difficult to find the most suitable algorithm for the ground surface among many filtering algorithms (Cai et al., 2019). That is because each algorithm includes different methods, and it is necessary for users to understand parameter conditions. Additionally, algorithms may display different results in different ground surfaces. Particularly in regions with high height difference, difficulties may be encountered in separating ground points from object points (Meng, Currit, & Zhao, 2010). In recent years, Cloth Simulation Filtering (CSF) algorithm has been attracting attention due to its low number of parameters and ease of configuration. CSF is an algorithm that is effectively used for point cloud filtering. This algorithm, which requires only one integer parameter, can obtain a starting terrain that resembles the real terrain (Cai et al., 2019). This study aims to determine the most suitable filtering parameters according to the characteristics of the land surface (ground structure, vegetation, height values, slope, etc.). The most

important parameters affecting the classification result are dense vegetation and sloping land type. In the present study, the performance of CSF and ATIN algorithms in filtering ground points is evaluated for a challenging terrain surface consisting of steep slopes and dense vegetation. The effects of CSF and ATIN filtering parameters on the results were evaluated since the study area consists of dense vegetation at high places and the steep slopes are in the form of stair steps against erosion. After filtering, the Digital Terrain Model was constructed by separating the ground points from non-ground points. The obtained terrain models were compared to the reference terrain model in terms of accuracy. As a result, the data processing processes, advantages and disadvantages of the two algorithms, which are found in different software, in filtering ground points were discussed.

2. Materials and Methods

2.1. Test Site

An area encompassing the steep and dense vegetation of the Kocaoğlanlı village in the Alanya district of Antalya, Turkey, located in the Mediterranean Region of Turkey, was selected as the study area (Figure 1). The altitude of the overall study area above sea level ranges between 181 to 300m and the area has a surface area of 28 hectares. Data of the study area were referenced in the UTM Projection system based on the WGS84 Datum. The steep slopes in the region are protected against erosion using a method called terracing, which involves forming the terrain in the form of stairs. On the ridges, there is a dense forest of maquis. Aerial laser scanning is a highly rapid and efficient method for delivering the laser signal to the ground surface on steep slopes with dense vegetation, such as agricultural or forest areas. Due to the presence of 7 buildings in the northeast and northwest portions of the study area, as well as dense forest areas and steep slopes in general, the digital terrain model of the area was developed using the airborne LiDAR method. Additionally, orthophotos generated from digital images acquired concurrently during the same flight were used as supplementary data to aid in the topography analysis.

Figure 1. Study area and types of terrain

2.2. LiDAR Data Acquisition

The LiDAR data used in the study were obtained through a flight that took place on September 26, 2018. The flight was carried out using a RIEGL VQ-580 laser scanner at a flight altitude of 450-500 meters. The raw data consists of 12.113.500 laser points. The density of LiDAR data is approximately 45-50 points per m^2. The LiDAR data used in the present study is in the LAS 1.1 format and contains GPS time information, flight lane information, density, scanning angle, and reflection information. RIEGL VQ-580 can operate at a near-infrared wavelength, a maximum pulse repetition rate of 380 kHz, and a flight altitude of approximately 1200 meters. Thanks to a wide vision range of 60^0, the scanner has the ability to scan from various angles and achieve accurate data. The scanner was also equipped to be connected to the GNSS\IMU system (Riegl Data Sheet VQ-580, 2015). Laser scanners collect data in a variety of formats, including oblique, parallel, elliptical, and Z-shaped. With a scanning angle of 60°, this scanner collects data in linear, unidirectional, and parallel scanning modes.

2.3. Ground Point Filtering Algorithms

In the present study, the algorithms ATIN and CSF were used to filter ground points. In the CSF algorithm, the process of filtering ground points is based on the logic of a basic physical process. First, it is assumed that a piece of cloth fell to the terrain surface from above, encompassing the whole surface. In this process, the final shape of the cloth surface is called DEM. In the production

of Digital Terrain Models, on the other hand, the algorithm applies a different methodology. First, the raw point cloud encompassing the study area is reversed, and a piece of cloth is dropped on the reverse surface. The rigidity value of the cloth that will cover the point cloud is determined. The ultimate shape taken by the cloth is DTM (Zhang et al., 2016) The interaction between the LiDAR points corresponding to the nodal points of the cloth is analyzed in this algorithm, and the raw point data is divided into ground and non-ground points. This surface, termed the cloth surface, is modeled as a grid of interconnected particles with a constant mass (such as the mass-spring model) (Provot, 1995). The three-dimensional positions of these particles determine the shape of the cloth surface. On the other hand, the relationship between the particles on the cloth surface conforms to Hooke's law of "virtual spring." The particles in **Figure 2** interact and move in response to three different types of springs. These are referred to as shear springs, traction springs, and flexion springs. To simulate the shape of the fabric at a given point in time, the three-dimensional positions of all particles are calculated. Newton's second law is taken as the basis to calculate the positions and velocities of the particles (Zhang et al., 2016).
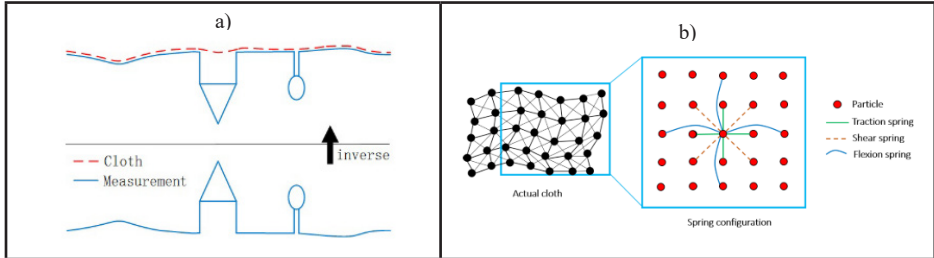
Figure 2. a) General overview of the CSF algorithm **b)** Schematic display of the mass-spring model (Zhang et al., 2016).

The filtering parameters of the CSF algorithm were classified as general and advanced. In the general parameters, the terrain characteristic of the area studied is determined. The terrain types in the general parameters are presented in three groups: steep slope, relief, and flat. The advanced parameters, on the other hand, consist of numerical values: cloth resolution, max iterations and classification threshold. *Cloth resolution* refers to the grid dimensions of the cloth surface covering the terrain surface. It represents the horizontal distance between two neighboring particles (nodes) in the cloth surface. *Max iterations* refer to the maximum number of iterations in the simulation. *Classification threshold* is a threshold value in which points are classified as ground and

object based on the distance in the simulated terrain (cloth) surface. The other algorithm used to classify ground points in the present study is the ATIN filtering algorithm developed by Axelsson. Many algorithms take height and slope value as the basis for filtering ground points. Among these algorithms, the Axelsson algorithm is one that performs an example of progressive classification and produces more successful results in determining ground points (Axelsson, 1999). Axelsson developed a triangular filtering algorithm. First, the algorithm forms a Triangular Irregular Network (TIN) surface starting from the few points with the lowest height, called nodal points, and progressively adds new points to the model. The point cloud is limited by a curvature determined by the parameters specified, and new points that are below this limit are added to the TIN surface. It operates in accordance with the angle to the TIN surface and the distance between the points constituting the surface (Axelsson, 2000). In the selection of the points Axelsson named nodal points, there are certain factor to take into consideration. First, the study area is divided into grids and the points with the lowest height are determined as ground points. The first point selection is verified with maximum building size. If the highest value of building height in the study area is 60 meters, the algorithm assumes the presence of a 60*60 area, and that there must be at least one earth point at ground level. Among these points, the one with the lowest elevation is regarded as the ground point. With this start, the algorithm forms the TIN surface from the first ground points it selects. The triangles in this first model are mostly below the ground level, and only the edges contact earth. The iteration parameters of the algorithm examine the proximity to the triangular plane for a point to be considered as ground point. The *iteration angle parameter* is the maximum angle between the prospective point and the peak point of the nearest triangle on the triangular surface. This parameter also controls how many points are classified on the ground layer. Another parameter of the algorithm, *iteration distance*, prevents the formation of large jumps between points when triangles are formed during iteration. This parameter prevents the emergence of high ground points in buildings with low height and low vegetation. When no more points are added on the TIN surface, the iteration process stops.

3. Results

3.1. Filtering Results with the CSF Algorithm

For the 12.113.500 raw LiDAR point data covering the study area, a filtering operation was performed using the CSF algorithm on the CloudCompare

software. Since the study area consists of steep slopes and sloping regions, the terrain type was set as steep slope in algorithm parameters. In the advanced parameters, the filtering process was carried out using various cloth resolution values (0.2, 0.3, 0.4, 0.5, 1, 2) with a classification threshold of 0.5 and a max iteration value of 1000. With the CSF algorithm, filtering was performed with various cloth resolution values, and ground and object points were parsed. A triangulation process was applied on the ground points separated from the object points, and DTM was created. When the filtering results are examined, it is observed that less ground points were produced as the cloth resolution value consecutively increased. With the increase in the cloth resolution parameter, it was observed that the deformations on the terrain surface progressively increased in the models produced. Figure 3 (A: 5.529.470 ground points were filtered using a 0.2 cloth resolution.; B: 5.419.973 ground points were filtered using a 0.3 cloth resolution.; C: 5.328.275 ground points filtered with 0.4 cloth resolution.; D: 5.218.743 ground points filtered with 0.5 cloth resolution.; E: 4.152.422 ground points filtered with 1 cloth resolution.; F: 1.368.301 ground points filtered with 2 cloth resolution.) shows the respective ground points and non-ground object points of the models obtained with various cloth resolution values, as well as visuals of the digital terrain models generated . The results of the filtering operations performed with various parameter values using the CSF algorithm were compared with the reference model in hillshade view. When DTM produced as a result of the application with a cloth resolution value of 0.2 is examined, it is observed that the filtering operation was generally successful in areas with steep slopes and dense vegetation, and the terrain surface was revealed. However, the buildings and tree groups located in the northwest of the study area could not be detected and filtered. When the general overview of the model produced by filtering with 0.3 cloth resolution is examined, unlike the terrain model produced with 0.2 cloth resolution, a building in the northwest region was filtered (Figure 4). When the DTM model produced with a cloth resolution filtering value of 0.4 is examined, it is observed that some of the buildings in the northwest and the building at the top of the slope, which could not be removed, are filtered and some of the trees are filtered better. In this context, better filtering was performed with a cloth resolution value of 0.4. The terrain model produced with 0.5 cloth resolution exhibited similar results with the model produced with 0.4 cloth resolution. The model could not remove the buildings in the area north of the region with increased slope. It was also unable to determine the ground characteristic below the tree group located in the west of the study area. When the DTM produced with a cloth resolution value of 1 is

examined, it is observed that, with the exception of a building in the northwest of the study area, the model gave the most successful result in filtering buildings. However, it could not fully detect the terrain in the south of the area and filed the surface. The cloth resolution value of 2 demonstrated the worst performance in the overall study area. Particularly the steep slopes were excessively softened and the terrain lost its true characteristic (Figure 5).
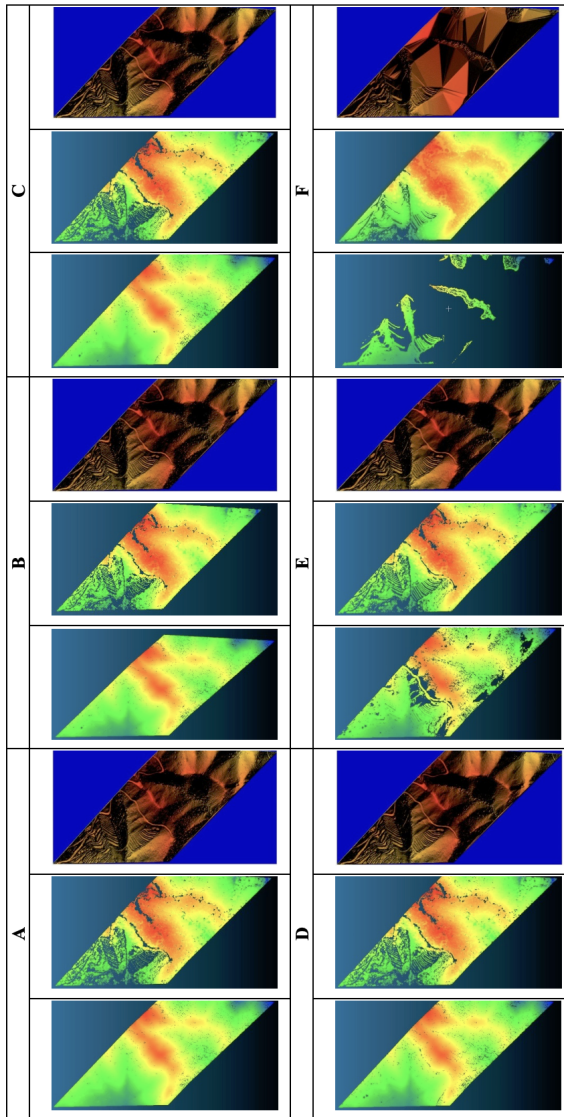
Figure 3. Ground points, non-ground object points separated as a result of filtering and DTM
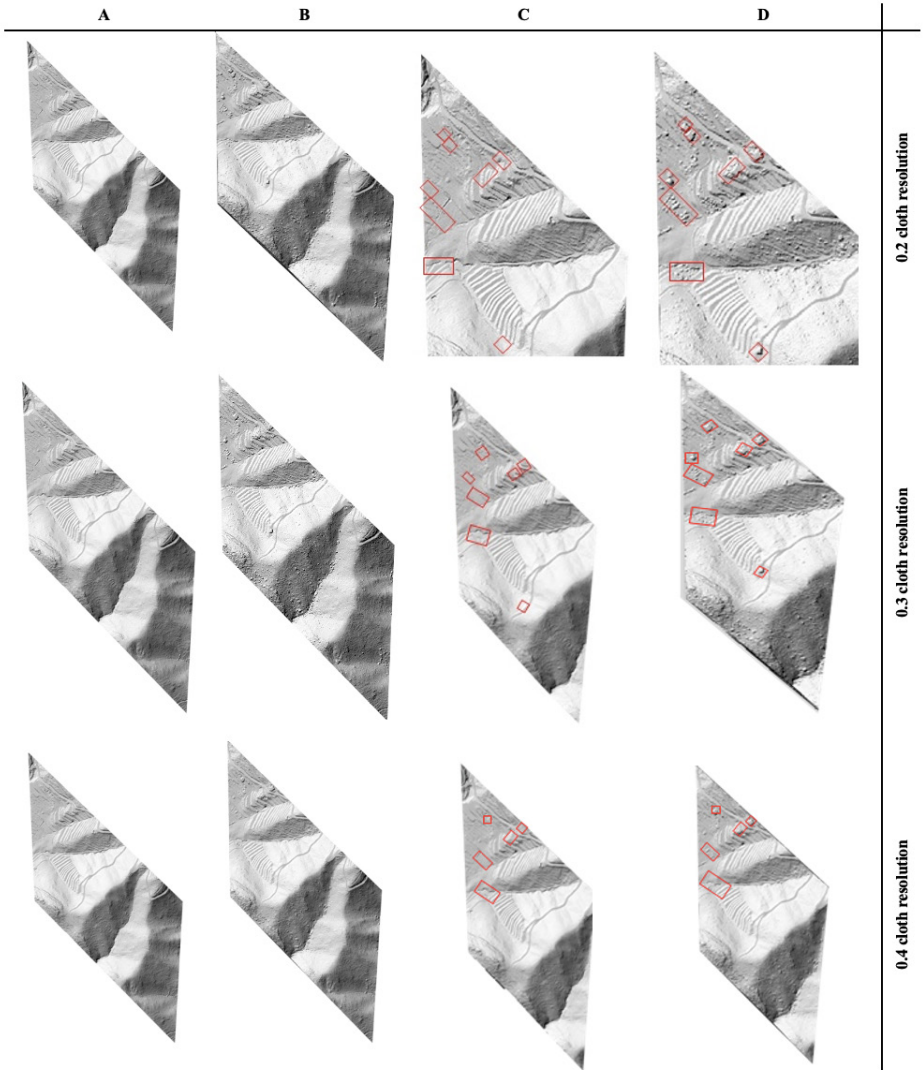
Figure 4. A-Reference DTM, **B-**DTM produced based on cloth resolution,
C-Filtered objects, **D-**Non-filtered objects.
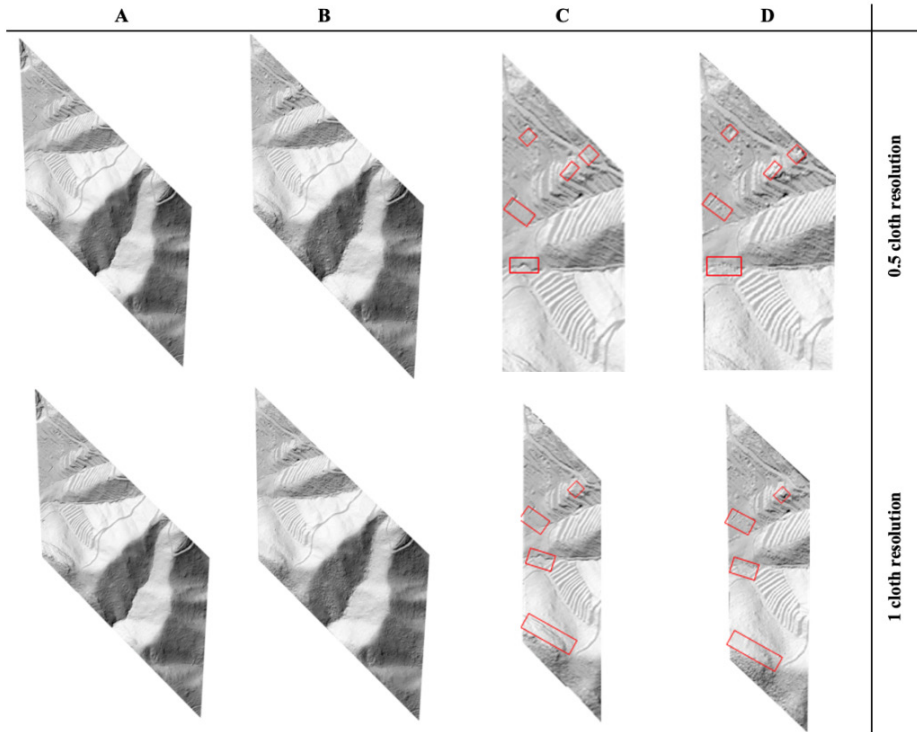
Figure 5. A-Reference DTM, **B-**DTM produced based on cloth resolution,
C-Filtered objects, **D-**Non-filtered objects.

3.2. Filtering Results with the ATIN Algorithm

Using the ATIN algorithm, 12.113.500 raw LiDAR point data were filtered, and the ground and non-ground points were parsed. At this stage, in order to make an effective filtering, the characteristics of the study area were examined by analyzing parameter values along with the recommended value ranges. In order to determine the terrain angle value in the ground filtering parameter, a slope map of the study area was created in the ArcMap 10.5 software and examined. As a result of these evaluations performed prior to the filtering process, filtering operations were performed by applying a maximum building size value of 100, an iteration distance value of 1.40m, a terrain angle value of 90° (steepest slope) and iteration angles of 4° ,6° ,8°, and 10°, respectively. Figure 6 (A: filtered with an iteration angle of 4°, Ground Points Filtered: 944.631; B: filtered with an iteration angle of 6°, Ground Points Filtered: 1.154.848; C: filtered with an iteration angle of 8°, Ground Points Filtered: 1.240.845; D: filtered with an

iteration angle of 10°, Ground Points Filtered: 1.294.56) shows the ground points and non-ground object points of the models obtained with various iteration angle values, as well as visual of the digital terrain models created.
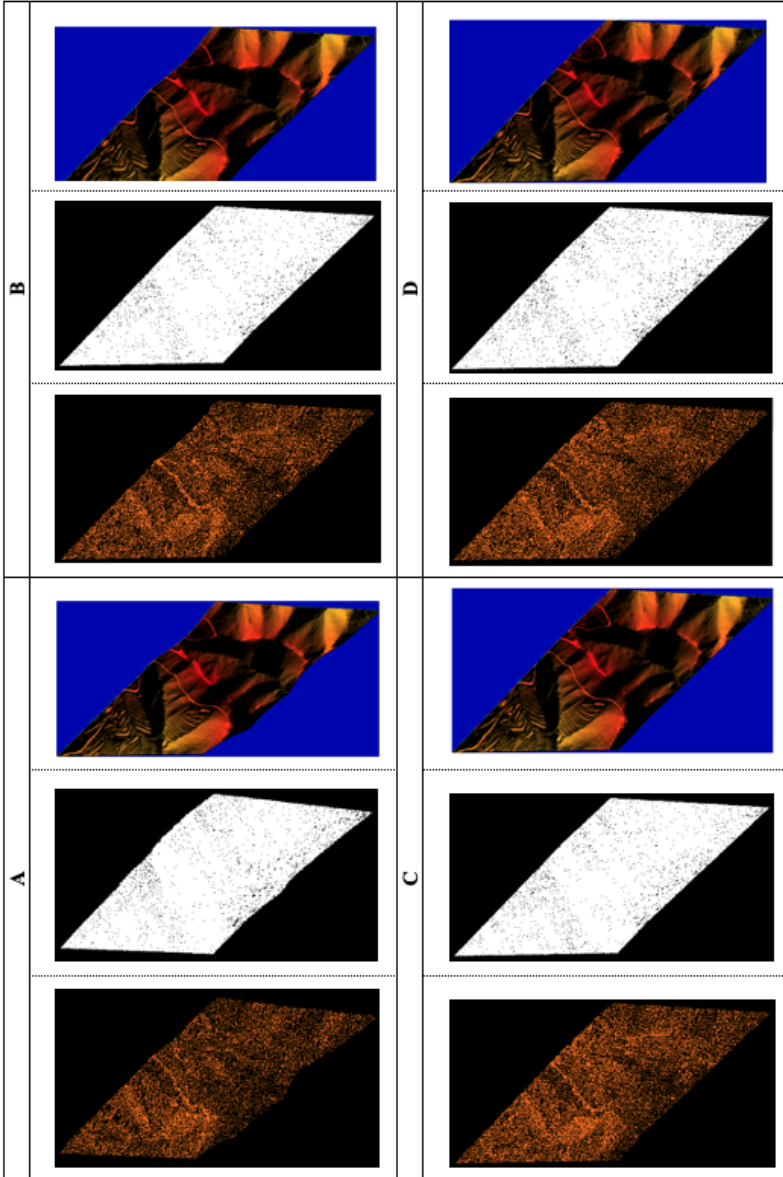
Figure 6. Ground points and non-ground object points
separated as a result of filtering, and DTM

For a more detailed examination, the terrain models produced as a result of filtering with various parameter values in the ATIN algorithm were compared with the reference model in hillshade view. First, when the model produced from the points filtered with an iteration angle value of 4° is examined, it is observed that a good performance was demonstrated in filtering the overall terrain surface. The terrain surface located below the dense wooded areas of the region was revealed. It is observed that all buildings in the study region were filtered in the model. However, it also flattened the artificially-filled ground along with the building in the steep slope located in the middle part of the area. Additionally, flatting is observed in the ground surface at the head of the steep slope located in the east of the study area. When the model produced through filtering with an iteration angle value of 6° is examined, it is observed that all buildings in the study area were filtered. The building in the steep slope located in northeast of the study area was filtered, and the artificially filled surface below the building was partially filed. Additionally, the ground surface on the other steep slope in the same area is more explicit. Compared with the model produced with an iteration angle value of 4°, better results were obtained. When the model produced with an iteration angle value of 8° is examined, it is observed that the study area was generally cleared of dense trees and other objects. In the determination of the terrain characteristic in the slope and the artificially-filled surface located in the northeast of the area, this model was more successful compared to those produced with iteration angle values of 4° and 6°, and produced results that are near the reference surface. However, the model was unable to filter a building at the head of a slope located in the northwest of the study area. The model produced with an iteration angle value of 10° produced similar results with the model created with an iteration angle value of 8°. There is a building in the area that was not filtered. The most successful results in determining the ground surface characteristic were produced. With these evaluations, the results nearest to the reference surface are observed (Figure 7).
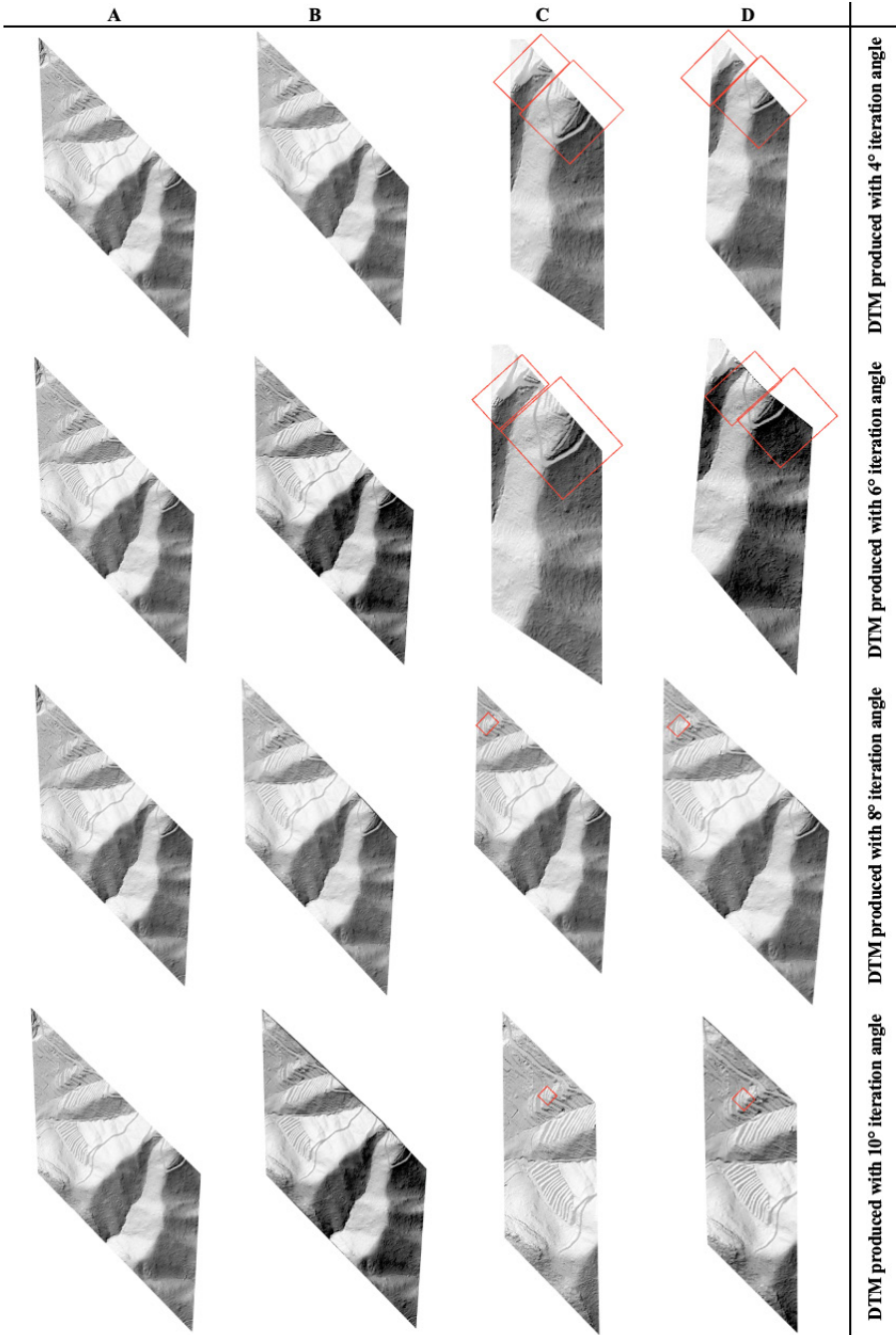
Figure 7. A-Reference DTM, **B-**DTM produced with iteration angle,
C-Filtered objects, **D-**Non-filtered objects.

3.3. Evaluation of the Filtering Results of the CSF and ATIN Algorithms

The accuracies of the digital terrain models created using different filtering algorithms were compared with the Digital Terrain Model with a horizontal accuracy of 5-10 cm and a vertical accuracy of 10 cm, and the root mean square error of the model was calculated from elevation differences. In Equation 1, Zi represents the elevation values in the model created while $\overline{Zi}$ represents the elevation values in the reference terrain model. The n value states the total number of points used in the assessment.

$$RMS_z = \sqrt{\frac{\sum_{i=1}^{n}(Z_i - \overline{Z}_i)^2}{n}} \tag{1}$$

When the results of the applications performed using the algorithms CSF and ATIN are evaluated, it is observed that the dense wooded areas located in the middle parts of the study area (except for CSF algorithm at a cloth resolution value of 2) were generally filtered effectively. However, when the filtering results for each parameter value are observed in detail using hillshade maps, it is observed that in certain regions of the study area, buildings are not filtered, tree groups are not removed, and flattening occurred in the terrain surface. When the application results are examined, it is observed that in the study area encompassing steep slopes, dense vegetation and buildings, a more accurate filtering process was performed and lower RMSE values were achieved using the ATIN algorithm. The effects of the filtering results can be seen in the regions marked in Figure 8. Tables 1 and 2 show the filtering results of the CSF and ATIN algorithms and their impact based on these regions.

Figure 8. Regions in the study area,
1) buildings **2)** tree groups **3)** ground surfaces

Table 1. CSF algorithm filtering results and their
impact on the regions shown in Figure 8

Cloth Resolution	Filtered Ground Points	RMSz (m)	Filtered Number of Buildings (1)	Filtered Trees (2)	Flattening on the Ground Surface (3)
0.2	5,529,470	± 0.47	1	Not filtered	No flattening
0.3	5,419,973	± 0.52	2	Not filtered	No flattening
0.4	5,328,275	± 0.44	4	Partially filtered	No flattening
0.5	5,218,743	± 0.34	4	Partially filtered	No flattening
1	4,152,422	± 0.68	6	Partially filtered	No flattening
2	1,368,301	±18.29	Faulty model	Faulty model	Faulty model

Table 2. ATIN algorithm filtering results and their impact on
the regions shown in Figure 8

Iteration Angle	Filtered Ground Points	RMSz (m)	Filtered Number of Buildings (1)	Filtered Trees (2)	Flattening on the Ground Surface (3)
4°	944.631	± 29.64	7	Filtered	No flattening
6°	1.154.848	± 1.52	7	Filtered	Partial flattening
8°	1.240.845	± 0.21	6	Filtered	No flattening
10°	1.294.566	± 0.20	6	Filtered	No flattening

4. Discussion

In the application initiated with 12.113.500-point data using the CSF algorithm, due to the fact that the study area consisted of densely-wooded and sloping regions, the terrain type was set as steep slope in the filtering parameters of the algorithm. In the values defined as advanced parameters, the filtering process was carried out using various cloth resolution values (0.2, 0.3, 0.4, 0.5, 1, 2) with a classification threshold of 0.5 and a max iteration value of 1000. The algorithm determined a number of ground points progressively decreasing with each cloth resolution value. When the terrain surface was examined for the filtering results on hillshade maps, it was observed that the terrain models created with cloth resolution values of 0.2, 0.3, 0.4, 0.5, and 1 demonstrated a good performance overall in regions with steep slopes and dense vegetation. However, they could not produce similar successful results in filtering the buildings located in the northwest of the study area and the tree group located at the head of a slope. The cloth resolution value of 0.2 involves the highest number

of ground points, although the model developed with this value was unable to filter any building located in the northwest of the study area. RMS value of the said model is ± 0.47 m. Following this, unlike the terrain model created with a cloth resolution value of 0.2, the model developed with a value of 0.3 filtered a building located in the northwest region but caused partial flattening in the steep slope located in the north of the area. RMS error value of the model produced with 0.3 cloth resolution was calculated as ± 0.52 m. The models created with the values 0.4 and 0.5 produced similar results and filtered a part of the buildings in the northwest. Although better results were observed in both values in terms of filtering the tree group located at the head of the slope, the models were unable to fully determine the ground characteristic. RMS error of the terrain models produced with cloth resolution values of 0.4 and 0.5 were calculated as ± 0.44 m. and ± 0.34 m, respectively. The DTM generated with a cloth resolution value of 1 produced the most successful results in filtering the buildings with the exception of one located in the northwest of the study area. However, the terrain structure in the south region could not be fully detected and flattening was observed in the surface. RMS error value of the model created with a cloth resolution value of 1 was calculated as ± 0.68 m. The terrain model produced with a cloth resolution value of 2 showed the worst performance compared to the other models. The steep slopes in the study area were excessively flattened and the natural structure of the terrain was disrupted. RMS error value of the model created with this value was calculated as ± 18.29 m. Overall, all values outside the cloth resolution of 2 produced good results in removing the dense vegetation located in the middle part of the study area. However, in filtering the buildings located in the northwest, a successful result could not be observed for any of the values. Among the values, the grid resolution value of 1 produced the best result in filtering the buildings. For filtering ground points using the ATIN algorithm, first, 4 main classes of points were prepared. With this classification, 12.113.500 non-processed points were first assigned to their assumed class. In order to detect the faulty points that could potentially be lower than the ground points, a class of low points was created while a class of underground points was created to detect the points that remain after the real ground surface following the ground classification. These classes were specified for a more accurate ground filtering and model production. The fixed values for the filtering parameters were set at a maximum building size value of 100, an iteration distance value of 1.40m, a maximum terrain angle value of 90° and iteration angles of 4° ,6° ,8°, and 10°, respectively, and the filtering operation was performed in order. At the

end of each filtering operation, non-ground points that can cause disruptions in the model were assigned to the low point class and separated from the ground points in the model creation phase. When the filtering results were examined, a different number of ground points was determined at each iteration value. It was observed that as the iteration angle value increased progressively, the number of ground points produced increased, as well. All of the values displayed food performance in the regions encompassing the densely vegetated regions with steep slopes, and successfully revealed the terrain characteristic. However, when the terrain models for which hillshade maps were created for a more detailed observation were examined, it was observed that the models created with iteration angle values of 4° and 6° filtered all buildings in the study area although they flattened the ground surface in the steep slope located in the northeast of the study area and were unable to fully detect the terrain surface. The flattening on the surface has a higher impact in the iteration angle value of 4°. Similar results are observed in the models created with iteration angle values of 8° and 10°. For these two values, there is a building in the area that could not be filtered. However, compared with the iteration angle values of 4° and 6°, the undetected and flattened terrain surface in the northeast of the study area produced the best results in the iteration angle values of 8° and 10°. The elevation accuracies of the models produced in RMS were calculated as ± 29.64 m for the iteration angle value of 4°, ± 1.52 for 6°, ± 0.21 m for 8° and ± 0.20 m for 10°. Based on these results, it was observed that the RMS value decreased as the iteration angle value increased, therefore producing better results in terms of both the visuals and accuracy. According to these evaluation results, in terms of the visuals and accuracy, it was concluded that the most suitable DTM for the current study area was produced in the ATIN filtering algorithm using iteration angle values of 8° and 10°.

5. Conclusions

In the present study, the performance of CSF and ATIN algorithms in filtering non-ground points on a rough terrain surface consisting of dense vegetation and steep slopes was tested with the aim of developing a DTM using raw airborne LiDAR data. The performance of both algorithms, which use different filtering techniques, in filtering ground points and producing DTM was examined. As a result of the filtering operation performed using the CSF algorithm within various value ranges, it was revealed that the cloth resolution parameter was effective in filtering ground points. As shown in application

results, as the cloth resolution value increases consecutively, the number of ground points filtered decreases, and a rough and faulty topography emerges. In order to determine more ground points in the steep and sloping terrains using the CSF algorithm and produce an accurate terrain model, it is necessary to use lower values in the cloth resolution parameter. As a result of the filtering process performed using the ATIN algorithm, it was revealed that the iteration angle value parameter was effective in filtering ground points. In the study area, where the maximum slope reaches up to 90°, it was found that more ground points are determined as the iteration angle value increases. For this reason, it is suggested to use higher iteration angle values in terrain types with high slope. As a result of the filtering operation and DTM production carried out using the ATIN and CSF algorithms with different parameters, it was observed that the models created using the ATIN algorithm had lower RMSE values and filtered more objects. However, when examined in detail, minor errors are found on the terrain surface. Therefore, objects that could not be removed even under the best circumstance are observed in the filtering results of both algorithms. This result revealed the necessity to also filter objects manually by making a detailed analysis of the terrain surface following the filtering process.

References

Ali, M. E. O., Taha, L., Mohamed, M. H. A., & Mandouh, A. A. (2021). Generation of digital terrain model from multispectral LiDar using different ground filtering techniques. *Egyptian Journal of Remote Sensing and Space Sciences, 24*(2), 181-189. doi:10.1016/j.ejrs.2020.12.004

Axelsson, P. (1999). Processing of laser scanner data—algorithms and applications. *ISPRS Journal of Photogrammetry and Remote Sensing, 54*(2), 138-147.

Axelsson, P. (2000). DEM Generation from laser scanner data using adaptive TIN models, . *International Archives of Photogrammetry and Remote Sensing, 33 (110-117).*

Cai, S. S., Zhang, W. M., Liang, X. L., Wan, P., Qi, J. B., Yu, S. S., . . . Shao, J. (2019). Filtering Airborne LiDAR Data Through Complementary Cloth Simulation and Progressive TIN Densification Filters. *Remote Sensing, 11*(9). doi:10.3390/rs11091037

Cateanu, M., & Ciubotaru, A. (2021). The Effect of LiDAR Sampling Density on DTM Accuracy for Areas with Heavy Forest Cover. *Forests, 12*(3). doi:10.3390/f12030265

Chen, C., Chang, B., Li, Y., & Shi, B. (2021). Filtering airborne LiDAR point clouds based on a scale-irrelevant and terrain-adaptive approach. *Measurement, 171,*108756. doi:10.1016/j.measurement.2020.108756

Chen, C., Guo, J., Wu, H., Li, Y., & Shi, B. (2021). Performance Comparison of Filtering Algorithms for High-Density Airborne LiDAR Point Clouds over Complex LandScapes. *Remote Sensing, 13*(14). doi:10.3390/rs13142663

Chen, C., Li, Y., Yan, C., Dai, H., Liu, G., & Guo, J. (2016). An improved multi-resolution hierarchical classification method based on robust segmentation for filtering ALS point clouds. *International Journal of Remote Sensing, 37*(4), 950-968. doi:10.1080/01431161.2016.1142687

Cheng, L., Tong, L. H., Wang, Y., & Li, M. C. (2014). Extraction of Urban Power Lines from Vehicle-Borne LiDAR Data. *Remote Sensing, 6*(4), 3302-3320. doi:10.3390/rs6043302

Cobby, D. M., Mason, D. C., Horritt, M. S., & Bates, P. D. (2003). Two-dimensional hydraulic flood modelling using a finite-element mesh decomposed according to vegetation and topographic features derived from airborne scanning laser altimetry. *Hydrological Processes, 17*(10), 1979-2000. doi:10.1002/hyp.1201

Cunningham, D., Grebby, S., Tansey, K., Gosar, A., & Kastelic, V. (2006). Application of airborne LiDAR to mapping seismogenic faults in forested mountainous terrain, southeastern Alps, Slovenia. *Geophysical Research Letters, 33*(20). doi:10.1029/2006gl027014

Doğruluk, M., Aydın, C. C., & Yanalak, M. (2018). Kırsal Alanlarda SYM Üretiminde Filtreleme Yöntemlerinin Performans Analizi: Hava LiDAR Uygulaması; İstanbul Örneği,. *Geomatik, 3(3), 242-253*.

Estornell, J., Hadas, E., Mart, J., & Lopez-Cortes, I. (2021). Tree extraction and estimation of walnut structure parameters using airborne LiDAR data. *International Journal of Applied Earth Observation and Geoinformation, 96*. doi:10.1016/j.jag.2020.102273

Guyot, A., Lennon, M., Thomas, N., Gueguen, S., Petit, T., Lorho, T., . . . Hubert-Moy, L. (2019). Airborne Hyperspectral Imaging for Submerged Archaeological Mapping in Shallow Water Environments. *Remote Sensing, 11*(19). doi:10.3390/rs11192237

Hancock, S., Anderson, K., Disney, M., & Gaston, K. J. (2017). Measurement of fine-spatial-resolution 3D vegetation structure with airborne waveform lidar: Calibration and validation with voxelised terrestrial lidar. *Remote Sensing of Environment, 188*, 37-50. doi:10.1016/j.rse.2016.10.041

Karasaka, L., & Keleş, S. H. (2020). CSF(Cloth simulation filtering) Algoritmasının Zemin Noktalarını Filtrelemedeki Performans Analizi. *Afyon Kocatepe Üniversitesi Fen ve Mühendislik Bilimleri Dergisi, 20(2), 267-275.*

Lang, T. S., Guild, R., Valenta, C. R., Carr, D., & Zutty, J. (2021, Apr 12-16). *Simulation and Optimization-based Method of Environmental Parameter Distribution from Airborne Bathymetric LiDAR Data.* Paper presented at the Conference on Laser Radar Technology and Applications XXVI, Electr Network.

Li, H., Ye, W., Liu, J., Tan, W., Pirasteh, S., Fatholahi, S. N., & Li, J. (2021). High-Resolution Terrain Modeling Using Airborne LiDAR Data with Transfer Learning. *Remote Sensing, 13*(17). doi:10.3390/rs13173448

Matikainen, L., Lehtomaki, M., Ahokas, E., Hyyppa, J., Karjalainen, M., Jaakkola, A., . . . Heinonen, T. (2016). Remote sensing methods for power line corridor surveys. *ISPRS Journal of Photogrammetry and Remote Sensing, 119*, 10-31. doi:10.1016/j.isprsjprs.2016.04.011

Meng, X., Currit, N., & Zhao, K. (2010). Ground filtering algorithms for airborne LiDAR data: A review of critical issues. *Remote Sensing, 2*(3), 833-860.

Meng, X. L., Wang, L., Silvan-Cardenas, J. L., & Currit, N. (2009). A multi-directional ground filtering algorithm for airborne LIDAR. *ISPRS Journal of Photogrammetry and Remote Sensing, 64*(1), 117-124. doi:10.1016/j.isprsjprs.2008.09.001

Meng, X. S., Lin, Y., Yan, L., Gao, X. L., Yao, Y. J., Wang, C., & Luo, S. Z. (2019). Airborne LiDAR Point Cloud Filtering by a Multilevel Adaptive Filter Based on Morphological Reconstruction and Thin Plate Spline Interpolation. *Electronics, 8*(10). doi:10.3390/electronics8101153

Paine, J. G., Collins, E. W., & Costard, L. (2018). Spatial Discrimination of Complex, Low-Relief Quaternary Siliciclastic Strata Using Airborne Lidar and Near-Surface Geophysics: An Example from the Texas Coastal Plain, USA. *Engineering, 4*(5), 676-684. doi: 10.1016/j.eng.2018.09.005

Pingel, T. J., Clarke, K. C., & McBride, W. A. (2013). An improved simple morphological filter for the terrain classification of airborne LIDAR data. *ISPRS Journal of Photogrammetry and Remote Sensing, 77*, 21-30. doi:10.1016/j.isprsjprs.2012.12.002

Popescu, S. C., Wynne, R. H., & Nelson, R. F. (2002). Estimating plot-level tree heights with lidar: local filtering with a canopy-height based variable window size. *Computers and Electronics in Agriculture, 37*(1-3), 71-95. doi:10.1016/s0168-1699(02)00121-7

Provot, X. (1995, May 17-19). *Deformation constraints in a mass-spring model to describe rigid cloth behavior.* Paper presented at the 1995 Conference on Graphics Interface (GI 95), Quebec City, Canada.

Sanchez, J. M., Alvarez, A. V., Vilarino, D. L., Rivera, F. F., Dominguez, J. C. C., & Pena, T. F. (2019). Fast Ground Filtering of Airborne LiDAR Data Based on Iterative Scan-Line Spline Interpolation. *Remote Sensing, 11*(19). doi:10.3390/rs11192256

Shaker, A., Yan, W. Y., & LaRocque, P. E. (2019). Automatic land-water classification using multispectral airborne LiDAR data for near-shore and river environments. *ISPRS Journal of Photogrammetry and Remote Sensing, 152*, 94-108. doi:10.1016/j.isprsjprs.2019.04.005

Soycan, M., Tunalıoğlu, N., Öcalan, T., Soycan, A., & Gümüş, K. (2011). Three Dimensional Modeling of a Forested Area Using an Airborne Light Detection and Ranging Method. *Arabian Journal for Science and Engineering, 36*(4), 581-595. doi:10.1007/s13369-011-0054-8

Stumpf, A., Malet, J. P., Allemand, P., Pierrot-Deseilligny, M., & Skupinski, G. (2015). Ground-based multi-view photogrammetry for the monitoring of landslide deformation and erosion. *Geomorphology, 231*, 130-145. doi:10.1016/j.geomorph.2014.10.039

Susaki, J. (2012). Adaptive Slope Filtering of Airborne LiDAR Data in Urban Areas for Digital Terrain Model (DTM) Generation. *Remote Sensing, 4*(6), 1804-1819. doi:10.3390/rs4061804

Thuestad, A. E., Risbol, O., Kleppe, J. I., Barlindhaug, S., & Myrvoll, E. R. (2021). Archaeological Surveying of Subarctic and Arctic Landscapes: Comparing the Performance of Airborne Laser Scanning and Remote Sensing Image Data. *Sustainability, 13*(4). doi:10.3390/su13041917

Trier, Ø. D., Reksten, J. H., & Løseth, K. (2021). Automated mapping of cultural heritage in Norway from airborne lidar data using faster R-CNN.

International Journal of Applied Earth Observation and Geoinformation, 95, 102241. doi:10.1016/j.jag.2020.102241

Tulldahl, H. M., Vahlberg, C., Axelsson, A., Karlsson, H., & Jonsson, P. (2007, Sep 17-19). *Sea floor classification from airborne lidar data.* Paper presented at the Conference on Lidar Technologies, Techniques, and Measurements for Atmospheric Remote Sensing III, Florence, ITALY.

Varlik, A., & Uray, F. (2021). Filtering airborne LIDAR data by using fully convolutional networks. *Survey Review*, 1-11. doi:10.1080/00396265.2021.1996798

Vosselman, G. (2000). Slope based filtering of laser altimetry data. *International archives of photogrammetry remote sensing, 33*(B3/2; PART 3), 935-942.

Vosselman, G., Coenen, M., & Rottensteiner, F. (2017). Contextual segment-based classification of airborne laser scanner data. *ISPRS Journal of Photogrammetry and Remote Sensing, 128*, 354-371. doi:10.1016/j.isprsjprs.2017.03.010

Yastikli, N., & Cetin, Z. (2017, Oct 14-15). *AUTOMATIC 3D BUILDING MODEL GENERATIONS WITH AIRBORNE LiDAR DATA.* Paper presented at the 4th International Workshop on Geoinformation Science / 4th ISPRS International Workshop on Multi-Dimensional and Multi-Scale Spatial Data Modeling (GeoAdvances), Karabuk Univ, Safranbolu Campus, Safranbolu, TURKEY.

Yu, H. Y., Lu, X. P., Ge, X. S., & Cheng, G. (2010, Jun 18-20). *Digital Terrain Model Extraction from Airborne LiDAR Data in Complex Mining Area.* Paper presented at the 18th International Conference on Geoinformatics, Peking Univ, Beijing, PEOPLES R CHINA.

Zhang, K. Q., Chen, S. C., Whitman, D., Shyu, M. L., Yan, J. H., & Zhang, C. C. (2003). A progressive morphological filter for removing nonground measurements from airborne LIDAR data. *Ieee Transactions on Geoscience and Remote Sensing, 41*(4), 872-882. doi:10.1109/tgrs.2003.810682

Zhang, W. M., Qi, J. B., Wan, P., Wang, H. T., Xie, D. H., Wang, X. Y., & Yan, G. J. (2016). An Easy-to-Use Airborne LiDAR Data Filtering Method Based on Cloth Simulation. *Remote Sensing, 8*(6). doi:10.3390/rs8060501

A NEW SCHIFF BASE: SYNTHESIS AND CHARACTERIZATION

Halime Güzin ASLAN[1]& Zülbiye KÖKBUDAK[2]

[1]*(Assoc. Prof. Dr.), Erciyes University, Faculty of Science*
E-mail: guzina@erciyes.edu.tr
ORCID: 0000-0002-2759-6583

[2]*(Prof. Dr.), Erciyes University, Faculty of Science*
E-mail: zulbiye@erciyes.edu.tr
ORCID: 0000-0003-2413-9595

1. Introduction

Pyrimidine contains nitrogen atom in the ring. It is found in uracil, thymine and cytosine. Derivatives of this ring play an important role in chemistry, biological and pharmacological activities such as anti-Alzheimer (Elmegeed et al., 2015), antimalarial (Manohar et al., 2015), Antioxidant (Cui et al., 2022), anticancer (Abbas et al., 2021), anticonvulsant (Wang et al., 2012), anti-depressant (Wang et al., 2012), anti-mycobacterial (Ballell et al., 2007), anti-HIV (Boyer et al., 2018), anti-inflammatory (Alfayomy et al., 2021), antihistaminic (Kaspersen et al., 2012), anti-Parkinson (Al-Harbi et al., 2013) (Figure 1). Therefore, the synthesis of these compounds has been accelerated in the last two decades.

Aminopyrimidine derivatives are frequently synthesized in organic chemistry. Various reactions of aminopyrimidine derivatives synthesized by us have been studied before (Önal & Yıldırım, 2007; Önal & Altural, 1999; Önal & Altural, 2006; Önal & Daylan, 2007; Aslan & Onal, 2013; Aslan et al., 2020; Aslan & Aydin, 2021). In addition to their catalytic and corrosion effects, their biological properties such as anticancer were studied (Karataş et al., 2022; Kokbudak et al., 2022; Kokbudak et al., 2020; Kokbudak et al., 2020;

Ferigita et al., 2023). Some pyrimidine derivatives with biological activity and medicinal importance given in figure 1.
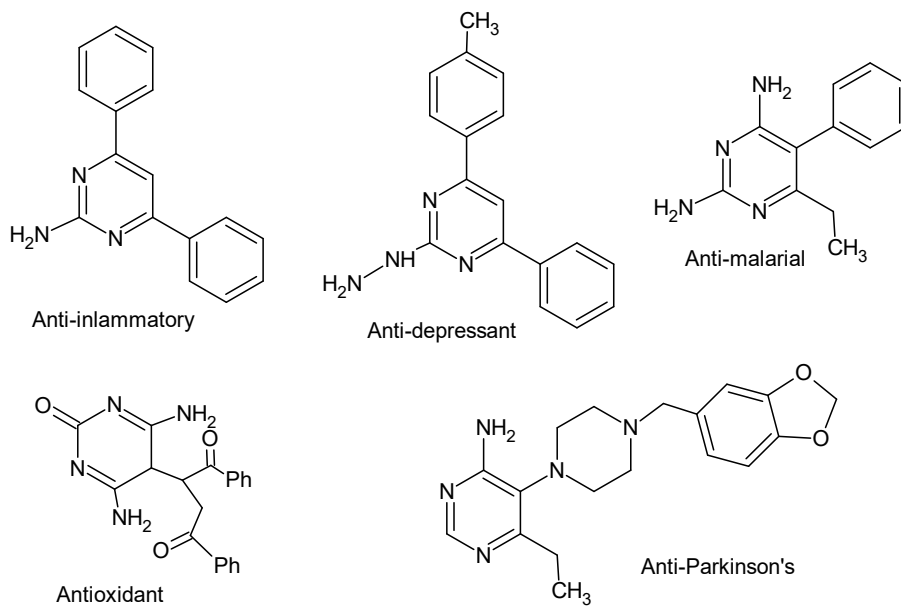
Figure 1. The pyrimidine derivatives with biological activity and medicinal importance

Schiff bases are versatile compounds. It is a group of compounds characterized by the presence of double bonds connecting carbon and nitrogen atoms. Such compounds, which are commonly found in nature, are also widely synthesized in the laboratory. Schiff bases are also widely used for industrial purposes as compounds containing pyrimidine rings. (Ceramella et al., 2022). Since Schiff bases are widely synthesized, they have been the subject of many studies. Many data on biological activity, anticancer activity, antioxidant and DNA binding activity are obtained in studies (Ceramella et al., 2022; Kargar et al., 2022; Kilic et al., 2022).

This short review provides an overview of the synthetic methods used for the preparation of Schiff bases and includes the synthesis and characterization of Schiff bases containing a new pyrimidine ring.

Compound **(Z1)**, synthesized in our previous studies (Aslan & Onal, 2013; Aslan et al., 2020; Aslan & Aydin, 2021) is shown in Figure 2.
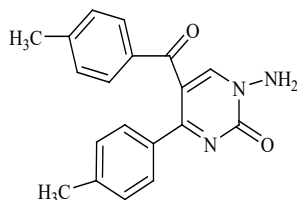
Figure 2. Compound **(Z1)**

From the reaction of compound **(Z1)** with ortho vanillin, the compound **(G1)** (Z)-1-(2-hydroxy-3-methoxybenzylideneamino)-5-(4-methylbenzoyl)-4-*p*-tolylpyrimidin-2(1*H*)-one was obtained.
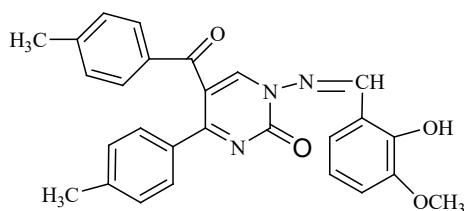
Figure 3. Compound **(G1)**

2. Experimental

The new schiff base was obtained by the synthesis steps we followed in our previous studies (Aslan & Onal, 2013; Aslan et al., 2020; Aslan & Aydin, 2021) Melting point device (Electrothermal 9100), DC AlufolienKieselgel 60 F254 (Merck) and TLC lamp (254/366 nm), FT-IR spectrophotometer, Bruker 400 MHz NMR device were used during the characterization of the material. Analyzes were carried out at Erciyes University Technology Research and Application Center.

2.1. Synthesis of Schiff Bases

Color: yellow; yield: 51%; m.p.: 187 °C. IR (cm^{-1}) ν(CH)$_{aro}$: 2919, ν(C-N): 1570, ν(C-OH): 1261, ^{1}H NMR (400 MHz, DMSO-d$_6$, ppm) δ: 10.06 (s, 2H, -OH), 9.43 (s, 2H, -CH), 8.63 (s, 2H, -CH$_{pyr}$), 7.78-6.89 (m, 24H, ArH), 2.50, 2.34 and 2.28 (s, 12H, -CH$_3$). ^{13}C NMR (100 MHz, DMSO-d$_6$, ppm) δ: 191.71, 170.60, 164.03, 151.68, 148.91, 144.70, 144.54, 141.23, 134.77, 134.53, 130.43, 129.74, 129.33, 129.19, 119.55, 118.73, 116.21, 116,04, 56.48, 21.63 and 21.37.

3. Results and Discussion

We comparatively examined the spectroscopic data of the compound **(Z1)** synthesized in our previous studies and the new compound **(G1)**. When the IR spectrum of compound **(Z1)** is examined; The split peak at 3307-3240 cm^{-1} shows NH$_2$, the peak around 3010 cm^{-1} shows aromatic C-H stretching vibrations, and the peaks at 2981 cm^{-1} show C-H stretching vibrations in methyl groups. The peaks at 1670-1643 cm^{-1} belong to the C=O groups. The peaks between 906-773 cm^{-1} in the fingerprint region of the spectrum belong to the skeleton vibration of the pyrimidine ring in the molecule. In the FT-IR spectrum of compound **(G1)**, it was observed that the –NH$_2$ stretching vibration disappeared due to the formation of the imine bond and a strong stretching vibration peak appeared at 1600 cm^{-1} due to the formation of the C=N bond. When Table 1 is examined, small shifts are observed in all stretching vibrations of the molecule.

Table 1. Significant IR Stretching Vibrations of Synthesized Compounds.

	v(NH$_2$)	v(CH)$_{aro}$	v(CH)$_{CH3}$	v(C=O)	v(C-N)	v(pyr)	v(C=N)
(Z1) cm^{-1}	3307-3240	3010	2981	1670-1643	1560	906-773	-
(G1) cm^{-1}	-	2919	3000	1693-1638	1570	903-772	1600
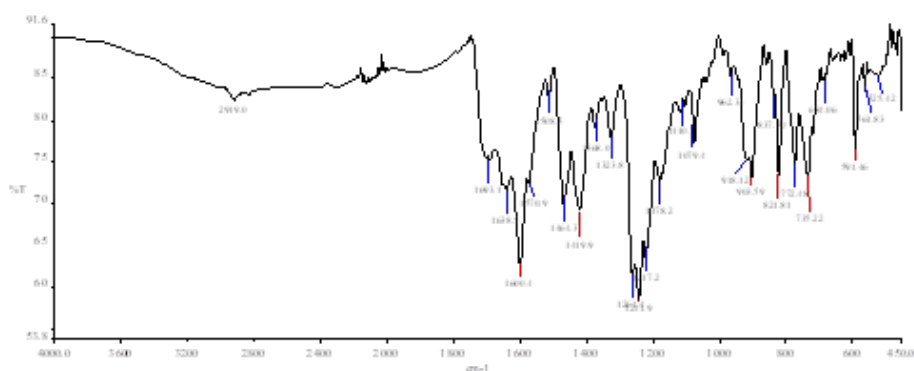
Figure 4. Compound **(G1)** FT-IR spectra
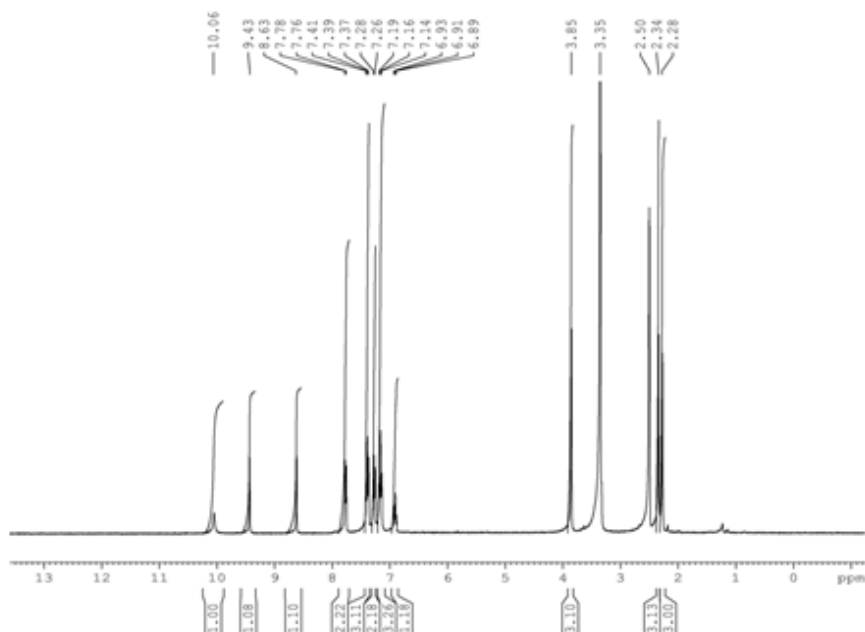
Figure 5. Compound **(G1)** ¹H NMR spectra

The peaks belonging to the 12 aromatic ring protons, 2 -CH_3, 1 -OCH_3, and 1 OH groups of compound **(G1)** were detected as a result of the evaluation of the ¹H NMR spectrum. Additionally, peaks belonging to 27 carbon atoms were marked in the ¹³C NMR spectrum. As a result of the evaluation of FT-IR and NMR spectra, it is understood that compound **(G1)** was obtained in pure form. A synthesis mechanism for the new compound formed is suggested in **Figure 6.**

In Schiff base synthesis, the oxygen in the aldehyde group acquires a partial positive charge by capturing a hydrogen. Free electron pairs in the amine nitrogen attack this oxygen. An intermediate situation occurs. In the next step, the water is separated from the environment and the characteristic C=N bond is formed. The compound obtained according to the given reaction scheme. The purity of the obtained compound was checked by TLC method. It was crystallized twice with ethanol. The results of the spectroscopic examinations are given collectively. The results obtained show that the compound was obtained in the expected structure.
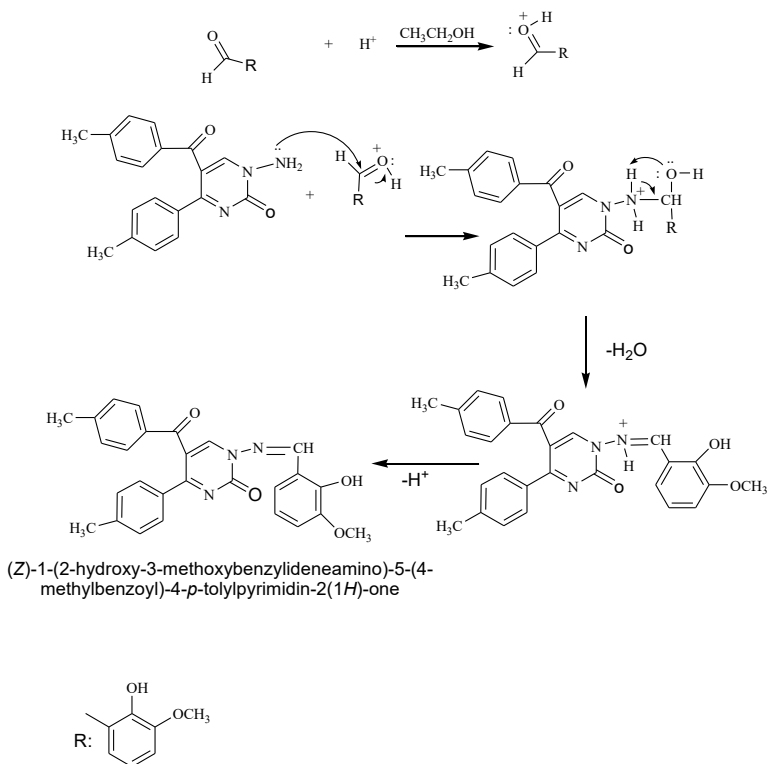
Figure 6. Proposed synthesis mechanism for compound **(G1)**

4. Conclusions

As a result of these studies, the pyrimidine derivative **(G1)** compound was synthesized based on **(Z1).** Experimental techniques were extensively used to determine the structures of the novel compound **(G1).** When the new Schiff base obtained is examined, it is seen that there are atoms containing free electron pairs on the compound. The compound can easily form a complex through these ends. In the second step of our study, it is planned to synthesize new complexes and use these compounds in drug research.

References

Abbas, N., Matada, G. S. P., Dhiwar, P. S., Patel, S., & Devasahayam, G. (2021). Fused and Substituted Pyrimidine Derivatives as Profound Anti-Cancer Agents. *Anti-Cancer Agents in Medicinal Chemistry*, 21(7), 861-893. doi:10.2174/1871520620666200721104431

Alfayomy, A. M., Abdel-Aziz, S. A., Marzouk, A. A., Shaykoon, M. S. A., Narumi, A., Konno, H., & Ragab, F. A. F. (2021). Design and synthesis of pyrimidine-5-carbonitrile hybrids as COX-2 inhibitors: Anti-inflammatory activity, ulcerogenic liability, histopathological and docking studies. *Bioorganic Chemistry*, 108. doi:ARTN 104555 10.1016/j.bioorg.2020.104555

Al-Harbi, N.O., Bahashwan, S.A., Fayed, A.A., Aboonq, M.S., & Amr, A.E.E. (2013). Anti-parkinsonism, hypoglycemic and antimicrobial activities of new poly fused ring heterocyclic candidates. *Int J Biol Macromol*, 57,165–73.

Aslan, G., & Onal, Z. (2013) Novel metal complexes, their spectrophotometric and QSAR studies. *Medicinal Chemistry Research,* 23(5), 2596–2607.

Aslan, H. G., Akkoc, S., & Kokbudak, Z. (2020). Anticancer activities of various new metal complexes prepared from a Schiff base on A549 cell line. *Inorganic Chemistry Communications*, 111. doi:ARTN 107645 10.1016/j.inoche.2019.107645

Aslan, H. G., & Aydin, L. (2021). Synthesis, Characterization and Theoretical Studies of N'-(4-methoxybenzylidene)benzenesulfonohydrazide, *J.Chem.Soc.Pak.*, 43(02), 212.

Ballell, L., Field, R. A., Chung, G. A. C., & Young, R. J. (2007). New thiopyrazolo[3,4-d]pyrimidine derivatives as anti-mycobacterial agents. *Bioorganic & Medicinal Chemistry Letters*, 17(6), 1736-1740. doi:10.1016/j.bmcl.2006.12.066

Boyer, P. L., Smith, S. J., Zhao, X. Z., Das, K., Gruber, K., Arnold, E., & Hughes, S. H. (2018). Developing and evaluating inhibitors against the RNase H active site of HIV-1 reverse transcriptase. *Journal of virology*, 92(13), e02203-02217.

Ceramella, J., Iacopetta, D., Catalano, A., Cirillo, F., Lappano, R., & Sinicropi, M. S. (2022). A Review on the Antimicrobial Activity of Schiff Bases: Data Collection and Recent Studies, *Antibiotics,* 11(2), 191; https://doi.org/10.3390/antibiotics11020191

Cui, J. M., Ji, X., Mi, Y. Q., Miao, Q., Dong, F., Tan, W. Q., & Guo, Z. Y. (2022). Antimicrobial and Antioxidant Activities of N-2-Hydroxypropyltrimethyl Ammonium Chitosan Derivatives Bearing Amino Acid Schiff Bases. *Marine Drugs*, 20(2). doi:ARTN 86 10.3390/md20020086

Elmegeed, G.A., Ahmed, H.H., Hashash, M.A., Abd-Elhalim, M.M., &Elkady, D.S. (2015). Synthesis of novel steroidal curcumin derivatives as

anti-Alzheimer's disease candidates: evidences-based on in vivo study. *Steroids*, 101, 78–89.

Ferigita, K. S. M., Saracoglu, M., AlFalah, M. G. K., Yilmazer, M. I. Kokbudak, Z., Kaya, S., & Kandemirli, F. (2023). Corrosion Inhibition of Mild Steel in Acidic Media Using New Oxo-Pyrimidine Derivatives: Experimental and Theoretical Insights, *Journal of Molecular Structure*, 135361, https://doi.org/10.1016/j.molstruc.2023.135361.

Karataş, H., Tüzün, B., & Kökbudak, Z. (2022). Could pyrimidine derivative be effective against Omicron of SARS-CoV-2? *Bratislava Medical Journal-Bratislavske Lekarske Listy*, 123(7).

Kargar, H., Ashfaq, M., Mehrjardi, M. F., Ardakani, R. B., Munawar, K. S., Tahir, M. N. (2022). Unsymmetrical Ni(II) Schiff base complex: Synthesis, spectral characterization, crystal structure analysis, Hirshfeld surface investigation, theoretical studies, and antibacterial activity, *Journal of Molecular Structure*, 1265 (5), 133381, https://doi.org/10.1016/j.molstruc..133381

Kaspersen, S.J., Sundby, E., Charnock, C., & Hoff, B.H. (2012). Activity of 6-arylpyrrolo[2,3-d]pyrimidine-4-amines to Tetrahymena. *Bioorg Chem*, 44, 35–41.

Kilic, A., Söylemez, R., Okumuş, V., (2022). Design, spectroscopic properties and effects of novel catechol spiroborates derived from Schiff bases in the antioxidant, antibacterial and DNA binding activity, *Journal of Organometallic Chemistry*, 960, 15 122228, https://doi.org/10.1016/j.jorganchem.2021.122228.

Kokbudak, Z., Akkoc, S., Karatas, H., Tuzun, B., & Aslan, G. (2022). In Silico and In Vitro Antiproliferative Activity Assessment of New Schiff Bases. *Chemistryselect*, 7(3). doi: ARTN e202103679 10.1002/slct.202103679

Kokbudak, Z., Aslan, H. G., & Akkoc, S. (2020). New Schiff Bases Based on 1-Aminopyrimidin-2-(1h)-One: Design, Synthesis, Characterization and Theoretical Calculations. *Heterocycles*, 100(3), 440-449. doi:10.3987/Com-20-14221

Kokbudak, Z., Saracoglu, M., Akkoc, S., Cimen, Z., Yilmazer, M. I., & Kandemirli, F. (2020). Synthesis, cytotoxic activity and quantum chemical calculations of new 7-thioxopyrazolo[1,5-f]pyrimidin-2-one derivatives. *Journal of Molecular Structure*, 1202. doi:ARTN 127261 10.1016/j.molstruc.2019.127261

Manohar, S., Pavan, V.S., Taylor, D., Kumar, D., Ponnan, P., Wiesner, L., & Rawat, D.S., (2015). Highly active 4-aminoquinoline-pyrimidine

based molecular hybrids as potential next generation antimalarial agents. *Rsc Advances*, 5(36), 28171-28186.

Önal, Z. & Yıldırım, İ. (2007). Reactions of 4-(4-Methylbenzoyl)-5-(4-methylphenyl)-2,3-furandione with Semi-/thiosemi-carbazones, *Heterocyclic Communications*, 13(2-3), 113-120. doi:doi:10.1515/HC.2007.13.2-3.113

Önal, Z., & Altural, B. (1999). Reactions of N-aminopyrimidine derivatives with 1, 3-dicarbonyl compounds. *Turkish Journal of Chemistry*, 23(4), 401-406.

Önal, Z., & Altural, B. (2006). Reactions of 1-amino-5-benzoyl-4-phenyl-1H-pyrimidine-2-thione with various carboxylic anhydrides. *Asian Journal of Chemistry*, 18(2).

Önal, Z., & Daylan, A. (2007). Reactions of 1-Amino-5-benzoyl-4-phenyl-1H-pyrimidine derivatives with various isothiocyanates. *Asian Journal of Chemistry*, 19(4).

Wang, S., Deng, X., Zheng, Y., Yuan, Y., Quan, Z., & Guan, L. (2012). Synthesis and evaluation of anticonvulsant and antidepressant activities of 5-alkoxy tetrazolo[1,5-c]thieno[2,3-e]pyrimidine derivatives. *European Journal of Medicinal Chemistry*, 56, 139-44.

RECENT TRENDS IN XEROGEL BASED NANOCOMPOSITES FOR SUPERCAPACITOR APPLICATIONS

Satiye KORKMAZ

(Assoc. Prof.), Karabük University,
E-mail: satiyekorkmaz@karabuk.edu.tr
ORCID: 0000-0002-7592-3366

1. Introduction

Porous materials synthesized after the development of various chemical production methods have potential applications in many fields, especially in energy storage (Datt, Ndiege and Larsen, 2012:239). They are classified into aerogel, xerogel and cryogel (hydrogel) according to their production methods. Aerogels attract attention with their unique properties, such as low density, refractive index, and small pore size; they have been used in the space industry for years, but new applications in various fields have recently been discovered (Bheekhun, Talib, Rahim and Hassan, 2013:406065). The aerogels' porosity, specific surface area, density and thermal conductivity can be controlled by the preparation strategy (Araby, Qiu, Wang, Zhao, Wang and Ma, 2016:9157; Pierre, 2011:3). Aerogels were first made from silica-based materials and can now be based on polymers, carbons, metals or metal oxides. Aerogels were first discovered by Samuel S. Kistler in 1931, who demonstrated that it is possible to remove the liquid from the gel under supercritical drying conditions (Gurav, Jung, Park, Kang and Nadargi, 2010: 409310). Later, in the 1960s, Teichner and Nicolaon succeeded in producing aerogels within hours using the sol-gel method (Teichner, Nicolaon, Vicarini and Gardes, 1976:245; Tamon, Sone, Mikami and Okazaki, 1997:493). Doping nanomaterials such as carbon, metal/metal oxide, and polymer to aerogels have increased their applications in energy storage, and aerogel-based composites are expected to play an essential role in future studies (Zuo, Zhang, Zhang, Miao, Fan and Liu,

2015:6806; Liu et all. 2015:154; Benad, Jürries, Vetter, Klemmed, Hübner and Leyens, 2018:145). Aerogels can also be thought of as foams of various shapes and sizes with much air between them. They contain very little solid matter and have a unique structure comprising about 99.8 % of air. The pores are large and in the micrometer range, and the significant gaps between the contacts give the aerogel lightness and a compact structure. In addition, aerogels have low thermal conductivity, can be transparent, opaque or colored, and can be functionalized by chemical reactions and physical storage techniques.

2. Aerogels and Xerogels

2.1. Structure and Properties

The word xerogel comes from the Greek root "Xero," meaning dry, and is a dry gel produced by the evaporation of a porous liquid under ambient conditions (Tüysüz and Schüth, 2012:127). They are glass-like materials with tiny pore sizes, high porosity, large surface area, and high mechanical and chemical stability. Xerogel's structure drastically changes during drying because of the immense stresses applied during evaporation and freezing. The sol-gel method used for preparing xerogels requires water and ethyl alcohol along with various metal alkoxide precursors. The remarkable properties of xerogels and aerogels come from the sol-gel method's flexibility, which can be combined with different drying methods. Their structure and morphology can be easily controlled during synthesis and drying (Tüysüz and Schüth, 2012:127).
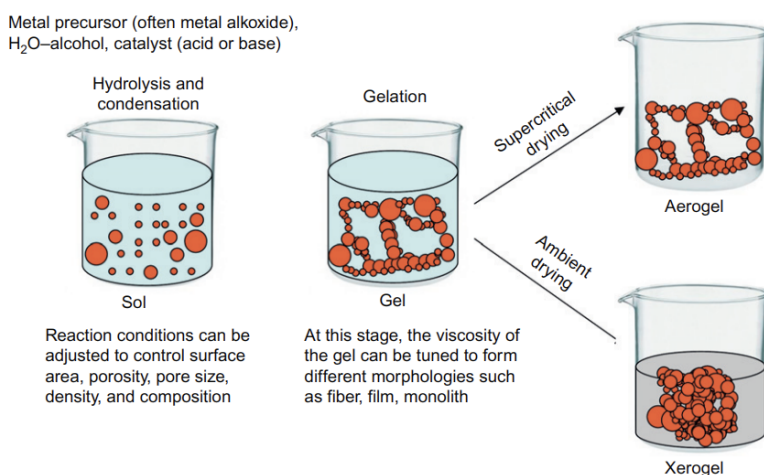
Fig. 1. Schematic illustration of the steps in preparing aerogels and xerogels
(Tüysüz and Schüth, 2012:127)

Inorganic gels' pore diameter is in the mesopore or micropore range, and they have a high surface area of about 1500 to 2000 m^2/g. About half of the atoms in the gel are on the surface; therefore, surface reactions can lead to significant changes in the gel's composition. The main difference between aerogels and xerogels is pore size and density. The size and shape of the pores can be controlled by using surfactants.

Measuring and predicting pore size is complicated because the drying of xerogel films begins before gelation. For bulk gel, the amount of shrinkage is determined by the network's pressure and modulus. However, the pressure gradient does not affect the stresses that cause cracking. The resulting stresses are independent of the drying speed; cracking for inorganic films occurs when the thickness exceeds the critical value of 1μm. This is because the strain energy stored in a certain volume surrounding the crack is released, which is used to create a new surface. No crack will form if the film is thin enough, no matter how much stress is applied. Thick films formed by depositing multiple layers must be roasted before depositing the next layer to increase their strength (Buschow, Flemings, Merton and Cahn, 2001). They exhibit optical properties such as transparency to visible light and high refractive indices. They can form covalent bonds by adhering to substrates such as glass and silica.

2.2. Applications and Challenge

Aerogels have emerged as an innovative material, arousing researchers' interest in recent years. Aerogels, which have attracted attention in areas such as filters, batteries, solar heat protection, automotive thermal insulation, and the textile industry, show high potential for supercapacitors with their ultra-porous structure and fuel cells, especially with their carbon-based derivatives. Porous xerogel films are used as membranes, while dense xerogel films are used in corrosion and abrasion protection. Xerogel films have long been used in optical coatings, i.e., reflective or antireflective films. They are of great interest in this field (Buschow, Flemings, Merton and Cahn, 2001). Xerogel powders with high surface area are used for catalyst substrates. They also have an important place in the electronics industry with their active use in sensors, batteries, and supercapacitors in recent years. On the other hand, research suggests that more efforts are needed to reduce the cost of aerogel production. Furthermore, an essential limitation of aerogel production is using autoclaves and supercritical fluid drying techniques, which are avoided while producing xerogels. Some aerogels have higher mechanical stability than their counterparts; however, their brittleness is a significant drawback for applications requiring mechanical

handling. Adding an active sorbent to the matrix to improve mechanical stability reduces capacity (Riley and Chong, 2020:2070101).

3. Supercapacitor Applications of Xerogel

Xerogels have attracted researchers' attention in recent years, as they have become an attractive material for supercapacitors due to the tunability of their structural properties by changing the conditions during the synthesis and processing of the materials. Fernandez et al. prepared chemically activated carbon xerogels to analyze the electrochemical behavior of carbon xerogels in supercapacitors and correlate the results with physicochemical parameters (Ferna'ndez, Arenillas, Calvo, Mene'ndez and Martins 2012:10249). As a result of electrochemical measurements performed to compare the charge storage capacities at different scan rates, they concluded that the significant carbon differences between the electrodes should be maintained by using larger discharge currents. The maximum specific capacitance for the produced supercapacitor electrodes was 284 F/g. The theoretical model developed for porous electrodes allowed them to obtain parameters that could explain electrodes' different behavior. In addition, the values researchers obtained using the BET method were compared with the capacitances obtained from EIS experiments.

NiO, which has attracted considerable attention in recent years due to its low cost, low toxicity, and environmentally friendly properties, has greatly interested researchers. Studies have shown that NiO materials are promising for supercapacitors (Liu and Anderson, 1996:124; Srinivasan and Weidner, 1997:210). The surface area of NiO, whose highest specific capacitance is 278 F/g, should be increased to improve its charge storage properties. The sol-gel method provides the materials with a high surface area and promotes the formation of a porous structure, accelerating the charge transfer. Taking advantage of the sol-gel, Cheng et al. also performed a heat treatment on the prepared NiOx xerogels (Cheng, Cao and Yang, 2006:734). Figure 2a (i) shows its effect on NiOx xerogels' specific surface area and pore volume. The specific surface area decreased when the temperature was increased from 200 to 300°C, reaching a maximum surface area of 285 m^2/g. The pore volume first increased with the temperature increase, remained constant between 280-400°C, and then decreased. This shift in surface area is a variation of the micropores of NiOx xerogels; the mesopore structure, on the other hand, remains almost constant regarding pore size distribution. The electrodes obtained from the prepared NiOx xerogels were characterized by the CV method, and their electrochemical

performances are shown in Figure 2a (ii). An increase was observed in the specific capacitance by increasing the heat treatment temperature from 110°C to 250°C. They obtained a current density of 2.0 mA/cm2 and a maximum specific capacitance of 696 F/g for NiO_x xerogels heat-treated at 250°C.

The literature review showed that better specific capacitance results could be obtained by increasing the BET surface area, considering that the surface area should be accessible to the electrolyte. In addition, parameters such as pore size, ion size, and pore size distribution also contribute to specific capacitance (Salitra, Soffer, Eliad, Cohen and Aurbach, 2000:2486; Kotz and Carlen, 2000:2483). For this reason, researchers have focused on developing substantial surface areas with pore sizes that can hold the largest amount of electrolyte and provide the fastest kinetic adsorption-desorption mechanism. Activated carbons with high BET surface area cause a decrease in specific capacitance with the increasing scan rate resulting from the slow kinetic mechanism due to the heterogeneous pore size distribution and the specific capacitance they exhibit at low scan rates. On the other hand, carbon nanomaterials such as CNT, graphene, etc., show high energy density but cannot achieve high specific capacitance. Resinol and formaldehyde-based carbon materials such as carbon aerogels, cryogels, and xerogels offer higher potential than activated carbons due to their low electrical conductivity but have a limited power density and energy capacity like other porous carbons (Rey-Raap, Angel Menendez and Arenillas, 2014:490). Regarding modifying carbon xerogels, capacitive properties can be improved through parameters such as pH, temperature, gelation time, dilution factor, drying conditions, and doping boron, nitrogen, and sulfur (Macías, Haro, Parra, Rasines and Ania, 2013:487; Zhou, Candelaria, Liu, Huang, Uchaker and CaO, 2014:8472). Another option is graphene oxide (GO), which is a good alternative for preparing carbon composite materials and has functional groups that facilitate dispersion in aqueous media. Fernandez et al. prepared GO-xerogel composites with specific electrical conductivity and porosity to produce carbon materials with stable capacitances at high rates (Ramos-Fernandez, Canal-Rodríguez, Arenillas, Angel Menendez, Rodríguez-Pastor and Martin-Gullon, 2018:456). They analyzed the results corresponding to 1 mV/s-500 mV/s CV and galvanostatic charge-discharge cycles for GO-xerogel composites prepared at three different GO concentrations. GO/Xerogel composites result in low electrochemical performance and low electrical conductivity. Thus, the best performance was obtained at the lowest concentration of GO, less than 2%. Higher ratios were reported to cause a decrease in energy and power densities.

Electrochemical measurements showed a specific capacitance of 120 F/g and power densities above 30 kW/kg at a very high scan rate of 500 mV/s. Figure 2b. shows the specific capacitance curve as a function of current density for carbonized carbon xerogel containing different amounts of GO and Ragone Plot. According to these values, GO/xerogel composites' specific capacitances, ranging from 135 to 160 F/g, are significantly higher than those of undoped carbon xerogels. In addition, Canal-Rodríguez et al. produced carbon xerogel hybrid electrodes for supercapacitors by designing a fast and economical process with different graphene percentages (3%, 9%) (Canal-Rodríguez, Angel Menendez and Arenillas, 2018:28) Graphene was doped to the structure to prevent the xerogel from collapsing during drying, and the electrical conductivity increased linearly with the amount of doped graphene. The xerogel electrodes produced by doping 3% and 9% graphene showed a 321% and 135% electrical conductivity increase, respectively, compared to pure xerogel electrodes. The 9% doping rate exhibited better power density, pore size, and electrical conductivity, while no change was observed in capacitance values. The Ragone plot obtained from the energy and power densities of materials with increasing GO content, calculated at current densities of 0.1, 0.2 and 0.5 A/g, is shown in Figure 2b (ii). Regarding the energy and power densities for the samples with different amounts of GO and without GO, the performance is almost two times higher than that of pure xerogels. In particular, the significant difference in power densities is due to the large differences in ESR, which is lower in the doped xerogels than in the pure sample. Moreover, although the ESR seems to play a more significant role than the BET's specific surface area, this parameter depends significantly on the electrical conductivity and impacts the power density of supercapacitors (Ling et all. 2014:14329).

Adding a conductive structure such as CNT or graphene into porous carbon is necessary to achieve higher electrical conductivity and a high specific surface area for supercapacitors made of carbon materials (Xia et all. 2016:1793; Meng, Zhang, Xu, Yue, Guo and Luo, 2011:18537; Markovic et all. 2012:743; Liu, Yang and Meng, 2013:1; Ling et all. 2014:14329; Chen, Song and Fan, 2015:92; Zhu et all. 2011:1537). On the other hand, it is not easy to obtain such a structure. Some researchers failed to achieve the desired performance for the supercapacitors they produced with GO-doped porous carbon due to insufficient pore volume or high doping amount (Xia et all. 2016:1793; Meng, Zhang, Xu, Yue, Guo and Luo, 2011:18537; Liu, Yang and Meng, 2013:1). Rodríguez et al. achieved the desired porous structure for carbon xerogels by using GO

suspension alone as a solvent (Canal-Rodríguez, Arenillas, Rey-Raap, Ramos-Fernandez, Martín-Gullon and Angel Menendez, 2017:291). GO doping was reported to increase the porous structure compared to undoped carbon xerogels. For xerogels, 2% GO doping was reported to cause the lowest capacitance drop and the highest capacitance when operated at 98 F/g at 16 A/g.

Transition metal oxides have been extensively studied for supercapacitors, but they are too expensive to be commercially attractive. In particular, amorphous aqueous V_2O_5 exhibits very high specific capacitance (Liu, Yu, Neff, Zhamu and Jang, 2010:4863). V_2O_5 xerogels have high charge storage capacities, but the lack of high electrical conductivity and low charge/discharge ratio limit their electrode applications (Wee, Soh, Cheah, Mhaisalkar and Srinivasan, 2010:6720; Wei, Scherer, Bower, Andrew, Ryhänen and Steiner, 2012:1857; Kudo et all. 2002:833). Therefore, activated carbon and carbon nanotubes have been used to improve the performance of V_2O_5 xerogels (Chen et all. 2011:791). Composite electrodes with high specific capacitance and superior cycling stability can be obtained by combining graphene's superior properties with metal oxides (Zhou, Wang, Yin, Li, Li and Cheng, 2012:3214; Wang et all. 2009:907; Wu et all. 2010:3187). Xu et al. synthesized graphene/V_2O_5 xerogel nanocomposites by hydrothermal method. The variation of the specific surface areas of V_2O_5 and Graphene/ V_2O_5 xerogels was examined by BET analyses. The surface areas of V_2O_5 and Graphene/V_2O_5 xerogels were reported to be 3.9996 and 7.6528 m^2/g, respectively. They obtained two times higher specific surface area than V2O5 xerogels, reporting that the electrical conductivity was also significantly improved (Xu et all. 2014:234). Figure 2c clearly shows CV curves of graphene/V_2O_5 xerogels nanocomposites and V_2O_5 xerogels; initial charge–discharge curves of V_2O_5 xerogels and graphene/V2O5 xerogels nanocomposites, specific capacitance versus discharge current density. In Figure 2c (i), the CV curves of the electrodes formed a rectangular curve at a scan rate of 10 mV/s, with the peaks attributed to surface redox reactions. Galvanostatic charge-discharge curves of graphene/V_2O_5 and V_2O_5 xerogels electrodes at current densities between 1 A/g and 10 A/g are shown in Figure 2c (ii and iii). The charge-discharge curves for both electrodes are comparable to those of redox and EDCL. Figure 2c (iv) shows that the specific capacitance of graphene-doped electrodes is higher because graphene increases the electronic conductivity. They reported specific capacitances of 195.4 and 184.6 F/g for electrodes whose electrochemical performance was tested at different current densities (1 A/g and 10 A/g).

Commercial supercapacitors are typically produced using activated carbon, but the electrolyte may sometimes negatively affect conductivity. The solution is mixing activated carbons with a conductive additive or binder to improve their conductivity. Canal-Rodríguez et al. proposed two approaches for producing supercapacitor electrodes: doping a conductive additive to the active material by physical mixing and doping a conductive additive while synthesizing the active material's precursor (Canal-Rodríguez, Menéndez, Montes-Morán and Arenillas, 2019:45) The supercapacitor performances of carbon xerogel, carbon black, or graphene added during and after synthesis were investigated, reporting that the sample doped with GO during the synthesis of organic gel showed the best performance with a specific capacitance of 98 F/g at 16 A/g. So, adding GO to carbon xerogel during synthesis seems the right way to prepare supercapacitor electrodes with superior performance and stability. In a study conducted by the same researcher with a different group, different hybrid activated carbon xerogels containing micronized graphite, GO, and carbon black were synthesized. They reported that although all hybrid electrodes exhibited high conductivity, GO doping outperformed pure activated carbon xerogels, and the highest capacitance value was 130 F/g (Canal-Rodríguez, Menendez, Montes-Moran, Martín-Gullon, Parra and Arenillas, 2019:693). The lowest performance was observed in micronized graphite-doped activated carbon xerogels.

d.
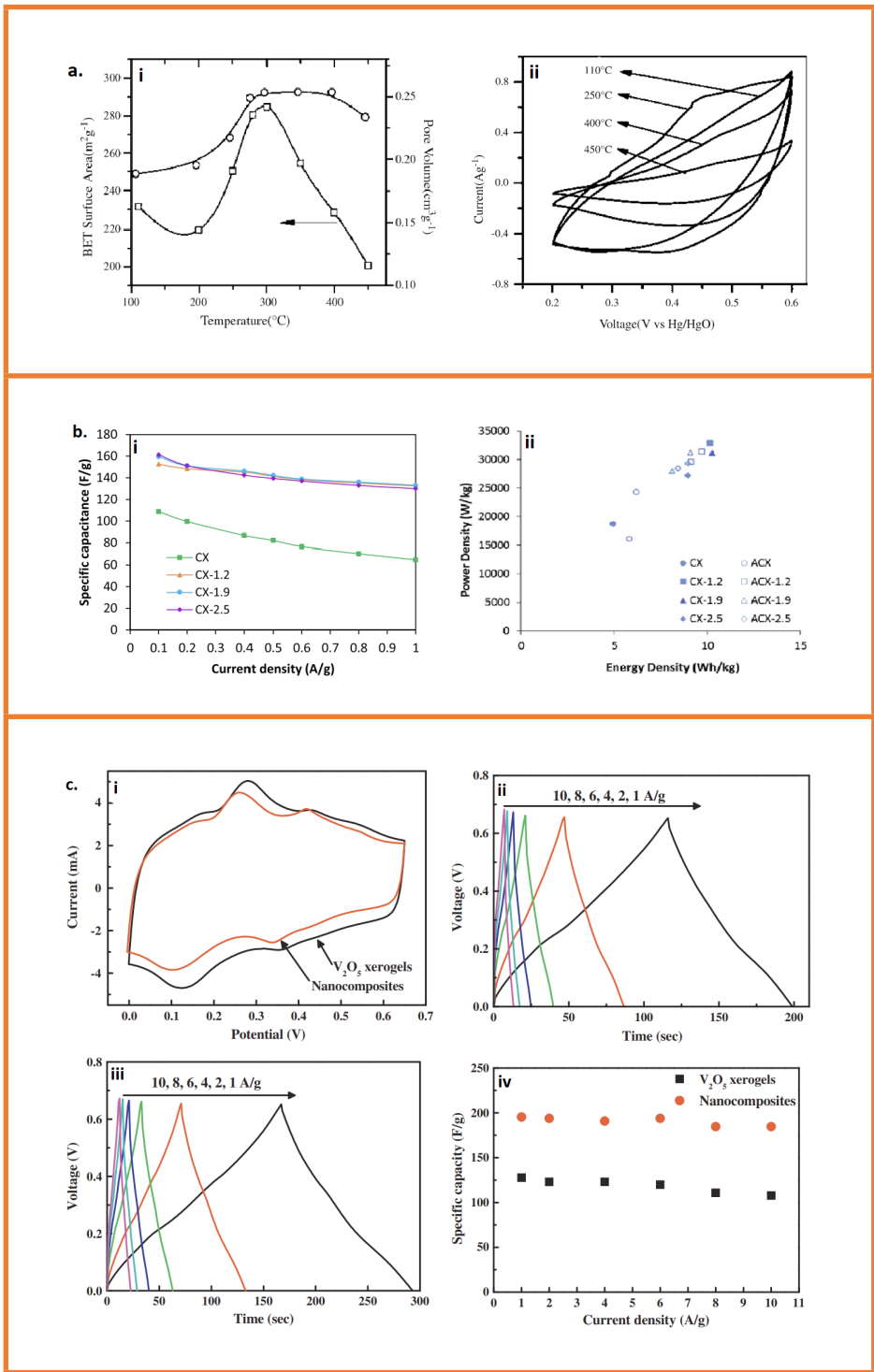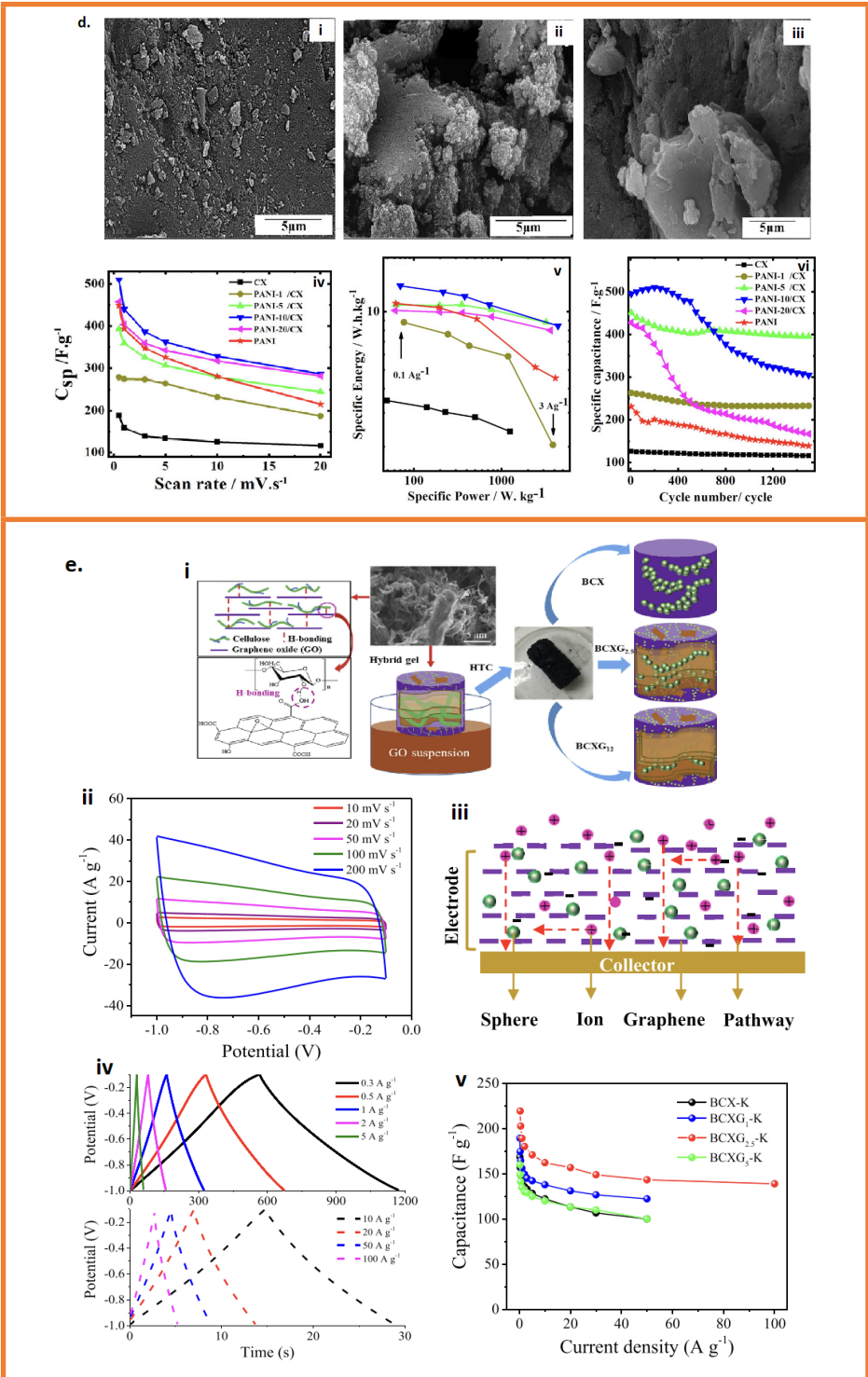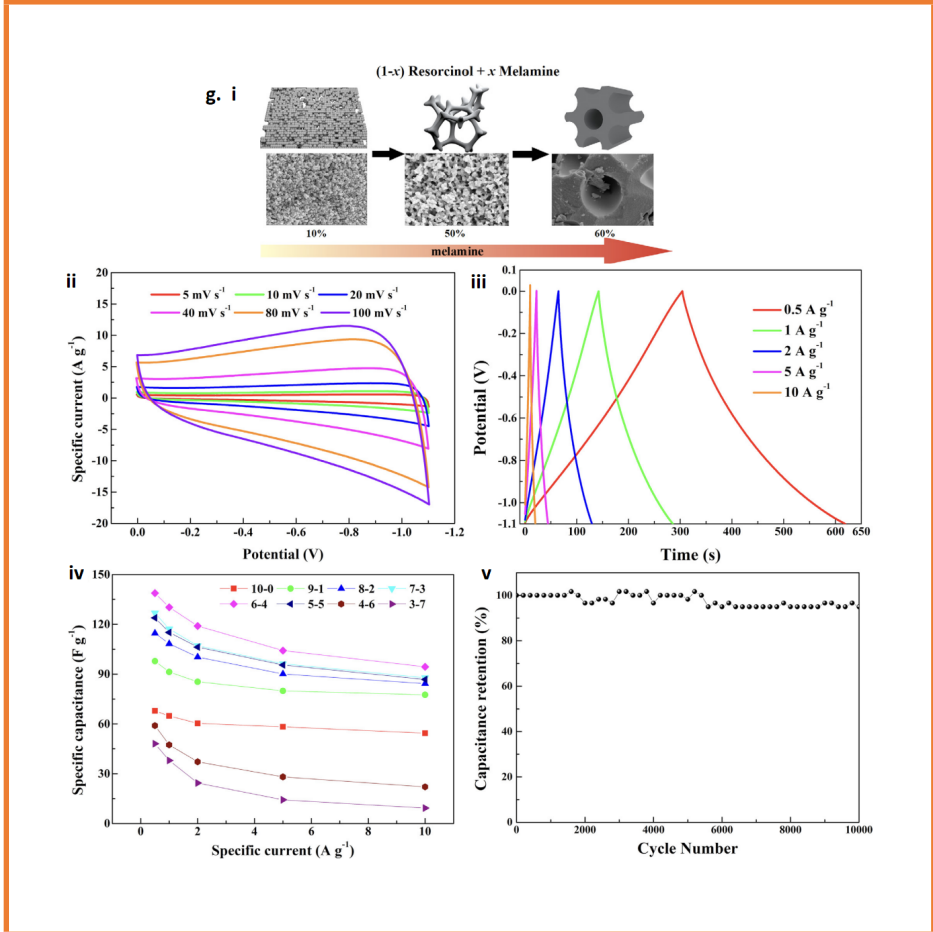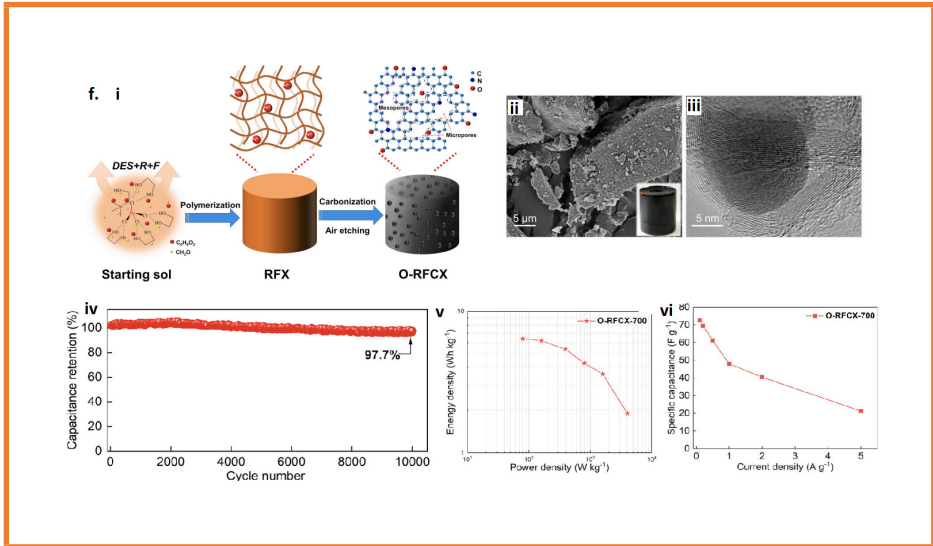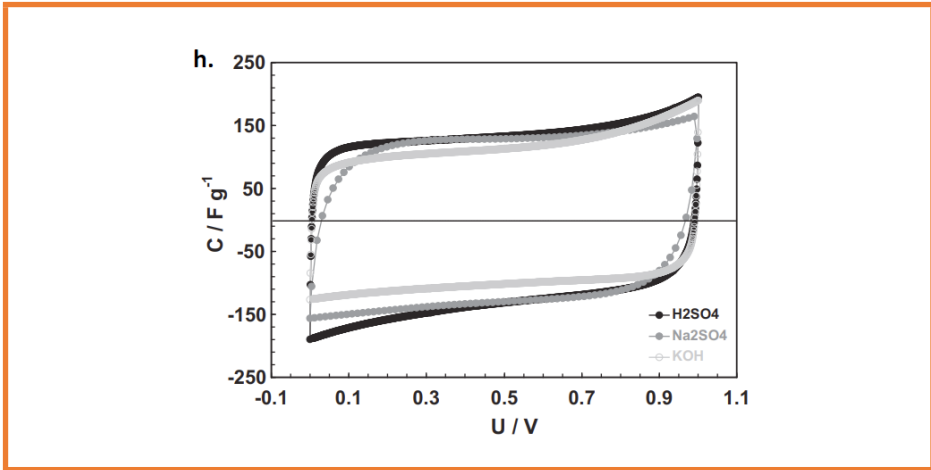
Fig.2. a) BET surface area (i), CV curves of the NiOx xerogels (ii), (Cheng, Cao and Yang, 2006:734), **b)** Specific capacitance of carbonized carbon xerogel with different amount of GO (i) and Ragone plot (ii) (Ramos-Fernandez, Canal-Rodríguez, Arenillas, Angel Menendez, Rodríguez-Pastor and Martin-Gullon, 2018:456), **c)** CV curves of graphene/V_2O_5 xerogels nanocomposites and V_2O_5 xerogels (i), initial charge–discharge curves of V_2O_5 xerogels and graphene/V_2O_5 xerogels nanocomposites respectivtely (ii and iii), specific capacitance versus discharge current density (iv) (Xu et all. 2014:234) **d)** SEM images of CX (i), PANI (ii) and PANI-5/CX (iii) composite, Specific capacitance as a function of scan rates (iv), ragone plots (v) and cycle life stability curves (vi) (Khammar, Abdelwahab, Abdel-Samad and Hassan, 2021:114848), **e)** Graphene functionalized carbon xerogel (i), CV curves at various scan rates (ii), the schematic diagram for ions' transfer pathways (iii), GCD curves at current densities (iv), specific capacitances versus current densities for different (v) (Yang, Jiang, Fei, Ma and Liu, 2018:813), **f)** Microporous graphitized carbon xerogel (i), SEM image of the carbon xerogel (ii), HRTEM image before acid etching (iii), cycling stability for 10,000 cycles (iv), Ragone plots in aqueous electrolyte (v), Rate performance (vi) (Chen et all. 2022:108781), **g)** The effect of melamine on the formation of carbon xerogel (i), CV curves at different scan rates (ii), Galvanostatic charge-discharge curve at different specific current density (iii), capacitances as a function of current densities (iv) and cycle live (v) (Lu, Huang, Hong, Wu, Li and Cheng, 2018:209), **h)** Cyclic voltammograms three electrolytes with a different pH (H_2SO_4, Na_2SO_4 and KOH) (Calvo, Lufrano, Staiti, Brigandì, Arenillas and Menéndez, 2013:776).

Recent studies have reported that polymeric structures containing GO nanosheets are more steady. It promotes the growth of carbon xerogels by hydrothermal means and promotes the reaction of other organic precursors (Martín-Jimeno, Suarez-García, Paredes, Martínez-Alonso and Tascon, 2015:137; Liu, Yang and Meng, 2013:1). Enterría et al. prepared activated carbon xerogels from a glucose/GO mixture by hydrothermal carbonization (HTC), a process promoting condensation and polymerization of saccharides in the solution. They evaluated their supercapacitor performance (Enterría et all. 2016:474). They reported that the nanomorphology significantly affects the supercapacitor performance after the measurements in a three-electrode cell using 1 M H_2SO_4 to determine the electrochemical behavior of the xerogels. Using low amounts of KOH during activation provides thin porous carbon walls that support electronic conduction and ionic diffusion; however, high amounts have been reported to degrade xerogels' electrochemical performance. Carbon xerogels with thinner carbon walls and high graphitic character exhibited a specific capacitance of 153 F/g vs. 223 at 100 mA/g.

PEO-PPO-PEO (polyethylene oxide-polypropylene oxide-polyethylene oxide) copolymers were combined with resorcinol formaldehyde for pore formation in carbon aerogels. The oxidative destruction of the oxygen-rich copolymers during carbonization provides independent pore formation in parallel with the formation of porous carbon derived from resorcinol formaldehyde. Liu et al. produced nitrogen-doped carbon xerogel electrodes for supercapacitors to study nitrogen doping and pore formation (Liu et all. 2015:32). First, they reported that nitrogen atoms significantly improved the electrochemical performance of resorcinol formaldehyde, and the decomposition of PEO-PPO-PEO micelles formed microchannels for electrolyte ions during carbonization. The researchers succeeded in producing a large number of micropores for supercapacitor electrodes by using the CO_2-assisted activation method to increase porosity. An ultra-high surface area of 4279 m^2/g and a specific capacitance of 271 F/g were obtained for the resulting electrodes. The study is important in providing a low-cost and practical preparation process and improving the conductivity and porosity of activated carbon.

Among conducting polymers, polyaniline and PANI are widely used in producing supercapacitor electrodes. PANI has especially come to the forefront in energy storage with its high-temperature resistance, flexibility, high electrochemical activity, and ability to be produced in various nanostructures (Lu, Chen, Zhou, Tong and Li, 2015:14843; Reddy, Lee and Gopalan, 2008:49;

Wang, Lin and Shen, 2016:225). The high conjugation of π electrons, which enables charge transfer along the molecular structure chains, plays an essential role in PANI's conductivity. However, it can lead to the deterioration of capacitance in the long run, especially during charge/discharge. Therefore, composites have been prepared with different carbon materials to increase PANI's stability and conductivity. Khammar et al. aimed to investigate the effect of PANI on the porosity and electrochemical performance of the structure and produced PANI/carbon xerogel composites with different mass ratios for supercapacitor electrodes (Khammar, Abdelwahab, Abdel-Samad and Hassan, 2021:114848()). The SEM analysis of the samples prepared by the researchers is shown in Figure 2d (i, ii and iii). In Figure 2d (i), the amorphous and compact structure of the carbon network indicates the successful synthesis of xerogels. The surface morphology shown in Figure 2d (ii) indicates the correct synthesis of pure PANI, characterized by the polymer chains' tight packing and the particles' isometric shape. This is important because it allows to enhance conductivity through the easy transfer of charge carriers over the polymer chains. The results of PANI/carbon xerogels composites in Figure 2d (iii) confirm the extent of PANI chains in xerogels. After getting CV measurements, the effect of scan rate on the CV behavior for different electrodes was investigated, and the results are shown in Figure 2d (iv). For the electrodes, the specific capacitance decreased with increasing scan rate, and the maximum specific capacitance was reported to increase with the amount of added PANI. The Ragone plot obtained from the calculated energy and power densities of the samples is shown in Figure 2d (v). The highest value of specific energy depends on the high specific capacitance obtained. The study reported that having PANI in the carbon xerogel structure increased the pore diameter and decreased the surface area, and the capacitance increased from 156 F/g to 612 F/g.

In recent years, porous carbons derived from renewable resources such as corn stover and cotton have attracted great interest as supercapacitor electrodes due to their low cost, easy processability, and high specific capacitance and cycling capabilities. Such biomass carbons can be synthesized by pyrolysis, which requires high energy, or by the simple, controllable, low-energy HTC method. However, the HTC process generates a large amount of reactive oxygen groups in carbonaceous materials. Conductive carbon materials, such as carbon nanofibers, CNTs, or graphene, can be doped into carbons to solve this problem. Some studies have reported that the possibility of graphene re-stacking during the synthesis of electrode materials leads to a decrease in the specific capacitance by reducing the surface area (Stoller, Park, Zhu, An and Ruoff, 2008:3498;

Luan et all. 2013:208). Cellulose, one of the biopolymer materials, transforms into a structure rich in hydroxyl groups when it interacts with GO. These structures have recently been reported to be good candidates for supercapacitor electrodes (Stoller, Park, Zhu, An and Ruoff, 2008:3498; Luan et all. 2013:208). Yang et al. produced low-cost and low-energy electrode materials with better electrochemical performance using hydrothermal carbonization combined with graphene modification instead of prolific biocarbon (Figure 2e (i)) [79]. Figure 2e (ii) shows that the initial rectangular CV curves are maintained at the 200 mV/s scan rate. The low resistance and diffusion of electrolyte ions through the hierarchical pores are explained in Figure 2e (iii). This result confirms that the interconnected porous network facilitates the transport of electrons and ions, which is in line with the CV measurements. The charge-discharge curves shown in Figure 2e (iv) indicate that the electrodes exhibit superior capacitive behavior with a linear and symmetrical high-speed capacity at current densities ranging from 0.3 to 100 A/g. The specific capacitances of the samples prepared with different GO weight ratios corresponding to different current densities are shown in Figure 2e (v). The produced supercapacitor was reported to exhibit a specific capacitance of 139 F/g at a high current of 100 A/g in an aqueous electrolyte and retain 100% of the initial capacitance, power density, and energy density after 10000 cycles at 5 A/g.

Since hydroxy benzenes used in the synthesis of gels are expensive and bound to fatty chains, natural precursors such as lignin are of interest to researchers because of their abundant availability and low cost. The raw material for xerogel production is obtained by acid precipitation of black liquor from sugarcane bagasse. By synthesizing carbon gels from lignin, the researchers could obtain specific areas as high as 780 m^2/g and specific capacitances as high as 254 F/g (Qu et all. 2010:8402; Xu, Zhou, Chen, Shi and Cao, 2018:258; Xu et all. 2015:3193; Perez-Cantu, Liebner and Smirnova, 2014:303; Chen, Xu, Wang and Li, 2011:1262; Grishechko, Amaral-Labat, Szczurek, Fierro, Kuznetsov and Celzard, 2013:19; Li et all. 2016:151; Yu, Chang and Wang, 2016:187; Jeon et all. 2015:428; Saha et all. 2014:900; Chang, Yu and Wang, 2016:1405; Salinas-Torres et all. 2016:641; Zhang, Zhao, Liu, Wang and Lin, 2015:518). Castro et al. prepared lignin-activated carbon xerogels at different Lignin/Lignin+Resolsinol mass ratios by synthesizing them from black liquor by sol-gel method (Castro, Teresa Izquierdo, Diossa, Zapata-Benabithe and Quintana, 2021:106296). A specific capacitance of 149.5 F/g was obtained from the xerogels with the highest mass ratio. The capacitance obtained is attributed to the increased lignin content promoting porosity.

There are several methods for inserting metals in the carbon matrix, including adding the dissolved metal precursor to the resorcinol mixture, creating a binding site for metal ions in resorcinol that can be polymerized using sol-gel, allowing dispersion of metal ions, and impregnation with metal salt and deposition of metal precursors on carbon gel by pyrolysis (Lee et all. 2010:947). Metal additives such as Fe, Co, Ni, Cu, Mn, Ag, Ti, Pd, Ru, and Pt have been investigated for carbon aerogels. Some of the electrochemical characterizations have been performed (Moreno-Castilla, Maldonado-Hodar, Rivera-Utrilla and Rodríguez-Castellon, 1999:345; Maldonado-Hódar, Moreno-Castilla, Rivera-Utrilla, Hanzawa and Yamada, 2000:4367; Baumann, Fox, Sachter, Yosizawa, Fu and Dresselhaus, 2002:7073; Cotet et all. 2007:434; Fu, Baumann, Cronin, Dresselhaus, Dresselhaus and Satcher, 2005:2647; Carrott, Marques and Riberio Carrott, 2010:75; Saha and Deng, 2009:12550; Cotet et all. 2006:2772; Job, Pirard, Marien and Pirard, 2004:3217; Moreno-Castilla, Moldonado-Hódar and Pérez-Cadenas, 2003:5650; Job, Maillard, Marie, Berthon-Fabry, Pirard and Chatenet, 2009:6591). To study the effect of metal doping in xerogels, Skowronski et al. investigated the physicochemical properties of Ni-doped carbon xerogels prepared by sol-gel polymerization (Skowronski and Osinska, 2012:911). They reported an increase in the surface area of the produced metal-doped carbon xerogels resulting from modifying the porous structure. As a result of the analysis of electrochemical performances by cyclic voltammetry and galvanostatic charge-discharge methods, the specific capacitances for 35% Ni-doped carbon xerogels were found to be 92 F/g and 120 F/g, respectively. The results show a higher specific capacitance than undoped carbon xerogels.

Since melamine has a very high nitrogen content, it can form organic gels with formaldehyde using a mechanism similar to resorcinol. Some studies have been done on synthesizing nitrogen-doped carbon materials with melamine and resorcinol-formaldehyde. Lu et al. prepared nitrogen-doped carbon xerogels derived from resorcinol melamine-formaldehyde by sol-gel. They reported that increasing the amount of melamine widened the channels and provided faster ion transport (Lu, Huang, Hong, Wu, Li and Cheng, 2018:209). Regarding the morphology of the samples, small particles and pores were observed in the samples without melamine; the particle sizes and pore sizes were reported to increase with increasing melamine content (Figure 2g (i)). For the samples with a 3D network structure, the channel diameter and the channel wall were in the micron range and expanded with the addition of melamine. As shown in the CV curves in Figure 2g (ii), at scan rates ranging from 5 mV/s to 100 mV/s, the CV curve also widens as the scan rate increases, maintaining its nearly rectangular

shape. The GCD curves at different current densities maintained a triangular shape for all current densities, indicating an excellent coulombic efficiency (Figure 2g (iii)). The specific capacitances of the samples at different current densities are shown in Figure 2g (iv), and all samples exhibited high specific capacitance. The decrease in capacitive stability with increasing melamine in the starting material is explained by the decrease in conductivity caused by the defects. Figure 2g (v) shows that almost 95% of the capacitance can be maintained after 10000 charge/discharge cycles, demonstrating superior cycling performance. Increasing the nitrogen ratio results in more defects in the structure, which leads to a deterioration of the rate performance. The highest performance researchers reported for specific capacitance was 139 F/g for the electrode with a resorcinol/melamine ratio of 6/4.

An ideal electrode material should have sufficient pores for fast ion transport and storage. Some studies have suggested using graphene or silicon as a template during metal ion-catalyzed synthesis to obtain such a structure (Wang, Lu, Yu, Xu, Zheng and Yu, 2015:2397; Mishra, Yadav and Verma, 2017:987; Yin, Zhang, Alhebshi, Salah and Alshareef, 2020:1900853; Shao, Wu, Lin, Taberna and Simon, 2020:3005). On the other hand, there are problems, such as silicon's irritating and toxic effect in the practical production process and the cost of graphene. Chen et al. used an iron-based eutectic solvent to polymerize resorcinol with formaldehyde (Figure 2f (i)) in the method developed to synthesize organic xerogels quickly and easily (Chen et all. 2022:108781). As shown in Figure 2f (ii), the aging process resulted in an organic gel that can be converted into dense monolithic carbon xerogel after carbonization. During the carbonization process, the iron embedded in the polymer matrix acted as a catalyst, promoting the formation of graphite crystal structures (Figure 2f (iii)). Figure 2f (iv) shows the electrodes exhibited superior cycle stability of 97.7% after 10000 discharge cycles. The Ragone plot in Figure 2f (v) determined the relationship between energy and power densities. A maximum power density of 79.4 kW/kg and an energy density of 6.4 Wh/kg were obtained for the supercapacitors. These results were reported to be high enough to be comparable to aqueous electrolytes. The gelation process was shortened with $Fe^{+3,}$ and a porous carbon xerogel with amorphous and graphitic properties can be obtained by pyrolysis. A specific capacitance of 209 F/g was obtained at a current density of 0.5 A/g for the xerogel with a high specific surface area of 587 m2/g and abundant surface oxygen functional groups (Figure 2f (vi)). The study is noteworthy for developing a method for rapidly preparing xerogels.

Reducing CO_2 emissions is vital for sustainable energy sources, and absorption techniques must be developed. Porous carbon materials are the next-generation CO_2 adsorbents with easy preparation, good adsorption properties, and environmentally friendly characteristics (Bae and Snurr, 2011:11586). This CO2 adsorbent has attracted attention, especially in producing energy storage devices, with its high specific surface area and porosity properties and super micro/meso porosity at high pressure (Casco, Martínez-Escandell, Silvestre-Albero and Rodríguez-Reinoso, 2014:230; Sevilla, Sangchoom, Balahmar, Fuertes and Mokaya, 2016:4710; Srinivas, Krungleviciute, Guo and Yildirim, 2014:335). Regarding various methods proposed so far to prepare microporous carbon materials, the hard template approach is a complex and time-consuming method, although it can be used to prepare many different materials (To et all. 2016:1001; Shi et all. 2015:335; Luo et all. 2016:255). On the other hand, the soft template method is simple and does not require complex equipment. Wang et al. used the soft template method to prepare porous carbon xerogels, obtaining materials with advanced micropores and a high specific area (963.3 m^2/g) (Wang, Miao, Liu, Zhang and Liu, 2021:126285). Electrochemical characterization for the prepared supercapacitor electrodes showed a specific capacity of 161 F/g at a current density of 1 A/g in 6 M KOH electrolyte and 99.4% efficiency after 1000 cycles.
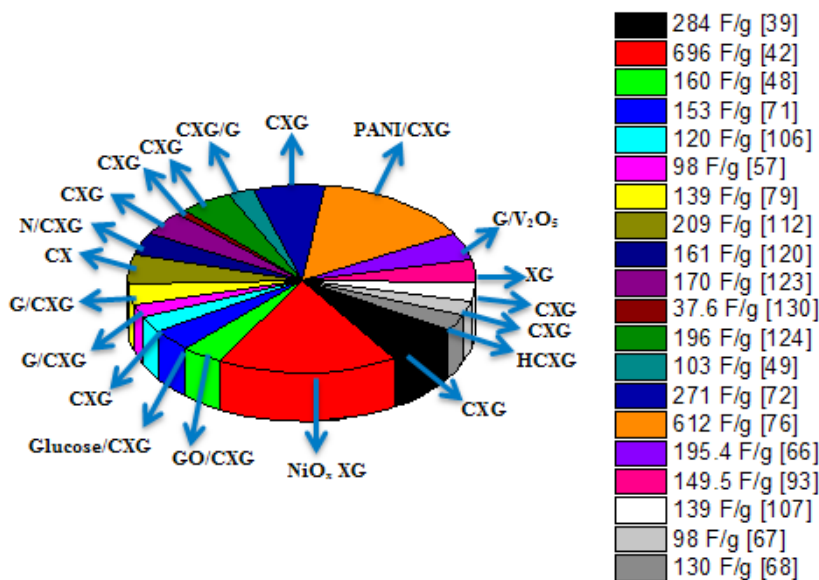
Fig.3. Comparison of the performances of xerogel-based supercapacitors.

The lengthy synthesis processes of carbon gels, which can be prepared without any binder and have attracted attention in energy applications due to their three-dimensional nanostructure, porous texture, and high electrical conductivity, have been solved using microwave technology (Calvo, Ania, Zubizarreta, Menéndez and Arenillas, 2010:3334; Calvo, Juárez-Pérez, Menéndez and Arenillas, 2011:541). Another essential property sought for supercapacitor electrodes is porosity. This problem can be overcome by changing the activation parameters in the chemical activation process to increase the microporosity of carbon xerogels. Calvo et al. aimed to produce different porous materials by varying the activation temperature and time of carbon xerogels to investigate the effect of porosity on supercapacitors' electrochemical performance (Calvo, Ferrera-Lorenzo, Menéndez and Arenillas, 2013:206). In addition, microwave heating, which has been used as an activation method in recent years, offers the advantages of significant energy savings and short process times. The researchers produced resorcinol-formaldehyde xerogels at different activation temperatures (500, 600, and 700 C) by microwave heating in 6-30 min intervals. The most suitable temperature for supercapacitor electrodes with a high surface area was 700 C. Electrochemical analysis showed a specific capacitance of 170 F/g. The highest energy storage performance was observed for the xerogel electrode activated for 6 min. The same researchers evaluated the supercapacitor electrodes according to size and electrode type. They found that cells with larger electrodes stored higher amounts of energy (Calvo, Lufrano, Staiti, Brigandì, Arenillas and Menéndez, 2013:776). On the other hand, regarding the electrochemical performances of aqueous electrolytes with different pH values (H_2SO_4, Na_2SO_4, and KOH, 1 M), the highest specific capacitance value was achieved in sulfuric acid with 196 F/g (Figure 2h). However, Na_2SO_4 has been reported to be the most suitable electrolyte for carbon xerogels due to the corrosive property of sulfuric acid.

In recent years, the capacitive deionization system, which has an adsorption system similar to supercapacitors, has attracted great interest for its use in water purification processes. Regarding various porous carbon materials, such as activated carbon, carbon aerogels, carbon nanotubes, and graphene, used as electrodes in both supercapacitors and capacitive deionization systems, carbon aerogels are one of the most widely used materials due to their specific surface area, low resistivity, and high electrical conductivity (Huang, Yang, Kang and Inagaki, 2017:470; Oladunni, Zain, Hai, Banat, Bharath and Alhseinat, 2018:291; Jung, Hwang, Hyun, Lee and Kim, 2007:377). Regarding carbon gels

called aerogels, cryogels, and xerogels, which are produced by different drying methods, xerogels are more economical than others because they are dried at ambient pressure and temperature (Elkhatat and Al-Muhtaseb, 2011:2887). However, despite the ease of preparation, some properties, such as specific area and porosity, are weaker than others and need improvement. To improve the performance of carbon xerogel, Alam et al. selected Na_2CO_3 and NaOH as catalysts. They obtained a specific capacitance of 37.6 F/g by optimizing the pH, liquid/mass ratio, and pyrolysis temperature parameters of the resorcinol-formaldehyde catalyst solution (Alam, Ahmad Mirbagheri and Reza Ghaani, 2019:01196). The results showed a significant increase in the capacitance of samples with the same pH by changing catalysts.

4. Conclusion

Studies of supercapacitors show that although they are commercially available, they are currently used only in low-power applications. Supercapacitors with high power density suffer from low energy density. Therefore, improving the energy density is still the basis of research. In addition to the low energy density of supercapacitors, significant progress has been made in recent years to solve some of their drawbacks, such as limited cycle life and cost. In particular, improving the manufacturing process and technology could be a good solution, but developing new active electrode materials and electrolytes is a major challenge. It is necessary to increase the effective surface area of the electrodes, the operating voltage range, or both to improve energy densities. Therefore, further research is needed to develop new materials with high surface area or to discover electrolytes that can withstand a wider voltage range. Better specific properties can be obtained by adding nanostructures to xerogels used as electrode materials. Regarding the studies on xerogel-based electrode materials, the energy storage potential of supercapacitors can be improved by focusing on composite or hybrid structured carbon aerogels and xerogels in future studies. In addition, the cost of carbon aerogel and xerogel production can be significantly reduced by using natural resources such as bamboo fiber, cotton, grapefruit peels and biomass through wastes as raw material instead of resorcinol and formaldehyde used as raw materials in xerogel production. Another important issue is that as wearable electronics become increasingly important, flexible supercapacitors produced for such applications should be able to absorb voltages. Since current technology fails to solve this problem, novel high-performance supercapacitors are being developed using thermally rechargeable, self-healing piezoelectric

and shape memory materials. If the solutions to these problems are carefully addressed, the energy densities of supercapacitors will become comparable to batteries.

In addition to carbon-based materials such as graphene, GO, and carbon nanotubes, natural resources and wastes are also used to produce xerogels. Using biomass as a raw material to produce xerogels can significantly reduce costs. In addition, resorcinol and formaldehyde, which are widely used in the production of carbon xerogels, are synthesized by the sol-gel method. Energy storage is one of the most important application areas of xerogels. The increasing use of renewable energy and the growing demand for electronic products has increased interest in devices with high energy storage capacity, such as supercapacitors. A comparison of the performances of xerogel-based supercapacitors is given in Figure 3. The performance of the aforementioned superior properties of xerogels in supercapacitor electrodes is remarkable. The review of the studies shows that some disadvantages of plain xerogels can be eliminated by various processes. Xerogels' performance in supercapacitors has been attempted to be improved by using different metal oxides, production methods, heat treatments, adding different nanostructures, and doping. Among these methods, doped xerogels exhibited the best performance. In addition, researchers are looking for solutions for the long production process of xerogels because simple, inexpensive, and applicable production processes are as crucial as supercapacitors' electrochemical performances. According to the studies, the performance of xerogel-based supercapacitors is essentially not at the desired level. Therefore, xerogels are still awaiting solutions as an exciting material to be developed for supercapacitor applications.

References

Alam, M., Ahmad Mirbagheri, S., Reza Ghaani, M. (2019). Multi-parameter optimization of the capacitance of Carbon Xerogel catalyzed by NaOH for application in supercapacitors and capacitive deionization systems, 5, e01196. https://doi.org/10.1016/j.heliyon.2019.e01196.

Araby, S., Qiu, A., Wang, R., Zhao, Z., Wang, C.H., Ma, J. (2016). Aerogels based on carbon nanomaterials, J. Mater. Sci. 51, 9157–9189. https://doi.org/10.1007/s10853-016-0141z.

Bae, Y.S., Snurr, R.Q. (2011). Development and evaluation of porous materials for carbon dioxide separation and capture, Angew. Chem. Int. Ed. 50, 11586–11596. https://doi.org/10.1002/anie.201101891.

Baumann, T.F., Fox, G.A., Sachter, J.H., Yosizawa, N., Fu, R., Dresselhaus, M.S. (2002). Synthesis and Characterization of Copper-Doped Carbon Aerogels, Langmuir 18, 7073-7076. https://doi.org/10.1021/la0259003.

Benad, A., Jürries, F., Vetter, B., Klemmed, B., Hübner, R., Leyens, C. (2018). Mechanical properties of metal oxide aerogels, Chem. Mater. 30, 145–152. https://doi.org/10.1021/acs.chemmater.7b03911.

Bheekhun, N., Talib, A., Rahim, A., Hassan, M.R. (2013). Aerogels in aerospace: an overview, Adv. Mater. Sci. Eng. 2013, 406065. https://doi.org/10.1155/2013/406065.

Buschow, K. H. J., Flemings, Merton C., Cahn, R. (2001). The Encyclopedia of Materials : Science and Technology, Place of publication not identified Pergamon Imprint.

Calvo, E.G., Ania, C.O., Zubizarreta, L., Menéndez, J.A., Arenillas, A. (2010). Exploring New Routes in the Synthesis of Carbon Xerogels for Their Application in Electric Double-Layer Capacitors, Energy Fuels 24, 3334–3339. https://doi.org/10.1021/ef901465j.

Calvo, E.G., Ferrera-Lorenzo, N., Menéndez, J.A., Arenillas, A. (2013). Microwave synthesis of micro-mesoporous activated carbon xerogels for high performance supercapacitors, Microporous and Mesoporous Materials, 168, 206–212. https://doi.org/10.1016/j.micromeso.2012.10.008.

Calvo, E.G., Juárez-Pérez, E.J., Menéndez, J.A., Arenillas, A. (2011). Fast microwave-assisted synthesis of tailored mesoporous carbon xerogels, J. Colloid Interface Sci. 357, 541–547. https://doi.org/10.1016/j.jcis.2011.02.034.

Calvo, E.G., Lufrano, F., Staiti, P., Brigandì, A., Arenillas, A., Menéndez, J.A. (2013). Optimizing the electrochemical performance of aqueous symmetric supercapacitors based on an activated carbon xerogel, Journal of Power Sources, 241, 776-782. https://doi.org/10.1016/j.jpowsour.2013.03.065.

Canal-Rodríguez, M., Angel Menendez, J., Arenillas, A. (2018). Performance of carbon xerogel-graphene hybrids as electrodes in aqueous supercapacitors, Electrochimica Acta, 276, 28-36. https://doi.org/10.1016/j.electacta.2018.04.143.

Canal-Rodríguez, M., Arenillas, A., Rey-Raap, N., Ramos-Fernandez, G., Martín-Gullon, I., Angel Menendez, J. (2017). Graphene-doped carbon xerogel combining high electrical conductivity and surface area for optimized aqueous supercapacitors, Carbon, 118, 291-298. https://doi.org/10.1016/j.carbon.2017.03.059.

Canal-Rodríguez, M., Menéndez, J.A., Montes-Morán, M.A., Arenillas, A. (2019). The relevance of conductive additive addition methodology for optimizing the performance of electrodes based on carbon xerogels in aqueous supercapacitors, Journal of Electroanalytical Chemistry, 836, 45-49. https://doi.org/10.1016/j.jelechem.2019.01.062.

Canal-Rodríguez, M., Menendez, J.A., Montes-Moran, M.A., Martín-Gullon, I., Parra, J.B., Arenillas, A. (2019). The role of conductive additives on the performance of hybrid carbon xerogels as electrodes in aqueous supercapacitors, Electrochimica Acta, 295, 693-702. https://doi.org/10.1016/j.electacta.2018.10.189.

Carrott, P.J.M., Marques, L.M., Riberio Carrott, M.M.L. (2010). Characterisation of the porosity of polymer and carbon aerogels containing Fe, Ni or Cu prepared from 2,4-dihydroxybenzoic acid by n-nonane pre-adsorption and density functional theory, Micropor. Mesopor. Mater. 131, 75-81. https://doi.org/10.1016/j.micromeso.2009.12.005.

Casco, M.E., Martínez-Escandell, M., Silvestre-Albero, J., Rodríguez-Reinoso, F. (2014). Effect of the porous structure in carbon materials for CO2 capture at atmospheric and high-pressure, Carbon 67, 230–235. https://doi.org/10.1016/j.carbon.2013.09.086.

Castro, C.D., Teresa Izquierdo, M., Diossa, G., Zapata-Benabithe, Z., Quintana, G.C. (2021). Synthesis of bio-based xerogels from lignin precipitated from the black liquor of the paper industry for supercapacitors electrodes, Biomass and Bioenergy, 155, 106296. https://doi.org/10.1016/j.biombioe.2021.106296.

Chang, Z., Yu, B., Wang, C. (2016). Lignin-derived hierarchical porous carbon for highperformance supercapacitors, J. Solid State Electrochem. 20, 1405–1412. https://doi.org/10.1007/s10008-016-3146-2.

Chen, F., Xu, M., Wang, L., Li, J. (2011). Preparation and characterization of organic aerogels from a lignin - resorcinol - formaldehyde copolymer, Bioresources 6, 1262–1272. https://doi.org/10.15376/biores.6.2.1262-1272.

Chen, L., Deng, J., Yuan, Y., Hong, S., Yan, B., He, S., Lian, H. (2022). Hierarchical porous graphitized carbon xerogel for high performance supercapacitor, Diamond & Related Materials, 121, 108781. https://doi.org/10.1016/j.diamond.2021.108781.

Chen, T.T., Song, W.L., Fan, L.Z. (2015). Engineering graphene aerogels with porous carbon of large surface area for flexible all-solid-state supercapacitors, Electrochim. Acta 165 92-97. https://doi.org/10.1016/j.electacta.2015.02.008.

Chen, Z., Augustyn, V., Wen, J., Zhang, Y., Shen, M., Dunn, B., Lu, Y. (2011). High-Performance Supercapacitors Based on Intertwined CNT/V2O5 Nanowire Nanocomposites, Adv. Mater. 23, 791. https://doi.org/10.1002/adma.201003658.

Cheng, J., Cao, G.P., Yang, Y.S. (2006). Characterization of sol–gel-derived NiOx xerogels as supercapacitors, Journal of Power Sources, 159, 734–741. https://doi.org/10.1016/j.jpowsour.2005.07.095.

Cotet, L.C., Baia, M., Popescu, I.C., Cosoveanu, V., Indrea, E., Popp, J., Danciu, V. (2007). Structural properties of some transition metal highly doped carbon aerogels, J. Alloys Comp. 434-435, 854-857. https://doi.org/10.1016/j.jallcom.2006.08.100.

Cotet, L.C, Gich, M., Roig, A., Popescu, I.C., Cosovenau, V., Molins, E., Danciu, V. (2006). Synthesis and structural characteristics of carbon aerogels with a high content of Fe, Co, Ni, Cu, and Pd, J. Non-Cryst. Solids 352, 2772-2777. https://doi.org/10.1016/j.jnoncrysol.2006.03.039.

Datt, A., Ndiege, N., Larsen, S.C. (2012). Development of porous nanomaterials for applications in drug delivery and imaging, Nanomaterials for Biomedicine ACS Symposium Series 1119, 239-258. https://doi.org/10.1021/bk-2012-1119.ch011.

Elkhatat, A.M., Al-Muhtaseb, S.A. (2011). Advances in tailoring resorcinolformaldehyde organic and carbon gels, Adv. Mater. 23, 2887-2903. https://doi.org/10.1002/adma.201100283.

Enterría, M., Martín-Jimeno, F.J., Suarez-García, F., Paredes, J.I., Pereira, M.F.R., Martins, J.I., Martínez-Alonso, A., Tascon, J.M.D., Figueiredo, J.L. (2016). Effect of nanostructure on the supercapacitor performance of activated carbon xerogels obtained from hydrothermally carbonized glucose-graphene oxide hybrids, Carbon, 105, 474-483. https://doi.org/10.1016/j.carbon.2016.04.071

Ferna'ndez, P.S., Arenillas, A., Calvo, E.G., Mene'ndez., J.A., Martins, M.E. (2012). Carbon xerogels as electrochemical supercapacitors. Relation between impedance physicochemical parameters and electrochemical behaviour, International journal of hydrogen energy, 37, 10249-10255. https://doi.org/10.1016/j.ijhydene.2012.01.154.

Fu, R., Baumann, T.F., Cronin, S., Dresselhaus, G., Dresselhaus, M.S., Satcher J.H. (2005). Formation of Graphitic Structures in Cobalt- and Nickel-Doped Carbon Aerogels, Langmuir 21, 2647-2651. https://doi.org/10.1021/la047344d.

Grishechko, L.I., Amaral-Labat, G., Szczurek, A., Fierro, V., Kuznetsov, B.N., Celzard, A. (2013). Lignin-phenol-formaldehyde aerogels and cryogels, Microporous Mesoporous Mater. 168, 19–29. https://doi.org/10.1016/j.micromeso.2012.09.024.

Gurav, J.L., Jung, I.K., Park, H.H., Kang, E.S., Nadargi, D.Y. (2010). Silica aerogel: Synthesis and applications, J. Nanomater. 2010, 409310. https://doi.org/10.1155/2010/409310.

Huang, Z.-H., Yang, Z., Kang, F., Inagaki, M. (2017). Carbon electrodes for capacitive deionization, J. Mater. Chem. A 5, 470-496. https://doi.org/10.1039/C6TA06733F.

Jeon, J.-W., Zhang, L., Lutkenhaus, J.L., Laskar, D.D., Lemmon, J.P., Choi, D., Nandasiri, M. I., Hashmi, A., Xu, J., Motkuri, R.K., Fernandez, C.A., Liu, J., Tucker, M.P., McGrail, P. B., Yang, B., Nune, S.K. (2015). Controlling porosity in lignin-derived nanoporous carbon for supercapacitor applications, Chem. Sus. Chem. 8, 428–432. https://doi.org/10.1002/cssc.201402621.

Job, N., Maillard, F., Marie, J., Berthon-Fabry, S., Pirard, J.P., Chatenet, M. (2009). Electrochemical characterization of Pt/carbon xerogel and Pt/carbon aerogel catalysts: First insights into the influence of the carbon texture on the Pt nanoparticle morphology and catalytic activity, J. Mater. Sci. 44, 6591-6600. https://doi.org/10.1007/s10853-009-3581-x.

Job, N., Pirard, R., Marien, J., Pirard, J.P. (2004). Synthesis of transition metal-doped carbon xerogels by solubilization of metal salts in resorcinol–formaldehyde aqueous solution, Carbon 42, 3217-3227. https://doi.org/10.1016/j.carbon.2004.08.013.

Jung, H.H., Hwang, S.W., Hyun, S.H., Lee, K.H., Kim, G.T. (2007). Capacitive deionization characteristics of nanostructured carbon aerogel electrodes synthesized via ambient drying, Desalination 216, 377-385. https://doi.org/10.1016/j.desal.2006.11.023.

Khammar, H., Abdelwahab, A., Abdel-Samad, H.S., Hassan, H.H. (2021). Synergistic performance of simply fabricated polyaniline/carbon xerogel composite as supercapacitor electrode, Journal of Electroanalytical Chemistry, 880,114848. https://doi.org/10.1016/j.jelechem.2020.114848.

Kotz, R., Carlen, M. (2000). Principles and applications of electrochemical capacitors, € Electrochim. Acta 45 (15-16) 2483-2498. https://doi.org/10.1016/S0013-4686(00)00354-6.

Kudo, T., Ikeda, Y., Watanabe, T., Hibino, M., Miyayama, M., Abe, H., Kajita, K. (2002). Amorphous V2O5/carbon composites as electrochemical supercapacitor electrodes, Solid State Ionics 152, 833-841. https://doi.org/10.1016/S0167-2738(02)00383-1.

Lee, Y.J., Jung, J.C., Park, S., Seo, J.G., Baeck, S.H., Yoon, J.R., Yi, J., Song, I.K. (2010). Preparation and characterization of metal-doped carbon aerogel for supercapacitor, Curr. Appl. Phys. 10, 947-951. https://doi.org/10.1016/j.cap.2009.11.078.

Li, H., Yuan, D., Tang, C., Wang, S., Sun, J., Li, Z., Tang, T., Wang, F., Gong, H., He, C. (2016). Lignin-derived interconnected hierarchical porous carbon monolith with large areal/volumetric capacitances for supercapacitor, Carbon N. Y. 100, 151–157. https://doi.org/10.1016/j.carbon.2015.12.075.

Ling, Z., Wang, G., Dong, Q., Qian, B., Zhang, M., Li, C., Qiu, J. (2014). An ionic liquid template approach to graphene-carbon xerogel composites for supercapacitors with enhanced performance, J. Mater. Chem. A 2 (35) 14329-14333. https://doi.org/10.1039/C4TA02223H.

Liu, C., Yu, Z., Neff, D., Zhamu, A., Jang, B.Z. (2010). Graphene-Based Supercapacitor with an Ultrahigh Energy Density, Nano Lett. 10, 4863. https://doi.org/10.1021/nl102661q.

Liu, K.C., Anderson, M.A. (1996). Porous nickel oxide/nickel film for electrochemical capacitors, J. Electrochem. Soc. 143 (1) 124–130. https://doi.org/10.1149/1.1836396.

Liu, L., Yang, J., Meng, Q. (2013). Graphene cross-linked phenol-formaldehyde hybrid organic and carbon xerogel during ambient pressure drying, J. Sol Gel Sci. Technol. 66 (1) 1-5. https://doi.org/10.1007/s10971-012-2958-5.

Liu, L., Yang, J., Meng, Q. (2013). Graphene cross-linked phenol-formaldehyde hybrid organic and carbon xerogel during ambient pressure drying, J. Sol Gel Sci. Technol. 66 (1) 1-5. https://doi.org/10.1007/s10971-012-2958-5.

Liu, W., Herrmann, A.K., Bigall, N.C., Rodriguez, P., Wen, D., Oezaslan, M., et al. (2015). Noble metal aerogels synthesis, characterization, and application as electrocatalysts, Acc. Chem. Res. 48, 154–162. https://doi.org/10.1021/ar500237c.

Liu, X., Li, S., Mi, R., Mei, J., Liu, L.M., Cao, L., Lau, W.M., Liu, H. (2015). Porous structure design of carbon xerogels for advanced supercapacitor, Applied Energy, 153, 32–40. https://doi.org/10.1016/j.apenergy.2015.01.141.

Lu, C., Huang, Y.H., Hong, J.S., Wu, Y.J., Li, J., Cheng, J.P. (2018). The effects of melamine on the formation of carbon xerogel derived from resorcinol and formaldehyde and its performance for supercapacitor, Journal of Colloid and Interface Science, 524, 209–218. https://doi.org/10.1016/j.jcis.2018.04.006.

Lu, X.-F., Chen, X.-Y., Zhou, W., Tong, Y.-X., Li, G.-R. (2015). α-Fe2O3@ PANI core–shell nanowire arrays as negative electrodes for asymmetric supercapacitors, ACS Appl. Mater. Interfaces 7 (27) 14843–14850. https://doi.org/10.1021/acsami.5b03126.

Luan, V.H., Tien, H.N., Hoa, T.L., Hien, N.T.M., Oh, E.S., Chung, J., Kim, E.J., Choi, W.M., Kong, B.S., Hur, S.H. (2013). Synthesis of a highly conductive and large surface area graphene oxide hydrogel and its use in a supercapacitor, J. Mater. Chem. A 1, 208. https://doi.org/10.1039/C2TA00444E.

Luo, W., Wang, Y., Chou, S., Xu, Y., Li, W., Kong, B., Dou, S.X., Liu, H.K., Yang, J. (2016). Critical thickness of phenolic resin-based carbon interfacial layer for improving long cycling stability of silicon nanoparticle anodes, Nano Energy 27, 255–264. https://doi.org/10.1016/j.nanoen.2016.07.006.

Macías, C., Haro, M., Parra, J.B., Rasines, G., Ania, C.O. (2013). Carbon black directed synthesis of ultrahigh mesoporous carbon aerogels, Carbon 63, 487-497. https://doi.org/10.1016/j.carbon.2013.07.024.

Maldonado-Hódar, F.J., Moreno-Castilla, C., Rivera-Utrilla, J., Hanzawa, Y., Yamada, Y. (2000). Catalytic Graphitization of Carbon Aerogels by Transition Metals, Langmuir 16, 4367-4373. https://doi.org/10.1021/la991080r.

Markovic, Z.M., Babic, B.M., Dramicanin, M.D., Holclajtner Antunovic, I.D., Pavlovic, V.B., Perusko, D.B., Todorovic Markovic, B.M. (2012). Preparation of highly conductive carbon cryogel based on pristine graphene, Synth. Met. 162 (9-10) 743-747. https://doi.org/10.1016/j.synthmet.2012.03.019.

Martín-Jimeno, F.J., Suarez-García, F., Paredes, J.I., Martínez-Alonso, A., Tascon, J.M.D. (2015). Activated carbon xerogels with a cellular morphology derived from hydrothermally carbonized glucose-graphene oxide hybrids and their performance towards CO2 and dye adsorption, Carbon 81, 137-147. https://doi.org/10.1016/j.carbon.2014.09.042.

Meng, F., Zhang, X., Xu, B., Yue, S., Guo, H., Luo, Y. (2011). Alkali-treated graphene oxide as a solid base catalyst: synthesis and electrochemical capacitance of graphene/carbon composite aerogels, J. Mater. Chem. 21 (46) 18537-18539. https://doi.org/10.1039/C1JM13960F.

Mishra, S., Yadav, A., Verma, N. (2017). Carbon gel-supported fe-graphene disks: synthesis, adsorption of aqueous Cr(VI) and Pb(II) and the

removal mechanism, Chem. Eng. J. 326, 987–999. https://doi.org/10.1016/j.cej.2017.06.022.

Moreno-Castilla, C., Maldonado-Hodar, F.J., Rivera-Utrilla, J., Rodríguez-Castellon, E. (1999). Group 6 metal oxide-carbon aerogels. Their synthesis, characterization and catalytic activity in the skeletal isomerization of 1-butene, Appl. Catal. A 183, 345-356. https://doi.org/10.1016/S0926-860X(99)00068-X

Moreno-Castilla, C., Moldonado-Hódar, F.J., Pérez-Cadenas, A.F. (2003). Physicochemical Surface Properties of Fe, Co, Ni, and Cu-Doped Monolithic Organic Aerogels, Langmuir 19, 5650-5655. https://doi.org/10.1021/la034536k.

Oladunni, J., Zain, J., Hai, A., Banat, F., Bharath, G., Alhseinat, E. (2018). A comprehensive review on recently developed carbon based nanocomposites for capacitive deionization : from theory to practice, Sep. Purif. Technol. 207, 291-320. https://doi.org/10.1016/j.seppur.2018.06.046.

Perez-Cantu, L., Liebner, F., Smirnova, I. (2014). Preparation of aerogels from wheat straw lignin by cross-linking with oligo(alkylene glycol)-α,ω-diglycidyl ethers, Microporous Mesoporous Mater. 195, 303–310. https://doi.org/10.1016/j.micromeso.2014.04.018.

Pierre, A.C. (2011). History of aerogels, in: M. Aegerter, N. Leventis, M. Koebel (Eds.), Aerogels Handbook, Advances in Sol-Gel Derived Materials TechnologiesSpringer, New York, NY, USA, 3–18.

Qu, Y., Tian, Y., Zou, B., Zhang, J., Zheng, Y., Wang, L., Li, Y., Rong, C., Wang, Z. (2010). A novel mesoporous lignin/silica hybrid from rice husk produced by a sol-gel method, Bioresour. Technol. 101, 8402–8405. https://doi.org/10.1016/j.biortech.2010.05.067.

Ramos-Fernandez, G., Canal-Rodríguez, M., Arenillas, A., Angel Menendez, J., Rodríguez-Pastor, I., Martin-Gullon, I. (2018). Determinant influence of the electrical conductivity versus surface area on the performance of graphene oxide-doped carbon xerogel supercapacitors, Carbon, 126, 456-463. https://doi.org/10.1016/j.carbon.2017.10.025.

Reddy, K.R., Lee, K.P., Gopalan, A.I. (2008). Self-assembly approach for the synthesis of electromagnetic functionalized Fe3O4/polyaniline nanocomposites: effect of dopant on the properties, Colloids Surf. A Physicochem. Eng. Asp. 320 (1–3) 49–56. https://doi.org/10.1016/j.colsurfa.2007.12.057.

Rey-Raap, N., Angel Menendez, J., Arenillas, A. (2014). Simultaneous adjustment of the main chemical variables to fine-tune the porosity of carbon xerogels, Carbon 78, 490-499. https://doi.org/10.1016/j.carbon.2014.07.030.

Riley, B.J., Chong, S. (2020). Environmental Remediation with Functional Aerogels and Xerogels, 4 (10) 2070101. https://doi.org/10.1002/gch2.202000013.

Saha, D., Deng, S. (2009). Hydrogen Adsorption on Ordered Mesoporous Carbons Doped with Pd, Pt, Ni, and Ru, Langmuir 25 (21) 12550-12560. https://doi.org/10.1021/la901749r.

Saha, D., Li, Y., Bi, Z., Chen, J., Keum, J.K., Hensley, D.K., Grappe, H.A., Meyer, H.M., Dai, S., Paranthaman, M.P., Naskar, A.K. (2014). Studies on supercapacitor electrode material from activated lignin- derived mesoporous carbon, Langmuir 30, 900–910. https://doi.org/10.1021/la404112m.

Salinas-Torres, D., Ruiz-Rosas, R., Valero-Romero, M.J., Rodríguez-Mirasol, J., Cordero, T., Morallon, E., Cazorla-Amoros, D. (2016). Asymmetric capacitors using lignin based hierarchical porous carbons, J. Power Sources 326, 641–651. https://doi.org/10.1016/j.jpowsour.2016.03.096.

Salitra, G., Soffer, A., Eliad, L., Cohen, Y., Aurbach, D. (2000). Carbon electrodes for double-layer capacitors. I relations between ion and pore dimensions, J. Electrochem. Soc. 147 (7) 2486-2493. https://doi.org/10.1149/1.1393557.

Sevilla, M., Sangchoom, W., Balahmar, N., Fuertes, A.B., Mokaya, R. (2016). Highly porous renewable carbons for enhanced storage of energy-related gases (H2 and CO2) at high pressures, ACS Sustain. Chem. Eng. 4, 4710–4716. https://doi.org/10.1021/acssuschemeng.6b00809.

Shao, H., Wu, Y.-C., Lin, Z., Taberna, P.-L., Simon, P. (2020). Nanoporous carbon for electrochemical capacitive energy storage, Chem. Soc. Rev. 49 (10) 3005–3039.https://doi.org/10.1039/D0CS00059K.

Shi, Q., Zhang, R.Y., Lu, Y.Y., Deng, Y.H., Elzatahrya, A.A., Zhao, D.Y. (2015). Nitrogen-doped ordered mesoporous carbons based on cyanamide as the dopant for supercapacitor, Carbon 84, 335–346. https://doi.org/10.1016/j.carbon.2014.12.013.

Skowronski, J.M., Osinska, M. (2012). Effect of nickel catalyst on physicochemical properties of carbon xerogels as electrode materials for supercapacitor, Current Applied Physics, 12, 911-918. https://doi.org/10.1016/j.cap.2011.12.009.

Srinivas, G., Krungleviciute, V., Guo, Z.X., Yildirim, T. (2014). Exceptional CO2 capture in a hierarchically porous carbon with simultaneous high surface area and pore volume, Energy Environ. Sci. 7, 335–342. https://doi.org/10.1039/C3EE42918K.

Srinivasan, V., Weidner, J.W. (1997). An electrochemical route for making porous nickel oxide electrochemical capacitors, J. Electrochem. Soc. 144 (8) L210–L213. https://doi.org/10.1149/1.1837859.

Stoller, M.D., Park, S., Zhu, Y., An, J. Ruoff, R.S. (2008). Graphene-based ultracapacitors, Nano Lett. 8, 3498. https://doi.org/10.1021/nl802558y.

Tamon, H., Sone, T., Mikami, M., Okazaki, M. (1997). Preparation and characterization of silica–titania and silica–alumina aerogels, J. Colloid Interface Sci. 188, 493–500. https://doi.org/10.1006/jcis.1997.4779.

Teichner, S.J., Nicolaon, G.A., Vicarini, M.A., Gardes, G.E.E. (1976). Inorganic oxide aerogels, Adv. Colloid Interface Sci. 5, 245–273. https://doi.org/10.1016/0001-8686(76)80004-8.

To, J.W., He, J.J., Mei, J.G., Haghpanah, R., Chen, Z., Kurosawa, T., Chen, S.C., Bae, W. G. (2016). Hierarchical N-Doped carbon as CO2 adsorbent with high CO2 selectivity from rationally designed polypyrrole precursor, J. Am. Chem. Soc. 138, 1001–1009. https://doi.org/10.1021/jacs.5b11955.

Tüysüz, H., Schüth, F. (2012). Chapter Two - Ordered Mesoporous Materials as Catalysts, Advances in Catalysis, 127-239. https://doi.org/10.1016/B978-0-12-385516-9.00002-8.

Wang, D., Choi, D., Li, J., Yang, Z., Nie, Z., Kou, R., Hu, D., Wang, C., Saraf, L.V., Zhang, J., Aksay, I.A., Liu, J. (2009). Self-Assembled TiO2–Graphene Hybrid Nanostructures for Enhanced Li-Ion Insertion, ACS Nano 3, 907. https://doi.org/10.1021/nn900150y.

Wang, H., Lin, J., Shen, Z.X. (2016). Polyaniline (PANi) based electrode materials for energy storage and conversion, J. Sci.: Adv. Mater. Dev. 1 (3) 225–255. https://doi.org/10.1016/j.jsamd.2016.08.001.

Wang, S., Miao, J., Liu, M., Zhang, L., Liu, Z. (2021). Hierarchical porous N-doped carbon xerogels for high performance CO2 capture and supercapacitor, Colloids and Surfaces A: Physicochemical and Engineering Aspects, 616, 126285. https://doi.org/10.1016/j.colsurfa.2021.126285.

Wang, X., Lu, L.L., Yu, Z.L., Xu, X.W., Zheng, Y.R., Yu, S.H. (2015). Scalable template synthesis of resorcinol-formaldehyde/graphene oxide composite aerogels with tunable densities and mechanical properties, Angew. Chem.Int. Ed. 54 (2015) 2397–2401. https://doi.org/10.1002/anie.201410668.

Wee, G., Soh, H.Z., Cheah, Y.L., Mhaisalkar, S.G., Srinivasan, M. (2010). Synthesis and electrochemical properties of electrospun V2O5 nanofibers as supercapacitor electrodes, J. Mater. Chem. 20, 6720. https://doi.org/10.1039/C0JM00059K.

Wei, D., Scherer, M.R., Bower, C., Andrew, P., Ryhänen, T., Steiner, U. (2012). A Nanostructured Electrochromic Supercapacitor, Nano Lett. 12, 1857. https://doi.org/10.1021/nl2042112.

Wu, Z.S., Ren, W., Wen, L., Gao, L., Zhao, J., Chen, Z., Zhou, G., Li, F., Cheng, H.M. (2010). Graphene Anchored with Co_3O_4 Nanoparticles as Anode of Lithium Ion Batteries with Enhanced Reversible Capacity and Cyclic Performance, ACS Nano 4, 3187. https://doi.org/10.1021/nn100740x.

Xia, X.H., Zhang, X.F., Yi, S.Q., Liu, H.B., Chen, Y.X., Chen, H., Yang, L., He, Y.D. (2016). Preparation of high specific surface area composite carbon cryogels from selfassembly of graphene oxide and resorcinol monomers for supercapacitors, J. Solid State Electrochem. 20 (6) 1793-1802. https://doi.org/10.1007/s10008-016-3196-5.

Xu, J., Sun, H., Li, Z., Lu, S., Zhang, X., Jiang, S., Zhu, Q., Zakharova, G.S. (2014). Synthesis and electrochemical properties of graphene/V2O5 xerogels nanocomposites as supercapacitor electrodes, Solid State Ionics, 262, 234–237. https://doi.org/10.1016/j.ssi.2013.10.060.

Xu, J., Zhou, X., Chen, M., Shi, S., Cao, Y. (2018). Preparing hierarchical porous carbon aerogels based on enzymatic hydrolysis lignin through ambient drying for supercapacitor electrodes, Microporous Mesoporous Mater. 265, 258–265. https://doi.org/10.1016/j.micromeso.2018.02.024.

Xu, X., Zhou, J., Nagaraju, D.H., Jiang, L., Marinov, V.R., Lubineau, G., Alshareef, H.N., Oh, M. (2015). Flexible, highly graphitized carbon aerogels based on bacterial cellulose/lignin: catalyst free synthesis and its application in energy storage devices, Adv. Funct. Mater. 25, 3193–3202. https://doi.org/10.1002/adfm.201500538.

Yang, X., Jiang, Z., Fei, B., Ma, J., Liu, X. (2018). Graphene functionalized bio-carbon xerogel for achieving high-rate and high-stability supercapacitors, Electrochimica Acta, 282, 813-821. https://doi.org/10.1016/j.electacta.2018.06.131.

Yin, J., Zhang, W., Alhebshi, N.A., Salah, N., Alshareef, H.N. (2020). Synthesis strategies of porous carbon for supercapacitor applications, Small Methods 4, 1900853. https://doi.org/10.1002/smtd.201900853.

Yu, B., Chang, Z., Wang, C. (2016). The key pre-pyrolysis in lignin-based activated carbon preparation for high performance supercapacitors, Mater. Chem. Phys. 181, 187–193. https://doi.org/10.1016/j.matchemphys.2016.06.048.

Zhang, W., Zhao, M., Liu, R., Wang, X., Lin, H. (2015). Hierarchical porous carbon derived from lignin for high performance supercapacitor, Colloids Surfaces A Physicochem. Eng. Asp. 484, 518–527. https://doi.org/10.1016/j.colsurfa.2015.08.030.

Zhou, G., Wang, D.W., Yin, L.C., Li, N., Li, F., Cheng, H.M. (2012). Oxygen Bridges between NiO Nanosheets and Graphene for Improvement of Lithium Storage, ACS Nano 6, 3214. https://doi.org/10.1021/nn300098m.

Zhou, Y., Candelaria, S.L., Liu, Q., Huang, Y., Uchaker, E., CaO, G. (2014). Sulfur-rich carbon cryogels for supercapacitors with improved conductivity and wettability, J. Mater. Chem. A 2 (22) 8472-8482. https://doi.org/10.1039/C4TA00894D.

Zhu, Y., Murali, S., Stoller, M.D., Ganesh, K.J., Cai, W., Ferreira, P.J., Pirkle, A., Wallace, R.M., Cychosz, K.A., Thommes, M., Su, D., Stach, E.A., Ruoff, R.S. (2011). Carbon based supercapacitors produced by activation of graphene, Science 332 (6037) 1537-1541. https://doi.org/10.1126/science.1200770.

Zuo, L., Zhang, Y., Zhang, L., Miao, Y.E., Fan, W., Liu, T. (2015). Polymer/carbon-based hybrid aerogels: Preparation, properties and applications, Materials (Basel) 8, 6806–6848. https://doi.org/10.3390/ma8105343.

SUPERCAPACITORS: COMPONENTS, CHARACTERIZATIONS AND PERFORMANCE EVALUATIONS

Satiye KORKMAZ

(Assoc. Prof.), Karabük University,
E-mail: satiyekorkmaz@karabuk.edu.tr
ORCID: 0000-0002-7592-3366

1. Introduction

The increasing use of renewable energy and the growing demand for electricity from electronic devices used in daily life have accelerated research on electrochemical energy storage. The objective is not only storing energy but also transmitting the stored energy efficiently; therefore, the demand for energy storage devices with high power density is increasing. However, a device that both stores considerable energy and has high power and energy density is not available to meet this demand. Supercapacitors have emerged as energy storage devices with excellent charge-discharge cycles, long lifetimes, and high power density. The operating principle of batteries, the most widely used energy storage device, is based on electron transfer that changes the chemistry of the electroactive compounds they contain; thus, the charge storage process is faradic. In supercapacitors, on the other hand, electrical charges are stored in the electrochemical bilayer of electrodes with high surface area, and the energy storage mechanism is based on redox reactions (Winter and Brodd, 2004:4245; Armand and Tarascon, 2008:652; Chu and Braatz, 2002:236). For this reason, supercapacitors have a power density nine times higher than lithium-ion batteries and have a higher charge-discharge cycle, which is remarkable. Other factors contributing to the capacitance are functional groups on the surface and the faradaic reactions between the electrode and the electrolyte (Conway, Birss and Wojtowicz; 1997:1). Therefore, using electrodes supported by a suitable structure can improve the performance of supercapacitors through

electrolyte diffusion and electronic conduction (Seredych, Koscinski, Sliwinska-Bartkowiak and Bandosz, 2012:243; Enterría, Castro-Muniz, Su ~ arez-García, Martínez-Alonso, Tascon and Kyotani, 2014:12023; Ferrero, Sevilla and Fuertes, 2015:239; Matsui, Tanaka and Miyake, 2013:737). Carbon gels, first produced by Pekala, are a unique structure prepared by polycondensation of resorcinol with formaldehyde using sodium carbonate as a catalyst (Pekala, 1089:3221). These gels are usually produced by solvent exchange, supercritical CO_2 drying, ambient temperature drying, or freeze drying (Pekala, 1089:3221; Pröbstle, M. Wiener and J. Fricke, 2003:213; Wu, Fu, Zhang, Dresselhaus, and Dresselhaus, 2004:2033; Kim, Hwang and Hyun, 2005:725, Jung, Hwang, Hyun, Lee and Kim, 2007:377; Lee, Jung, Yi, Baeck, Yoon and Song, 2010:682; Tamon, Ishizaka, Yamamoto and Suzuki, 2000:1099).

Aerogel is the substance produced by supercritical drying, while the structure obtained by drying in an inert atmosphere is called xerogel. The dried products are then subjected to heat treatment to obtain carbon gels. The aerogel-type resorcinol formaldehyde (RF) is widely used because of its ability to transform into carbon aerogels during pyrolysis. Carbon gels' improved micropores and mesopores provide advantages for adsorption and catalysis processes. At the same time, their high electrical conductivity makes them promising for electrochemical applications (Reichenauer, Emmerling, Fricke and Pekala, 1998:210, Czakkel, Marthi, Geissler and László, 2005:124; Kadirvelu, Goel and Rajagopal, 2008:502). Various metals can be easily doped into xerogels to form carbon-based composites.

2. Supercapacitors

Energy has become a global issue due to population growth and the use of non-renewable energy sources to generate electricity (Rajeswari Yogamalar, Kalpana and Muhammed Shafi, 2022:105727). Therefore, storing the energy obtained from renewable energy sources efficiently became crucial. In recent years, the increase in portable energy sources has decreased the interest in studies involving energy sources with high storage capacity and long operating times. Today, the energy storage and conversion technologies that power portable electronic devices are fuel cells, batteries, and supercapacitors (Qaisar, Mojtaba, Hunt Michael, Peter, and Rizwan, 2020:5847). Supercapacitors have been widely used in electric vehicles, electronic devices, airplanes, and smart grids with their high power density, long cycle life, and superior charge-discharge characteristics (Khalid, 2019:4559). As shown in the Ragon graph in Figure

1, the gap between the power and energy density of batteries can be filled by supercapacitors.
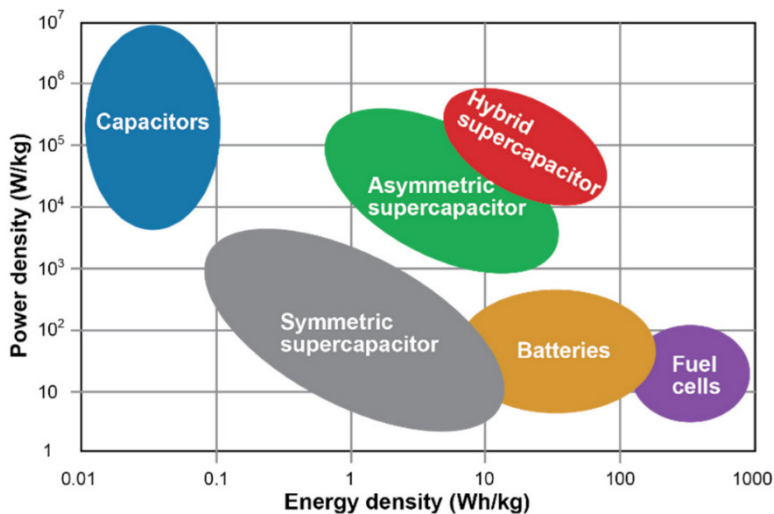
Fig. 1. Different electrical storage devices are positioned in the Ragone plot according to their power and energy densities (Vandeginste, 2022:862).

Although supercapacitors have a lower energy density than batteries, they are characterized by their ultra-high power density. In addition, their virtually unlimited cycle life and ability to store charge in seconds have attracted much interest in electric vehicles, storage systems, and industrial energy management systems (Huang, Zhu, Sarkar and Zhao, 2019:100901). In addition to studies on their high power density, intensive research on supercapacitors in recent years has focused on improving their energy density and design. These issues can be addressed by improving the performance of supercapacitor components. The key factors in selecting electrode materials, the most critical component of supercapacitors, are low production cost, low weight, large surface area, controllable morphology, and high porosity.

2.1. Components of Supercapacitors

2.1.1. Electrode

The electrode material is the most critical component that determines the performance of a supercapacitor. The review of the research on electrodes, which has become the focus of the supercapacitor literature, shows that significant efforts have been made to increase energy density. Achieving the

desired performance in electrode materials for supercapacitors is possible by developing materials with high surface area and porosity. Activated carbon, carbon nanotubes (CNTs), graphene, transition metal oxides, and conductive polymers have attracted significant interest from researchers as supercapacitor electrode materials. Carbon materials, which have the advantages of high surface area, high porosity, electrical conductivity, and low cost, have become an intensively researched material for supercapacitor electrodes. Surface treatment of carbon materials with high surface areas, such as activated carbon, carbon nanotubes, graphene, and carbon aerogels, increases the specific capacitance by promoting pore formation (Kar, 2021). On the other hand, doping these materials with elements such as nitrogen, oxygen, boron, sulfur, and phosphorus also significantly increases the capacitance. Large surface area, high crystallinity, and especially high nitrogen doping significantly increase capacitance (Lamba et all, 2022:103871). Supercapacitor electrodes made of transition metal oxides and conductive polymers have been reported to provide high charge storage capability and increased energy density. However, they have been reported to have low cycle life and limited operating voltage (Lee, Kim and Lee, 2001:A19).
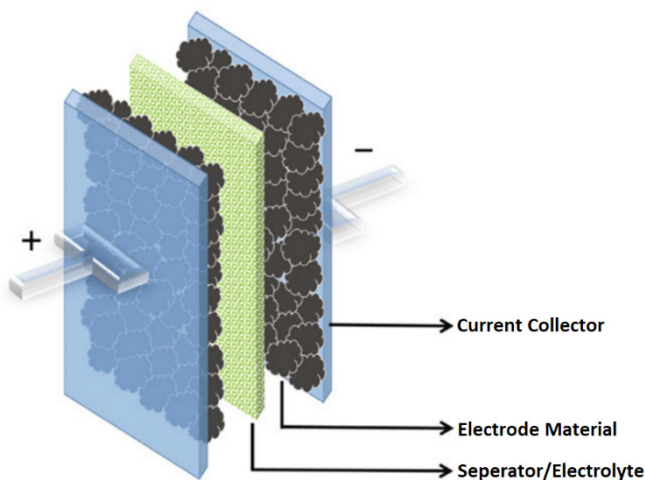
Fig. 2. Components of Supercapacitor (Samantara and Ratha, 2018).

2.1.2. Electrolyte

The electrolyte is the second principal component that affects supercapacitor performance, directly affecting the supercapacitor cell's operating voltage range, rate capability, cycling stability, and resistance. Energy density, an essential

characteristic of supercapacitors that needs to be improved, varies inversely with the square of the operating voltage range, and resistivity varies inversely with the power capacity; therefore, the higher the operating voltage and conductivity of the electrolyte, the higher the energy and power density. For this reason, electrolyte selection is critical in designing high-performance supercapacitors. Electrolytes are characterized by their ionic conductivity, operating voltage range, stability, and reliability. The practical approaches for improving supercapacitors' specific capacitance and energy density include developing hybrid gel electrolytes to improve the electrode-electrolyte interaction mechanism, developing characterization models to observe charge storage processes, and doping redox-active materials into electrolytes. Significant developments in portable electronics can be achieved, especially with the increasing active use of hybrid gel electrolytes in supercapacitors (Bhat, Patil and Rakhi, 2022:104222).

2.1.3. Current Collector

Supercapacitor electrode materials are prepared by coating the anode and cathode with active materials. The active materials are deposited on the collectors using appropriate methods, achieving desired dimensions. The current collectors used to conduct the electric current to both sides are usually made of foil or conductive polymers.

2.2. Characterization and Performance Evaluation of Supercapacitor

In conventional supercapacitors, the separation between the electrodes is provided by a dielectric material, and charge accumulation is achieved by electrostatic attraction or induced transient polarization between two oppositely charged particles. In electrostatic double-layer capacitors (EDLC), charge accumulation is achieved by oppositely charged ions. Supercapacitors create an environment that facilitates the movement of electrons and ions using an electrolyte instead of the dielectric material used in conventional capacitors. The high performance is ensured by the high surface area of the carbons used in supercapacitors, different synthesis techniques, functional groups, and additives used in electrodes derived from carbon-based starting materials. On the other hand, the surface diffusion process significantly increases the charge storage capacity of the electrodes.

Supercapacitors have two types of charge storage processes: faradic and non-faradic. Faradic processes predominate in pseudocapacitive and battery-like storage mechanisms. They are called electrochemical double-

layer capacitors (EDLC) because charge storage electrolyte ions form a double layer on the surfaces of electrostatically stable conductive electrodes having high surface area and porous structure (Zhu, 2019:1901081). The amount of stored charge and potential varies linearly; a single capacitance value can be calculated. This reversible and fast process ensures EDLCs have high power density and long cycle life. Researchers focus their efforts on electrode materials with large surface area, high porosity and conductivity, long cycle life, and exhibiting thermodynamic stability over a wide operating voltage range to improve the performance of EDLCs (Miao, Song, Zhu, Li, Gan and Liu, 2020:945; Raj, Basu, Mohapatra and Padhy, 2020:136501; Abbas, Mirzaeian, Hunt, Hall and Raza, 2020:5847; Navarro, Torres, Blanco, Herran, Lafoz and N′ajera, 2021:3060). The charge storage characteristics exhibited by battery-like electrodes are similar to those of batteries. However, unlike batteries, the relationship between stored charge and applied potential is not linear because no phase transformation occurs in the charge-discharge process (Babu, Simon and Balducci, 2020:2001128). The process is slow and less reversible because it is a diffusion-controlled charge storage mechanism. On the other hand, faradic and capacitive energy storage mechanisms are integrated into a single electrode in hybrid supercapacitors, another research area that has attracted attention recently. Hybrid supercapacitors, which are of great interest, especially for electric vehicles, combine the advantages of both electrode types and contribute significantly to increasing high power density and capacitance along with the energy density, which is one of the most critical parameters of supercapacitors to be developed.

A supercapacitor can be characterized by three parameters, namely specific capacitance, operating voltage range, and effective series resistance (ESR). Typical three-electrode systems used to determine supercapacitor performance include the electrode under test, the reference electrode, and the counter electrode. The key parameters used to evaluate measurement results are capacitance, energy and power density, internal resistance, and cycle life.

2.2.1. Cyclic Voltammetry (CV)

Cyclic voltammetry is based on applying a linearly varying operating voltage across the two electrodes of a two-electrode device or between the operating and reference electrodes for three electrodes. The applied voltage moves linearly back and forth over a specified voltage range, and the incremental potential change per second is referred to as the scan rate. The specified operating voltage range depends on the electrolyte's operational stability.
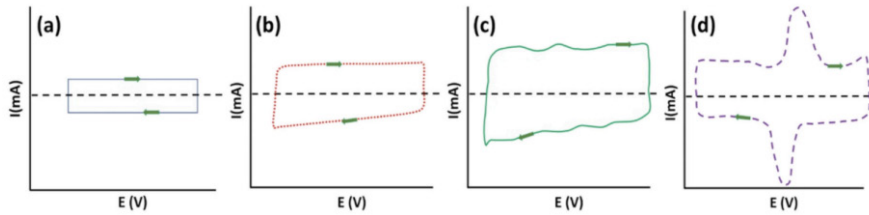
Fig. 3. CV curves of **a)** ideal capacitor, **b)** commercial EDLC, **c)** Pseudo-capacitive electrode, and **d)** battery-type electrode system (Yogamalar, Kalpana and Shafi, 2022:105727).

The instantaneous current values taken from cathodic and anodic scans are calculated and plotted as current vs. potential to determine the electrochemical reactions of the supercapacitor. The CV method optimizes the operating voltage range depending on the electrolyte material, active electrode material, and some essential parameters. Figure 3 shows the CV cycles of batteries with different storage characteristics (Yogamalar, Kalpana and Shafi, 2022:105727).

2.2.3. Constant Current Charge-Discharge (CCCD)

Galvanostatic charge-discharge (GCD) or constant current charge-discharge (CCCD) measurement differentiates supercapacitors in DC. In this technique, a continuous charge-discharge process is performed on a supercapacitor or a single electrode. The voltage varies as a function of time when a constant current is applied. Like the CV technique, meaningful information is obtained about the charge storage process and the series resistance of the supercapacitor. Specific capacitance, equivalent serial resistance, cycle stability, energy, and power densities can be calculated from the discharge curve. The stability and cycling performance of the supercapacitor is evaluated by the observed charge-discharge cycle as a function of the number of cycles. Unlike the voltage variation in the CV, the current is kept constant during this process; therefore, the CCCD provides more accurate information for evaluating the capacitive characteristic.

2.2.4. Electrochemical Impedance Spectroscopy (EIS)

Electrochemical impedance spectroscopy (EIS) is a technique where AC signals of small amplitude are applied to the supercapacitor to see its frequency response. It is commonly used in AC line filtering but has recently been widely used to characterize electrochemical supercapacitors. Electrochemical impedance spectroscopy, also called AC impedance spectroscopy, analyzes impedance data of supercapacitors at open-circuit voltage under a small voltage

amplitude of ±5 mV or ±10 mV in a wide frequency range from 1 mHz to 1 MHz. It is a basic method for analyzing the electrode/electrolyte interface reaction mechanisms and investigating the conductivity and charge transfer properties. The frequency response recorded by charging/discharging the supercapacitor results from the scan rate at which the low-amplitude AC signal is superimposed. Therefore, the response can be associated with the scan rate applied during the cyclic voltammetry method. The phase shift at the displayed frequency can indicate whether the device is capacitive or not. In addition, the EIS method is very important for providing information about the supercapacitor's effective series resistance (ESR), which allows an explicit calculation of the specific power. The method provides information on supercapacitors' specific capacitance, energy, and power densities by explaining the charge transfer and storage mechanism.

2. Conclusion

The energy storage mechanism of supercapacitors is voltage independent, and the total specific area of the electrode is a critical part of the charge storage performance. Therefore, the electrode material selected to improve the electrochemical performance of supercapacitors is critical for achieving higher energy storage capacity and high power density. Carbon, an essential group of materials, is remarkable as a supercapacitor electrode material with its high conductivity, high surface area, corrosion resistance, pore structure, and low cost (Pandolfo and Hollenkamp, 2006:11). On the other hand, graphene is an allotrope of carbon with excellent chemical and mechanical properties. It provides superior electrical conductivity and high specific surface area with its two-dimensional structure. The discovery of graphene has opened new horizons in the field of energy storage. Since supercapacitors' charge storage mechanism is mainly based on the electrostatic adsorption of electrolyte ions on the electrode surface, the surface area is a critical factor affecting capacitance.

References

Abbas, Q., Mirzaeian, M., Hunt, Michael R.C., Hall, P., Raza, R. (2020). Current State and Future Prospects for Electrochemical Energy Storage and Conversion Systems, Energies 13, 5847. https://doi.org/10.3390/en13215847.

Armand, M., Tarascon, J.M. (2008). Building better batteries, Nature 451 (7179) 652-657. https://doi.org/10.1038/451652a.

Babu, B., Simon, P., Balducci, A. (2020). Fast Charging Materials for High Power Applications, Adv. Energy Mat. 10, 2001128. https://doi.org/10.1002/aenm.202001128.

Bhat, T.S., Patil, P.S., Rakhi, R.B. (2022). Recent trends in electrolytes for supercapacitors, Journal of Energy Storage 50, 104222. https://doi.org/10.1016/j.est.2022.104222.

Chu, A., Braatz, P. (2002). Comparison of commercial supercapacitors and high-power lithium-ion batteries for power-assist applications in hybrid electric vehicles: 1 initial characterization, J. Power Sources 112 (1) 236-246. https://doi.org/10.1016/S0378-7753(02)00364-6.

Conway, B.E., Birss, V., Wojtowicz, J. (1997). The role and utilization of pseudocapacitance for energy storage by supercapacitors, J. Power Sources, 66 1-14. https://doi.org/10.1016/S0378-7753(96)02474-3.

Czakkel, O., Marthi, K., Geissler, E., László, K. (2005). Influence of drying on the morphology of resorcinol-formaldehyde-based carbon gels, Micropor. Mesopor. Mater. 86, 124-133. https://doi.org/10.1016/j.micromeso.2005.07.021.

Enterría, M., Castro-Muniz, A., Su ~ arez-García, F., Martínez-Alonso, A., Tascon, J.M.D., Kyotani, T. (2014). Effects of mesostructure order on electrochemical performance of hierarchical micro-mesoporous carbons, J. Mater. Chem. A 2, 12023-12030. https://doi.org/10.1039/C4TA00778F.

Ferrero, G.A., Sevilla, M., Fuertes, A.B. (2015). Mesoporous carbons synthesized by direct carbonization of citrate salts for use as high-performance capacitors, Carbon 88, 239-251. https://doi.org/10.1016/j.carbon.2015.03.014.

Huang, S., Zhu, X., Sarkar, S., Zhao, Y. (2019). Challenges and opportunities for supercapacitors, APL Mater. 7, 100901. https://doi.org/10.1063/1.5116146.

Jung, H.H., Hwang, S.W., Hyun, S.H., Lee, K.H., Kim, G.T. (2007). Capacitive deionization characteristics of nano-structured carbon aerogel electrodes synthesized via ambient drying Desalination 216, 377-385. https://doi.org/10.1016/j.desal.2006.11.023.

Kadirvelu, K., Goel, J., Rajagopal, C. (2008). Sorption of lead, mercury and cadmium ions in multi-component system using carbon aerogel as adsorbent, J. Hazard. Mater. 153, 502-507. https://doi.org/10.1016/j.jhazmat.2007.08.082.

Kar, K. K. (2021). Handbook of Nanocomposite Supercapacitor Materials III, Springer Cham. https://doi.org/10.1007/978-3-030-68364-1.

Khalid, M. (2019). A Review on the Selected Applications of Battery-Supercapacitor Hybrid Energy Storage Systems for Microgrids, Energies 12, 4559. https://doi.org/10.3390/en12234559.

Kim, S.J., Hwang, S.W., Hyun, S.H. (2005). Preparation of carbon aerogel electrodes for supercapacitor and their electrochemical characteristics, J. Mater. Sci. 40, 725-731. https://doi.org/10.1007/s10853-005-6313-x.

Lamba, P., Singh, P., Singh, P., Singh, P., Bharti, Kumar, A., Gupta, M., Kumar, Y. (2022). Recent advancements in supercapacitors based on different electrode materials: Classifications, synthesis methods and comparative performance, Journal of Energy Storage 48, 103871. https://doi.org/10.1016/j.est.2021.103871.

Lee, Ha Y., Kim, S.W., Lee, Hee Y. (2001). Expansion of active site area and improvement of kinetic reversibility in electrochemical pseudocapacitor electrode, Electrochem. Solid State Lett. 4, A19. **https://doi.org/**10.1149/1.1346536.

Lee, Y.J., Jung, J.C., Yi, J., Baeck, S.H., Yoon, J.R., Song, I.K. (2010). Preparation of carbon aerogel in ambient conditions for electrical double-layer capacitor, Curr. Appl. Phys. 10, 682-686. https://doi.org/10.1016/j.cap.2009.08.017.

Matsui, T., Tanaka, S., Miyake, Y. (2013). Correlation between the capacitor performance and pore structure of ordered mesoporous carbons, Adv. Powder Technol. 24, 737-742. https://doi.org/10.1016/j.apt.2013.03.003.

Miao, L., Song, Z., Zhu, D., Li, L., Gan, L., Liu, M. (2020). Performance analysis, challenges and future perspectives of nickel based nanostructured electrodes for electrochemical supercapacitors, Mater. Adv. 1, 945–966. https://doi.org/10.1016/j.jmrt.2021.01.027.

Navarro, G., Torres, J., Blanco, M., Santos-Herran, M., Lafoz, M., N´ajera, J. (2021). Present and Future of Supercapacitor Technology Applied to Powertrains, Renewable Generation and Grid Connection Applications, Energies 14, 3060. https://doi.org/10.3390/en14113060.

Pandolfo, A.G., Hollenkamp, A.F. (2006). Carbon properties and their role in supercapacitors, J. Power Sources 157 (1) 11-27. https://doi.org/10.1016/j.jpowsour.2006.02.065.

Pekala, R.W. (1989). Organic aerogels from the polycondensation of resorcinol with formaldehyde, J. Mater. Sci. 24, 3221-3227. https://doi.org/10.1007/BF01139044.

Pröbstle, H., Wiener, M., Fricke, J. (2003). Carbon Aerogels for Electrochemical Double Layer Capacitors, J. Porous Mater. 10, 213-222. https://doi.org/10.1023/B:JOPO.0000011381.74052.77.

Qaisar, A., Mojtaba, M., Hunt Michael, R.C., Peter, H., Rizwan, R. (2020). Futuristic Direction for R&D Challenges to Develop 2D Advanced Materials

Based Supercapacitors, Energies 13, 5847. https://doi.org/10.1149/1945-7111/abb40d .

Rajeswari Yogamalar, N., Kalpana, S., Muhammed Shafi, P. (2022). An overview, methods of synthesis and modification of carbon-based electrodes for supercapacitor, Journal of Energy Storage 55, 105727. https://doi.org/10.1016/j.est.2022.105727.

Reichenauer, G., Emmerling, A., Fricke, J., Pekala, R.W. (1998). Microporosity in carbon aerogels, J. Non-Cryst Solids 225, 210-214. https://doi.org/10.1016/S0022-3093(98)00118-5.

Samantara, A.K., Ratha S., (2018). Components of Supercapacitor. In: Materials Development for Active/Passive Components of a Supercapacitor. SpringerBriefs in Materials. Springer, Singapore. https://doi.org/10.1007/978-981-10-7263-5.

Seredych, M., Koscinski, M., Sliwinska-Bartkowiak, M., Bandosz, T.J. (2012). Active pore space utilization in nanoporous carbon-based supercapacitors: effects of conductivity and pore accessibility, J. Power Sources 220, 243-252. https://doi.org/10.1016/j.jpowsour.2012.07.074.

Tamon, H., Ishizaka, H., Yamamoto, T., Suzuki, T. (2000). Influence of freeze-drying conditions on the mesoporosity of organic gels as carbon precursors, Carbon 38,1099-1105. https://doi.org/10.1016/S0008-6223(99)00235-3.

Vandeginste, V. (2022). A Review of Fabrication Technologies for Carbon Electrode-Based Micro-Supercapacitors, Appl. Sci, 12(2), 862. https://doi.org/10.3390/app12020862.

Winter, M., Brodd, R.J. (2004). What are batteries, fuel cells, and supercapacitors? Chem. Rev. 104 (10) 4245-4269. https://doi.org/10.1021/cr020730k.

Wu, D., Fu, R., Zhang, S., Dresselhaus, M.S., Dresselhaus, G. (2004). Preparation of low-density carbon aerogels by ambient pressure drying, Carbon 42, 2033-2039. https://doi.org/10.1016/j.carbon.2004.04.003.

Zhu, Q., Zhao, D., Cheng, M., Zhou, J., Owusu, K. A., Mai, L., Yu, Y. (2019). Energy Storage Data Reporting in Perspective—Guidelines for Interpreting the Performance of Electrochemical Energy Storage Systems, Adv. Energy Mater. 9, 1901081. https://doi.org/10.1002/aenm.201902007.

SYNTHESIS AND MOLECULAR DOCKING STUDY OF A NOVEL THIOPHENE AND SCHIFF BASE INCORPORATED PYRIMIDINE RING

Halis KARATAŞ [1] & Burçin TÜRKMENOĞLU[2] & Zülbiye KÖKBUDAK[3]

[1](Asst.), Erciyes University, E-mail: haliskaratash@erciyes.edu.tr
ORCID: 0000-0001-5473-5588

[2](Assoc. Prof.), Erzincan Binali Yıldırım University,
E-mail: burcin.turkmenoglu@erzincan.edu.tr
ORCID: 0000-0002-5770-0847

[3](Prof. Dr.), Erciyes University, E-mail: zulbiye@erciyes.edu.tr
ORCID: 0000-0003-2413-9595

1. Introduction

Having two nitrogen atoms at position 1 and 3 in a six membered heterocycle, Pyrimidines, a fundamental group of organic chemistry, are famous for their wide spectrum of bioactivities that partake importantly to many crucial processes within living organisms. These sophisticated molecules are key components of RNA, DNA, co-enzymes, and numerous bioactive compounds, making them fundamental for the transmission of genetic information, protein synthesis, and many other metabolic pathways. They commonly found in nature include cytosine, thymine, uracil, and more complex pyrimidine derivatives (Lagoja, 2005). The impeccable pairing of pyrimidines with purines is indispensable for the structure and functions of the double helix in DNA, enabling transcription and accurate genetic replication (Ono, Torigoe, Tanaka, & Okamoto, 2011). They, also, contribute to the production of deoxyribonucleotide triphosphates (dNTPs) required for DNA replication and ribonucleotide triphosphates (NTPs) used in transcription. Pyrimidine-based

coenzymes, such as coenzyme A (CoA), Flavin adenine dinucleotide (FAD), and Flavin mononucleotide (FMN), participate in various biochemical reactions. CoA, for instance, is involved in the Krebs cycle and fatty acid metabolism, playing a crucial role in energy production (Wang, 2016).

There are many commercially available drugs and therapeutic agents contain pyrimidine moieties or are pyrimidine analogs at market, which are used in the treatment of various diseases, including cancer, viral infections, malaria, and psychological diseases. They also operate as the basis for several antibiotics such as trimethoprim, which inhibit bacterial dihydrofolate reductase, a key enzyme in folate metabolism (Gupta et al., 2010).

Thiophene, another heterocyclic structure containing a sulfur in the five-membered ring, is characterized by its aromatic structure and a distinctive odor. Thiophene is a curicial group in the field of organic chemistry, frequently serving as a precursor for the synthesis of various important compounds, including pharmaceuticals, agrochemicals, and materials such as semi-conductive polymers (Åslund et al., 2009; Liu et al., 2013; Mishra, Jha, Kumar, & Tomer, 2011; Turkoglu, Cinar, & Ozturk, 2019).

Duloxetine
(Treatment of anxiety disorder)

Tiletamine
(Anesthetic agent)

Tienilic acid
(Treatment of hypertension)

Pyrimethamine
(Treatment of malaria)

Risperidone
(Antipsychotic)

Idoxuridine
(anti-herpesvirus)

Relugolix
(Treatment of prostate cancer)
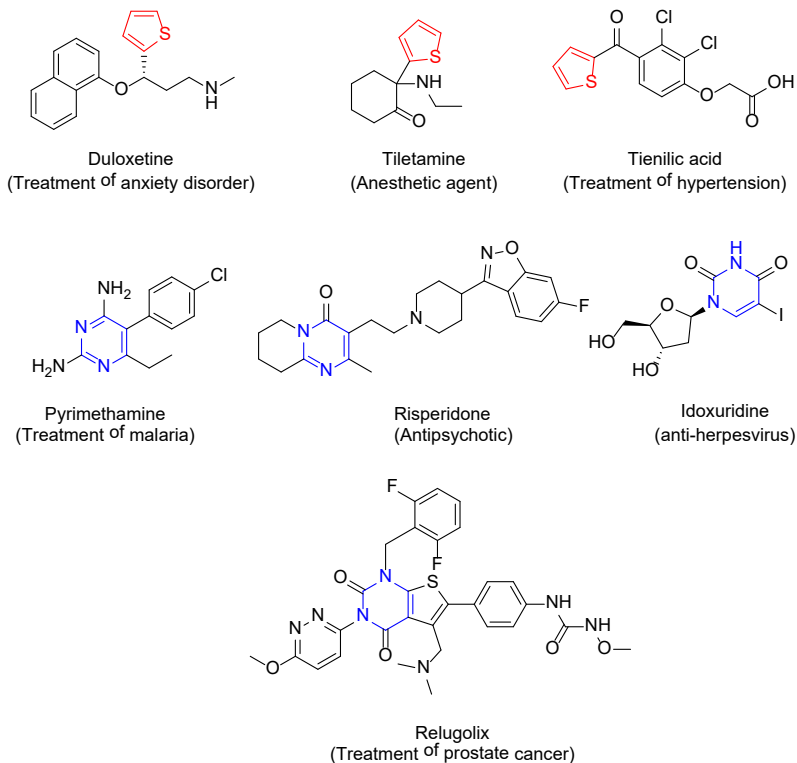
Figure 1. Some commercially available pyrimidine or thiophene bearing drugs

Thiophene's versatile reactivity and significance in both the laboratory and industrial applications have made it a noteworthy and widely studied compound in the realm of organic chemistry.

N-aminopyrimidines can be used as a key group for synthesis of heterocyclic compounds. Hence, many important studies have been done on such compounds (G. Aslan, Akkoç, Akkurt, Özdemir, & Kökbudak, 2018; G. Aslan & Onal, 2014; H. G. Aslan, Akkoç, & Kökbudak, 2020; H. G. Aslan, Akkoç, Kökbudak, & Aydın, 2017; Çimen, Akkoç, & Kökbudak, 2018; ZÜLBİYE KÖKBUDAK, ASLAN, & AKKOÇ, 2020; Zülbiye Kökbudak et al., 2020; ZÜLBİYE ÖNAL & Altural, 1999, 2006; ZÜLBİYE ÖNAL & DAYLAN, 2007).

Schiff base, also known as azomethine or imine, is synthesized by the condensation reaction of primary amine and aldehyde/ketone. They have well-rounded pharmacophore properties that are boadly used in the design and development of bioactive compounds (da Silva et al., 2011). The prominence of Schiff base bearing bioactive pyrimidine derivatives is increasing (Akkoc et al., 2022; Cakmak, Basaran, & Senturk, 2022; Jasinska et al., 2022; Zülbiye Kökbudak, Akkoç, Karataş, Tüzün, & Aslan, 2022). Schiff bases are extensively utilized in organometalic chemistry. Owing to containing an imine group, they can easily coordinate with most metal ions (Shivakumar, Shashidhar, Vithal Reddy, & Halli, 2008; Yamada, 1999). Schiff bases have been reported to demonstrate wide spectrum of biologic activity such as antimalarial, antitumor, antimicrobial, antifungal, antibacterial, anti-inflammatory and analgesic, and antidepressant, activities (Dhar & Taploo, 1982; Przybylski, Huczynski, Pyta, Brzezinski, & Bartl, 2009).

Pyrimidine and thiophene derivatives last to be a subject of fascination and exploration, uncovering new areas for research and innovation in the range of chemistry and biology. Hence, synthesis and biological applications of these kind of heterocycles are of great significance in the range of medicinal and synthetic organic chemistry.

At this context, a Schiff base and a thiophen bearing pyrimidine derivative was synthesized and characterized by using elemental analysis and spectroscopic analysis including ^{1}H-NMR, ^{13}C-NMR and FT-IR. The general outline of the reaction is exhibited in Scheme 2. In the first step of the study, 1-aminopyrimidine-2-one derivative (**1**) was synthesized from methyleneaminopyrimidine derivative according to the literature procedure (**Scheme 1**) (Atioğlu, Karataş, & Kökbudak, 2021; Zülbiye Önal & Yıldırım, 2007). By a condensation reaction of (1) with commercially available 2-thiophenecarboxaldehyde in ethyl alcohol, ***Z)-5-benzoyl-4-phenyl-1-***

(thiophen-2-ylmethyleneamino)pyrimidin-2(1H)-one (**2**) was synthesized. In the reaction p-toluene sulfonic acid was used as a catalyst.
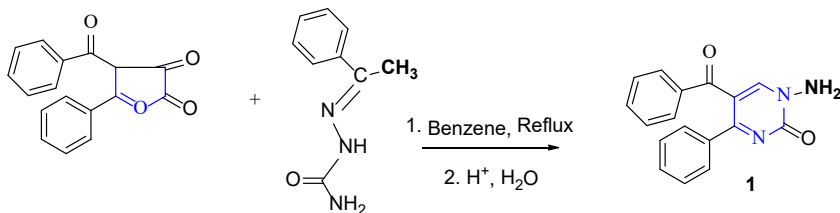
Scheme 1. Synthesis of N-aminopyrimidine (**1**)

In addition, molecular docking studies of compound (**2**), which was synthesized and whose structures were determined, were applied in this study. Molecular docking is undoubtedly the most preferred target-based method in computer-aided drug design methods recently. Whether it can be a drug candidate on anticancer or not has been investigated theoretically by interacting compound (**2**) with two different receptors. These receptors have been selected as Vascular Endothelial Growth Factor Receptor 2 (VEGFR-2) and Epidermal Growth Factor Receptor (EGFR), which are important in the cancer pathway. The targets used in molecular docking are EGFR) (O. Aboelez, Belal, Xiang, & Ma, 2022), VEGFR-2 (Aziz et al., 2016). In this study, the binding modes of compound (**2**) interacting with targets were analyzed with the Schrödinger 2021-2 Glide program (Schrödinger Release 2021-2: Glide).

2. Experimental

2.1. Reagents and Materials

Reagents and solvents used were commercially purchased. The starting material **1** was synthesized in our laboratory according to the literature procedure. The homogeneity was occasionally checked by TLC by using Camag TLC lamp (254/366 nm) and DC Alufolien Kieselgel 60 F254 (Merck). The spectra of the molecule were recorded using the facilities of Erciyes University (ERÜ) Technology Research and Application Center (TAUM). Microanalysis essay was done by Leco CHNSO-932 Elemental Analyzer. Digital melting point apparatus, Electrothermal 9100, was utilized as melting point determination.

2.2. Synthesis of (Z)-5-benzoyl-4-phenyl-1-(thiophen-2-ylmethyleneamino)pyrimidin-2(1H)-one (2)

The mixture of compound **1** (1 mmol) and 2-thiophenecarboxaldehyde (1.5 mmol) was refluxed for 7 hours in 15 mL of ethanol at presence of PTSA

as catalyst. After this time, ethyl alcohol was evaporated, and diethyl ether was added and stirred for a night. The Schiff base **2** obtained was purified with crystallization in ethyl alcohol. The synthesis scheme of (2) is in Scheme 2. Yield: 56%; m.p.: 197-199 °C; color: yellow. IR (cm⁻¹): 3100 (Aromatic C-H stretch) 1652.9 (C=O stretch), 1614,4 (C=N stretch). ¹H-NMR (400 MHz, DMSO-d₆): δ (ppm) = 9.43 (s, 1H, -N=CH), 8.62 (s, 1H, -CH in pyrimidine ring), 7.98-7.27 (m, 13H, Ar-H). ¹³C-NMR (100 MHz, DMSO) δ 192.09, 171.68, 161.39, 150.13, 148.77, 140.54, 137.29, 137.13, 137.00, 133.99, 131.29, 131.21, 130.04, 129.16, 129.12, 128.76, 128.36, 117.18. Elemental analysis calculated for $C_{22}H_{15}N_3O_2S$: C, 68.56; H, 3.92; O, 8.30. Found: C, 68.61; H, 3.88; O, 8,32

2.3. Molecular Docking Study

The procedure in the molecular docking method consists of three stages (İrem Bozbey Merde, Önel, Akkoç, Karaköy, & Türkmenoğlu, 2023; İrem B. Merde, Önel, Türkmenoğlu, Gürsoy, & Dilek, 2022):

The first step is to optimize the synthesized compound. This optimization procedure is calculated with the LigPrep interface (Schrödinger Release 2021-2: LigPrep) of the Schrödinger 2021-2 Glide program. The ligand preparation procedure was applied for compound **(2)** .

The second step is the preparation of the selected targets, which are downloaded from the protein database. The protein preparation procedure must be performed for each target individually. Since the interactions on two different targets were examined in this study, the ProteinPrep wizard of the Schrödinger 2021-2 Glide program was utilized for each target. In ligand-target calculation, compound **(2)** interacted with EGFR and VEGR-2 proteins, which are important in anticancer. Crystal structures of PDB ID: 4HJO (Park, Liu, Lemmon, & Radhakrishnan, 2012) for EGFR and PDB ID: 4ASD (McTigue et al., 2012) for VEGFR-2 were obtained from the protein database, respectively. Then, the coordinates of these proteins were determined with the Glide GridBox and the binding site with important amino acid residues was determined.

The third step is the *in silico* activation of the target determined with compound **(2)** used as the ligand. The determination of the ligand-target interactions was also realized with the Schrödinger 2021-2 software program. As a result of these interactions, both 3-dimensional interaction diagrams in the binding site and binding parameter values 2-dimensional and were obtained.

3. Results and Discussion

3.1. Characterization of Compound 2

In the first step, the compound (**1**) was prepared as reagent according to the literature (**Scheme 1**) and then, the new Schiff base (**2**) was obtained via reaction of the (**1**) and 2-thiophenecarboxaldehyde in yields 56%. By using spectroscopic methods and elemental analysis, structure of synthesized compound (**2**) was illuminated. The synthesis of compound (**2**) is simply explained in **Scheme 2.**
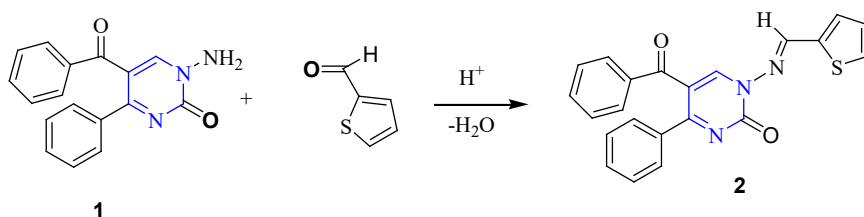
Scheme 2. Synthesis of (Z)-5-benzoyl-4-phenyl-1-(thiophen-2-ylmethyleneamino)pyrimidin-2(1*H*)-one (**2**)

The synthesis of compound (2) was achieved in 56% yield by the reaction of aminopyrimidine (compound (1)) and 2-thiophenecarboxaldehyde. In IR spectrum, the disappearance of a band at (3300-3200) cm^{-1} for (-NH$_2$) group which exists in start material. In the IR spectrum, the C=O absorption bands were observed at 1652.9 cm^{-1}. In ^{1}H-NMR, the singlet peak of -N=CH proton at 9,43 ppm and -CH proton in the pyrimidine ring at 8.62 ppm were marked. Between δ 7.99 and 7.28 ppm, aromatic protons were observed as multiplet. In ^{13}C NMR spectrum, eighteen peaks were shown for eighteen different carbon atoms in compound (**2**). ^{13}C NMR signals were observed at δ 192.09 and 171.86 (s, benzoly carbons' signal), 161.39 (imine carbon's peak) and 150.13-117.18 (m, aromatic carbons). The data obtained as a result of the analyzes fully confirmed the structure of Schiff base.

3.2. Molecular Docking

Considering drugs containing thiophene and pyrimidine rings that affect different diseases, the crystal structures interacting with these drugs have been theoretically investigated. With these determined crystal structures, compound (**2**) was labeled in molecular docking, respectively. As a result of this interaction,

both the active amino acid residues and the parameter values in the active region of the molecule were determined and presented.

Analyzed parameter values of compound **(2)** interacting with both EGFR and VEGFR-2 are presented in Table 1. The interaction values were calculated separately for each crystal structure in Table 1, and the binding modes were also examined.

First, the binding results of the EGFR target interacted with compound **(2)** in Table 1 were analyzed. These results are docking score, XP Gskor, Glide gscore, Glide energy, ΔG_{Bind} energy values, and Glide emodel are -5.907 kcal/mol, -5.907 kcal/mol, -5.907 kcal/mol -44.013 kcal/mol, -43.61 kcal/mol, -65.721 kcal/mol, respectively. It is known that among these values, especially the docking score and ΔG_{bind} energy values are important. These values in Table 1 are also remarkable.

Table 1. Binding parameter values of compound **(2)** interacting with EGFR (PDB ID: 4HJO) and VEGFR-2 (PDB ID: 4ASD) targets in molecular docking.

Parameters	EGFR-Compound (2)	VEGFR-2- Compound (2)
Docking Score	-5.907 kcal/mol	-6.171 kcal/mol
XP Gscore	-5.907 kcal/mol	-6.171 kcal/mol
Glide Gscore	-5.907 kcal/mol	-6.171 kcal/mol
Glide energy	-44.013 kcal/mol	-54.505 kcal/mol
Glide emodel	-65.721 kcal/mol	-74.309 kcal/mol
MM-GBSA ΔG_{Bind}	-43.61 kcal/mol	-43.93 kcal/mol

In addition to the numerical results of the EGFR- compound **(2)** interaction in Table 1, the binding modes were also investigated via *in silico* method. When the 2-dimensional and 3-dimensional interaction diagrams presented in Figure 2 were examined, it was determined that compound **(2)** was docked in the active binding site of the target. It also hydrogen bonded with Met769, one of the most important amino acid residues of EGFR in Figure 2. It is also docked in the active binding site.
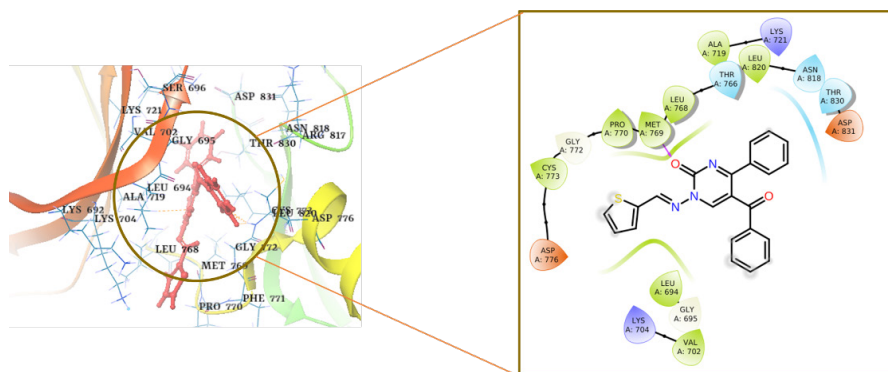
Figure 2. 2D and 3D interaction diagrams of compound
(2) with crystal structure PDB ID:4HJO.

In Table 1, the interaction values of the second target, VEGFR-2, and the docking results of compound **(2)** are presented. The docking score value between VEGFR-2 and compound **(2)** is -6.171 kcal/mol, the Glide energy value is -54.505 kcal/mol, the Glide emodel value is -74.309 kcal/mol and the free binding energy value is -43.93 kcal/mol.
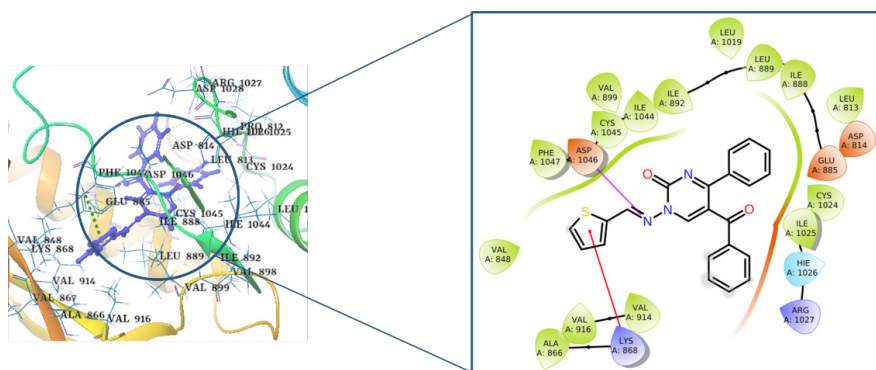
Figure 3. 2D and 3D interaction diagrams of compound
(2) with crystal structure PDB ID:4ASD.

The binding parameter value results between VEGFR-2 and compound **(2)** in Table 1 are also interesting. When the binding modes between the ligand and the target are examined in Figure 3, there is a hydrogen bond interaction with the amino acid Asp1046 and a cation-π bond interaction with the amino acid Lys868. It also interacts with important amino acids at the active binding site.

4. Conclusion

In this work, the new compound (**2**) was prepared by condensation reaction of the 1-aminopyrimidin-2(1*H*)-one (**1**) derivative and 2-thiophenecarboxaldehyde in absolute ethanol. The structure of synthesized compound (**2**) was supported by spectral analysis. The theoretical interaction of the synthesized compound (**2**) with the target crystal structures was investigated by molecular docking. The binding parameter values and binding modes of compound (**2**), which theoretically interacts with targets known to be important in cancer, such as both EGFR and VEGFR-2, are remarkable.

References

Akkoc, S., Karatas, H., Muhammed, M. T., Kökbudak, Z., Ceylan, A., Almalki, F., . . . Ben Hadda, T. (2022). Drug design of new therapeutic agents: molecular docking, molecular dynamics simulation, DFT and POM analyses of new Schiff base ligands and impact of substituents on bioactivity of their potential antifungal pharmacophore site. *Journal of Biomolecular Structure and Dynamics*, 1-14. doi:10.1080/07391102.2022.2111360

Aslan, G., Akkoç, S., Akkurt, M., Özdemir, N., & Kökbudak, Z. (2018). Synthesis, spectroscopic characterization and catalytic activity of 1-(2-hydrox-ybenzylideneamino)-5-(4-methylbenzoyl)-4-(4-methylphenylpyrimidin)-2 (1 H)-one. *Journal of the Chinese Advanced Materials Society*
6(2), 145-155.

Aslan, G., & Onal, Z. (2014). Novel metal complexes, their spectrophotometric and QSAR studies. *Medicinal Chemistry Research, 23*(5), 2596-2607.

Aslan, H. G., Akkoç, S., & Kökbudak, Z. (2020). Anticancer activities of various new metal complexes prepared from a Schiff base on A549 cell line. *Inorganic Chemistry Communications, 111*, 107645.

Aslan, H. G., Akkoç, S., Kökbudak, Z., & Aydın, L. (2017). Synthesis, characterization, and antimicrobial and catalytic activity of a new Schiff base and its metal (II) complexes. *Journal of the Iranian Chemical Society, 14*(11), 2263-2273.

Åslund, A., Sigurdson, C. J., Klingstedt, T., Grathwohl, S., Bolmont, T., Dickstein, D. L., . . . Konradsson, P. (2009). Novel pentameric thiophene derivatives for in vitro and in vivo optical imaging of a plethora of protein aggregates in cerebral amyloidoses. *ACS chemical biology, 4*(8), 673-684.

Atioğlu, Z., Karataş, H., & Kökbudak, Z. (2021). The crystal structure of 5-benzoyl-1-[(E)-(4-fluorobenzylidene) amino]-4-phenylpyrimidin-2 (1H)-one, C24H16FN3O2. *Zeitschrift für Kristallographie-New Crystal Structures, 236*(5), 1035-1037.

Aziz, M. A., Serya, R. A. T., Lasheen, D. S., Abdel-Aziz, A. K., Esmat, A., Mansour, A. M., . . . Abouzid, K. A. M. (2016). Discovery of potent VEGFR-2 inhibitors based on furopyrimidine and thienopyrimidne scaffolds as cancer targeting agents. *Scientific reports, 6*(1), 24460.

Cakmak, R., Basaran, E., & Senturk, M. (2022). Synthesis, characterization, and biological evaluation of some novel Schiff bases as potential metabolic enzyme inhibitors. *Archiv Der Pharmazie, 355*(4). doi:ARTN e2100430

10.1002/ardp.202100430

Çimen, Z., Akkoç, S., & Kökbudak, Z. (2018). Reactions of aminopyrimidine derivatives with chloroacetyl and isophthaloyl chlorides. *Heteroatom Chemistry, 29*(4), e21458.

da Silva, C. M., da Silva, D. L., Modolo, L. V., Alves, R. B., de Resende, M. A., Martins, C. V. B., & de Fátima, Â. (2011). Schiff bases: A short review of their antimicrobial activities. *Journal of Advanced Research, 2*(1), 1-8.

Dhar, D. N., & Taploo, C. (1982). Schiff-bases and their applications. *Journal of Scientific*

Industrial Research, 41(8), 501-506.

Gupta, J. K., Chaudhary, A., Dudhe, R., Varuna, K., Sharma, P., & Verma, P. (2010). A review on the synthesis and therapeutic potential of pyrimidine derivatives. *International journal of pharmaceutical sciences and research, 1*(5), 34-49.

Jasinska, A., Szklarzewicz, J., Jurowska, A., Hodorowicz, M., Kazek, G., Mordyl, B., & Gluch-Lutwin, M. (2022). V(III) and V(IV) Schiff base complexes as potential insulin-mimetic compounds - Comparison, characterization and biological activity. *Polyhedron, 215*. doi:ARTN 115682

10.1016/j.poly.2022.115682

Kökbudak, Z., Akkoç, S., Karataş, H., Tüzün, B., & Aslan, G. (2022). In Silico and In Vitro Antiproliferative Activity Assessment of New Schiff Bases. *Chemistryselect, 7*(3), e202103679.

Kökbudak, Z., Aslan, H., & Akkoç, S. (2020). New Schiff Bases Based on 1-Aminopyrimidine-2-(1H)-one: Design, Synthesis, Characterization and Theoretical Calculations. *Heterocycles, 100*(3).

Kökbudak, Z., Saracoglu, M., Akkoç, S., Cimen, Z., Yilmazer, M. I., & Kandemirli, F. (2020). Synthesis, cytotoxic activity and quantum chemical calculations of new 7-thioxopyrazolo [1, 5-f] pyrimidin-2-one derivatives. *Journal of Molecular Structure, 1202*, 127261.

Lagoja, I. M. (2005). Pyrimidine as constituent of natural biologically active compounds. *Chemistry Biodiversity, 2*(1), 1-50.

Liu, M., Chen, Y., Zhang, C., Li, C., Li, W., & Bo, Z. (2013). Synthesis of thiophene-containing conjugated polymers from 2, 5-thiophenebis (boronic ester) s by Suzuki polycondensation. *Polymer Chemistry, 4*(4), 895-899.

McTigue, M., Murray, B. W., Chen, J. H., Deng, Y.-L., Solowiej, J., & Kania, R. S. (2012). Molecular conformations, interactions, and properties associated with drug efficiency and clinical performance among VEGFR TK inhibitors. *Proceedings of the National Academy of Sciences, 109*(45), 18281-18289.

Merde, İ. B., Önel, G. T., Akkoç, S., Karaköy, Z., & Türkmenoğlu, B. (2023). Focusing on New Piperazinyl-methyl-3 (2H) pyridazinone Based Derivatives: Design, Synthesis, Anticancer Activity and Computational Studies. *ChemistrySelect, 8*(25), e202300910.

Merde, İ. B., Önel, G. T., Türkmenoğlu, B., Gürsoy, Ş., & Dilek, E. (2022). Pyridazinones containing the (4-methoxyphenyl) piperazine moiety as AChE/BChE inhibitors: design, synthesis, in silico and biological evaluation. *Medicinal Chemistry Research, 31*(11), 2021-2031.

Mishra, R., Jha, K., Kumar, S., & Tomer, I. (2011). Synthesis, properties and biological activity of thiophene: A review. *Der Pharma Chemica, 3*(4), 38-54.

O. Aboelez, M., Belal, A., Xiang, G., & Ma, X. (2022). Design, synthesis, and molecular docking studies of novel pomalidomide-based PROTACs as potential anti-cancer agents targeting EGFRWT and EGFRT790M. *Journal of Enzyme Inhibition and Medicinal Chemistry, 37*(1), 1196-1211.

Ono, A., Torigoe, H., Tanaka, Y., & Okamoto, I. (2011). Binding of metal ions by pyrimidine base pairs in DNA duplexes. *Chemical society reviews, 40*(12), 5855-5866.

Önal, Z., & Altural, B. (1999). Reactions of N-aminopyrimidine derivatives with 1, 3-dicarbonyl compounds. *Turkish Journal of Chemistry, 23*(4), 401-406.

Önal, Z., & Altural, B. (2006). Reactions of 1-amino-5-benzoyl-4-phenyl-1H-pyrimidine-2-thione with various carboxylic anhydrides. *Asian Journal of Chemistry, 18*(2).

Önal, Z., & Daylan, A. (2007). Reactions of 1-Amino-5-benzoyl-4-phenyl-1H-pyrimidine derivatives with various isothiocyanates. *Asian Journal of Chemistry, 19*(4).

Önal, Z., & Yıldırım, İ. (2007). Reactions of 4-(4-methylbenzoyl)-5-(4-methylphenyl)-2, 3-furandione with semi-/thiosemi-carbazones. *Heterocyclic Communications, 13*(2-3), 113-120.

Park, J. H., Liu, Y., Lemmon, M. A., & Radhakrishnan, R. (2012). Erlotinib binds both inactive and active conformations of the EGFR tyrosine kinase domain. *Biochemical Journal, 448*(Pt 3), 417.

Przybylski, P., Huczynski, A., Pyta, K., Brzezinski, B., & Bartl, F. (2009). Biological properties of Schiff bases and azo derivatives of phenols. *Current Organic Chemistry, 13*(2), 124-148.

Schrödinger Release 2021-2: Glide, S., LLC, New York, NY, 2021.

Schrödinger Release 2021-2: LigPrep, S., LLC, New York, NY, 2021.

Shivakumar, K., Shashidhar, Vithal Reddy, P., & Halli, M. (2008). Synthesis, spectral characterization and biological activity of benzofuran Schiff bases with Co (II), Ni (II), Cu (II), Zn (II), Cd (II) and Hg (II) complexes. *Journal of Coordination Chemistry, 61*(14), 2274-2287.

Turkoglu, G., Cinar, M. E., & Ozturk, T. (2019). Thiophene-based organic semiconductors. *Sulfur Chemistry*, 79-123.

Wang, L. (2016). Mitochondrial purine and pyrimidine metabolism and beyond. *Nucleoside, Nucleotides Nucleic Acids, 35*(10-12), 578-594.

Yamada, S. (1999). Advancement in stereochemical aspects of Schiff base metal complexes. *Coordination Chemistry Reviews, 190*, 537-555.

SEROTONERGIC SYSTEM AND POULTRY: A NUTRIGENOMICS PERSPECTIVE

Orcun AVSAR[1] & Menderes SUICMEZ[2]

[1](Assist. Prof. Dr.), Hitit University, Faculty of Arts
and Sciences, Department of Molecular Biology and Genetics
E-mail: orcunavsar@hitit.edu.tr
ORCID: 0000-0003-3556-6218

[2](Prof. Dr.), Hitit University, Department of Molecular Biology and
Genetics
E-mail: menderessuicmez@hitit.edu.tr
ORCID:0000-0003-0890-8235

1. Introduction

Advances in animal breeding and the feed industry have made it possible to achieve the desired quality and quantity of yield in poultry. In addition to these improvements in phenotypic traits, in recent years, in parallel with developments in molecular biology and genetics, research in animal genetics and biotechnology has sought to elucidate the molecular mechanisms of parameters related to complex quantitative traits such as productivity and quality in poultry. In this context, recent developments in molecular genetics have led to the emergence of new fields such as 'nutrigenomics' and 'nutrigenetics', based on scientific knowledge of the effects of diet on the genome and developments in omics technologies.

2. Nutrigenomic Studies in Poultry

While nutrigenomics is the study of how nutrients, food forms and dietary strategies affect the genome, nutrigenetics is a subset of nutrigenomics that focuses on understanding how genetic variants interact with nutrients and the consequences of these interactions (Figure 1) (Ferguson et al., 2016). From a nutrigenomics perspective, nutrients are being considered as signalling

molecules that can be detected by the cell and affect metabolite generation and gene and protein expression (Ganguly et al., 2018). From a genetic perspective, nutrients act as transcription factors that bind to DNA and, after interacting with the appropriate receptor, can induce gene expression (Bouchard-Mercier et al., 2013). Nutrigenomic applications, including genomic, proteomic and transcriptomic technologies, is designed to help understand how nutrition affects the genome and the mechanisms underlying these relationships when assessing the quality and quantity of poultry yields (Ipcak et al., 2015). In addition, the use of DNA microarray technology allows the researchers to elucidate how nutrition alters gene expression and how this modulation is associated with animal performance and health. One of the most important environmental factors causing various changes in the poultry genome is nutrition. Feed ingredients, nutrient levels and feed additives in poultry diets have been reported to affect gene expression in different ways (Ipcak, 2017; Ganguly et al., 2018). First, they can act as direct ligands, such as transcription factors, and alter gene expression. Secondly, the concentration of substrates or products resulting from the metabolism of feed ingredients by different pathways can alter gene expression. Thirdly, nutrients or metabolites can directly affect cell signalling, which is responsible for gene expression. For example, changes in gene expression occur in pancreatic beta cell, liver, muscle, and adipose tissue, etc. (Figure 2) (Berná et al., 2014). They can regulate improved performance and animal health by influencing biological systems.

Nutrigenomic studies in broilers have been used to explain the underlying reasons for the relationship between feeding with different compound feeds or feed additives and productivity (Alagawany et al., 2022). Nutrigenomic studies can help us fully understand the effects of compound feeds and feeding practices used by revealing patterns of gene expression that are associated with early feeding. Thus, nutrigenomics offers a way to define exactly which feeds and feed additives used in compound feeds should be fed to poultry, at what levels and when to achieve maximum benefit (Jha et al., 2019). It has been reported that when broiler chickens are fed mixed diets with a high mineral content (100% NRC) in the early stages, there is an increase in the expression level of the cyclin D1 gene, which is involved in cell cycle regulation in broilers and is important for gut health (Brennan, 2015). In a study of turkey embryos exposed to heat stress, it was reported that selenium supplementation reduced the expression of the hsp70 gene, allowing the stressed embryos to continue to grow normally (Ganguly et al., 2018). Nutrigenomics seeks to

elucidate the biological mechanisms underlying the interactions between the genome and nutrients in poultry (Meroni et al., 2020) and it is very effective in the understanding the effects of nutrition on performance, health and disease in poultry. In this context, information from nutrigenomic studies will help poultry breeders and producers to understand how poultry should be fed for optimal performance and health, and to develop new compound feeds and feeding programmes (Brennan, 2015).

Early development of the gastrointestinal system in broiler chickens is critical for both maximising nutrient utilisation and optimising growth in poultry. It has been reported that during the early period of feeding, especially the composition of the pre-start mixes, the digestibility of the nutrients and the feed additives added to the mixes have a significant effect on the fattening performance and the immune system of broiler chickens in the future (Jha et al., 2019; Ravindran and Abdollahi, 2021). However, understanding the effects of feeding different pre-start rations on the growth performance, gut microbiota, immune system and health of broiler chickens requires an understanding of how the nutrients in different pre-start rations affect the expression of specific genes or metabolic pathways (Ganguly et al., 2018).

It has also been determined that the feeding of different pre-starter diets to broiler chickens has a significant effect on the content of microorganisms in the gut (Adewole and Akinyemi, 2021; Zhang et al., 2022). Recently, it has been found that altering the gut microbial content, depending on the composition of the diet and the additives added to the diet, can significantly affect the brain function, feed consumption and welfare of broiler chickens (Kogut, 2022). This interaction between the gut microbiota and the brain has led to the concept of the microbiota-gut-brain axis, which is modulated by the composition and nutrient content of the compound feed consumed (Foster and McVey Neufeld, 2013). In other words, interaction between the central nervous system and the gut microbiota involves the hypothalamic-pituitary-adrenal (HPA) axis, the vagus nerve, and the immune system. Depending on the composition of the diet consumed by poultry, molecules such as various metabolites, short fatty acid chains, acetylcholine, histamine, dopamine, serotonin and GABA synthesized by the gut microbiota are thought to influence brain function (Gonzalez-Arancibia et al., 2019). For example, it has been shown that stimulation of vagal afferent fibres from the upper intestinal tract in birds causes the release of various neurotransmitters such as serotonin, dopamine, norepinephrine and GABA in the brain and affects neurotransmission (Han et al., 2018).
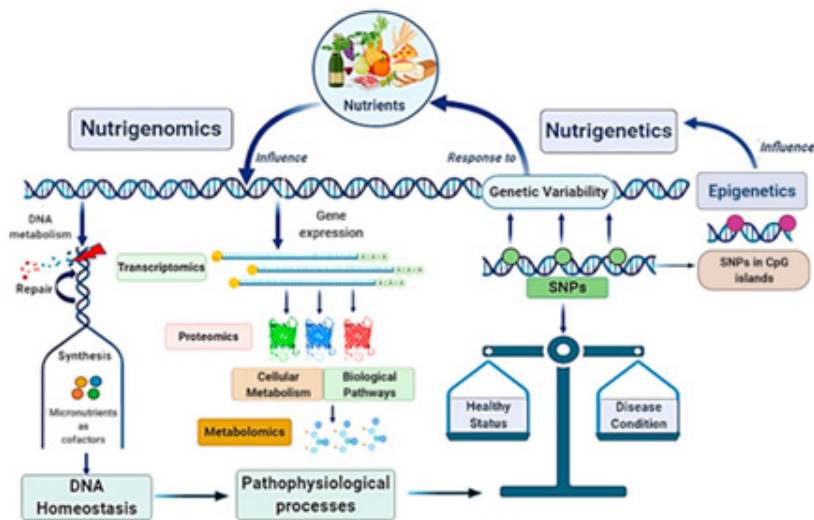
Figure 1. Nutrigenomics versus nutrigenetics (Dallio et al., 2021).
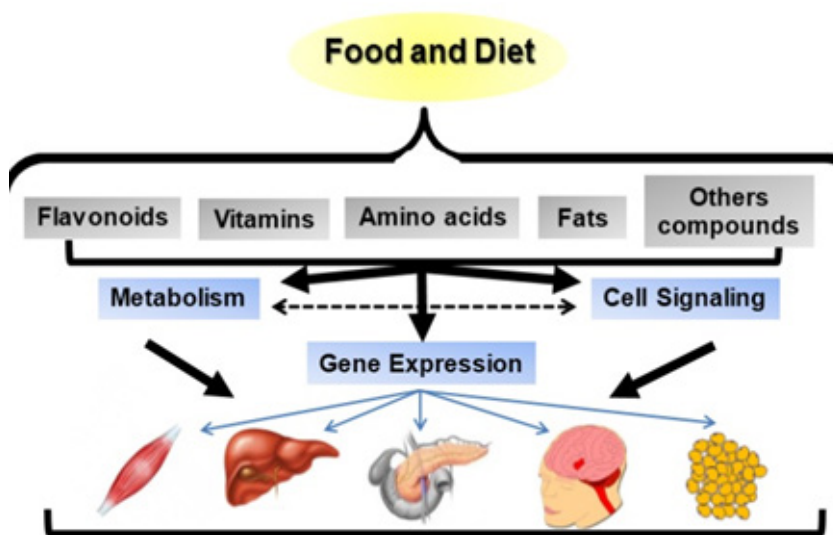
Figure 2. Nutrients come from food and diet may alter gene expression in different ways (Berná et al., 2014).

3. Serotonergic (5-HTergic) System in Broilers

The serotonergic system includes the central neurotransmitter serotonin and the peripheral signalling molecule serotonin (de Haas and van der Eijk, 2018). Serotonin (5-hydroxytryptamine, 5-HT) is a bioamine neurotransmitter

produced in the central nervous system from the amino acid tryptophan and modulates various physiological functions such as appetite, growth, reproduction, sleep, pain, emotion, cognition, acquisition of feed consumption habits, foraging behavior, feed intake and welfare in poultry. Serotonin (5-HT) is also a morphogen that influences the development of the embryonic brain. Serotonin is known to inhibit hyperphagia in the central nervous system of birds, thereby reducing nutrient consumption (Zendehdel et al., 2017; Fujita et al., 2022). Furthermore, serotonin has an effect on the physical, physiological and mental health of animals (Huang et al., 2019).

However, it is not yet known how serotonergic genes in the central nervous system are regulated by different starter diets fed to broilers in the early period. It is hypothesised that feeding broiler chickens different pre-start rations in the early period may differentially affect the gut microbiota and, indirectly, the serotonergic system in the central nervous system. This is because the feeding of broiler chickens with different rations is reported to be the most important factor that changes the gut microbiota (Pan and Yu, 2014). Changes in serotonin secretion in the central nervous system may also alter the feed intake and feeding habits of broilers and broiler chickens (Baranyiova, 1990; Kjaer and Phi-van, 2016). Depending on the change in feed and nutrient consumption, the microbial content and morphological structure of the small intestine and the fattening performance of broilers and chickens may also change.

On the other hand, enterochromaffin cells, a type of neuroendocrine cell in the gut, synthesise non-neuronal serotonin in chickens (Lyte et al., 2021). Peripheral serotonin is mainly found in the enterochromaffin cells and in the platelets of the blood. Peripheral serotonin is involved in gut motility, immune regulation, secretion, inflammation, energy metabolism, and vasoconstriction/dilation. Peripheral and central serotonin interact each other in the bloodstream and are influenced by vagus nerve activation, microbiota in the gut, hormones, short-chain fatty acids (SCFAs), enzymes, and cytokines (Figure 3) (de Haas and van der Eijk, 2018).

Tryptophan, the precursor of 5-HT, is used as a feed additive and is of interest because it cannot be produced in sufficient quantities by the animal's own body. Tryptophan supplementation in poultry has been reported to improve the performance of growth by influencing feed efficiency, appetite, protein synthesis, amino acid balance and immune response (Linh et al., 2021). Tryptophan as a supplement in poultry diets has been shown to affect egg and meat quality, productivity, antioxidant status, and the immune system through

the stimulation of the serotonergic system (Figure 4). The genetic background of the broiler, the amount of tryptophan in the diet and the physiological status of the broiler influence the improvement of meat and egg quality, immunity and productivity in poultry (Fouad et al., 2021).
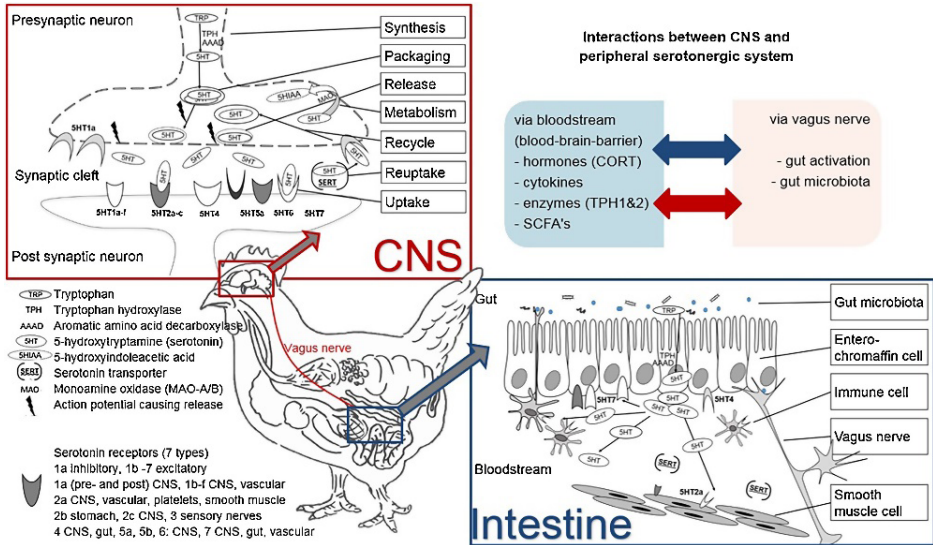
Figure 3. The chicken's serotonergic system (de Haas and van der Eijk, 2018).
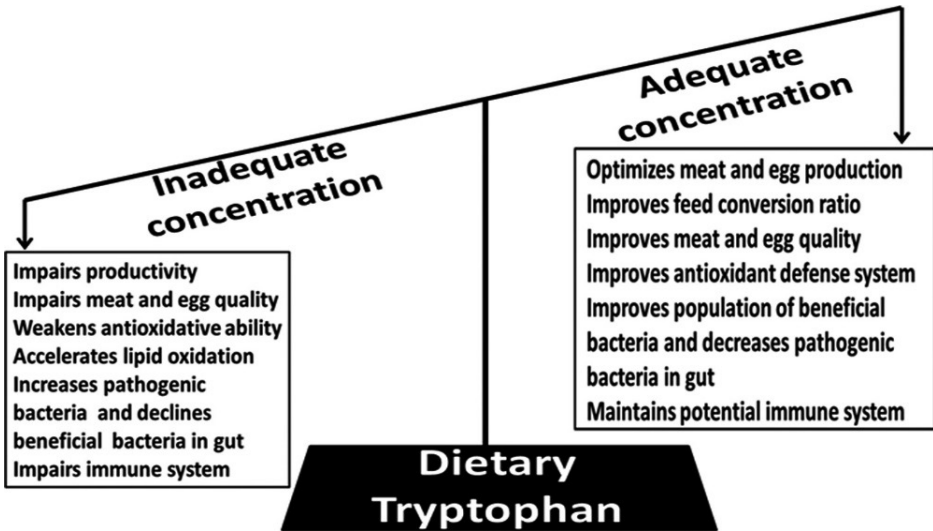
Figure 4. Effects of tryptophan supplementation in poultry
(Fouad et al., 2021).

4. Conclusion

The central and peripheral serotonergic system is crucial for the physical and mental health of broilers and chickens. Therefore, the serotonergic system may have a major influence on the quality and quantity of yield in poultry. It needs to be clarified in detail how feeding with different diets affects the genes associated with the serotonergic system such as *TPH2, SERT, 5-HT2A* and *5-HT2C* genes in broilers. Therefore, there is a need for more comprehensive nutrigenomic studies to elucidate the effect of the serotonergic system in broilers and chickens.

References

Adewole, D., Akinyemi, F. (2021). Gut microbiota dynamics, growth performance, and gut morphology in broiler chickens fed diets varying in energy density with or without bacitracin methylene disalicylate (BMD). *Microorganisms,* 9(4):787.

Alagawany, M., Elnesr, S.S., Farag, M.R., El-Naggar, K., Madkour, M. (2022). Nutrigenomics and nutrigenetics in poultry nutrition: An updated review. *World's Poultry Science Journal,* 78(2): 377-396.

Baranyiova, E. (1990). Effects of serotonin on the food intake in chickens in the early post-hatching period. *Acta Veterinaria Brno,* 59: 23-33.

Berná, G., Oliveras-López, M.J., Jurado-Ruíz, E., Tejedo, J., Bedoya, F., Soria, B., Martín, F. (2014). Nutrigenetics and nutrigenomics insights into diabetes etiopathogenesis. *Nutrients,* 6(11):5338-69.

Bouchard-Mercier, A., Paradis, A.M., Rudkowska, I., Lemieux, S., Couture, P., Vohl, M.C. (2013). Associations between dietary patterns and gene expression profiles of healthy men and women: a cross-sectional study. *Nutrition Journal,* 12: 24.

Brennan, K.M. (2015). Practical applications of nutrigenomics poultry nutrition. *26th Australian Poultry Science Symposium,* Sydney, New South Wales.

Dallio, M., Romeo, M., Gravina, A.G., Masarone, M., Larussa, T., Abenavoli, L., Persico, M., Loguercio, C., Federico, A. (2021). Nutrigenomics and nutrigenetics in metabolic- (dysfunction) associated fatty liver disease: novel insights and future perspectives. *Nutrients,* 13(5):1679.

de Haas, E.N., van der Eijk, J.A.J. (2018). Where in the serotonergic system does it go wrong? Unravelling the route by which the serotonergic

system affects feather pecking in chickens. *Neuroscience and Biobehavioral Reviews,* 95:170-188.

Ferguson, J.F., Allayee, H., Gerstzen, R.E., Ideraabdullah, F., Kris-Etherton, P.M., Ordovas, J.M., Rimm, E.B., Wang, T.J., Bennett, B.J. (2016). Nutrigenomics, the microbiome, and the gene-environment interactions: New directions in cardiovascular disease research, prevention and treatment: A scientific statement from the American Heart Association. *Circulation: Cardiovascular Genetics,* 9: 291-313.

Foster, J.A., McVey Neufeld, K.A. (2013). Gut-brain axis: how the microbiome influences anxiety and depression. *Trends in Neurosciences,* 36(5):305-12.

Fouad, A.M., El-Senousey, H.K., Ruan, D., Wang, S., Xia W., Zheng, C. (2021). Tryptophan in poultry nutrition: Impacts and mechanisms of action. *Journal of Animal Physiology and Animal Nutrition,* 105(6):1146-1153.

Fujita, T., Aoki, N., Mori, C., Fujita, E., Matsushima, T., Homma, K.J., Yamaguchi, S. (2022). Serotonergic neurons in the chick brainstem express various serotonin receptor subfamily genes. *Frontiers in Physiology,* 12:815997.

Ganguly, S., Para, P.A. (2018). Nutrigenomics in poultry nutrition- An overview. Recent Research Trends in Veterinary Sciences and Animal Husbandary. 1:15-30.

Gonzalez-Arancibia, C., Urrutia-Pinones, J., Illanes-Gonzalez, J., Martinez-Pinto, J., Sotomayor-Zarate, R., Julio-Pieper, M., Bravo, J.A. (2019). Do your gut microbes affect your brain dopamine? *Psychopharmacology,* 236: 1611-1622.

Han, W., Tellez, L.A., Perkins, M.H., Perez, I.O., Qu, T., Ferreira, J., Ferreira, T.L., Quinn, D., Liu, Z.W., Gao, X.B., Kaelberer, M.M., Bohórquez, D.V., Shammah-Lagnado, S.J., de Lartigue, G., de Araujo, I.E. (2018). A neural circuit for gut-induced reward. *Cell,* 175(3):665-678.e23.

Huang, X., Kuang, S., Applegate, T.J., Lin, T.L., Cheng, H.W. (2019). The development of the serotonergic and dopaminergic systems during chicken mid-late embryogenesis. *Molecular and Cellular Endocrinology,* 493:110472.

Ipcak, H.H., Isık, R., Alcicek, A. (2015). Nutrigenomics; an emerging science in poultry production. *3rd International Poultry Meat Congress,* Antalya, Turkey.

Ipcak, H.H., Ozuretmen, S., Keskin, N., Alcicek, A. (2017). Besin maddelerinin kanatlı hayvanların gen ekspresyon seviyeleri üzerine etkileri. *4th International Poultry Meat Conference,* Antalya, Turkey.

Jha, R., Singh, A.K., Yadav, S., Berrocoso, J.F.D., Mishra, B. (2019). Early nutrition programming (in ovo and post-hatch feeding) as a strategy to modulate gut health of poultry. *Frontiers in Veterinary Science,* 6: 82.

Kjaer, J.B., Phi-van, L. (2016). Evidence for the association of a deleted variant in the 5′-flanking region of the chicken serotonin transporter (5-HTT) gene with a temporary increase in feed intake and growth rate. *Animals,* 6(10):63.

Kogut, M.H. (2022). Role of diet-microbiota interactions in precision nutrition of the chicken: facts, gaps, and new concepts. *Poultry Science,* 101(3):101673.

Linh, N.T., Guntoro, B., Hoang Qui, N. (2021). Immunomodulatory, behavioral, and nutritional response of tryptophan application on poultry. *Veterinary World,* 14(8):2244-2250.

Lyte, J.M., Shrestha, S., Wagle, B.R., Liyanage, R., Martinez, D.A., Donoghue, A.M., Daniels, K.M., Lyte, M. (2021). Serotonin modulates Campylobacter jejuni physiology and invitro interaction with the gut epithelium. *Poultry Science,* 100(3):100944.

Meroni, M., Longo, M., Rustichelli, A., Dongiovanni, P. (2020). Nutrition and genetics in NAFLD: The perfect binomium. *International Journal of Molecular Sciences,* 21: 2986.

Pan, D., Yu, Z. (2014). Intestinal microbiome of poultry and its interaction with host and diet. *Gut Microbes,* 5(1):108-19.

Ravindran, V., Abdollahi, MR. (2021). Nutrition and digestive physiology of the broiler chick: State of the art and outlook. *Animals (Basel),* 11(10):2795.

Zendehdel, M., Sardari, F., Hassanpour, S., Rahnema, M., Adeli, A., Ghashghayi, E. (2017). Serotonin-induced hypophagia is mediated via α2 and β2 adrenergic receptors in neonatal layer-type chickens. *British Poultry Science,* 58: 298-304.

Zhang, Q., Zhang, S., Wu, S., Madsen, M.H., Shi, S. (2022). Supplementing the early diet of broilers with soy protein concentrate can improve intestinal development and enhance short-chain fatty acid-producing microbes and short-chain fatty acids, especially butyric acid. *Journal of Animal Science and Biotechnology,* 13(1):97.

SOME FRUIT AND TREE CHARACTERISTICS OF POMEGRANATE VARIETIES GROWED IN KOCAKÖY DISTRICT OF DIYARBAKIR

Semra BURKAN[1]& Sevcan AYTAÇ[2]

[1]*Fırat University, Deparment of Biotechnology, Elazığ*
E-mail: semra_burkan@hotmail.com
ORCID: 0000-0003-1214-9534

[2]*Fırat University, Deparment of Electronics and Automation, Elazığ*
E-mail: saytac@firat.edu.tr
ORCID: 0000-0001-6689-2337

1. Introduction

The biodiversity of plant species other than pomegranate, fig, almond, walnut and pistachio is a common rich heritage of people and a source of national wealth for other countries. Some measures should be taken to protect this heritage and pass it on to future generations. The most important of these are scientific studies that will determine all the life forms of all plants in the countries (Şimşek ve Kara, 2016; Burkan, S., 2018).

Pomegranate is one of the important fruit species that has been cultivated since ancient times, and it is stated that its fruit has been eaten by human beings for approximately 6500 years and has been used as a cure for some diseases. In addition, it is estimated that the first written sources on the name of pomegranate were written in the mid-16th century BC. It is stated that the name pomegranate passed from Persian to Turkish (Anonim, 2008; Burkan, S., 2018).

In (Şimşek ve İkinci, 2017; Burkan, S., 2018), As a result of many studies on pomegranate (Punica granatum L.), its importance is increasing in our age due to its benefits to human health. While this fruit is consumed fresh, it can be processed into fruit juice and concentrate, wine, jam and liqueur, and is used as

a colorant and sweetener in various foodstuffs. At the same time, pomegranate fruit has a positive effect on human health.

As it is known, Pomegranate, known as the fruit of the subtropical and tropical climate zone, belongs to the Punicaceae family of the Myrtiflora order, and its most important species is Punica granatum (Tibet ve Baktır, 1991; Burkan, S., 2018). The South Caucasus, which is considered the homeland of pomegranate, is the region between South Asia, West Asia, Iran, Afghanistan, Anatolia and the Mediterranean (Dokuzoğuz ve Mendilcioğlu, 1978; Burkan, S., 2018). As a result, there are pomegranate genotypes that can grow wild in many parts of our country (Tibet ve Baktır, 1991; Burkan, S., 2018). In general, in addition to the fact that the pomegranate plant can grow in many different soil types, it has been determined that its trees can withstand temperatures down to -10 oC, whereas it has been observed that the branches die at temperatures of -15 oC and below, and the entire pomegranate tree dies at -20 oC. On the other hand, it has been determined that there are some types of two and older branches that can withstand temperatures down to –20 oC (Anonim, 2016; Burkan, S., 2018). Therefore, it has been shown that this fruit species has a wide distribution area (Yılmaz, 2007; Burkan, S., 2018).

In some regions of our country, the pomegranate tree is grown as a hedge and ornamental plant on the edges of gardens. However, in recent years, this type of fruit has been grown in closed gardens. Pomegranates sometimes adapt to different ecologies. This type of fruit is easy to propagate. Fruit can be obtained from the pomegranate tree at an early age. In addition, high productivity can be achieved in the area where the pomegranate garden is established. (Gündoğdu ve ark., 2015; Burkan, S., 2018).

The pomegranate plant is evaluated differently. For example, the tree, fruit, shape, root, trunk, leaves and flowers of pomegranate have been the subject of various branches of art and are often evaluated in these fields. In addition, since pomegranate is consumed fresh, this fruit is used in molasses, sour, juice, canned and vinegar. In addition, this fruit is used in the dye and pharmaceutical industry, citric acid and animal feed and in some industrial areas. Vegetable oil can be produced from pomegranate seeds, and knitted baskets and baskets can be made from its branches. Fresh pomegranate fruit and its juice are both refreshing and digestive, and are sometimes used as a refreshing additive in drinks (Onur 1983; Burkan, S., 2018).

The flowers of the pomegranate tree are bisexual. These flowers are eye-catching with their bright orange and red colors. They occur singly or in small clusters on spur branches. Their calyx ring is tubular, can consist of up to 5 to

7 divisions, and is spear-like in shape. There are two types of flowers on the pomegranate tree. In the first, the calyx of the flowers is cylindrical and wide. Their flowers are the size of a small pomegranate fruit and these are the flowers that form the fruit on the pomegranate tree. In the second, the flowers are both abortive and sterile, and they do not bear fruit (Dokuzoğuz ve Mendilcioğlu 1978; Burkan, S., 2018).

Although some studies have been conducted on pomegranate genotypes and varieties in various regions of Turkey, as a result of scanning the literature, it has been determined that, to my knowledge, no research has been conducted on the determination of fruit quality and some chemical properties of pomegranates grown in both Diyarbakır province and its affiliated districts. This study was conducted in the regions where intensive pomegranate cultivation is carried out in Kocaköy district. Therefore, it is useful to conduct research. Local and important standard pomegranate varieties grown in the Kocaköy district of Diyarbakır province in the Southeastern Anatolia Region are highly appreciated by consumers. The majority of these pomegranates consist of local pomegranate varieties such as Hınara Tırş, Hınara Şirin, Hınara Zer, Hınara Sor and Hınara Meğoş, Zivzik and Hicaz standard pomegranate varieties, as well as pomegranates that are loved and consumed by the local people. However, no research has been conducted on pomegranate varieties and genotypes in this district to date. For this reason, pomological and some tree and fruit characteristics of local and important standard pomegranate varieties grown in Kocaköy district were determined. Türkiye Agricultural Production Map is given in Figure 1.1.

Figure 1.1. Türkiye agricultural production map (Anonymous, 2017a; Burkan, S., 2018).

According to the Turkish Statistical Institute, Turkey's Pomegranate Production values on a regional basis are given (Table 1.1). As a result, pomegranate cultivation is carried out in Turkey, which is among the top pomegranate-producing countries, especially in the Mediterranean, Aegean and Southeastern Anatolia regions. 465,200 tons of pomegranate was produced in our country. The region with the highest pomegranate production was the Mediterranean with 247,422 tons, and the second place was in the Aegean with 151,339 tons. The region with the least pomegranate production is Northeastern Anatolia with 13 tons.

Table 1.1. Pomegranate production values by regions of Turkey
(TUIK, 2016; Burkan, S., 2018)

Regions	Area of mass orchards	Production	Average yield per tree	Number of trees of fruit-bearing age	Number of trees that do not bear fruit	Total number of trees
Mediterrenian	136.181	247.422	40	6.248.877	1.488.804	7.737.681
Aegean	87.313	151.339	33	4.590.972	749.423	5.340.395
S.Eastern Anatolia	71.980	53.352	21	2.510.750	1.053.642	3.564.392
Eastern Marmara	5.004	7.390	28	263.641	38.275	301.916
Western Marmara	2.386	2.246	21	108.013	63.943	171.956
West anatolia	1.865	1.926	41	47.065	53.260	100.325
West Blacksea	162	656	21	30.901	9.842	40.743
East Blacksea	0	276	16	17.402	9.597	26.999
Istanbul	30	33	17	1.930	380	2.310
N.Eastern Anatolia	0	13	37	350	35	385
Turkey	305.302	465.200	27.5	13.858.784	3.481.808	17.340.592

Table 1.2. Production values of our important provinces in pomegranate production (TUIK, 2016; Burkan, S., 2018).

Provinces	Area of mass orchards	Production	Average yield per tree	Number of trees of fruit-bearing age	Number of trees that do not bear fruit	Total number of trees
Antalya	56.252	111.041	40	2.797.054	505.632	3.302.686
Muğla	35.161	73.183	37	1.964.893	144.503	2.109.396
Mersin	40.741	66.595	46	1.448.740	505.643	1.954.383
Adana	21.345	44.861	44	1.013.660	153.855	1.167.515
Denizli	26.339	44.751	32	1.418.142	280.340	1.698.482
Hatay	12.884	20.430	24	836.200	206.164	1.042.364
Gaziantep	17.484	18.578	30	613.878	64.262	678.140
Aydın	13.142	14.969	30	497.756	166.908	664.664
İzmir	7.294	13.023	28	472.550	94.269	566.819
Şanlıurfa	21.334	9.489	11	835.301	325.102	1.160.403
Adıyaman	14.641	7.748	18	437.566	540.888	978.454
Kilis	9.051	6.544	20	325.836	36.204	362.040
Siirt	5.417	6.377	43	147.570	28.002	175.572
Bilecik	3.278	6.032	34	176.490	7.860	184.350
Manisa	5.276	5.295	23	230.781	61.966	292.747
Mardin	1.803	2.965	42	70.705	40.062	110.767
Osmaniye	2.556	2.149	26	81.758	87.610	169.368
Karaman	1.715	1.814	45	40.620	44.560	85.180
Burdur	783	1.319	43	30.390	8.125	38.515
Çanakkale	973	881	28	31.855	35.980	67.835
Diyarbakır	1.119	857	22	38.302	6.052	44.354
TURKEY	102.691	109.609	31.714	243.810	167.199	221.562

According to the Turkish Statistical Institute, the production values of the provinces that are important in Turkey's pomegranate production are given (Table 1.2). In this context, pomegranate production is significant in 21 provinces in total. Among the provinces producing pomegranates, Antalya ranks first with 111,041 tons, Muğla ranks second with 73,183 tons, and Mersin ranks third with 66,595 tons. Diyarbakır ranks twenty-first in terms of pomegranate production and has a production of 857 tons (TUİK, 2016; Burkan, S., 2018).

Diyarbakır is under the influence of a harsh and continental climate and a semi-arid plateau climate. While the summers are dry, very hot and long, the winters are cold and rainy. The winters of this province, located in the Southeastern Anatolia Region, are less cold compared to Eastern Anatolia. The temperatures of this province mostly vary between +46.2°C and -24.2°C (Anonim, 2017b; Burkan, S., 2018).

The average annual temperature of this province is 15.6 °C, the average annual precipitation is 530 mm, the driest month is August (0 mm), the rainiest month is January (79 mm), the hottest month is July (29.7 °C) and the hottest month of the year is July (29.7 °C). The lowest temperature month was determined in January (2.2°C) (Anonim, 2017c; Burkan, S., 2018). When the climate characteristics of Diyarbakır are examined, it is seen that it is a province mostly suitable for pomegranate cultivation. The map of Diyarbakır province is given in Figure 1.2 (Anonim, 2017d; Burkan, S., 2018). When the map is examined, there are a total of 17 districts, 4 centers (Sur, Yenişehir, Kayapınar and Bağlar) and 13 others. In this context, fruit cultivation is carried out in all districts (Table 1.3).
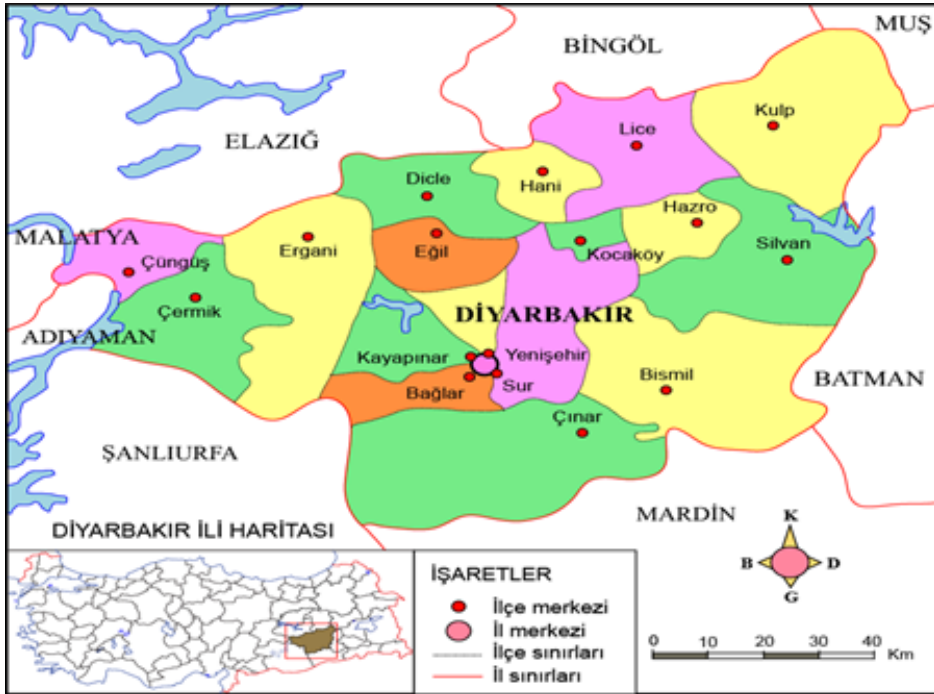
Figure 1.2. Diyarbakir province map (Anonim, 2017d; Burkan, S., 2018).

When Table 1.3 is examined, a total of 16 fruit species grow in Diyarbakır. A total of 23,328 tons of fruit were produced from these fruits. Mulberry ranks first with the highest fruit production with 10,147 tons, while Almond ranks second with 3,671 tons and Pistachio ranks third with 2,224 tons. The least production was in Olives with 31 tons.

Table 1.3. Diyarbakir fruit production values (TÜİK, 2016; Burkan, S., 2018)

Name of the product	Area of mass orchards	Production	Average yield per tree	Number of trees of fruit-bearing age	Number of trees that do not bear fruit
Mulberry	10.059	10.147	21	491.125	35.842
Almond	8.065	3.671	11	329.733	116.472
pistachios	4.603	2.224	14	154.241	72.335
Pear	4.846	1.701	21	80.930	37.328
Walnut	4.124	1.255	21	60.245	22.627
Plum	12.696	915	16	56.298	11.231
Pomegranate	1.119	857	22	38.302	6.052
Apricot	2.157	700	19	37.737	9.189
Fig	1.895	628	19	33.863	9.830
Cherry	1.358	275	14	19.202	5.183
Quince	817	265	17	15.855	1.860
Cherry	731	263	14	18.495	3.390
Peach	549	205	18	11.253	1.475
nectarine	4	111	15	7.438	143
Zerdali	154	80	16	4.850	1.470
Olive	45	31	7	4.600	2.850
Total	53.222	23.328	16.562	1.364.161	337.277

Pomegranate cultivation is carried out in 9 districts out of 17 districts of Diyarbakır (Table 1.4). According to this chart, the highest pomegranate production occurs in Çermik district with 335 tons, while Dicle ranks second with 218 tons. Kocaköy ranks seventh with 33 tons of pomegranate production. Hazro district ranks last with 13 tons. (TÜİK, 2016; Burkan, S., 2018).

Table 1.4. Pomegranate production values of Diyarbakır province
(TÜİK, 2016; Burkan, S., 2018)

District Name	Area of mass orchards	Production	Average yield per tree	Number of trees of fruit-bearing age	Number of trees that do not bear fruit	Total number of trees
Çermik	50	335	20	16.600	1.500	18.100
Dicle	70	218	37	5.950	1.440	7.390
Ergani	30	86	16	5.500	672	6.172
Lice	125	66	23	2.870	1.200	4.070
Eğil	28	50	22	2.250	0	2.250
Çüngüş	700	41	27	1.500	650	2.150
Kocaköy	60	33	14	2.400	250	2.650
Kayapınar	27	15	21	710	50	760
Hazro	29	13	25	522	290	812
Diyarbakır	1.119	857	22	38.302	6.052	44.354

Fruit production values of Kocaköy district (Table 1.5) are given (TUİK, 2016; Burkan, S., 2018). According to (Table 1.5), 7 fruit types, including Mulberry, Pomegranate, Almond, Nectarine, Peach, Apricot and Cherry, grow in this district. The most produced fruit type in this district was Pomegranate with 33 tons. The total production of pomegranate is almost equivalent to the production of all other fruits. According to the production values of the fruits grown in Kocaköy district, it would be beneficial to expand pomegranate cultivation in this region.

Table 1.5. Kocaköy district fruit production values (TÜİK, 2016; Burkan, S., 2018)

Name of the product	Area of mass orchards	Production	Average yield per tree	Number of trees of fruit-bearing age	Number of trees that do not bear fruit	Total number of trees
Pomegranate	60	33	14	2.400	250	2.650
Almond	60	19	9	2.170	530	2.700
Cherry	44	8	11	730	305	1.035
Peach	5	3	21	140	10	150
Nectarine	2	2	13	75	10	85
Apricot	6	2	16	125	10	135
Mulberry	1	1	18	55	2	57
Total	178	67	12	5.695	1.117	6.812

2. Conclusion

Pomegranate cultivation has been increasing in our country in recent years. Since the importance of pomegranate fruit for human health has increased, the demand for this fruit has increased. The economic value of pomegranate fruit has increased.

Positive developments in the transportation of this fruit can be considered as the start of breeding studies to obtain new, high quality and standard varieties needed in the domestic and foreign markets. For this reason, obtaining quality pomegranate varieties through breeding research carried out in the Aegean, Mediterranean and Southeastern Anatolia Regions and establishing commercial closed gardens with them are effective in expanding pomegranate production areas and increasing production.

REFERENCES

Anonim, 2008. Meyve suyu endüstrisi derneği.

Anonim, 2017a. Türkiye nar üretim yöreleri.

Anonim, 2017b. Diyarbakır   iklim   ve   bitki örtüsü.

 Anonim, 2017c. İklim: Diyarbakır.

Anonim, 2017d. Diyarbakır haritası.

Burkan, S. (2018). *Kocaköy (Diyarbakır) ilçesinde yetiştirilen önemli standart ve mahalli nar (Punica granatum L.) çeşitlerinin bazı ağaç ve meyve özellikleri* (Master's thesis, Fen Bilimleri Enstitüsü).

Dokuzoğuz, M., Mendilcioğlu, K., 1978. Ege Bölgesi nar çeşitleri üzerinde pomolojik çalışmalar.

Gündoğdu, M., Yılmaz, H., Canan, İ., 2015. Nar (*Punica granatum* L.) çeşit ve genotiplerin fizikokimyasal karakterizasyonu. *Uluslararası Tarım ve Yaban Hayatı Bilimleri Dergisi (UTYHBD)*1(2): 57 – 65.

Onur, C., 1983. *Akdeniz Bölgesi Narlarının Seleksiyonu* (doktora tezi). Alata Bahçe Kültürleri Araştırma Eğitim Merkezi Yayın No:46. Mersin.

Şimşek, M., İkinci, A. 2017. Narın (*Punica granatum* L.) insan sağlığına etkileri. *Harran Tarım ve Gıda Bilimleri Dergisi,* 21(4): 494-506

Şimsek, M., Kara, A., (2016). Diyarbakir fruit growing potential an overview. *International Diyarbakir Semposium* 2-5 October 2016, Diyarbakır-Turkey.

Tibet, H., Baktır, İ., 1991. Narlarda çiçeklenme derim. *Narenciye Araştırma Enstitüsü Dergisi,* 8(4): 66- 173, Antalya.

TÜİK, 2016. Türkiye İstatistik Kurumu. Yılmaz, C., 2007. *Nar.* Hasad Yayıncılık, Ağustos 2007, İstanbul.

EVOLUTION OF HOUSING CULTURE KONYA EXAMPLE

Mustafa Alper DÖNMEZ

(Ph.D. Research Asistant), Konya Technical University,
Faculty of Architecture and Design,
Architecture, Konya, Türkiye
E-mail: madonmez@ktun.edu.tr
ORCID: 0000-0002-7765-9888

1. Introduction

Human beings spend most of their lives in the structures they produce. In particular, the spaces we call "housing" are the type of buildings where most of this time is spent. Houses are important in many ways and are the subject of research because they are the structures with which human beings come into most contact. Many scientists have produced numerous works on Konya residences to date (Fırat, 1996; Kuşcu, 2006; Yoldaş, 2007; Dikici Köseoğlu, 2009; Çağlayan, 2010; Hatır, 2014; Hatipoğlu, 2015; Temizci, 2017). In these paper, Konya housing morphology, typology, development process, etc. By evaluating many issues, Konya housing production process has been tried to be clarified and passed on to future generations. In these studies produced on Traditional Konya houses (Berk, 1951; Sözen & Dülgerler, 1979; Ulusoy, 1992; Kunduracı 2000; Yazıcı 2010; Aygör, 2015; Dönmez, 2021), Apartments (Süslü, 2009; Ulusoy, 1999; Utku, 2015) and gated communities (Yetkin, 2009; Yıldız, 2011; Koç Şahinoğlu 2019) the features of the houses according to the period they were in analyzed and scientific results presented. In this way, each work, different from each other, created the housing history of Konya as a whole. However, since these studies were periodic or typological, they could not address Konya housing development with a holistic approach, and therefore the network of relationships in a broader perspective could not be revealed. In this study, all periods and typologies of Konya houses

were evaluated as a whole by conducting literature research and on-site investigations. In this way, it is aimed to produce original results that will contribute to the literature.

2. Konya Houses

When the literature studies produced about houses are examined, it is seen that residential buildings were formed under the influence of cultural (customs and traditions, beliefs and values, etc.), physical (topography, climate, location, natural resources, etc.), political (zoning laws, incentive laws, tax policies, etc.), social (family and social structure, demographic structure, etc.), economic (credit availability, income distribution, etc.) and technological (water, heating, electrical installation, etc.) factors in the periods when they were built and transformed over time. The effects of these factors on the production process lead to the formation of the unique identities of the houses and their emergence as different design products. Houses in Konya can generally be grouped under three main headings which is traditional houses, apartments and gated communities.

2.1. Traditional Konya Houses

As a result of the analyzes and findings obtained about traditional Konya houses, it is seen that there was a unity in traditional Konya houses from the early 19th century to the first quarter of the 20th century from plan design to material selection from facade layout to decoration (Dönmez, 2017). This stylistic unity is preserved similarly regardless of whether traditional Konya houses are built in the city or on its border (Berk, 1951). When the residential areas of traditional Konya houses are examined, it is seen that they are generally clustered around mosques, tombs and similar important historical and religious reference points (Dönmez, 2017). Traditional Konya houses are built in a detached style, generally in a large garden, with a maximum of 3 floors and an interior hall plan (Fig. 1).

Figure 1. Traditional Konya Houses **a-)** Nakipoğlu H. **b-)** Hasip Dede H.
c-) Kadem H. **d-)** Fahrettin Altay H. **e-)** Mimar H.

Since the residential garden is surrounded by high walls, the household can live freely here (Berk, 1951). The plan layout of traditional Konya houses is arranged in two parts as "Harem" and "Selamlık". The Selamlık section, where guests other than the household and close relatives are hosted, is called "Hariciye" in Konya (Dönmez, 2021). Hariciyes are generally designed to have their own entrance door, isolated from the living space of the household. In traditional Konya houses, each room is designed as a multifunctional independent living space (Dönmez, 2017). There are traditional reinforcement elements inside the rooms, which is a covered cupboard called gusulhane for washing, a Yüklük of drawers for storing belongings, fixed seating areas called Seki for sitting, etc. Aesthetic concern on facades; In general, it is tried to be produced with the mobility that the bay windows give to the facade and the composition of the facade parts proportional to each other (fig 1). It is noteworthy that in recent examples, decorations have become increasingly intense, especially on street facades (Aygör, 2005). This is an indication that traditional houses try to establish a relationship with the public space in their periodic development. The main building materials of traditional Konya houses are adobe, stone and wood, which are easily obtained from the region (Karpuz, 1999). In houses produced with masonry construction technique, stone materials are generally used in basement floor construction, adobe materials are used in walls, and wooden materials are largely used in windows, doors, cabinets, etc. It is seen to be used in places.

2.2. Apartment of Konya

After World War I (1915-1919), the Ottoman Empire was occupied and struggled for independence until 1923. The state and nation of the Republic of Turkey, established after 1923, undertook the economic difficulties of the collapsed Empire. Under these economic conditions, Hayat apartment building, the first apartment building in Konya, was built in 1937 (Ulusoy, 2007). Under these economic conditions, Hayat apartment building, the first apartment building in Konya, was built in 1937 (Ulusoy, 2007). However, World War II, which started in 1939 and lasted until 1945, both aggravated the economic conditions throughout the country and made it difficult to supply the resources required for construction technology (Altıparmak, 2021). For these reasons, the Kibrit apartment building, the second apartment building in Konya, could only be built in 1951 (Ulusoy, 1999). Although the apartment buildings mentioned above have divided flats "housing", the entire building is detached in accordance with the legal regulations. With the Condominium Law No. 634 enacted on 23 June 1965, the property rights of independent flats in the building became law (TBMM, 1965). With the enactment of the Condominium Law, it is observed that apartment building has accelerated in Turkey and Konya. Especially the developments that started with industrialization accelerated the migration from villages to cities from the 1960s to the 1980s and gradually increased the need for housing in city centers (Öktem, 2011). In order to prevent slums that occur due to the inability to meet the housing needs, illegal housing prevention zone (IHPZ) have been established by the municipalities and collective housing has been encouraged by the state in order to provide more housing production. As a result of the analysis and findings obtained on the Konya apartments examined between 1937 and 1993 within the scope of the study, it is seen that the apartments have a certain unity of style from their positioning to plan construction, material selection and their relationship with the streets (Fig 2). At the same time, it can generally be said that the apartments built in every region of Konya maintain almost the same character.
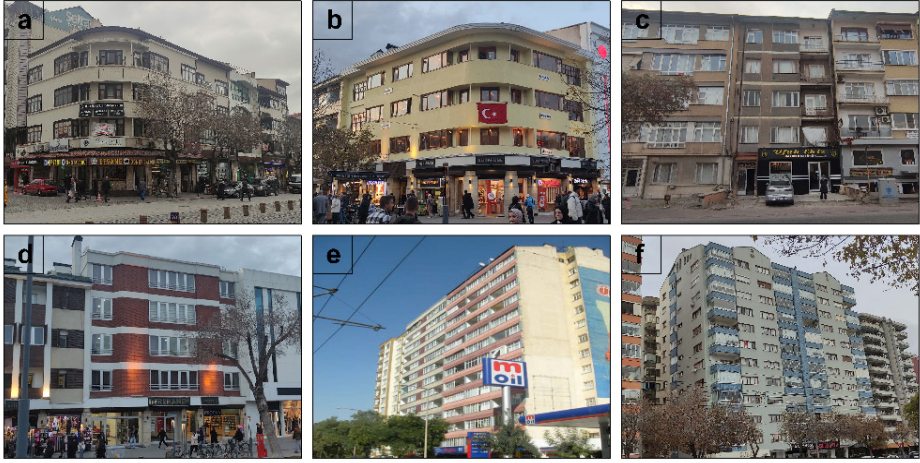
Figure 2. Konya Apartments **a-)** Hayat A. **b-)** Kibrit A. **c-)** Ankara A.   **d-)** Karacihan A. **e-)** Bakkallar A. **f-)** Altan A.

When the residential areas of apartment buildings are examined, it is seen that they are clustered especially in areas close to the new trade centers of the city and in ilegal housing prevention zone (Yenice, 2005; Ulusoy, 2006). Apartments, which are generally created by bringing together independent flats (housing) in a single building block with a very small common garden, are formed by repeating standard plan types, generally called 2+1, 3+1 and 4+1 within the building (Fig 2). The plan layout of apartments is generally divided into two parts: the entrance hall and the night hall. The rooms are clustered around these two interior halls according to their functions. The Hariciye, which was designed to host guests in traditional residences, has been replaced by sofas and living rooms in apartments. There are movable furniture is used such as couch, wardrobe etc. in the rooms which emerged with European influences instead of traditional fittings Seki, Yüklük, etc. Each room is designed to fulfill its own function. Bathrooms were designed in apartments instead of Gusülhanes, which were used for washing in traditional houses. Apartments block have been produced in the form of a multi-storey disproportionate structure, far from the human dimension, using the reinforced concrete carcass construction technique with the developing technology (Fig 2).

2.3. Gated Community of Konya

Gated communities began to be seen in the United States since the 1960s, and later in developed and developing countries (Şahinoğlu, 2019). In Turkey,

as a result of the increasing waves of migration from villages to cities due to the economic change and globalization in the 1980s, housing problems, unplanned urbanization and social segregation began to emerge in cities. As a result, gated community settlements began to appear first in Istanbul, where urbanization problems were first and intensely experienced, and then in other large cities that received immigration (Tümer, 2008). Especially with the enactment of the Mass Housing Law No. 2487 on July 8, 1981, the public authority encouraged the production of mass housing. However, while this law supports low-income users and cooperatives, it excludes upper and middle-income segments and build-sell construction companies (Karasu, 2017). With the new Mass Housing Law No. 2985 enacted in 1984, the housing size limit, which was limited to 100 m2 in the Mass Housing Law No. 2487, was increased to 150 m2, thus paving the way for luxury housing construction with public resources. (Karasu, 2017). Build-and-sell companies that had the opportunity for credit and government support began to rapidly produce Gated communities, after this date. Gated communities; where people in similar income groups prefer to live together (Roitman, 2010), public spaces are privatized and outside access is limited (Blakely and Snyder, 1997), they are mostly located in prestigious locations of the city (Kurtuluş, 2005) and offer various opportunities to their residents (Roitman, 2010; Şahinoğlu, 2019) are mass housing projects. At the same time, it is seen that gated communities are being planned to include mixed housing types in order to appeal to different users. While gated communities have advantages such as high quality of life, security, social facilities, partial privacy, and more specialized recreation areas, they also have disadvantages such as isolation from city life, gradual decrease in public spaces, privatization of social areas and social segregation. As a result of the analyzes and findings obtained on the Konya security sites examined between 1990 and 2020 within the scope of the study; It is seen that gated community buildings have a certain unity of style, from layout and floor plan design to material selection, from facade arrangements to residential areas (Fig 3). At the same time, it can be said that the gated communities built in every region of Konya maintain almost the same character. When the residential areas of gated communities with a large volume are examined, it is seen that they are clustered especially in urban transformation zones and city peripheries. It has been determined that the gated communities, which consist of 6-7 building blocks with an average of 7-12 floors around a very large garden, are isolated from the street and facing their own gardens (Fig 3). It is generally seen that these gardens have social facilities, camellias, walking paths, children's playgrounds and similar additional recreational areas planned

for the socialization of site users. Most of the gated community buildings, which are created by repeating and mixing standardized plan types, have a parking garage in the basement. By evaluating the requests and opinions of end users, it has been determined that they are generally produced by project offices with the sell-build model.
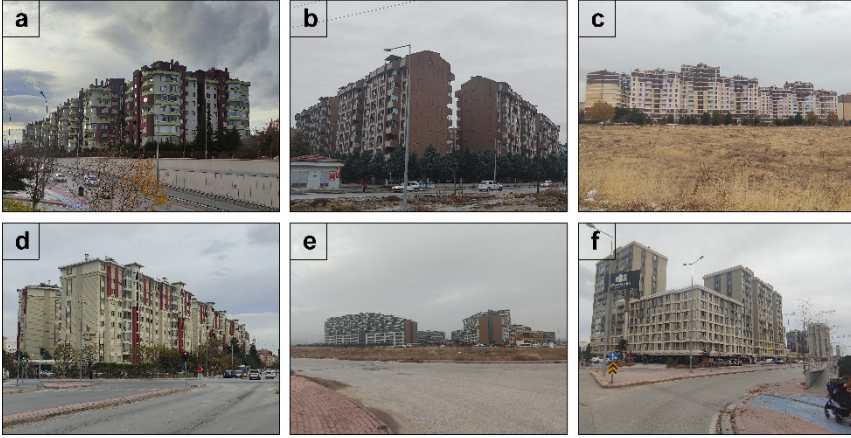
Figure 3. Konya Gated Communities **a-)** Güzelbahçe GC. **b-)** Beyzade GC. **c-)** Garanti Konut GC. **d-)** Altın Koza GC. **e-)** Naturapark GC. **f-)** Temaşehir

3. Method

Within the scope of the study, 6 examples of traditional houses, apartments and gated communities from 3 different typologies located in the center of Konya were examined on site and documented with photographs. In determining the houses selected to be used within the scope of the study, choices were made according to the historical development process of each typology and the location of the compound. In addition, examples with a maximum of 1 block and 25 flats were considered in the selection of apartment blocks typology, and examples with at least 4 blocks and 100 flats were considered in the selection of gated communities. 18 selected residential buildings were evaluated with a comparative method based on their layout plan and plan features.

4. Result and Discussion

Documenting the residences, which are an important component of Konya's urban fabric, with a typological study is extremely important for architectural history and architectural design studies. Within the scope of this study, the characteristic features of 3 different housing typologies were examined through

layout and plan schemes over the 18 housing examples examined. The general findings obtained are presented comparatively in Table 1 and Table 2.

Table 1. Layout Plan Feature

	Typology	Constr. Date	Residence Name	Compound Location	Garden/Land Ratio (%)	Distance Between Building Blocks (M)	Relationship with the Street	Outhouses	User and Usage Method
Layout Plan Features (1850)									
Traditional Turkish House	Mid 19th C.	Nakipoğlu House	Landmarks of the City	%80	20-30	Facing the Garden	Barn, Toilet, Kitchen etc.	Individual Private
	Mid 19th C.	Hasipdede House	Landmarks of the City	%70	20-30	Facing the Garden	Barn, Toilet, Kitchen etc.	Individual Private
	Mid 19th C.	Koyunoğlu House	Landmarks of the City	%60	20-30	Facing the Garden	Barn, Toilet, Kitchen etc.	Individual Private
	Mid 19th C.	KADEM House	Landmarks of the City	%50	5-10	Facing the Garden	Barn, Toilet, Kitchen etc.	Individual Private
	Early 20th C.	Fahrettin Altay House	Landmarks of the City	%35	5-10	Facing the Street	Not Found	Individual Private
	Early 20th C.	Mimar House	Landmarks of the City	%30	0	Facing the Street	Not Found	Individual Private
(1936)									
Apartments	1937	Hayat Apartment	Landmarks of the City	%1	0	Facing the Street	Not Found	Similar Type Common Usage
	1951	Kibrit Apartment	Landmarks of the City	%1	0	Facing the Street	Not Found	Similar Type Common Usage
	1962	Ankara Apartment	New Commercial Areas	%2	0	Facing the Street	Not Found	Similar Type Common Usage
	1976	Karacihan Apartment	New Commercial Areas	%1	0	Facing the Street	Not Found	Similar Type Common Usage
	1976	Bakkallar Apartment	illegal Housing Prevention zone	%3	0	Facing the Street	Not Found	Similar Type Common Usage
	1993	Altan Apartment	illegal Housing Prevention zone	%5	5-10	Facing the Street	Not Found	Similar Type Common Usage
(1994)									
Gated Communities	1994	Güzelbahçe Gated Communities	Urban Gentrification Zone	%50	10-30	Facing the Garden	Social Facility Cafeteria, Camellia etc.	Similar Type Common Usage
	2004	Beyzade Gated Communities	Urban Gentrification Zone	%50	10-30	Facing the Garden	Social Facility Cafeteria, Camellia etc.	Mixed Type Common Usage
	2005	Garanti Konut Gated Communities	Urban Fringe	%50	10-30	Facing the Garden	Social Facility Cafeteria, Camellia etc.	Mixed Type Common Usage
	2010	Altın Koza Gated Communities	Urban Gentrification Zone	%50	10-30	Facing the Garden	Social Facility Cafeteria, Camellia etc.	Mixed Type Common Usage
	2018	Naturapark Gated Communities	Urban Fringe	%45	0-30	Facing the Garden	Social Facility Cafeteria, Camellia etc.	Mixed Type Common Usage
	2020	Tema Şehir Gated Communities	Urban Gentrification Zone	%40	0-30	Facing the Garden	Social Facility Cafeteria, Camellia etc.	Mixed Type Common Usage
(2020)									

When the compound locations of the houses belonging to the 3 typologies in Table 1 are examined, it is seen that the traditional houses are clustered around landmarks of the city such as Mevlana Tomb and Alaeddin Mosque. As for the apartment buildings, it was determined that the early Hayat and Kibrit apartments were built at landmark points of the city, while the Bakkallar and Altan apartments were built in the illegal housing prevention zone, and the other two apartments were built on the new trade axis of the city. While it is observed that gated communities are generally built in urban transformation areas, as seen in the examples of Beyzade (scrapyard), Güzelbahçe (former tile factory), Altın Koza (former fire station) and Tema Şehir (former housing area); It is seen that some examples, such as Garanti Konut and Naturapark, were built on the urban fringes where large areas of land are available. When the Garden / Land ratios of the residences are examined, the ratios in traditional houses, apartments and sites vary between 30-80%, 1-5%, 40-50%, respectively. This shows that large gardens, which almost disappeared with the apartment typology, are being used again in gated communities. While it was determined that the distances between the buildings in the Konya Traditional houses examined varied between 10 and 30 meters, 5 of the apartments block selected as examples were adjacent and the distance between the blocks in 1 building was 5 to 10 meters. It is seen that this situation prevents the houses in the apartment block from benefiting effectively from the sun and wind. This problem has been solved by increasing the distance between blocks (0-30m) in Gated communities,. In addition, it is observed that gated communities are designed with an introverted plan scheme similar to traditional residences, with the extension of the garden usage area and the distance between blocks. This shows that, compared to the apartments block, the other two groups were designed with a more secure and privacy-oriented design approach, and that there is a bond between them based on culture and need. In addition, in traditional houses and gated communities with large gardens, the presence of outbuildings located in the garden is observed. When the outbuildings of the buildings were examined, while there were stables, toilets, kitchens, external rooms and similar additions in 4 of the traditional houses, no outbuildings were encountered in the other two. There are no outbuildings in apartment buildings due to land use. Additional areas such as coal sheds, boiler rooms and similar areas required due to necessity have been resolved in the basement floors. All gated communities have cafeterias, camellia areas, social facilities and similar outbuildings.

Table 2. Plan Feature

				Plan Features				
Typology	Const. Date	Residence Name	Number of Floor	Plan Scheme	Room Usage Type	Bathing Area	Guest Section	Furniture Type
Traditional Turkish House	Mid 19th C.	Nakipoğlu House	Ground + 1	Various Types According to Need	Multifunctional Common space	Private Use (Gusulhane)	Hariciye	Stationary Furniture
	Mid 19th C.	Hasipdede House	Ground + 1	Various Types According to Need	Multifunctional Common space	Private Use (Gusulhane)	Hariciye	Stationary Furniture
	Mid 19th C.	Koyunoğlu House	Ground + 1	Various Types According to Need	Multifunctional Common space	Private Use (Gusulhane)	Not Reached	Stationary Furniture
	Mid 19th C.	KADEM House	Ground + 1	Various Types According to Need	Multifunctional Common space	Private Use (Gusulhane)	Room / İnterior Hall	Stationary Furniture
	Early 20th C.	Fahrettin Altay House	Basement Ground + 2	Various Types According to Need	Multifunctional Common space	Shared Use (Bath)	Room / İnterior Hall	Loose Furniture
	Early 20th C.	Mimar House	Basement Ground + 1	Various Types According to Need	Single Function Shared space	Shared Use (Bath)	Room / İnterior Hall	Loose Furniture
Apartments	1937	Hayat Apartment	Basement Ground + 3	Standard Monotype	Single Function Shared space	Shared Use (Bath)	Saloon	Loose Furniture
	1951	Kibrit Apartment	Basement Ground + 3	Standard Monotype	Single Function Shared space	Shared Use (Bath)	Saloon	Loose Furniture
	1962	Ankara Apartment	Basement Ground + 4	Standard Monotype	Single Function Shared space	Shared Use (Bath)	Saloon	Loose Furniture
	1976	Karacihan Apartment	Basement Ground + 4	Standard Monotype	Single Function Shared space	Shared Use (Bath)	Room	Loose Furniture
	1976	Bakkallar Apartment	Basement Ground + 12	Standard Monotype	Single Function Shared space	Shared Use (Bath)	Saloon	Loose Furniture
	1993	Altan Apartment	Basement Ground + 11	Standard Monotype	Single Function Shared space	Shared Use (Bath)	Saloon	Loose Furniture
Gated Communities	1994	Güzelbahçe Gated Communities	Basement Ground 7 Floor	Standard Monotype	Multifunctional Private and Shared space	Shared Use (Bath)	Saloon	Loose Furniture
	2004	Beyzade Gated Communities	Basement Ground 8 Floor	Standard Mixed Type	Multifunctional Private and Shared space	Shared and Private Use (Bath/Shower)	Saloon	Loose and Embedded Furniture
	2005	Garanti Konut Gated Communities	Basement Ground 10-11 Floor	Standard Mixed Type	Multifunctional Private and Shared space	Shared and Private Use (Bath/Shower)	Saloon	Loose and Embedded Furniture
	2010	Altın Koza Gated Communities	Basement Ground 9 Floor	Standard Mixed Type	Multifunctional Private and Shared space	Shared and Private Use (Bath/Shower)	Saloon / Guest Room	Loose and Embedded Furniture
	2018	Naturapark Gated Communities	Basement Ground 6-9 Floor	Standard Mixed Type	Multifunctional Private and Shared space	Shared and Private Use (Bath/Shower)	Saloon / Guest Room	Loose and Embedded Furniture
	2020	Tema Şehir Gated Communities	Basement Ground 6-14 Floor	Standard Mixed Type	Multifunctional Private and Shared space	Shared and Private Use (Bath/Shower)	Saloon / Guest Room	Loose and Embedded Furniture

Timeline markers (left axis): 1850, 1936, 1994, 2020

When Table 2 is examined, it is observed that the number of floors has increased from 2 floors to 15 floors in parallel with the zoning legislation throughout the historical process. When the plan schemes of the 3 typologies are examined, it is observed that the planning in traditional houses is shaped according to need, while as a result of the standardization brought by industrialization, type projects have begun to be used in apartments and gated communities. However, while the use of a single type of plan scheme in apartment buildings ignores different user requests, the production of mixed type projects in gated communities ensures that various user requests are met. In this context, the similarity between traditional housing and gated community typologies is observed. When the room usage patterns of the houses are examined according to Table 2, it is seen that the rooms in traditional houses are generally designed to perform sleeping, washing, eating, sitting and similar functions together. However, while there are rooms specialized for functions in apartments and gated communities, it is seen that in closed communities there are also special spaces for personal use such as en-suite showers, dressing rooms, guest rooms and so on. When the Selamlik sections of the houses are examined; While the use of Hariciye is seen in 2 traditional houses, it is seen that the Selamlık space is designed as a interior hall and a guest room in the other 4 traditional houses. The Selamlık space has turned into a space called saloon in the apartments block, and there are additional guest rooms in 2 buildings along with the saloon in the gated communities. When the use of furniture in the rooms in residences is examined, the presence of fixed furniture such as Yüklük, Seki, Gusülhane, etc. in traditional residences draws attention, while the use of European style movable furniture is seen in all apartments block. In Gated communities, in addition to the use of movable furniture, built-in furnishing elements are generally used in the parent shower, dressing room, built-in wardrobe and kitchen. Only the Güzelbahçe site does not have an en-suite shower and dressing room.

When the results in Tables 1 and 2 are evaluated in general, the campus location selection, contractor and production philosophy of the 3 typologies are different. The number of floors is constantly increasing from past to present, and the average number of floors is different in each typology. However, when looking at the garden/land usage ratio, it is seen that there are similarities between traditional residences and gated communities and that the use of large gardens is preferred, while in apartment buildings, not much space is allocated for gardens due to land usage. Additionally, when the distances between the blocks are examined, it is seen that there is a similarity between traditional houses and gated

communities. While most apartment buildings are planned in an adjacent order, there is distance between blocks in traditional housing and gated communities. In addition, there are outbuildings designed for socialization purposes in the large gardens of Traditional Turkish houses and gated communities. When the relationships of the buildings belonging to the 3 typologies with the street are examined, it is seen that the traditional houses and the gated communities are designed oriented towards their own gardens, while the apartments are designed directly towards the street. In this context, it can be seen that traditional houses and gated communities are planned in a similar way, with a design approach that gives more importance to privacy, meets the need for security, and provides more opportunities for socialization than apartments. When viewed as a plan scheme, in traditional houses the number of rooms is designed according to need, while in apartments, type projects are preferred with the standardization brought by the industry, and in gated communities, mixed type projects developed for various users in the middle and upper segments of the society are preferred. Considering the room uses, unlike traditional houses, apartments and housing estates have spaces specialized according to function, while there are also spaces for private use in the housing estates, as in traditional houses.

5. Conclusion

Typological research on houses, which are an important component of Konya's urban fabric, is very important for architectural design, architectural history and urban morphology studies. Within the scope of this study, three different housing typologies produced over a period of approximately 200 years were examined from different perspectives and the general findings were compiled within the scope of the study. When the 3 housing typologies built in different periods in Konya are examined in general, they prefer different regions in terms of settlement preference. User type, contractor and usage pattern differ in all three typologies. While traditional houses were built in a detached style, apartments and gated communities were built as mass housing. The Selamlık structure, designed to host guests, has transformed and preserved its existence in every typology. It is seen that some traditional Turkish house design features, which were ignored in apartment buildings built under Western influence, have been modernized and re-emerge in the recently produced gated communities. While large gardens, which provide free living space for their users, are not included in the apartment typology, especially in Traditional Konya houses, it is seen that they are modernized and included again in gated communities suitable

for public use. Similarly, while it is seen that the need for security, which is one of the user requirements, can be met with gardens and high walls surrounding the house in traditional houses, this need has been ignored and could not be met in apartments. As a result, the production of gated communities surrounded by high walls has become increasingly widespread in recent years, responding to the security expectations of users. In addition, while apartment buildings are designed towards the street, gated communities surrounded by high walls and traditional residences are planned with an understanding of their inner gardens. When the number of blocks and floors of housing types are examined, it is noted that as the process progresses, the number of floors of residential buildings and the areas they cover on the ground gradually increase. In this context, residential buildings from past to present; It is observed that they are expanding vertically and horizontally, and that they are no longer a unit that forms the urban texture, but are seeking to become a focal point with their contradictions to the urban texture. The findings obtained within the scope of this study are aimed to provide a basis for future housing research and to contribute to future housing designs.

REFERENCES

1. Altıparmak, E. (2021). Konutta değişim ve dönüşüm sürecinin analizi: Konya örneği [Master's thesis, Selçuk University- Hacettepe University] Konya. https://tez.yok.gov.tr/UlusalTezMerkezi/TezGoster?key=tqUiYt63sTQLTpoz-MJ92QmNGtb-N_vq4CyyDNnzcAnkTZbzPNkOSmQ4yxfFGOonT

2. Aygör, E. (2005). 20. yüzyıl ilk yarısı Konya evlerinde cephe ve demir parmaklıklar, (Publication No. 161720) [Master's thesis, Selçuk University] Konya, S.U. Campus Repository

3. Aygör, E. (2015). 19. yüzyıl sonu ve 20. yüzyıl başlarında Konya evlerinin mimari gelişimi ve değişimi, (Publication No. 422537) [Doctoral dissertation, Selçuk University] https://tez.yok.gov.tr/UlusalTezMerkezi/TezGoster?key=Br_XTptK8CZ70f0JGX9xEgTlRTgnE58d97KWzJkLcVx-1Pxom_rts01Kf0doL4P6K

4. Berk, C. (1951). Konya evleri, *İstanbul Matbaacılık T. A. O.*, 206.

5. Çağlayan. N., (2010). Kooperatifçilik yolu ile konut üretimimin Konya örneğinde irdelenmesi (Publication No. 275125) [Master's thesis, Selcuk

6. Dönmez, M.A. (2017). Konya evlerinde mahremiyet ve tevazunun mekana yansıması (Publication No. 467425) [Master's thesis, Selcuk University],https://

tez.yok.gov.tr/UlusalTezMerkezi/TezGoster?key=q3-d9QtLoVA2OMExHSkJ-paEMTLkUmJyGz8thPnRxDK6VR9PN1HTocoH_Hc0dS9iS

7. Dönmez, M. A. (2021). Konutlarda dönemsel farklılıkların tespiti için derin öğrenme tabanlı bir cephe analiz yöntemi: Konya örneği (Publication No. 714933) [Doctoral dissertation, Konya Tecnical University] https://tez.yok.gov.tr/UlusalTezMerkezi/TezGoster?key=5XiSE4yCP_gmnukpMEp65X-f9QjN-sOz8K4vATAC-r2PvXuMw1HaIbheZx4i4OkDT

8. Köseoğlu, B. D. (2009). 1950-1970 yılları arasında yapılan müstakil konut alanlarında değişim: Konya örneği. (Publication No. 245785) [Master's thesis, Selcuk University]

9. Kunduracı O., (2000). Konya Evlerinden Süsleme Örnekleri, Yeni ipek yolu Konya ticaret odası dergisi, Özel Sayısı-3, Pp: 8-13.

10. Fırat, N. (1996). 1900-1930 Yılları Arasında Konya'da Türk Mimarisi. (Publication No. 51705) [Doctoral dissertation, Ankara University]

11. Hatipoğlu. B. (2015), el yönetimler yoluyla üretilmiş toplu konut projelerinde kullanıcı memnuniyeti: Konya örneği, (Publication No. 418767) [Master's thesis, KTO Karatay University]

12. Hatır, M. E., (2014), Konya İli, Karatay İlçesi'nde Bulunan, Geleneksel Üç Evin Restorasyon Önerisi, (Publication No. 371633) [Master's thesis, Selçuk University]

13. Karasu M. A. (2017). Nasıl bir toplu konut idaresi, *The Journal of Social Sciences Institute*, Cilt: 1 Sayı: Özel Sayı – 4. ISSN: 1302-6879. http://www.yyusbedergisi.com/dergiayrinti/nasil-bir-toplu-konut-idaresi_377

14. Karpuz, H. (1999). Osmanlı'da konut mimarisi: Konya örneği, tarihi, *Kültürü ve Sanatıyla 3. Eyüp Sultan Sempozyumu: Tebliğler*, İstanbul, sayfa: 390-401.

15. Kurtuluş, H. (2005). İstanbul'da kentsel ayrışma, *Bağlam Yayıncılık*, İstanbul.

16. Kuşcu, A. C., (2006), Sürdürülebilir Mimarlık Bağlamında Geleneksel Konya Evi Üzerine Bir İnceleme, (Publication No. 201325) [Master's thesis, Yıldız Tecnical University]

17. Öktem, B. (2011). İstanbul'da neoliberal kentleşme modelinin sosyo-mekansal izdüşümleri, *İ.Ü. Siyasal Bilgiler Fakültesi Dergisi*, (44), ss.23-40. http://dergipark.gov.tr/download/article-file/5274

18. Roitman, S. (2010). Gated communities: definitions, causes and consequences, *Urban Design and Planning*, Vol. 163 (dp1), pp. 31-38.

19. Sözen, M. ve Dülgerler, O. N., 1979, Konya Evlerinden Örnekler, *ODTÜ Mimarlık Dergisi,* 5 (1), 79-101.

20. Süslü, Ş. (2009). Konya'da apartman yapılarının tarihi süreç içinde cephe özelliklerinin gelişimi, (Publication No. 237332) [Master's thesis, Selçuk University], Konya. https://tez.yok.gov.tr/UlusalTezMerkezi/TezGoster?key=UPP_Zu9isEmWGFXFCBYasQBFa7FyLfHZx2jrSVqV_QlkEkjz85nbYrzOM4XHnVRJ

21. Şahinoğlu Koç. İ. (2019). Konya havzan bölgesindeki güvenlikli sitelerde cephe algısının araştırılması, (Publication No. 549121) [Master's thesis, Konya Tecnical University], Konya. https://tez.yok.gov.tr/UlusalTezMerkezi/TezGoster?key=T1mWGp9MngYYkCSgiJvtVjaUyM96hINROAgOay1kY-Dhk3pDDyRSCQ6f7VNcTmd9X

22. TBMM, (1965). Kat Mülkiyeti Kanunu, (Publication No. 23/6/1965/634), Ankara. https://www.mevzuat.gov.tr/MevzuatMetin/1.5.634.pdf

23. Tümer, H. Ö. and Dostoğlu N. (2008). Bursa'da dışa kapalı konut yerleşmelerinin oluşum süreci ve sınıflandırılması, *Uludağ Üniversitesi Mühendislik-Mimarlık Fakültesi Dergisi*, Vol: 13 Issue 2, Bursa.

24. Temizci. A., (2017). Değişen yaşam döngüsünde tüketim odaklı tasarlanan markalaşan lüks konutlar, (Publication No. 478636) [Master's thesis, KTO Karatay University] https://tez.yok.gov.tr/UlusalTezMerkezi/TezGoster?key=7lOJX8w_8PRQU1mSHU6jimsPLyJz_hDFAkxKRsvvG-zs2Z_LxpTHS0fXTFdNioDl

25. Ulusoy, M., (1992). 19. Yy. Konya Ev Mimarisine Avrupa Mimarisinin Etkileri, *Selçuk Üniversitesi*, Konya, 67-146.

26. Ulusoy, M. (1999). Konya'da apartman yapılarının tarihsel gelişimi, (Publication No. 85457) [Doctoral dissertation, Selçuk University] Konya. S.U. Campus Repository

27. Ulusoy, M., (2006). Konya'da apartman yapılarının tarihsel gelişimi, *Memleket A.Ş*, Konya.

28. Ulusoy, M. (2007). Geleneksel Konya evleri ve Avrupa etkisi, Konya, *Memleket İletişim A.Ş*,

29. Utku, T., (2015). Kafeye Dönüşmüş Apartmanlarda Kullanıcı Memnuniyeti: Konya Örneği, (Publication No. 397118) [Master's thesis, Gazi University]

30. Yazıcı, B. (2010). 19. Yy. Geleneksel Konya Konutlarında İşlev Dönüşümü ve Etkileri, (Publication No. 251399) [Master's thesis, Selçuk University], https://tez.yok.gov.tr/UlusalTezMerkezi/TezGoster?key=NtBAevXN-hYaNqJFoAcdBdmAlL9U9POnatXB8LIeH6yf63iV8HcjJygXyCiGaUZW

31. Yenice M. S. (2005). Kentsel planlama sürecinde Konya kent formunun gelişimi üzerine bir araştırma, (Publication No. 167646) [Master's

thesis, Konya Tecnical University], https://tez.yok.gov.tr/UlusalTezMerkezi/TezGoster?key=pPKKNi4sz1aRaVz8gj3jxGsJh9Ro5QuhUV34MQN7d-dk3L-LEQjy-eBcX2YLge-7z

32. Yıldız E. (2011). Konya'da dışa kapalı konut yerleşmelerinde kullanıcı memnuniyeti araştırması, (Publication No. 380908) [Master's thesis, Konya Tecnical University]

33. Yetkin, G. (2009). Toplu konut uygulamalarındaki fiziksel mekân özelliklerinin irdelenmesi "Konya örneği". (Publication No. 237360) [Master's thesis, Selcuk University]

34. Yoldaş, N. G. (2007). Anadolu geleneksel konut dokusundaki çıkmaz sokak işlevinin günümüzdeki durumunun irdelenmesi. (Publication No. 212373) [Master's thesis, Selçuk University]

COMPARATIVE ANALYSIS OF FATAL MOTORCYCLE ACCIDENTS IN TÜRKİYE WITH DATA MINING

Gizem KUTLUATA ÇINAR[1]& Özlem ALPU[2*]

[1]*Eskisehir Osmangazi University, Graduate School of Natural and Applied Sciences, Department of Statistics, Eskisehir*
E-mail:gizemkutluata5@gmail.com
ORCID: 0000-0003-4380-9435

[2]*(Prof.Dr.) Eskisehir Osmangazi University, Faculty of Science, Department of Statistics, Eskisehir*
E-mail:oalpu@ogu.edu.tr
ORCID: 0000-0002-2302-2953

1. Introduction

People's transportation habits and the transportation networks they have developed increase the density on these networks with the increasing population. In order to facilitate traffic, regulations continue to be made in many areas such as larger roads and zoning works. Despite this, accidents occur even in places where traffic is not heavy and inspections are carried out.

According to the report published by the World Health Organization (WHO) in 2018, 1.35 million people die every year in the world due to traffic accidents (WHO, 2018). Traffic accidents increase or decrease in parallel with the income status of countries. Again, according to the study conducted by the World Health Organization in 2020, the causes of death in low-income countries were investigated and it was determined that traffic accidents ranked 7th among the main causes of death. (WHO, 2020). In 2016, the highest rate of road traffic fatalities per 100,000 inhabitants was 26.6 in Africa and 20.7 in Southeast Asia, compared to 9.3 in Europe (WHO, 2018). When fatalities are categorized, 26% are pedestrians and cyclists and 28% are 2- or 3-wheeled motorized vehicles

(WHO, 2018). Various action plans around the world aim to reduce the number of casualties in traffic accidents.

Traffic accidents are classified as fatal, injury and property damage. In 2020, 983,808 traffic accidents occurred in Turkey, of which 150,275 were fatal/injurious and 833,533 were property damaged (TURKSTAT, 2021). While the number of fatalities per 100,000 vehicles in developed countries such as Germany and Japan is approximately 15, this number is 44 in Turkey (Çağlayan et al., 2010). In 2020, there were 4,866 deaths and 226,266 people were injured in traffic accidents in Turkey. Of these fatalities, 49% were drivers, 30% were passengers and 19% were pedestrians. When analyzing the factors causing the accidents, 88% of the accidents were caused by driver error. Looking at the months in which accidents occurred, the highest number of fatal and injury accidents occurred in August (TURKSTAT, 2021).

When analyzing traffic accidents involving fatalities and injuries, the distribution of fault status is classified as driver, passenger, pedestrian, vehicle, and road, and a total of 177,867 faults were identified in these accidents. (TURKSTAT, 2021).

According to Table 1, there are 24,144,857 registered vehicles in Turkey in 2020 (TURKSTAT, 2020). Vehicles were classified into 9 different types. Table 1 shows the number of vehicles, number of vehicles involved in fatal and injury accidents, number of drivers killed and number of injured drivers for each type.

Table 1. Accident Statistics by Vehicle Type (TURKSTAT, 2020)

Type of Vehicle	Type of Vehicle	Number of Vehicles Involved in Fatal/Injury Accidents	Number of Driver Deaths	Number of Injured Drivers
Car	13.099.041	122.493	876	43.768
Minibus	493.395	5.726	21	1.050
Bus	212.407	3.918	10	341
Pickup	3.938.732	36.987	233	10.955
Truck	610.979	6.007	74	1.829
Tow truck	248.691	5.851	100	1.920
Motorcycle-motorbike	3.512.576	45.753	735	39.918
Tractor	1.958.727	2.997	196	1.321
Other vehicle	70.309	13.393	159	9.786
Total	**24.144.857**	**243.125**	**2.404**	**110.888**

Table 2. Fatality Rate by Vehicle Type (TURKSTAT, 2020)

Vehicle type	Fatality rate %
Tractor	6,54
Tow truck	1,71
Motorcycle-motorbike	1,61
Truck(Lorry)	1,23
Other vehicle	1,19
Car	0,72
Pickup Truck	0,63
Minibus	0,37
Bus	0,26

Table 3. Injury Rate by Vehicle Type (TURKSTAT, 2020)

Vehicle type	Injuriy rate %
Motorcycle-motorbike	87,25
Other vehicle	73,07
Tractor	44,08
Car	35,73
Tow truck	32,81
Truck	30,45
Pickup	29,62
Minibus	18,34
Bus	8,70

Analyzing Table 2 and Table 3 in terms of the number of vehicles involved in fatal and injury accidents, it can be seen that tractor-type vehicles have the highest fatality rate at 6% and motorcycle and motorbike-type vehicles have the highest injury rate at 87%. In terms of the number of vehicles involved in fatal and injury accidents, motorcycle and motorbike drivers have the highest rate of 87% resulting in injury. This can be interpreted as accidents involving vehicles with less physical protection are more likely to result in death or injury.

In terms of time and practicality, the use of motorized two or three-wheeled vehicles has been increasing worldwide over the years, as they are a more convenient alternative to cars (Montella et al., 2019). Especially with the Covid-19 pandemic, people's desire to meet their needs without leaving home has led to a great increase in service, and competitive applications such as fast

delivery have entered our lives. However, the dense motorcycle traffic network has also brought rule-breaking and accidents.

Table 4. Accident Statistics of Motorcycle Type Vehicles (TURKSTAT, 2020)

Number of vehicles	Number of Vehicles Involved in Fatal/Injury Accidents	Number of Driver Deaths (Accident Scene)	Number of Driver Deaths (Post-Accident)	Total Number of Deaths Drivers	Total Number of Injured Drivers
3.512.576	45.753	230	505	735	39.918

According to Table 4, a total of 243,125 vehicles were involved in fatal and injury traffic accidents in Turkey in 2020, of which 45,753 were motorcycles and motorbikes. Therefore, 19% of the vehicles involved in fatal/injury traffic accidents are motorcycles. Of the total 2,404 driver fatalities, 735 were motorcyclists. In this context, 21% of the people who lost their lives in traffic accidents were motorcyclists. While the total number of injured drivers is 110,888, 39,918 of them are motorcyclists and 35% of the total number of injured people are motorcyclists (TURKSTAT, 2020).

In this study, three algorithms commonly used in data mining are used to determine the factors that are effective in determining whether there is a motorcycle or motorbike fatality, and to compare these algorithms in terms of various performance criteria.

2. Material and Method

From the dawn of time to the present day, the flow of information in every domain has been constant. Faster and more efficient ways of exchanging information have been developed, and access to information has been made possible by methods developed day after day. In integration with the developing technology, large data sets have emerged and various algorithms have been developed to obtain meaningful information from these data. In this way, fast, easy and more information has been accessed. Getting meaningful information by using algorithms after different data pre-processing discovering patterns and insights from large datasets falls within the scope of data mining.

It is possible to mention data mining wherever there is data. Especially medicine, banking, telecommunications, insurance, e-commerce, education and transportation are the leading areas where data mining techniques are used.

When examining the steps to discover information in data mining, the first step is to preprocess the existing data. Missing or inconsistent data is examined. When it is ensured that each data set is clean and processable, it is decided which technique to use. The results are evaluated using the chosen technique and algorithm, and the usefulness of the information obtained is investigated. Among the algorithms used for regression, the algorithm that most accurately shows the relationship between the dependent and independent variables is considered the algorithm with the best performance.

The techniques used in data mining are based on the characteristics of the data set. Models are classified as either descriptive or predictive. Predictive models aim to predict results by modeling the existing data set. Descriptive models, on the other hand, make definitions based on the relationships within the data.

Data mining models can be analyzed into different categories according to their functions: predictive models such as classification and regression models; descriptive models such as clustering models, association rules, and sequential patterns (Albayrak and Yılmaz, 2009).

In this study, classification techniques using Logistic Regression, Random Forest, and Naive Bayes algorithms were applied to the 2020 fatal-injury traffic accident data involving motorcycles and motorbikes.

Measures such as confusion matrix, accuracy, sensitivity or recall, specificity, precision, F-measure and ROC (receiver operating characteristics) curves were used to measure and compare the performance of the models obtained using data mining classification methods.

3. Application

The aim of this study was to determine the factors that affect the loss of life as a result of fatal motorcycle and motorbike accidents in Turkey in 2020 and to determine the classification model that gives the best prediction. The dataset of 39,832 accidents was preprocessed according to the modeling. All variables in the dataset were obtained from the data in the fatal-injury traffic accident report and the level status and descriptive statistics of the variables are shown in detail in Table 5.

Table 5. Variables, Levels and Descriptive Statistics in the Study

Variable	*Variable Level*	*Number*	*Percentage*
Type of Vehicle	Motorcycle	34.068	85,53
	Motorbike	5.764	14,47
Vehicle Location After the Accident	in accident scene	37.984	95,36
	Leaving the scene of an accident in case of obligation	1420	3,56
	Hit and run	428	1,07
Intended Use of the Vehicle	Private	39.279	98,61
	Commercial	284	0,71
	Police	181	0,45
	Other Public	59	0,15
	Military	15	0,04
	Foreign	14	0,04

Table 5. Variables, Levels and Descriptive Statistics in the Study
(Continued)

Vehicle Movement	Driving to in the right direction	34748	87,24
	Changing lanes	731	1,84
	From the left of the vehicle in front	444	1,11
	From the right of the vehicle in front	361	0,91
	Going backwards	13	0,03
	Joining to the traffic lane	272	0,68
	Leaving from the traffic lane	54	0,14
	Turning left	1286	3,23
	Turning right	585	1,47
	Making a u-turn	91	0,23
	Parked	17	0,04
	Stopped/waiting	186	0,47
	Slowing down	45	0,11
	One way/divided road going in the opposite direction	482	1,21
	Not detected	517	1,3
Vehicle İmpact Section	Front	24733	62,09
	Left	6333	15,9
	Right	6017	15,11
	Back	1282	3,22
	No visible damage	987	2,48
	Left front headlight	119	0,3
	Left front fender	87	0,22
	Right front headlight	74	0,19
	Right front fender	64	0,16
	Right rear headlight	41	0,1
	Right rear fender	22	0,06
	Under the vehicle	21	0,05
	Left rear fender	19	0,05
	Left rear fender	18	0,05
	Top of the vehicle	15	0,04

Table 5. Variables, Levels and Descriptive Statistics in the Study (Continued)

Vehicle Damage Rating	Light Damage	23.890	59,98
	Unable to Move	4820	12,1
	Functional damage	3949	9,91
	Heavy damage	3157	7,93
	No Damage	2743	6,89
	Not detected	1273	3,2
Vehicle Fuel Type	Gasoline	36.746	92,25
	Unspecified	1885	4,73
	Electricity	417	1,05
	Diesel	269	0,68
	CNG	236	0,59
	Other	168	0,42
	Gasoline-LPG	96	0,24
	Non-motorized	9	0,02
	Gasoline - Electricity	4	0,01
	Diesel-LPG	1	0
	LPG	1	0
Age of the driver	13-25	18564	46,61
	26-36	10591	26,59
	37-50	6639	16,67
	51-65	3010	7,56
	65+	946	2,37
	0-12	82	0,21

Table 5. Variables, Levels and Descriptive Statistics in the Study
(Continued)

Gender of the Driver	Male	38480	96,61
	Female	1352	3,39
Driving License	Yes	30206	75,83
	No	18406	46,21
	Not detected	1269	3,19
Educational Background of the Driver	High School	11750	29,5
	Primary	11014	27,65
	Unspecified	8947	22,46
	Secondary	4255	10,68
	University	3866	9,71
Test of the Driver	Checked by a health facility	25714	64,56
	Controlled by the traffic police	11302	28,37
	Unable to check	2816	7,07
Alcohol Test Result of the Driver	Dr. Uncertain	14558	36,55
	Non-alcoholic	11583	29,08
	Dr. Non-alcoholic	8146	20,45
	Unspecified	2733	6,86
	0.5 Pr. Less	977	2,45
	Dr. Alcoholic	424	1,06
	0.9-1.5 Pr	410	1,03
	2.0 Pr. Bigger	386	0,97
	1.6-2.0 Pr	285	0,72
	0.5-0.8 Pr	162	0,41
	0.2 Pr. Less	94	0,24
	0.2-0.5 Pr	74	0,19
Seat Belt Usage	Not Detected	35586	89,34
	Helmet Attached	2213	5,56
	No helmet	1105	2,77
	Helmet Not Attached	928	2,33
Accident Result of Driver	Injured	35317	89,27
	Not injured	4093	10,27
	Dead	145	0,37
	Crime scene abandonment	35	0,09

Table 5. Variables, Levels and Descriptive Statistics in the Study (Continued)

Driver Fault	Flawless	14472	36,33
	Not adapting the vehicle speed to the conditions required by the road, weather and traffic	12318	30,92
	Failure to observe the priority of passage at intersections, passages and narrow pavements	2868	7,2
	Failure to comply with lane following and changing rules	2537	6,37
	Hit from behind	2037	5,11
	Failure to follow the rules of Changing Direction	908	2,28
	Failure to comply with other traffic safety rules	773	1,94
	Entering places where there is a no-vehicle traffic sign	707	1,77
	Intersection, failure to observe priority of passage	697	1,75
	Failure to stop at a red light or stop sign	645	1,62
	Passing through no-passing zones	400	1

Table 5. Variables, Levels and Descriptive Statistics in the Study (Continued)

Accident Time	18:00-19:59	6.418	16,11
	16:00-17:59	6.125	15,38
	14:00-15:59	5.696	14,3
	12:00-13:59	4.788	12,02
	20:00-21:59	4642	11,65
	22:00-22:59	3290	8,26
	10:00-11:59	2947	7,4
	08:00-09:59	2405	6,04
	00:00-01:59	1772	4,45
	06:00-07:59	801	2,01
	02:00-03:59	687	1,72
	04:00-05:59	261	0,66
Accident Province	İstanbul	6205	15,58
	İzmir	3021	7,58
	Antalya	2562	6,43
	Mersin	1817	4,56
	Muğla	1772	4,45
	Hatay	1649	4,14
	Ankara	1535	3,85
	Bursa	1428	3,59
	Adana	1342	3,37
	Manisa	1275	3,2
	Aydın	1271	3,19
	Balıkesir	1060	2,66
	Gaziantep	927	2,33
	Konya	859	2,16
	Denizli	722	1,81
	Kocaeli	720	1,81
	Samsun	622	1,56
	Şanlıurfa	621	1,56
	Osmaniye	501	1,26
	Tekirdağ	472	1,18
	Eskişehir	471	1,18
	Sakarya	471	1,18
	Çanakkale	427	1,07
	Kahramanmaraş	395	0,99

Table 5. Variables, Levels and Descriptive Statistics in the Study (Continued)

Accident Location	Settlement Location	37404	93,9
	Outside Settlement	2428	6,1
Road Type	Divided road	19586	49,17
	Two-way road	16190	40,65
	One-way road	3994	10,03
	Other	62	0,16
Road Pavement	Asphalt	36440	91,48
	Parquet	2922	7,34
	Concrete	173	0,43
	Surface Coating	139	0,35
	Stabilize	79	0,2
	Soil	79	0,2
Class of the Road	Road	27.727	69,61
	Street	5941	14,92
	State Road	3236	8,12
	Other	1443	3,62
	Highway	569	1,43
	Service road	268	0,67
	Provincial road	259	0,65
	Village road	135	0,34
	Connection road	126	0,32
	Facility (property) front or inside	78	0,2
	Parking area	42	0,11
	Forest road	8	0,02
Horizontal Condition of the Road	Straight road	36888	92,61
	Curve	2667	6,7
	Dangerous curve	277	0,7

Table 5. Variables, Levels and Descriptive Statistics in the Study (Continued)

Vertical Condition of the Road	No slope	33211	83,38
	Sloping	6394	16,05
	Dangerous slope	154	0,39
	Hilltop	73	0,18
Intersection Status	No intersection	20938	52,57
	Four-way	7754	19,47
	Three-way (T)	6343	15,92
	Roundabout	1969	4,94
	Other type of intersection	1635	4,1
	Three-way (Y)	1041	2,61
	Interchange	122	0,31
	Level crossing	30	0,08
Gateway Status	No passage	36051	90,51
	Pedestrian crossing	3454	8,67
	School crossing	155	0,39
	Controlled railroad	143	0,36
	Uncontrolled railroad	29	0,07
Day Light Condition	Day	26235	65,86
	Night	12693	31,87
	Fore-night	904	2,27
Weather Condition	Clear	36.499	91,63
	Rain	1.960	4,92
	Cloudy	1.137	2,85
	Fog	115	0,29
	Watery	53	0,13
	Snowy	44	0,11
	Strong wind	19	0,05
	Hail	2	0,01
	Dust/sand storm	2	0,01

Table 5. Variables, Levels and Descriptive Statistics in the Study (Continued)

Surface of the Road	Dry	36287	91,1
	Wet/Damp	3321	8,34
	Other slippery surface	133	0,33
	Frosted	38	0,1
	Flooding/Puddle	32	0,08
	Snowy	21	0,05
First Aid Person	Health Team	37.500	94,15
	Citizen	2065	5,18
	Traffic police	267	0,67
Type of Accident	Side impact	18671	46,87
	Rollover/Skidding/Tumble	7653	19,21
	Rear impact	3849	9,66
	Mutual collision	3228	8,1
	Pedestrian collision	2278	5,72
	Collision with obstacle/object	982	2,47
	Side-by-side collision	939	2,36
	Run-off-the-road	890	2,23
	Collision with a stopped vehicle	435	1,09
	A Person falling from a vehicle	337	0,85
	Collision with a parked car	243	0,61
	Collision an animal	238	0,6
	Multiple collisions	51	0,13
	Pile up	24	0,06
	An object falling from the vehicle	14	0,04
Involved in Accident the Number of Vehicles	Two vehicles	27104	68,05
	Single vehicle	11084	27,83
	Multi-vehicle	1644	4,13

Table 5. Variables, Levels and Descriptive Statistics in the Study (Continued)

Collision Location Status	On the road	37.004	92,9
	On the banquette	696	1,75
	Roadside (off the banquette)	562	1,41
	Pedestrian crossing	369	0,93
	Not detected	327	0,82
	On the sidewalk	300	0,75
	In the center median	289	0,73
	Other	255	0,64
	Level crossing	14	0,04
	Stop/Station	14	0,04
	School crossing	2	0,01
Accident Road Defect Status	No road problems contributed to the accident	39606	99,43
	Other road problem	111	0,28
	Single pothole on the road	48	0,12
	Lane collapse	25	0,06
	Loose material on the road surface	18	0,05
	Sitting on the wheel track	13	0,03
	Partial or single collapse	9	0,02
	Low banquette	2	0,01
Road Defect Status	No	35.913	90,16
	Yes	3785	9,5
	Not suitable	134	0,34
Pedestrian Road Status	No	27.208	68,31
	Yes	12.580	31,58
	Not suitable	44	0,11

Table 5. Variables, Levels and Descriptive Statistics in the Study (Continued)

Safety Lane/Banket Status	No	30.289	76,04
	Yes	9.456	23,74
	Not suitable	87	0,22
Total Deaths	0	39663	99,58
	1	154	0,39
	2	13	0,03
Whether there was a fatal accident	Not fatal	39.673	99,58
	Fatal	159	0,42
Whether there was an injury accident	Injury	39.673	99,6
	Not injury	159	0,4
Victim Type	Passenger	6.651	73,34
	Pedestrian	2.159	26,66
Age of Person Involved in Accident	13-25	4.209	43,18
	26-36	1.360	16,79
	37-50	1.146	14,15
	0-12	973	12,02
	51-65	732	9,04
	65+	390	0,98
Gender of the Person Involved in the Accident	Male	5616	60,56
	Female	3194	39,44
Pedestrian Defect Type	Flawless	7012	86,59
	Failure to obey traffic lights and signs	505	6,24
	Acting in a way that endangers traffic on the carriageway	309	3,82
	Other	97	1,2
	Failure to take warning measures to prevent collision in low visibility day and night	82	1,01
	Failure to obey traffic rules when crossing the road	37	0,46
	Entering the carriageway	34	0,42
	Not driving on the left side of the carriageway	22	0,27

Table 5. Variables, Levels and Descriptive Statistics in the Study (Continued)

Passenger's Helmet Condition	Helmet on	4713	58,2
	Unspecified	2159	26,66
	Not detected	532	6,57
	Yes	362	4,47
	No	332	4,1
Passenger's Position in the Vehicle	Back seat	4056	50,09
	Unspecified	2192	27,07
	Not detected	1369	16,91
	Intermediate Corridor	183	2,26
	Front seat	132	1,63
	On-vehicle	132	1,63
	Inside the safe	34	0,42
Accident Result of Person Involved in Accident	Injured	8788	99,74
	Dead	22	0,26

Analyzing the descriptive statistics of the variables shown in Table 5, the vehicle type is 85% motorcycle and 14% motorbike. The position of the vehicle after the accident is 95%, and 87% of the vehicles involved in the accident were traveling in the right direction. The part of the vehicle hit in the accident is the front part of the vehicle with a rate of 62%. The degree of damage to the vehicle after the accident is 59% for lightly damaged vehicles.

When the profile of the drivers involved in the accident was analyzed, it was found that 46% of the drivers were between the ages of 13 and 25. Regarding the gender of the drivers, it was found that 96% of the drivers were male, which is the gender group with the highest probability of being involved in an accident. It was found that 75% of the drivers had a driver's license. When the education level of the drivers involved in the accident was analyzed, it was found that 29% of the drivers were high school graduates and 64% of the drivers were checked by a health institution. In the post-accident situation of the drivers involved in the accident, it was found that most of the drivers were injured with a rate of 89%. This can be explained by the fact that there are more injured drivers than fatalities due to the high volume of traffic in the city and the fact that the speed limit in the city is not high. In the case of driver fault, 36% of the drivers involved in the accident were found to be at fault and 38% were found to be at fault for speeding.

Analyzing the months in which the accidents occurred, it was found that the most accidents occurred in August with a rate of 12%. It is assumed that the use of motorcycles and motorbikes is highest in the summer months, which is in parallel with the accidents. When the time of the accidents is analyzed, it is found that most of the accidents occur between 18:00-19:59 with a rate of 16%. This can be interpreted as the fact that the traffic flow is high during rush hour and this situation causes accidents.

Regarding the type of road on which the accidents occur, 49% of the accidents occur on divided roads and 91% of the accidents occur on asphalt roads. When analyzing the road type, 69% of the accidents occur on avenues. When analyzing the horizontal level of the road, it can be seen that 92% of the accidents occur mostly on straight roads and 83% of the accidents occur mostly on uneven roads. In the case of crossroads, 52% of the accidents occur in places where there are no crossroads and 90% of the accidents occur in places where there are no crossroads.

When the type of accident was analyzed, it was found that the most common type was side collision with 46% and two-vehicle collisions with 68%. When the crash location of the accidents is analyzed, it is seen that most of the collisions occur on the road with a rate of 92%. When it was analyzed whether there was any road defect affecting the accident, it was determined that there was no road defect with a rate of 99%.

When the injury rate after the accident was analyzed, it was found that there was at most 1 injured person with a rate of 80%. When the fatality rate after the accident was analyzed, it was found that there was no fatality with a rate of 99%.

4. Results

This study attempted to determine statistically significant variables that cause accidents by using observation data of 56 variables in 39,832 accidents involving motorcycles and motorbikes that resulted in fatalities in 2020, and to estimate the data mining method that provides the best performance in obtaining these results. Due to the imbalance in the data set, the data was balanced by oversampling. Then, fatal accident status was taken as the dependent variable and the variables determined to be statistically significant, validity-reliability criteria, and criteria based on the complexity matrix were examined to determine the data mining method that provides the best performance.

4.1. Determination of the Variables Affecting the Occurrence of Fatal Accidents

In 2020, a total of 159 fatal accidents involving motorcycles and motorized bicycles occurred, and 167 people lost their lives in these accidents. Among the 56 variables listed in Table 5, the best-first forward, best-first backward, and greedy stepwise algorithms are used to determine the fatal accidents involving motorcycles and motorbikes, and are listed in Table 6.

Table 6. Variables affecting the occurence of fatal accidents with variable selection algorithms

Index	Best First Forward	Best First Backward	Greedy Stepwise
1	Position of the vehicle after the accident	Position of the vehicle after the accident	Position of the vehicle after the accident
2	Vehicle Damage rating	Vehicle Damage rating	Vehicle Damage rating
3	Driver gender	Driver gender	Driver gender
4	Driver seat belt	Driver seat belt	Driver seat belt
5	Driver accident result	Driver accident result	Driver accident result
6	Driver fault	Driver fault	Driver fault
7	Accident settlement status	Accident settlement status	Accident settlement status
8	Road type	Road type	Road type
9	Weather conditions	Weather conditions	Weather conditions
10	Accident road defect	Accident road defect	Accident road defect
11	Damaged element	Damaged element	Damaged element
12	Passenger/Pedestrian accident result	Passenger/Pedestrian accident result	Passenger/Pedestrian accident result

As a result of the variable selection algorithms, the number of variables that affect whether there is a fatal accident or not is determined to be 12 by all three algorithms.

4.2. Performance Metrics for Different Data Mining Algorithms in Fatal Accidents

In order to compare the reliability values obtained by using different data mining classification methods, the number of correctly classification (CCN), correct classification rates (CCR), kappa statistics, mean absolute error (MAE),

root mean square error (RMSE) and relative absolute error (RAE) values are calculated separately from the criteria used and are shown in Table 7.

Table 7. Reliability Measures for Fatal Accidents

Method	CCN	CCR (%)	Kappa Stat.	MAE	RMSE	RAE	RRAE
Naive Bayes	61.440	96,69	0,934	0,049	0,157	9,83	31,30
Random Forest	**62.701**	**98,69**	**0,973**	**0,018**	**0,095**	**3,61**	**18,91**
Logistic Regression	62.019	97,60	0,952	0,033	0,131	6,66	26,23

From Table 7, we see that the Random Forest algorithm gives the best results in all reliability criteria. It is followed by logistic regression. The validity measures are shown in Table 8.

Table 8. Validity Criteria for Fatal Accidents

Method	True Positive Rate	False Positive Rate	Sensitivity	Recall	F-Measure	MCC	ROC Area	DG Curve
Naive Bayes	0,967	0,033	0,967	0,967	0,967	0,934	0,996	0,996
Random Forest	**0,987**	**0,013**	**0,987**	**0,987**	**0,987**	**0,974**	**0,999**	**0,999**
Logistic Regression	0,976	0,024	0,976	0,976	0,976	0,952	0,998	0,998

From Table 8, we see that all the validity criteria obtained with the Random Forest method give the best results. These methods are Random Forest, Logistic Regression and Naive Bayes algorithms, respectively, when evaluated within the validity criteria considered. Similarly, the highest correct classification rate belongs to the Random Forest method with 98.67%. Logistic regression with 97.60%, followed by Naive Bayes with 96.69%.

5. Conclusion and Discussion

In this study, the factors affecting fatal accidents involving motorcycles and motorbikes in Türkiye in 2020 were identified using data mining

classification techniques, and it was found that the Random Forest algorithm gave the best prediction in terms of the performance criteria considered. In addition, the variables that determine the fatal accidents involving motorcycles and motorbikes were found to be the location of the vehicle after the accident, vehicle damage rating, driver gender, driver seat belt, driver accident result, driver defect, accident location, road type, weather condition, accident road defect, damaged element, and passenger/pedestrian accident result variables.

In 2020, among the variables that determine whether the result of motorcycle and motorized bicycle accidents occurring in Türkiye is fatal or not, the variable of accident location and the method that provides the best prediction result is the Random Forest method, which is similar to the findings in the study of Whab and Jiang, (2019). It was determined that helmet use, road type, driver gender variables are important variables in determining accidents, which is consistent with the study of Chang et al. (2019). The fact that road defect is an important variable in determining accidents is similar to the study of Shiau et al., (2015). In addition, Montella et al. (2019) also stated that road defect is an important variable in determining the severity of accidents.

It is seen that the driver seat belt variable is among the important variables determining fatal accidents. Here, it is important for motorcycle and motorized bicycle users to wear helmets, it is not enough to just put the helmet on their heads and go on a journey, but it is important to wear the locks in order to prevent the helmet from coming off the head in any collision and not to cause head trauma.

It can be seen that the settlement status variable is one of the important variables in determining fatalities. Higher vehicle speeds in rural areas compared to urban areas increase the likelihood of fatal accidents. Therefore, speed enforcement and motorcycle rider training should be more effective.

Accident road defects are among the important variables that determine other fatal accidents. It is very important for highway authorities and municipalities to show sensitivity in the maintenance and repair of roads in order to prevent accidents due to any road defects.

References

Albayrak, A.S. & Koltan Yılmaz, Ş. 2019. Veri Madenciliği Karar Ağacı Algoritmaları ile İMKB Verileri Üzerine Bir Uygulama. Süleyman Demirel Üniversitesi İktisadi ve İdari Bilimler Fakültesi Dergisi, (14) , s.31-52.

Chang, L.-Y., & Chen, W.-C. (2005). Data mining of tree-based models to analyze freeway accident frequency. Journal of Safety Research, 36(4), 365–375. doi:10.1016/j.jsr.2005.06.013.

Çağlayan, C., Hamzaoglu, O., Yavuz, C. İ., & Yüksel, S. (2010). Traffic Accidents Resulting in Death and Injury on an International Road Passing Through a City in Kocaeli, Turkey. Archives of Environmental & Occupational Health, 65(2), 5964.doi:10.1080/19338240903390255

Montella, A., Oña, R., Mauriello, F., Riccardi, M.R. & Silvestro G. 2019, A data mining approach to investigate patterns of powered two-wheeler crashes in Spain. Accident Analysis & Prevention, 134, 1-15p, 105251. doi:10.1016/j. aap.

Shiau, Y. R., Tsai, C. H., Hung, Y. H., & Kuo, Y. T. (2015). The application of data mining technology to build a forecasting model for classification of road traffic accidents. Mathematical Problems in Engineering, 1-8p, 170635.

TURKSTAT (2020). Karayolu Trafik Kaza İstatistikleri, 2020, https://data.tuik.gov.tr/Bulten/Index?p=Road-Traffic-Accident-Statistics-2020- 37436, access date: 04.03.2023.

TURKSTAT (2021). Karayolu Trafik Kaza İstatistikleri, 2021, https://data.tuik.gov.tr/Bulten/Index?p=Road-Traffic-Accident-Statistics-2021,4565 45658, access date: 02.03.2023.

Yontar, İ., Aras, B. 2018, Motosiklet Kullanımının Kentsel Trafik Güvenliği Üzerine Etkisi: İzmir Üzerine Bir Araştırma, Bitlis Eren Üniversitesi Sosyal Bilimler Üniversitesi Dergisi, 7,2, s.611-640.

Wahab, L., & Jiang, H. 2019. A multinomial logit analysis of factors associated with severity of motorcycle crashes in Ghana. Traffic Injury Prevention, 20(5), 521– 527.doi:10.1080/15389588.2019.1616699.

World Health Organization. (2018), Global status report on road safety, Ganeva, Licence: CCBY-NC-SA 3.0 IGO, p.11. World Health Organization, (2020), Global Status Report on Road Safety 2018.https://www.who.int/violence_injury_prevention/road_safety_status/2018/en/.

CHAPTER XIX

CLASSICAL OPTIMIZATION TECHNIQUES

Adi Omaia FAOURI[1] & Pelin KASAP[2*]

*[1](PhD Student), Department of Statistics, Ondokuz Mayis University,
Samsun, Turkey, e-mail: adi.faouri@gmail.com
ORCID:0000-0003-4499-1240*

*[2](Assoc. Prof. .Dr.), Department of Statistics, Ondokuz Mayis University,
Samsun, Turkey, e-mail: pelin.kasap@omu.edu.tr
ORCID:0000-0002-1106-710X
[*]Corresponding author*

1. Introduction

Optimization simply means to find the best possible solutions out of the available alternatives under the given circumstances. Optimization Techniques are very important in solving real life problems and various optimization techniques have been successfully used in different fields to solve problems. Every optimization problem has three main components: an objective function, independent variables, known as decision or design variables, and constraints. A physical problem can be mathematically expressed as an objective function of either one or more than one independent variables. The classical techniques are used for finding the optimum solution for optimization problems. According to the classical optimization theory these techniques operate under the assumption that the derivatives are continuous and the function is twice differentiable. These analytical techniques employ differential calculus procedures to locate the optimum positions. The practical uses of classical optimization techniques are restricted because certain practical subjects incorporate non-continuous and perhaps non-differentiable functions. The development of calculus-based optimization techniques provides a base for most numerical optimization techniques and helps to overcome the limitations of classical optimization methods (Cesari, 2012). Typically, numerical optimization

techniques begin from an arbitrary starting point that is chosen within a certain search space, near the real solution, and proceed iteratively toward the optimum solution. Optimization issues can be categorized according to the type of objective function that is in operation. When the objective function is nonlinear, gradient-based numerical techniques and elimination methods are recommended to used. Regarding the gradient-based techniques, numerical optimization algorithms have two main parameters to select: the length of each step and the directional path of the search. On the other hand, elimination techniques can also be used to figure out the optimal value of the complicated unimodel that involves non-continuous and possibly non-differentiable functions (Nocedal & Wright, 1999).

This chapter provides the required conditions for necessity and sufficiency for a local maximum or local minimum of both single and multivariable classical optimization techniques, along with examples to find the optimal solution. Furthermore, gradient-based numerical optimization techniques, including Steepest Descent and Newton, as well as elimination techniques, including Fibonacci in addition to Golden Section methods, are discussed.

2. The Required Conditions for Necessity and Sufficiency of Classical Optimization Techniques

The required conditions for necessity and sufficiency for the local optimum of a single-variable function are given by the next two theorems (Reklaitis, et al., 1983):

Theorem 2.1. If a function of one variable $f(x)$ is defined in the interval $a \leq x \leq b$ and has a local minimum at $x = x^*$, where $a < x^* < b$, and if the derivative $\frac{df(x)}{dx} = f'(x)$ exists as a finite number at $x = x^*$, then $f'(x) = 0$, it's necessary, which is still not adequately sufficient, in order to determine the function's optimum positions.

Theorem 2.2. Let the derivatives of a single-variable function

$$f'(x^*) = f''(x^*) = \cdots = f^{(n-1)}(x^*) = 0,$$

but $f^{(n)}(x^*) \neq 0$. Then $f(x^*)$ is

(i) a minimum value of $f(x)$ if $f^{(n)}(x^*) > 0$ and n is even; (ii) a maximum value of $f(x)$ if $f^{(n)}(x^*) < 0$ and n is even; (iii) neither a maximum nor a minimum if n is odd so in this case the point x^* is called a point of inflection. This is a required sufficiency condition for determining either the function's minimum or maximum position.

According to theorems 2.1 and 2.2, the required conditions for necessity and sufficiency must be achieved in order to determine the optimum locations. In other words, the basic steps to find the optimum point for any function of a single variable are to simply differentiate it once and set it to zero to be solved for x to determine x^*. Then the second derivative (n is even) is obtained to evaluate whether it is less than zero (concave), then a local maximum x^* exists, or greater than zero (convex), then a local minimum x^* exists, as illustrated in figure 2.1.
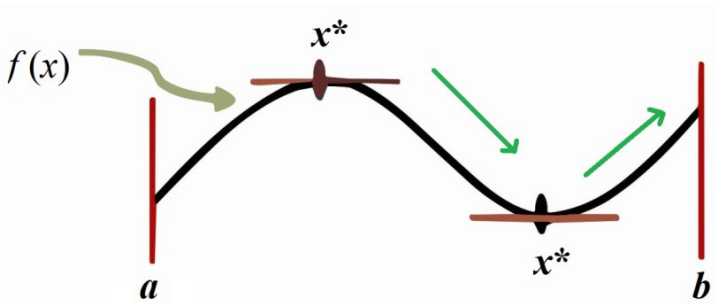
Figure 2.1

Example 2.1. Determine the local optimum points of the following function.

$$f(x) = 2x^3 - 3x^2 - 12x + 4$$

Solution:

Since
$$f'(x) = 6x^2 - 6x - 12 = 6(x + 1)(x - 2),$$
$$f'(x) = 0 \ at \ x = -1, x = 2.$$

The second derivative is
$$f''(x) = 12x - 6 = 6(2x - 1).$$

Since $f''(-1) = -18$, thus $x = -1$ is a local maximum. Therefore
$$f_{max}(x) = f(x = -1) = 11.$$

Since $f''(2) = 18$, and thus $x = 2$ is a local minimum. Therefore
$$f_{min}(x) = f(x = 2) = -16$$

and the maximum and minimum points are shown in figure 2.2.
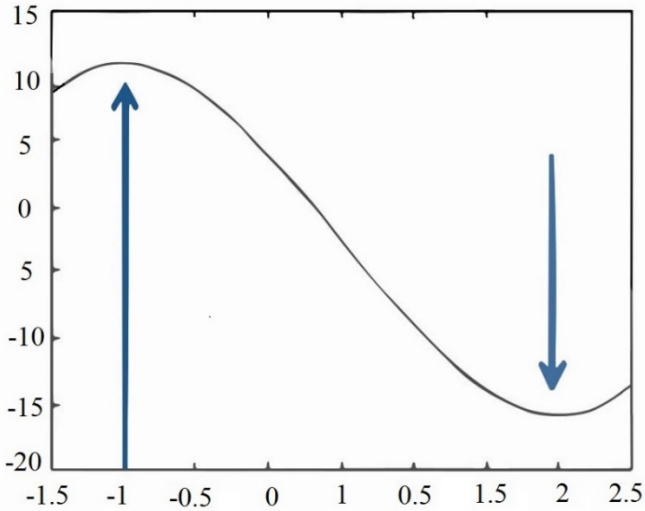
Figure 2.2

Finding the optimum points of any function with multivariables follows the same procedure; the only difference is that we are working with matrices. The required criteria for necessity and sufficiency conditions for a multivariable function's relative minimum (or maximum) points are provided by the next two theorems (Rao, 2019):

Theorem 2.3. If a function of multivariable $f(X)$ has a local minimum (or maximum) at $X = X^*$, and the $f'(X)$ exist at X^*, then

$$\frac{\partial f}{\partial x_1}(X^*) = \frac{\partial f}{\partial x_2}(X^*) = \cdots = \frac{\partial f}{\partial x_n}(X^*) = 0,$$

it's necessary, which is still not adequately sufficient, in order to determine the function's optimum positions.

Theorem 2.4. If a function of multivariable $f(X)$ has a relative optimum at $X = X^*$, then the second partial derivative matrix (the Hessian matrix) of $f(X)$ evaluated at X^* is (i) positive definite when X^* is a relative minimum point, and (ii) negative definite when X^* is a relative maximum point. This is a sufficient condition for determining the optimum positions of the function.

For calculation simplicity, say we have a function of two different variables $f(x_1, x_2)$, then the Hessian matrix of $f(X)$ is presented by

$$H = \begin{bmatrix} \dfrac{\partial^2 f}{\partial x_1^2} & \dfrac{\partial^2 f}{\partial x_1 x_2} \\ \dfrac{\partial^2 f}{\partial x_2 x_1} & \dfrac{\partial^2 f}{\partial x_2^2} \end{bmatrix}.$$

Note: It is easy to evaluate the positive or negative definiteness of a matrix A of n-order using its determinants as

$$A_1 = |a_{11}|, \quad A_2 = \begin{vmatrix} a_{11} & a_{12} \\ a_{21} & a_{22} \end{vmatrix}, \dots, A_n = \begin{vmatrix} a_{11} & a_{12} \cdots a_{1n} \\ a_{21} & a_{22} \cdots a_{2n} \\ \vdots & \vdots & \vdots \\ a_{n1} & a_{n2} & a_{nn} \end{vmatrix}$$

Only when every value in the matrices $A_1, A_2, A_3, \dots, A_n$ is positive, then the A matrix is considered positive-definite. On the other hand, if and only if the sign of A_j is $(-1)^j$ for $j = 1, 2, \dots, n$ then the matrix A is considered negative definite.

Example 2.2. Find the optimum locations of the following function

$$f(x_1, x_2) = 20x_1 + 26x_2 + 4x_1x_2 - 4x_1^2 - 3x_2^2$$

Solution:

According to the required necessity conditions for the $f(x_1, x_2)$ that's yield

$$\frac{\partial f}{\partial x_1} = 20 + 4x_2 - 8x_1 = 0, \qquad \rightarrow x_1 = \frac{20 + 4x_2}{8},$$

$$\frac{\partial f}{\partial x_2} = 26 + 4x_1 - 6x_2 = 0, \qquad \rightarrow x_1 = \frac{6x_2 - 26}{4}$$

After simplification

$$\frac{20 + 4x_2}{8} = \frac{6x_2 - 26}{4} \rightarrow x_2 = 9,$$

$$x_1 = 7.$$

The extreme points of the $f(x_1, x_2)$ are $x_1^* = 7$, $x_2^* = 9$. To determine if the solution is a minimum or a maximum, the sufficient condition is applied to $f(x_1, x_2)$. The partial derivatives of second order for $f(x_1, x_2)$ at (x_1^*, x_2^*) are presented by

$$\frac{\partial^2 f}{\partial x_1^2} = -8, \qquad \frac{\partial^2 f}{\partial x_2^2} = -6, \qquad \frac{\partial^2 f}{\partial x_1 x_2} = 4, \qquad \frac{\partial^2 f}{\partial x_2 x_1} = 4$$

The H matrix of $f(x_1, x_2)$ is given by

$$H = \begin{bmatrix} \dfrac{\partial^2 f}{\partial x_1^{2}} & \dfrac{\partial^2 f}{\partial x_1 x_2} \\ \dfrac{\partial^2 f}{\partial x_2 x_1} & \dfrac{\partial^2 f}{\partial x_2^{2}} \end{bmatrix} = \begin{bmatrix} -8 & 4 \\ 4 & -6 \end{bmatrix}$$

The determinants of H_1 and H_2 are

$$H_1 = |-8| = -8, \quad H_2 = \begin{vmatrix} -8 & 4 \\ 4 & -6 \end{vmatrix} = +32.$$

Since

$$\frac{\partial^2 f}{\partial x_1^2} = -8 < 0 \text{ and } \left(\frac{\partial^2 f}{\partial x_1^2} \frac{\partial^2 f}{\partial x_2^2} \right) - \left(\frac{\partial^2 f}{\partial x_1 x_2} \frac{\partial^2 f}{\partial x_2 x_1} \right) = 32 > 0,$$

that corresponds with the negative definite rule for the H matrix. Thus, $f(x_1, x_2)$ is negative-definite where (x_1^*, x_2^*) is located. Therefore

$$f_{max}(x_1, x_2) = 187$$

and the optimum points are shown in figure 2.3.
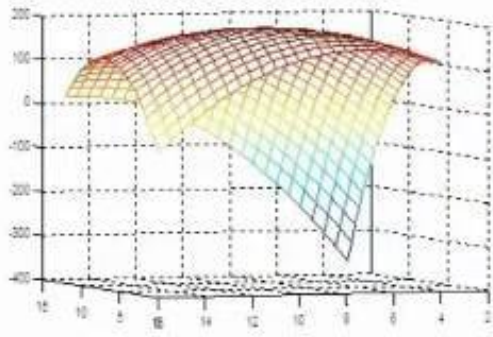
Figure 2.3

When the first derivatives $\partial f / \partial x_1 = \partial f / \partial x_2 = 0$, the H matrix may not be positive or negative definite at that point (x_1^*, x_2^*). When that occurs, the point (x_1^*, x_2^*) is referred to as a saddle point since it isn't considered either the local maximum or the local minimum in this case. For example the following function $f(x_1, x_2) = x_1^2 - x_2^2$ the first derivatives are

$$\frac{\partial f}{\partial x_1} = 2x_1 = 0 \rightarrow x_1 = 0, \qquad \frac{\partial f}{\partial x_2} = -2x_2 = 0, \rightarrow x_2 = 0$$

The partial derivatives of second-order of $f(x_1, x_2)$ at (x_1^*, x_2^*) are presented by

$$\frac{\partial^2 f}{\partial x_1^2} = 2, \quad \frac{\partial^2 f}{\partial x_2^2} = -2, \quad \frac{\partial^2 f}{\partial x_1 x_2} = 0, \quad \frac{\partial^2 f}{\partial x_2 x_1} = 0$$

The H of $f(x_1, x_2)$ is given by

$$H = \begin{bmatrix} \dfrac{\partial^2 f}{\partial x_1^2} & \dfrac{\partial^2 f}{\partial x_1 x_2} \\ \dfrac{\partial^2 f}{\partial x_2 x_1} & \dfrac{\partial^2 f}{\partial x_2^2} \end{bmatrix} = \begin{bmatrix} 2 & 0 \\ 0 & -2 \end{bmatrix}$$

The determinants of H_1 and H_2 are

$$H_1 = |2| = +2, \quad H_2 = \begin{vmatrix} 2 & 0 \\ 0 & -2 \end{vmatrix} = -4$$

Since

$$\frac{\partial^2 f}{\partial x_1^2} = 2 > 0, \text{and} \left(\frac{\partial^2 f}{\partial x_1^2} \cdot \frac{\partial^2 f}{\partial x_2^2} \right) - \left(\frac{\partial^2 f}{\partial x_1 x_2} \cdot \frac{\partial^2 f}{\partial x_2 x_1} \right) = -4 < 0$$

Given that this matrix lacks positive and negative definiteness, the point (x_1^*, x_2^*) is a saddle point. It is marked in red on the figure 2.4 shown below
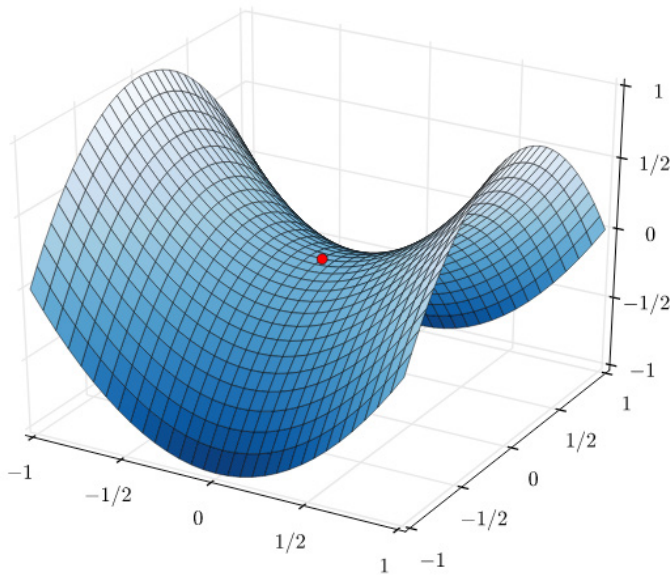
Figure 2.4

3. Gradient-Based Numerical Optimization Techniques

Gradient-based techniques lead the search by utilizing the gradient's information, or the objective function's direction. Until they reach a local optimum or a convergence requirement is satisfied, they begin at an initial random point and update iteratively by taking little steps along the gradient.

The distinction between all numerical techniques is the way they compute the step size along a specified search direction. The major advantages of gradient-based techniques can be stated as follows: they are quick and efficient when the objective function is smooth, convex, and differentiable. Additionally, they could enhance the search by exploiting the structure and features of the objective function. The primary drawback of gradient-based techniques is their sensitivity to the function's noise, step size, and initial point selection. Furthermore, the possibility of getting trapped at saddle points or local optima may prevent them from exploring the global optimum (Rao, 2019).

In this section, the two main gradient-based methods for solving single and multivariable optimization problems—steepest descent and Newton's method—are covered with examples.

3.1. Steepest Descent Technique

Particularly, the earliest technique for a nonlinear function's minimization is the classical steepest descent method. The gradient descent is also another name for this method. It is recognized as the first method for solving a nonlinear problem employing the gradient, as suggested by Cauchy in 1847 (Meza, 2010). As with all classical numerical techniques, the method begins with an initial point and continues by selecting the search directional path that creates a sharp angle with the gradient, which is considered to be negative, with specific steps to generate new estimates. However, as mentioned before, measuring the length of each step along a specified search directional path is the basis of nearly all of the minimization techniques. So the only challenge remaining is determining how long the step should be (Theodoridis, 2020). The steepest descent technique is considered efficient and simple, which is the main advantage of this method. The steps of the gradient descent technique can be summarized as follows:

1. Start with an initial point X_1 and set the iteration number as $i = 1$.
2. Calculate the search direction Si as $S_i = -\nabla f_i = -\nabla f(X_i)$
3. Determine the step length λ_i^* in the direction S_i as

$$f(X_i + \lambda_i^* S_i), \quad \frac{df}{d\lambda} = 0 \rightarrow \lambda_i = \lambda_i^*$$

3. Find the new point as $X_{i+1} = X_i + \lambda_i^* S_i = X_i - \lambda_i^* \nabla f_i$

4. Test the new point, X_{i+1}, for optimality. If X_{i+1} is optimum, stop the process. Otherwise, set the new iteration number $i = i + 1$ and go back to step 2 (Rao, 2019).

Example 3.1. Apply minimization for

$$f(x_1, x_2) = x_1 - x_2 + 2x_1^2 + 2x_1 x_2 + x_2^2$$

by Steepest descent technique using the initial point $X_1 = \begin{bmatrix} 0 \\ 0 \end{bmatrix}$. Stop after the first three iterations, unless the convergence is satisfied before.

Solution:

Iteration1:

$X_1 = \begin{bmatrix} 0 \\ 0 \end{bmatrix}$, The gradient of $f(x_1, x_2)$ is :

$$\nabla f = \begin{bmatrix} 1 + 4x_1 + 2x_2 \\ -1 + 2x_1 + 2x_2 \end{bmatrix} \to \nabla f_1 = \begin{bmatrix} 1 \\ -1 \end{bmatrix}$$

Therefore,

$$S_1 = -\nabla f_1 = -\begin{bmatrix} 1 \\ -1 \end{bmatrix} = \begin{bmatrix} -1 \\ 1 \end{bmatrix}$$

To determine X_2, we must find the length of the first step, λ_1^*. For this, we minimize $f(X_1 + \lambda_1^* S_1)$ based on λ_1^*.

$$f(X_1 + \lambda_1^* S_1) = f\left(\begin{bmatrix} 0 \\ 0 \end{bmatrix} + \lambda_1^* \begin{bmatrix} -1 \\ 1 \end{bmatrix}\right) = f\left(\begin{bmatrix} -\lambda_1^* \\ \lambda_1^* \end{bmatrix}\right)$$

$$= f(-2\lambda_1^* + \lambda_1^{*2})$$

we get

$$\frac{df}{d\lambda_1^*} = 0 \to -2 + 2\lambda_1^* = 0 \to \lambda_1^* = 1.$$

$$X_2 = X_1 + \lambda_1^* S_1 = \begin{bmatrix} 0 \\ 0 \end{bmatrix} + 1\begin{bmatrix} -1 \\ 1 \end{bmatrix} \to X_2 = \begin{bmatrix} -1 \\ 1 \end{bmatrix}$$

Test X_2

$$\nabla f_2 = \begin{bmatrix} -1 \\ -1 \end{bmatrix} = \begin{bmatrix} 0 \\ 0 \end{bmatrix}$$

Not optimum, next iteration.

Iteration 2:

$$X_2 = \begin{bmatrix} -1 \\ 1 \end{bmatrix}, \quad S_2 = -\nabla f_2 = -\begin{bmatrix} -1 \\ -1 \end{bmatrix} = \begin{bmatrix} 1 \\ 1 \end{bmatrix}$$

To minimize

$$f(X_2 + \lambda_2^* S_2) = f\left(\begin{bmatrix} -1 \\ 1 \end{bmatrix} + \lambda_2^* \begin{bmatrix} 1 \\ 1 \end{bmatrix}\right) = f\left(\begin{bmatrix} -1 + \lambda_2^* \\ 1 + \lambda_2^* \end{bmatrix}\right),$$

$$= f(-1 - 2\lambda_2^* + 5\lambda_2^{*2}),$$

we get

$$\frac{df}{d\lambda_2^*} = 0 \rightarrow -2 + 10\lambda_2^* = 0 \rightarrow \lambda_2^* = 0.2$$

$$X_3 = X_2 + \lambda_2^* S_2 = \begin{bmatrix} -1 \\ 1 \end{bmatrix} + 0.2 \begin{bmatrix} 1 \\ 1 \end{bmatrix} \rightarrow X_3 = \begin{bmatrix} -0.8 \\ 1.2 \end{bmatrix}$$

Test X_3

$$\nabla f_3 = \begin{bmatrix} 0.2 \\ -0.2 \end{bmatrix} \neq \begin{bmatrix} 0 \\ 0 \end{bmatrix}$$

Not optimum, continue to the next iteration since the gradient's components are not zero.

Iteration 3:

$$X_3 = \begin{bmatrix} -0.8 \\ 1.2 \end{bmatrix}, \quad S_2 = -\nabla f_3 = -\begin{bmatrix} 0.2 \\ -0.2 \end{bmatrix} = \begin{bmatrix} -0.2 \\ 0.2 \end{bmatrix}$$

To minimize

$$f(X_3 + \lambda_3^* S_3) = f\left(\begin{bmatrix} -0.8 \\ 1.2 \end{bmatrix} + \lambda_3^* \begin{bmatrix} 0.2 \\ -0.2 \end{bmatrix}\right) = f\left(\begin{bmatrix} -0.8 + 0.2\lambda_3^* \\ 1.2 + 0.2\lambda_3^* \end{bmatrix}\right),$$

$$= f\left(-1.2 - 0.08\lambda_3^* + 0.04\lambda_3^{*2}\right),$$

we get

$$X_4 = X_3 + \lambda_3^* S_3 = \begin{bmatrix} -0.8 \\ 1.2 \end{bmatrix} + 1 \begin{bmatrix} -0.2 \\ 0.2 \end{bmatrix} \rightarrow X_4 = \begin{bmatrix} -1 \\ 1.4 \end{bmatrix}$$

Test X_4

$$\nabla f(X_3) = \begin{bmatrix} -0.2 \\ -0.2 \end{bmatrix} \neq \begin{bmatrix} 0 \\ 0 \end{bmatrix} = \nabla f_4$$

Not optimum, next iteration. Since $f_4 \neq \begin{bmatrix} 0 \\ 0 \end{bmatrix}$ is not the optimum solution, we must go on to the next iteration in order to find the optimum one, but we stop here in accordance with the three iterations stated in the question. Unfortunately, this method is not primarily used since, in most real-world applications, it is known to be extremely slow and is rarely used in practice, regardless of its simplicity. Alternative, more efficient techniques like the Newton, conjugate gradient, and quasi-Newton methods are frequently utilized (Meza, 2010).

3.2. Newton's Method

A common classical optimization technique that uses gradients is Newton's method. Isaac Newton introduced it for solving nonlinear equations, and Joseph Raphson improved it later in 1690. That's why this technique is also

referred to as the Newton-Raphson method in the literature (Ypma, 1995). This method approximates the roots of the objective function by starting with an initial guess, then using tangent lines to create a A set of estimates until reaching the optimum solution or the convergence criteria is satisfied (Polyak, 2007). Unlike the steepest decent method, the Newton method in its classic form has a fixed step size of 1, to obtain the optimum for any positive definite quadratic function, and the directional path of the search is provided by the Hessian matrix (Venter, 2010). This method's primary benefit is that it locates roots quickly and effectively. The steps of Newton's method can be stated down as follows:

1. Start with an arbitrary initial point X_1 and set the iteration number as $i=1$.

2. Calculate the gradient as ∇f_i

3. Calculate the inverse of the H matrix H_i^{-1}

4. Calculate the search direction as $S_i = -H_i^{-1}\nabla f_i$

5. Find the new point as $X_{i+1} = X_i - H_i^{-1}\nabla f_i = X_i + S_i$

6. Test the new point, X_{i+1}, for optimality. If X_{i+1} is optimum, stop the process. Otherwise, set the new iteration number $i = i + 1$ and go back to step 2 (Rao, 2019).

Example 3.2. Minimize $f(x_1,x_2) = x_1 - x_2 + 2x_1^2 + 2x_1x_2 + x_2^2$ by using Newton's method with the initial point $X_1 = \begin{bmatrix} 0 \\ 0 \end{bmatrix}$. Stop after the first three iterations, unless the convergence is satisfied before.

Solution:

Iteration1:

The gradient of $f(x_1,x_2)$ is

$$\nabla f_1 = \begin{bmatrix} 1 + 4x_1 + 2x_2 \\ -1 + 2x_1 + 2x_2 \end{bmatrix} = \begin{bmatrix} 1 \\ -1 \end{bmatrix}.$$

The partial derivatives of second-order of $f(x_1,x_2)$ at (x_1^*, x_2^*) are presented by

$$\frac{\partial^2 f}{\partial x_1^2} = 4, \qquad \frac{\partial^2 f}{\partial x_2^2} = 2, \qquad \frac{\partial^2 f}{\partial x_1 x_2} = 2, \qquad \frac{\partial^2 f}{\partial x_2 x_1} = 2.$$

The H of $f(x_1,x_2)$ is

$$H_1 = \begin{bmatrix} \dfrac{\partial^2 f}{\partial x_1^2} & \dfrac{\partial^2 f}{\partial x_1 x_2} \\ \dfrac{\partial^2 f}{\partial x_2 x_1} & \dfrac{\partial^2 f}{\partial x_2^2} \end{bmatrix} = \begin{bmatrix} 4 & 2 \\ 2 & 2 \end{bmatrix}.$$

$$H_1^{-1} = \frac{1}{(4 \times 2) - (2 \times 2)} \begin{bmatrix} 2 & -2 \\ -2 & 4 \end{bmatrix} = \frac{1}{4} \begin{bmatrix} 2 & -2 \\ -2 & 4 \end{bmatrix} = \begin{bmatrix} 0.5 & -0.5 \\ -0.5 & 1 \end{bmatrix}$$

The directional path of the search S_1 is

$$S_1 = -H_1^{-1} \nabla f_1 \rightarrow S_1 = - \begin{bmatrix} 0.5 & -0.5 \\ -0.5 & 1 \end{bmatrix} \begin{bmatrix} 1 \\ -1 \end{bmatrix} = \begin{bmatrix} 1 \\ -1.5 \end{bmatrix}.$$

Determining X_2

$$X_2 = X_1 - H_1^{-1} \nabla f_1 = X_1 + S_1 = \begin{bmatrix} 0 \\ 0 \end{bmatrix} - \begin{bmatrix} 1 \\ -1.5 \end{bmatrix} = \begin{bmatrix} -1 \\ 1.5 \end{bmatrix} \rightarrow X_2 = \begin{bmatrix} -1 \\ 1.5 \end{bmatrix}$$

Test X_2

$$\nabla f(X_2) = \nabla f_2 = \begin{bmatrix} 0 \\ 0 \end{bmatrix} = \begin{bmatrix} 0 \\ 0 \end{bmatrix}$$

It is optimum stop.

As a result, for this quadratic function, in a single iteration, the method successfully converged. In spite of this method's main advantages, it is not particularly helpful in real-world applications because of the difficulty of computing the elements of the Hessian matrix at every step. However, the majority of gradient-based techniques just use first-order gradient information.

4. Elimination Techniques

As previously indicated, if the problems contain non-continuous and perhaps non-differentiable functions, then classical techniques for optimization have restricted usage for several of the difficulties that arise in many scientific areas. For that reason, other numerical techniques, including elimination methods, can be helpful in this situation. In the elimination methods, the first interval of uncertainty, which is the interval at which the optimum solution must be included, is step-by-step decreased to the desired precision. The primary limitation of these techniques is their requirement for a unimodel objective function to be optimized. In order to optimize an objective function that is known to be multimodel, its range must be separated into multiple parts, each of which must be handled independently as a unimodel function. This allows for the use of elimination techniques.The elimination method procedure is the opposite

of classical techniques, in which the objective function's values are initially obtained at a various of the design variables, and conclusions regarding the optimum solution are then made. (Gill, et al, 1981). In this section, the two main popular elimination methods for solving unimodel optimization problems—Fibonacci and golden section—are covered with examples.

4.1. Fibonacci Elimination Method

Among all the elimination methods, the most well-known, efficient, and complex method, according to the literature, is the Fibonacci Method, which uses the famous Fibonacci sequence in the picking of pieces from the objective function to get optimized. Leonardo of Pisa, also known as Fibonacci, initially presented the Fibonacci numbers in 1202 (Scott & Marketos, 2014). The Fibonacci numbers, $\{F_n\}$, are defined as

$$F_0 = F_1 = 1, \qquad F_n = F_{n-1} + F_{n-2}, n = 2,3,4,\cdots$$

which generates the sequence $1, 1, 2, 3, 5, 8, 13, 21, 34, 55, 89, \ldots$

The following requirements must be achieved for the Fibonacci search method to be applied to a real-world problem (Rao, 2019):

- It is necessary to know the first interval of uncertainty that contains the optimum.
- In the first uncertainty interval, the objective function that is being optimized must be unimodal.
- This technique is unable to determine the precise optimum. There will only be one interval that is known as a last interval of uncertainty.
- The number of objective function assesments to be used in the search or the necessary trials n needs to be determined in advance.

The steps of Fibonacci elimination method can be summarized as follows:

1. Define $L_0 = b - a$ the first interval of uncertainty in $a \leq x \leq b$ and n be the entire amount of trials that need to be carried out.

2. Define $L_2^* = \frac{F_{n-2}}{F_n} L_0$ and place the first two trials at points x_1 and x_2. This gives

$$x_1 = a + L_2^*, \qquad x_2 = b - L_2^*$$

3. Find $f(x_1)$ and $f(x_2)$ as shown in figure 4.1
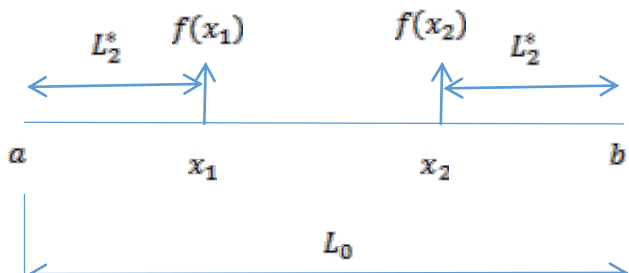
Figure 4.1

4. Compare $f(x_1)$ and $f(x_2)$

- If $f(x_1) < f(x_2)$, as shown in figure 4.2, delete $[x_2, b]$ and calculate $x_j = a + (x_2 - x_1)$, $j = 3, 4, ..., n$
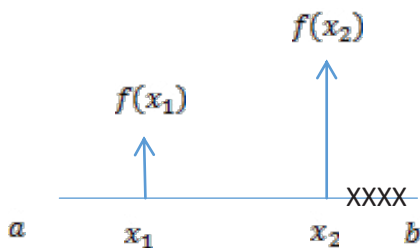
Figure 4.2

- If $f(x_1) > f(x_2)$, as shown in figure 4.3, delete $[a, x_1]$ and calculate $x_j = x_1 + (b - x_2)$, $j = 3, 4, ..., n$
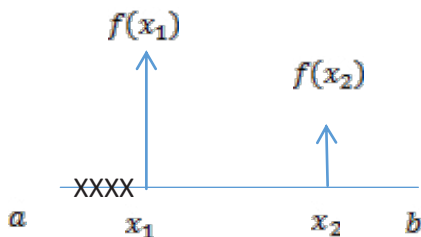
Figure 4.3

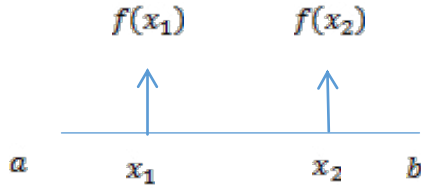- If $f(x_1) = f(x_2)$ as shown in figure 4.4, calculate $x_j = a + \frac{F_{n-j}}{F_n}(b - a)$, $j = 3, 4, ..., n$

Figure 4.4

5. Continue the process by repeating the steps until the number of trials n is finished and the last interval $[x, x + L_n]$ is located.

6. Calculate the proportion of the last to the first interval of certainty $\frac{L_n}{L_0}$.

Example 4.1. Minimize $f(x) = e^x - sinx$ in the interval [-1,1] by using the Fibonacci method with $n = 4$.

Solution:

Hence $n = 4$, $a = -1$, $b = 1$ and $L_0 = 1 - (-1) = 2$, that yield

$$L_2^* = \frac{F_{n-2}}{F_n} L_0 = \frac{2}{5} \times 2 = 0.8.$$

Thus, the positions of the first two trials are given by

$x_1 = a + L_2^* = -1 + 0.8 = -0.2$ with $f(x_1) = 1.0174$

and

$x_2 = b - L_2^* = 1 - 0.8 = 0.2$ with $f(x_2) = 1.0227,$

as shown in figure 4.5.
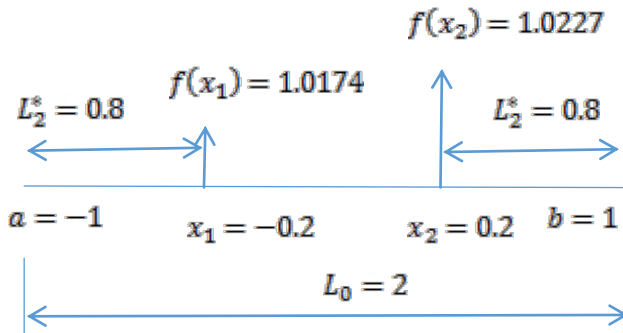
Figure 4.5

Since $f(x_1) < f(x_2)$, the interval $[x_2, b]$ will be deleted as shown in figure 4.6.
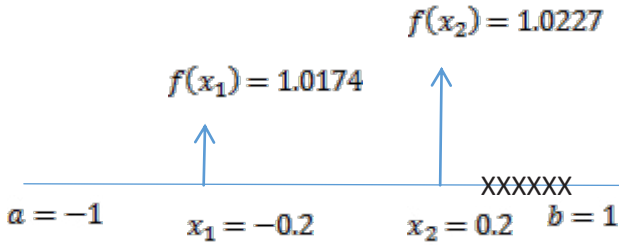
Figure 4.6

The uncertainty interval L_2 is calculated as $L_2 = 0.2 - (-1) = 1.2$ for the third trial which is placed at x_3. The value of x_3 is given as

$$x_3 = a + (x_2 - x_1) = -1 + (0.2 - (-0.2)) = -0.6$$

with $(x_3) = 1.1135$. Since $f(x_1) < f(x_3)$, the interval $[a, x_3]$ will be deleted as shown in figure 4.7.
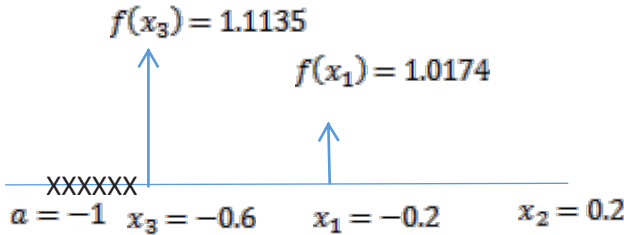
Figure 4.7

For the next trial the interval L_3 is calculated as $L_3 = 0.2 - (-0.6) = 0.8$ and it is located at x_4. The value of x_4 is given as

$$x_4 = x_3 + (x_2 - x_1) = -0.6 + (0.2 - (-0.2)) = -0.2$$

Since $x_4 = x_1$, the x_4 is found again by the following formula

$$x_4 = a + \frac{F_{n-j}}{F_n}(b - a) = x_3 + \frac{F_{4-4}}{F_4}(x_2 - x_3)$$

$$= -0.6 + \frac{1}{5}(0.2 - (-0.6)) = -0.6 + 0.16 = -0.44$$

with $f(x_4) = 1.070$. Since $f(x_1) < f(x_4)$ the interval $[x_3, x_4]$ will be deleted as shown in figure 4.8.

$$f(x_4) = 1.070$$

$$f(x_1) = 1.0174$$

XXXXXX

$x_3 = -0.6$ $x_4 = -0.44$ $x_1 = -0.2$ $x_2 = 0.2$
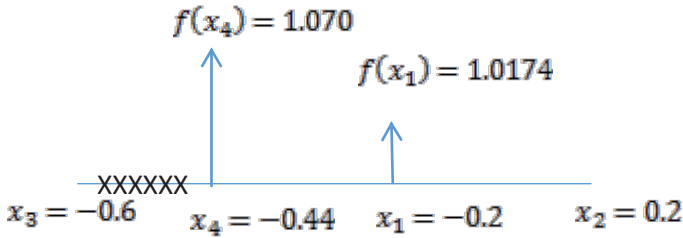
Figure 4.8

The last interval of uncertainty is obtained as

$$L_4 = [-0.44, 0.2] = 0.2 - (-0.44) = 0.64$$

as shown in the figure 4.9

$x_4 = -0.44$ $x_2 = 0.2$

$$L_4 = 0.64$$
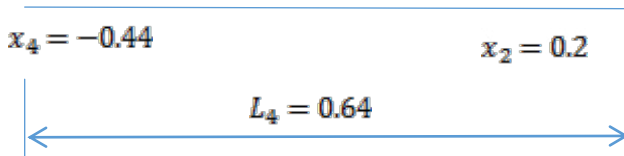
Figure 4.9

The proportion of the last to the first interval of uncertainty is

$$\frac{L_4}{L_0} = \frac{0.64}{2} = 0.32$$

as shown in figure 4.10.

$$L_0 = 2$$

$$L_4 = 0.64$$

$a = -1$ $x_4 = -0.44$ $x_2 = 0.2$ $b = 1$
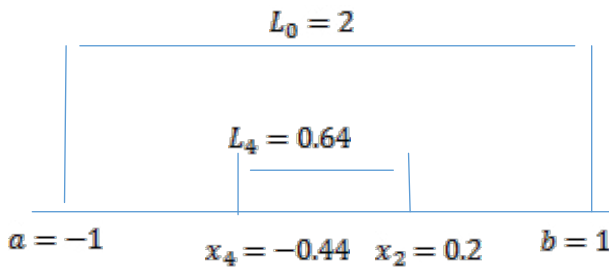
Figure 4.10

4.2. Golden Section Methods

The Golden Section Optimization Method is a unique optimization algorithm inspired by the golden ratio to find the optimum points for unimodal

objective functions by successfully narrowing the interval of certainty. This method, which is based on the Fibonacci sequence, is also known as the golden ratio method or the golden mean method. It makes use of the golden ratio, which is simply that if the length of a line is split into two uneven parts (a and b), the proportion of the whole $(a + b)$ to the bigger part (a) is equal to the proportion of the bigger (a) to the lesser (b). Its expressed in sympols as

$$\gamma = \frac{a+b}{a} = \frac{a}{b} \cong 1.618$$

The same as Fibonacci elimination technique this method based on the assessment of the objective function at different points in the certainty interval and reducing it as much as possible to reach the optimum.

The steps of golden section elimination method can be summarized like this:

1. Define $L_0 = b - a$ the first interval of uncertainty in $a \leq x \leq b$
2. Define

$$L_2^* = \frac{L_0}{\gamma^2} = \frac{L_0}{1.618^2} = 0.382 L_0$$

and position the first two trials at points x_1 and x_2, which provides

$x_1 = a + L_2^*, \qquad x_2 = b - L_2^*,$

3. Find $f(x_1)$ and $f(x_2)$, as shown in figure 4.11.
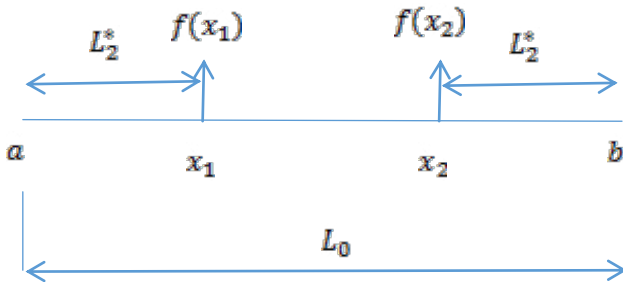
Figure 4.11

4. Compare $f(x_1)$ and $f(x_2)$
   - If $f(x_1) < f(x_2)$, as shown in figure 4.12, delete $[x_2, b]$ and calculate
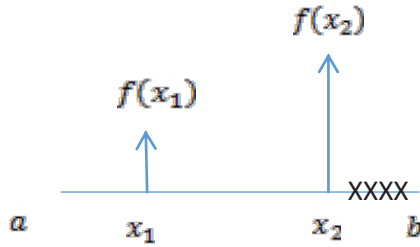$x_j = a + (x_2 - x_1), j = 3, 4, ..., n.$

$$f(x_2)$$

$$f(x_1)$$

XXXX

a x_1 x_2 b

Figure 4.12

- If $f(x_1) > f(x_2)$, as shown in figure 4.13, delete $[a, x_1]$ and calculate $x_j = x_1 + (b - x_2)$, $j = 3, 4, ..., n$.
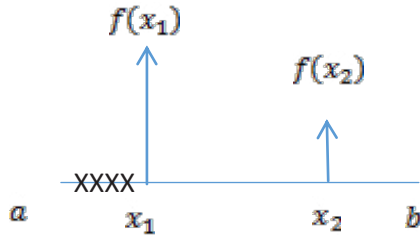
$$f(x_1)$$

$$f(x_2)$$

XXXX

a x_1 x_2 b

Figure 4.13

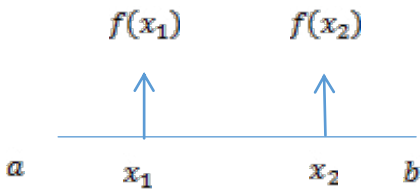- If $f(x_1) = f(x_2)$, as shown in figure 4.14, calculate $x_j = a + \frac{(b-a)}{\gamma^j}$, $j = 3, 4, ..., n$.

$$f(x_1)$$ $$f(x_2)$$

a x_1 x_2 b

Figure 4.14

5. Continue the process by repeating the steps until the number of trials n is finished and the last interval $[x, x + L_n]$ is located.

6. Calculate the proportion of the last to the first interval of certainty $\frac{L_n}{L_0}$.

Example 4.2. Minimize $f(x) = e^x - sinx$ in the interval [-1,1] by using the golden section method with $n = 4$.

Solution:

Hence $n = 4$, $a = -1$, $b = 1$ and $L_0 = 1 - (-1) = 2$, that yield
$L_2^* = 0.382 \times L_0 = 0.382 \times 2 = 0.764$
Consequently, the first two trials' positions are provided by
$x_1 = a + L_2^* = -1 + 0.764 = -0.236$ with $f(x_1) = 1.0236$
and
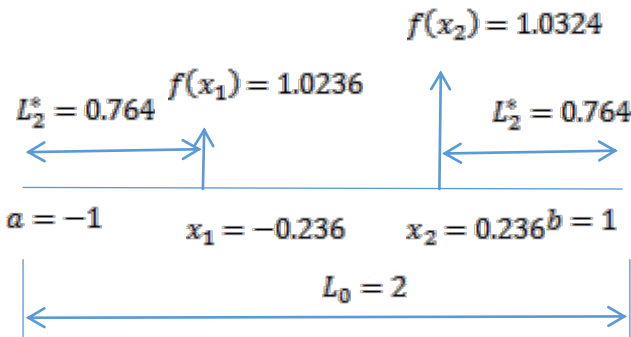$x_2 = b - L_2^* = 1 - 0.764 = 0.236$ with $f(x_2) = 1.0324$,
as shown in figure 4.15.

Figure 4.15

Since $f(x_1) < f(x_2)$, the interval $[x_2, b]$ will be deleted as shown in figure 4.16
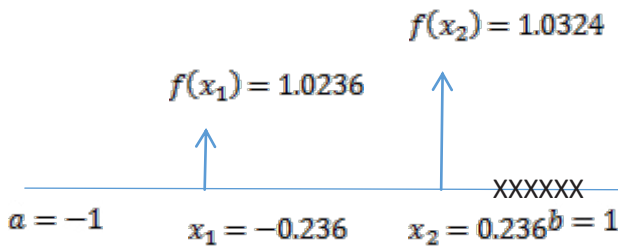
Figure 4.16

The uncertainty interval L_2 is calculated as $L_2 = 0.236 - (-1) = 1.236$ for the third trial which is placed at x_3. The value of x_3 is given as
$x_3 = a + (x_2 - x_1) = -1 + (0.236 - (-0.236)) = -0.528$

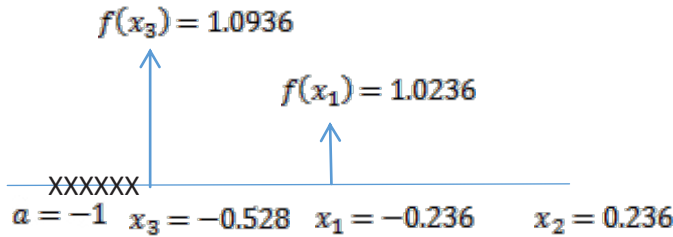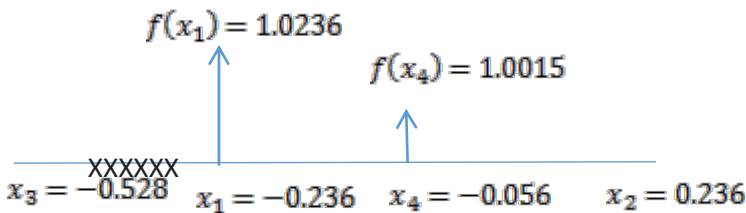with $f(x_3) = 1.0936$. Since $f(x_3) < f(x_1)$, the interval $[a, x_3]$ will be deleted as shown in figure 4.17.

Figure 4.17

For the next trial the interval L_3 is calculated as

$0.236 - (-0.528) = 0.764$

and it is located at x_4. The value of x_4 is given as

$x_4 = x_3 + (x_2 - x_1) = -0.528 + (0.236 - (-0.236)) = -0.056$

with $f(x_4) = 1.0015$. Since $f(x_4) < f(x_1)$ the interval $[x_3, x_1]$ will be deleted as shown in figure 4.18

Figure 4.18

The last interval of uncertainty is obtained as

$L_4 = [-0.236, 0.236] = 0.236 - (-0.236) = 0.472$,
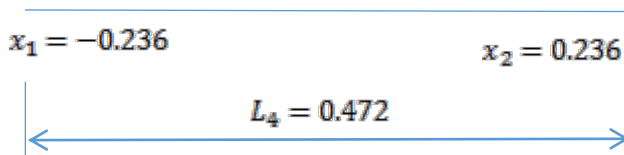
as shown in the figure 4.19.

Figure 4.19

the proportion of the last to the first interval of uncertinity is

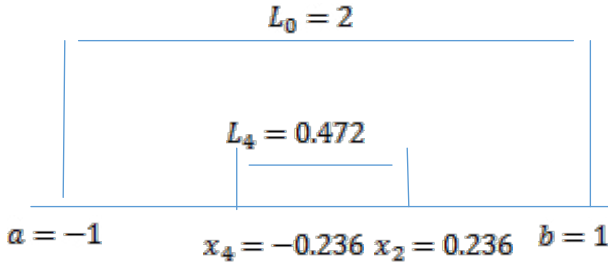$$\frac{L_4}{L_0} = \frac{0.472}{2} = 0.236,$$

as shown in figure 4.20.

$$L_0 = 2$$

$$L_4 = 0.472$$

$$a = -1 \qquad x_4 = -0.236 \;\; x_2 = 0.236 \quad b = 1$$

Figure 4.20

5. Conclusion

The classical optimization techniques are analytical techniques that use differential calculus to find the optimum of continuous and differentiable functions. According to the optimization theory, the required conditions for necessity and sufficiency must be achieved in order to detect a function's optimum positions when applying classical optimization techniques to a single or multivariable function. Classical optimization techniques based on gradient methods are used to find optimal solutions for nonlinear objective functions. All these techniques rely on the directional path of the search and the length of each step when optimizing functions, and calculating them is the main distinction between all gradient methods. One of the first techniques for minimizing an ordinary nonlinear function is the steepest descent method. It is a first-order method, meaning that at each step, it only takes into consideration the objective function's first derivative. However, in spite of its simplicity, it is known to be quite slow to converge, and it is not often used in practice. Alternatively, more fast and efficient techniques like Newton's method are used. Nevertheless, Newton's method is a two-order method, as it uses each of the first and second derivatives, which makes it costly for real-world applications due to the complexity of computing the elements of the Hessian matrix at every step. Elimination techniques can also be used to optimize nonlinear unimodal functions, regardless of whether they are discontinuous or non-differentiable. Between the elimination methods, Fibonacci and the golden section techniques are fast, accurate, robust, and derivative-free. However, unlike classical

techniques, elimination methods are not applied to multimodal functions. All classical optimization methods are sensitive to the selected initial point, which means that in some cases, other methods based on random search, like meta-heuristic algorithms, can be more efficient and can be recommended to optimize nonlinear objective functions.

References

Nocedal, J., & Wright, S.J. (Eds.). (1999). *Numerical optimization*. New York, NY: Springer New York.

Cesari, L. (2012). *Optimization—theory and applications: problems with ordinary differential equations* (Vol. 17). Springer Science & Business Media.

Reklaitis, G. V., Ravindran, A., & Ragsdell, K. M. (1983). Engineering optimization: Methods and applications.

Rao, S.S. (2019). *Engineering optimization: theory and practice*. John Wiley & Sons.

Meza, J.C. (2010). Steepest descent. *Wiley Interdisciplinary Reviews: Computational Statistics*, *2*(6), 719-722.

Theodoridis, S. (2020). Chapter 5–Online learning: the stochastic gradient descent family of algorithms. *Machine Learning, 2nd edn. A Bayesian and Optimization Perspective*, 179-251.

Raphson, J. Analysis aequationum universalis seu ad aequationes algebraicas resolvendas methodusgeneralis, et expedita, ex nova inflnitarum serierum doctrina deducta ac demonstrata, London, 1690, Microfilm copy: University Microfilms, Ann Arbor, MI.

Ypma, T.J. (1995). Historical development of the Newton–Raphson method. *SIAM review*, *37*(4), 531-551.

Polyak, B.T. (2007). Newton's method and its use in optimization. *European Journal of Operational Research*, *181*(3), 1086-1096.

Venter, G. (2010). Review of Optimization Techniques, in: Encycl. Aerosp. Eng., John Wiley & Sons, Ltd, Chichester, UK, pp. 1–12.

Gill, P.E., Murray, W., & Wright, M.H. Practical Optimization, Academic Press, London 1981.

Scott, T.C., & Marketos, P. (2014). On the origin of the Fibonacci Sequence. *MacTutor History of Mathematics*, *23*.